

**DESIGN, ANALYSIS AND EXPERIMENTAL
INVESTIGATION OF Cu-CI BASED INTEGRATED
SYSTEMS**

By

TAHIR ABDUL HUSSAIN RATLAMWALA

A Thesis Submitted in Partial Fulfillment
of the Requirements for the degree of Doctor of Philosophy
in
Mechanical Engineering

University of Ontario Institute of Technology
Faculty of Engineering and Applied Science

Oshawa, Ontario, Canada

© Tahir Abdul Hussain Ratlamwala, 2013

Abstract

Burning fossil fuels for power generation results in emissions of greenhouse gases such as carbon dioxide (CO₂) and air pollutants such as nitrogen oxides (NO_x) and sulfur oxides (SO_x), which are harmful to living creatures and the natural environment. Due to the negative effects of using fossil fuels, significant research is being carried out in the area of alternative energy carriers such as hydrogen, which can replace fossil fuels in the future. Hydrogen can be produced in a relatively environmentally friendly manner by using the copper-chlorine (Cu-Cl) thermochemical water splitting cycle (TWSC) due to its minimal reliance on fossil fuels, relatively lower operating temperature requirement and better overall efficiency as compared to other TWSCs. The electrolysis step of the Cu-Cl cycle is one of the most important steps, since it produces the hydrogen gas. The dependence of the Cu-Cl cycle on the electricity grid to run the electrolysis step impacts the overall environmental sustainability of the process.

The aim of this study is to perform experimental investigations of the hybrid photocatalytic hydrogen production reactor for the Cu-Cl cycle. The electrochemical, energy, exergy and exergoeconomic analyses of the hybrid reactors are carried out to observe the effects of variation in different operating parameters on the performance of the system. The comparative energy and exergy analyses of two solar-based integrated systems are also conducted to show how the performance of integrated systems can be improved by recovering reflected solar light intensity in the photocatalytic hydrogen production reactor.

The results obtained from the photo-electrochemical experimental study show that an increase in the voltage, solar light intensity, concentration of CuCl and concentration of ZnS increases the hydrogen production rate. The experimental results also show that the amount of voltage generated by inducing solar light intensity on titanium dioxide increases with an increase in the concentration of the titanium dioxide. The results based on electrochemical modeling of the hybrid reactor show that an increase in current density results in a higher voltage requirement by the hybrid photocatalytic reactor. The experimental hydrogen production rate and cost of hydrogen production is observed to

increase from 1.28 to 1.47 L/s and 3.28 to 3.36 C\$/kg, respectively, with a rise in reactor temperature. Energy and exergy analyses of the solar-based integrated systems show that the rates of hydrogen production by systems 1 and 2 increase from 126.9 to 289.4 L/s and 154.1 to 343.9 L/s, respectively, with a rise in solar light intensity. The exergy efficiencies of systems 1 and 2 increase from 47.98 to 50.82% and 56.87 to 59.64%, respectively, with a rise in ambient temperature.

Acknowledgements

I would like to express my sincere gratitude to my supervisor Prof. Ibrahim Dincer, for providing me with this extraordinary opportunity to work on the cutting edge project being pursued at UOIT. I am also greatly thankful to Prof. Mohamed Gadalla, who helped me throughout my master's study phase and provided me with useful guidance. I would also like to thank Prof. Ibrahim Dincer for his continued guidance, positive encouragement and moral support throughout my PhD study.

I would also like to thank Dr Zhaolin Wang, Dr. Calin Zamfirescu, Dr. Musharaf Rabbani, Dr. Halil Hamut, Dr. Ahmet Ozbilen, Mr. Sayem Zafar, Mr. Edward Secnik and Mr. Gord Koehne for their continuous support throughout my PhD study.

I am also greatly thankful to my parents; Abdul Hussain Ratlamwala and Nafisa Abdul Hussain Ratlamwala, my wife; Zahrah Tahir, my siblings; Hussain Abdul Hussain, Naquiya Abdul Hussain and Fatima Abdul Hussain and my family; Yousuf and Tasneem Ezzi, Asgher Ali and Hasina Ratlamwala, Shabbir Hussain and Hussaina Ratlamwala and Huzaifa and Mariam Ratlamwala for their unvarying encouragement and support throughout my study period. I will also like to thank my Uncle and Aunts, Dr. Ali Akbar and Tahira Bohra, Moiz and Rasheeda Motiwala and Shabbir and Fatima Beawewala for providing me with guidance and family like atmosphere in Canada. If there is any honor associated with this degree then it belongs to them.

Furthermore, the financial support provided by the Ontario Research Fund (ORF) and the Natural Sciences and Engineering Research Council of Canada (NSERC) are gratefully acknowledged.

Table of Contents

Abstract	i
Acknowledgements	iii
Table of Contents	iv
List of Tables	vi
List of Figures	vii
Nomenclature	xii
Chapter 1: Introduction.....	1
1.1 Energy Need.....	1
1.2 Hydrogen and the Environment	2
1.3 Thermochemical Water Splitting Cycles and the Environment.....	3
1.4 Motivation	4
1.5 Objectives.....	5
1.6 Summary of Approach and Rationale	8
Chapter 2: Literature Review.....	10
2.1 Cu-Cl Cycle for Hydrogen Production.....	11
2.2 Photocatalytic Hydrogen Production	13
Chapter 3: Experimental Setup and Procedure.....	19
3.1 Reactor Design	19
3.2 Design of Experiments	22
3.3 Experimental Setup	23
3.4 Experimental Procedure	28
3.5 Experimental Errors and Measurement Uncertainties	30
Chapter 4: Integrated System Development and Description.....	35

4.1	Hybrid Photo-electrocatalytic Hydrogen Production Reactor	35
4.2	Integrated Solar Thermal, Cu-Cl Cycle and Photocatalytic Reactor System.....	37
Chapter 5: Analyses and Optimization		45
5.1	Electrochemical Modeling	45
5.2	Energy and Exergy Analyses	48
5.3	Integrated System.....	51
5.4	Exergoeconomic Analysis.....	76
5.5	Optimization Study	77
Chapter 6: Results and Discussion		83
6.1	Experimental Results of Photo-electrocatalytic Hydrogen Production	83
6.2	Experimental Results of Photocatalytic Hydrogen Production.....	96
6.3	Results of Hybrid Photocatalytic Hydrogen Production Reactor.....	109
6.4	Results of Integrated Systems	119
6.5	Results of Optimization Study for Experimental System	140
6.6	Results of Optimization Study for Integrated Systems	142
Chapter 7: Conclusions and Recommendations		145
7.1	Conclusions	145
7.2	Recommendations	149
References.....		151

List of Tables

Table 2.1 Cost comparison of TWSCs hydrogen production methods	14
Table 2.2 Advantages and disadvantages associated with different photocatalysts category.....	18
Table 3.1. Factorial design of experiments for photocatalytic experiments.....	24
Table 3.2. Factorial design of experiments for photo-electrocatalytic experiments.....	25
Table 5.1. Parameters of photocatalytic hydrogen production reactor.	48
Table 5.2. The parameters assumed for integrated systems.....	78
Table 5.3. Thermodynamic properties of the Cu-Cl Cycle at sample running conditions.	79
Table 5.4. Cost of material of hybrid photocatalytic reactor.	80
Table 5.5. Constraints associated with the optimization study of hybrid photocatalytic reactor.	80
Table 5.6. Constraints associated with the optimization study of integrated systems.....	82
Table 6.1. Analysis of variance for rate of hydrogen production by photo-electrocatalytic experiments.....	85
Table 6.2. Analysis of variance for rate of hydrogen production by photocatalytic experiments.....	97
Table 6.3. Constraints for multi-objective optimization of hybrid reactor with respect to hydrogen production rate and cost of hydrogen production.	140
Table 6.4. Constraints for multi-objective optimization of hybrid reactor with respect to exergy efficiency and cost of hydrogen production.....	141
Table 6.5. Constraints for multi-objective optimization of the integrated system with respect to exergy efficiency and cost of hydrogen production.	143

List of Figures

Fig. 1.1. Global warming potential of different hydrogen production systems (modified from Ozbilen et al. [2]).	3
Fig. 1.2. Acidification potential of different hydrogen production systems (modified from Ozbilen et al. [2]).	4
Fig. 3.1. Process flow diagram of the hybrid photocatalytic hydrogen production reactor.	20
Fig. 3.2. Experimental setup.	21
Fig. 3.3. Experimental setup for photocatalytic experiments.	23
Fig. 3.4. Experimental setup for photo-electrocatalytic experiments.	25
Fig. 3.5. The pressure sensor used for experimental measurements [102].	27
Fig. 3.6. The sensor utilized to record the pH reading of the solutions [103].	28
Fig. 3.7. The solar simulator used in the experiments.	29
Fig. 3.8. The power supply employed in the experiments [106].	29
Fig. 3.9. The pyranometer used to measure the solar light intensity during the experiments [107].	30
Fig. 3.10. The sensors interface used to record experimental values digitally [108].	30
Fig. 4.1. Schematic of the hybrid photocatalytic hydrogen production reactor.	36
Fig. 4.2. Schematic diagram of the integrated systems. (a) system 1 and (b) system 2.	40
Fig. 4.3. Schematic diagram of the four step Cu-Cl cycle.	42
Fig. 4.4. Schematic diagram of heat exchanger network and integrated Kalina cycle.	43
Fig. 6.1. Normal probability distribution of residuals for photo-electrocatalytic hydrogen production process.	87
Fig. 6.2. Effects of run number on residuals for photo-electrocatalytic hydrogen production process.	87

Fig. 6.3. Box-Cox plot for power transformation of photo-electrocatalytic hydrogen production process.	88
Fig. 6.4. Model prediction versus actual hydrogen production rate of photo-electrocatalytic hydrogen production process.	89
Fig. 6.5. Effects of applied voltage and solar light intensity on photo-electrocatalytic hydrogen production for mass or concentration of ZnS of 2 g or 0.013 g/mL and mass or concentration of CuCl of 5 g or 0.033 g/mL.	90
Fig. 6.6. Effects of applied voltage and solar light intensity on photo-electrocatalytic hydrogen production for mass or concentration of ZnS of 2 g or 0.013 g/mL and mass or concentration of CuCl of 8 g or 0.053 g/mL.	91
Fig. 6.7. Effects of applied voltage and solar light intensity on photo-electrocatalytic hydrogen production for mass or concentration of ZnS of 2 g or 0.013 g/mL and mass or concentration of CuCl of 9 g or 0.06 g/mL.	91
Fig. 6.8. Effects of applied voltage and solar light intensity on photo-electrocatalytic hydrogen production for mass or concentration of ZnS of 3 g or 0.020 g/mL and mass or concentration of CuCl of 5 g or 0.033 g/mL.	92
Fig. 6.9. Effects of applied voltage and solar light intensity on photo-electrocatalytic hydrogen production for mass or concentration of ZnS of 3 g or 0.020 g/mL and mass or concentration of CuCl of 8 g or 0.053 g/mL.	93
Fig. 6.10. Effects of applied voltage and solar light intensity on photo-electrocatalytic hydrogen production for mass or concentration of ZnS of 3 g or 0.020 g/mL and mass or concentration of CuCl of 9 g or 0.06 g/mL.	93
Fig. 6.11. Effects of applied voltage and mass of CuCl on photo-electrocatalytic hydrogen production rate.	94
Fig. 6.12. Effects of applied voltage and mass of ZnS on photo-electrocatalytic hydrogen production rate.	95
Fig. 6.13. Effects of mass of ZnS and mass of CuCl on photo-electrocatalytic hydrogen production rate.	96

Fig. 6.14. Normal probability distribution of residuals for photocatalytic hydrogen production process.	98
Fig. 6.15. Effects of run number on residuals for photocatalytic hydrogen production process.....	98
Fig. 6.16. Box-Cox plot for power transformation of photocatalytic hydrogen production process.....	99
Fig. 6.17. Model prediction versus actual hydrogen production rate of photocatalytic hydrogen production process.	99
Fig. 6.18. Effects of solar light intensity on photocatalytic hydrogen production rate...	100
Fig. 6.19. Effects of mass of CuCl on photocatalytic hydrogen production rate.....	101
Fig. 6.20. Effects of mass of ZnS on photocatalytic hydrogen production rate.	102
Fig. 6.21. Effects of solar light intensity and mass of CuCl on photocatalytic hydrogen production rate at mass or concentration of ZnS of 2 g or 0.013 g/mL.....	103
Fig. 6.22. Effects of solar light intensity and mass of CuCl on photocatalytic hydrogen production rate at mass or concentration of ZnS of 3 g or 0.020 g/mL.....	104
Fig. 6.23. Effects of solar light intensity and mass of CuCl on photocatalytic hydrogen production rate at mass or concentration of ZnS of 4 g or 0.027 g/mL.....	104
Fig. 6.24. Effects of mass of CuCl and mass of ZnS on photocatalytic hydrogen production rate at solar light intensity of 400 W/m ²	105
Fig. 6.25. Effects of mass of CuCl and mass of ZnS on photocatalytic hydrogen production rate at solar light intensity of 450 W/m ²	106
Fig. 6.26. Effects of mass of CuCl and mass of ZnS on photocatalytic hydrogen production rate at solar light intensity of 500 W/m ²	106
Fig. 6.27. Effects of solar light intensity and mass of ZnS on photocatalytic hydrogen production rate.	107
Fig. 6.28. Effects of titanium dioxide on partial pressure of hydrogen.	108
Fig. 6.29. Effects of titanium dioxide on hydrogen production.....	109

Fig. 6.30. Effects of mass of titanium dioxide on voltage and mass of CuCl on electrical conductivity of anolyte solution.....	110
Fig. 6.31. Effects of current density on voltage requirement.....	111
Fig. 6.32. Effects of current density on hydrogen production rate and cost of hydrogen production.	112
Fig. 6.33. Effects of current density on energy and exergy efficiencies.....	113
Fig. 6.34. Effects of reactor temperature on hydrogen production rate and cost of hydrogen production.	114
Fig. 6.35. Effects of reactor temperature on energy and exergy efficiencies.	115
Fig. 6.36. Effects of concentration of CuCl on hydrogen production rate and cost of hydrogen production.	116
Fig. 6.37. Effects of ambient temperature on energy and exergy efficiencies.....	117
Fig. 6.38. Effects of electrode distance on hydrogen production rate and cost of hydrogen production.	118
Fig. 6.39. Effects of reactor temperature on scale up hydrogen production rate and cost of hydrogen production.	119
Fig. 6.40. Effects of solar light intensity on hydrogen production rates.....	122
Fig. 6.41. Effects of solar light intensity on total exergy destruction rate.....	123
Fig. 6.42. Effects of solar light intensity on energy and exergy efficiencies.....	124
Fig. 6.43. Effects of view factor on hydrogen production rates.	124
Fig. 6.44. Effects of view factor on total exergy destruction rate.....	126
Fig. 6.45. Effects of view factor on energy and exergy efficiencies.	127
Fig. 6.46. Effects of mass fraction of hydrochloric acid at state 11 on hydrogen production rates.....	128
Fig. 6.47. Effects of mass fraction of hydrochloric acid at state 11 on energy and exergy efficiencies.	129

Fig. 6.48. Effects of mass flow rate of zinc sulfide on hydrogen production rates.	130
Fig. 6.49. Effects of mass flow rate of zinc sulfide on energy and exergy efficiencies.	130
Fig. 6.50. Effects of electrolyzer pressure on energy and exergy efficiencies.	131
Fig. 6.51. Effects of molten salt inlet temperature on hydrogen production rates.....	132
Fig. 6.52. Effects of molten salt inlet temperature on energy and exergy efficiencies... ..	133
Fig. 6.53. Effects of concentration ratio of heliostat field system on hydrogen production rates.	134
Fig. 6.54. Effects of concentration ratio of heliostat field system on total exergy destruction rate.....	135
Fig. 6.55. Effects of concentration ratio of heliostat field system on energy and exergy efficiencies.	136
Fig. 6.56. Effects of ambient temperature on hydrogen production rates.....	137
Fig. 6.57. Effects of ambient temperature on total exergy destruction rate.....	137
Fig. 6.58. Effects of ambient temperature on energy and exergy efficiencies.....	138
Fig. 6.59. Exergy destruction ratios for the components of the integrated systems.	139
Fig. 6.60. Multi-objective optimization of the hybrid reactor with respect to hydrogen production rate and cost of hydrogen production.	141
Fig. 6.61. Multi-objective optimization of the hybrid reactor with respect to exergy efficiency and cost of hydrogen production.....	142
Fig. 6.62. Multi-objective optimization of the integrated system with respect to exergy efficiency and cost of hydrogen production.....	143
Fig. 6.63. Average hydrogen production cost of selected methods (Data from [134- 136]).	144

Nomenclature

A	Area, m ²
c	Specific cost, C\$/kg
\dot{C}	Cost rate, C\$/s
C	Electrode constant; Concentration ratio
c_p	Specific heat, kJ/kg K
d	Distance (m); Diameter (m)
Df	Degree of freedom
\dot{E}_n	Energy rate, kW
E_xR	Exergy destruction ratio
ex	Specific exergy, kJ/kg
\dot{E}_x	Exergy rate, kW
E^0	Open circuit voltage, V
F	Faraday's constant, C/mol
F_r	View factor
h	Specific enthalpy, kJ/kg
HHV	Higher heating value, kJ/kg
I	Solar light intensity, W/m ²
i	Current density, A/cm ²
i_o	Exchange current density, A/cm ²
k	Electrical conductivity, 1/ohm m
m	Mass, kg
\dot{m}	Mass flow rate, kg/s
M	Molecular weight, kg/kmol; Molarity, mol/L

mf	Mass fraction, kg/kg
MV	Mean square value
n	Number of electrons exchanged
N	Number of data points
P	Pressure, kPa
R_u	Universal gas constant, kJ/mol K
\dot{Q}	Heat flow rate, kW
T	Temperature, K
s	Specific entropy, kJ/kg K
SS	Sum of Squares
V	Voltage, V
\bar{V}	Volume, mL
\dot{V}	Volume flow rate, L/s; production rate L/s
\dot{W}	Work rate, kW
x	Concentration of ammonia-water mixture, kg/kg
y	Mole fraction, mol/mol
\dot{Z}	Operating/equipment cost rate, C\$/s

Greek Letters

η	Efficiency
Σ	Summation
σ	Membrane thickness, m
γ	Activity coefficient
Δ	Difference
ε	Emissivity

ρ	Density, kg/m ³
σ	Stefan-Boltzmann constant, W/m ² K ⁴
δ	Thickness, m
λ	Thermal conductivity, W/m K

Subscripts

A	Anode
abs	Absorbed
AM	Anode to membrane
avg	Average
c	Constant
C	Cathode; Cold
CEM	Cation exchange membrane
ch	Chemical
CM	Cathode to membrane
con	Condenser
cond	Conduction
conv	Convection
convr	Conversion
des	Desired
dest	Destruction
elec	Electrolyzer
em	Emissivity
en	Energy
eq	Equipment

ex	Exergy
ext	External
<i>fc</i>	Forced convection
g	Generator
H	Hot; Heliostat
HE	Heat exchanger
hw	Hot water
H ₂	Hydrogen
i	i th state
insu	Insulation
k	k th state
Kc	Kalina cycle
LOF	Lack of fit
m	m th state
ms	Molten salt
MT	Model term
nc	Normal convection
p	Pump
PC	Photocatalytic
PE	Pure error
ph	Physical
R	Residual
rec	Receiver
ref	Reflection

req	Required
rev	Reversible
S	Separator
s	Solar
sol	Solution
sol1	Solution 1
sol2	Solution 2
su	Scale up
sys1	System 1
sys2	System 2
surf	Surface
th	Thermal
turb	Turbine
tot	Total
w	Wall
whr	With heat recovery
wi	With integration
wohr	Without heat recovery
o	Out
0	Dead/reference state

Acronyms

AHTR	Advanced high temperature reactor
ANOVA	Analysis of Variance
bpy	2,2-bipyridine

bpm	2,2'-bipyrimide
CEM	Cation exchange membrane
DMA	Dimethylaniline
DMF	Dimethylformamide
DOE	Design of experiment
dpp	2,3'-bis(2-pyridyl)pyrazine
EES	Engineering equation solver
HHV	Higher heating value
Ln	Logarithm
LCA	Life cycle assessment
LINMAP	Linear programming technique for multidimensional analysis
MHR	Modular helium reactor
Phen	1,10-phenanthroline
PSU	Power supply unit
RESS	Residual
SEP	Separator
SMR	Steam methane reforming
tpy	2.2',6',2''-terpyridine
TWSCS	Thermochemical water splitting cycles
VHTR	Very high temperature reactor

Chapter 1: Introduction

1.1 Energy Need

Energy plays a vital role in our daily lives as it is required to operate almost all systems and applications around us. At present, fossil fuels act as base energy carriers that emit harmful greenhouse gases such as carbon dioxide (CO_2) and air pollutants such as nitrogen oxides (NO_x) and sulfur oxides (SO_x) that contribute to environmental damages. The Earth has experienced an increase of 24.4% in CO_2 emissions from 1990 to 2004 [1]. Such a rapid increase in CO_2 will result in human beings living in an environment having rates of atmospheric CO_2 concentrations well above 550 parts per million [1], which can lead to devastating consequences in terms of human health and climate change.

An unprecedented increase in greenhouse gas emissions has led researchers to look for alternative energy carriers than fossil fuels, which can be obtained in a comparatively environmentally benign manner. A common alternative energy carrier being studied is hydrogen. However, hydrogen is not readily available in the environment and is not regarded as an energy source but an energy carrier. At present, the technologies that are capable of producing hydrogen depend on fossil fuels that do not lead away from a fossil fuel-based economy. Thermochemical water splitting cycles (TWSCs) are technologies that can produce hydrogen in a comparatively environmentally friendly manner. However, current TWSCs use an electrolyzer to generate hydrogen from different solutions, which makes them dependent on the electricity grid. The conventional electrolysis step in TWSCs can be replaced by hybrid photocatalytic reactors that utilize solar light intensity as a fuel rather than electrical energy.

Apart from hydrogen production, storage and safe transport is also a challenge faced by researchers. Hydrogen is a highly flammable gas with low ignition energy, which makes it one of the most dangerous gases to transport and store. The problems of storage and transport were also faced by fossil fuels when they were first utilized on a large scale, but were overcome by extensive research. In the same manner, these are early days for hydrogen and it is expected that sooner or later researchers will be able to invent a technology that can safely store and transport hydrogen.

1.2 Hydrogen and the Environment

The major hindrance in shifting from a fossil fuel to a hydrogen-based economy is that the systems that are used to produce hydrogen utilize fossil fuels in one way or another. The most common systems used to produce hydrogen at present are steam methane reforming and electrolysis. Both of these systems depend highly on fossil fuels, which cancels out the positive attributes of using hydrogen as an energy carrier. An alternative and very promising technology for hydrogen production is the thermochemical water splitting cycle. These cycles require high-temperature heat as opposed to electricity and use a combination of different chemicals to produce hydrogen. The utilization of heat and different combinations of chemicals make thermochemical water splitting cycles comparatively more environmentally benign and efficient at the same time.

Life cycle assessment (LCA) can be used to study the environmental impacts of thermochemical water splitting cycles. A life cycle assessment study carried out by Ozbilen et al. [2] highlighted the impact of different hydrogen production methods on the environment. Figure 1.1 shows that the nuclear-based four-step Cu-Cl cycle has the lowest global warming potential (0.56 kg CO₂ eq.) followed by the nuclear-based sulfur cycle (0.86 kg CO₂ eq.), wind-based electrolysis (0.97 kg CO₂ eq.), nuclear-based high-temperature electrolysis (2.0 kg CO₂ eq.), biomass-based electrolysis (2.4 kg CO₂ eq.), solar-based electrolysis (2.5 kg CO₂ eq.), nuclear-based ISPRA Mark 9 (2.52 kg CO₂ eq.) and natural gas steam reforming (11.89 kg CO₂ eq.). The figure highlights the fact that present systems to produce hydrogen (steam methane reforming and water electrolysis) are affecting the environment in a negative manner, creating the need for more eco-friendly hydrogen production processes such as thermochemical water splitting cycles. Figure 1.2 shows a slightly different picture as it plots the acidification potential of several hydrogen production systems. The wind-based electrolysis pathway has the lowest acidification factor (2.58 g SO₂ eq.) followed by the nuclear-based 4-step Cu-Cl cycle (2.84 g SO₂ eq.), nuclear-based sulfur cycle (4.3 g SO₂ eq.), nuclear-based high-temperature electrolysis (4.84 g SO₂ eq.), solar-based electrolysis (8.06 g SO₂ eq.), nuclear-based ISPRA Mark 9 (11.25 g SO₂ eq.), natural gas steam reforming (14.52 g SO₂ eq.) and biomass-based electrolysis (29.03 g SO₂ eq.). Thus, thermochemical water

splitting cycles have one of the lowest acidification potentials whereas biomass-based electrolysis has the highest. The results obtained by Ozbilen et al. [2] reassured that at present nuclear-based thermochemical water splitting cycles is a promising advanced technology for hydrogen production.

1.3 Thermochemical Water Splitting Cycles and the Environment

The majority of thermochemical water splitting cycles recycle chemicals used during hydrogen production, which reduces waste. Another benefit of thermochemical water splitting cycles is that their high-temperature thermal energy requirements can be fulfilled by solar thermal technologies or by nuclear waste heat. However, one drawback is the electrical energy demand of the electrolyzer. Although the electrolyzer used in thermochemical water splitting cycles contains chemicals that lower the electrical input to the system, significant inputs of electrical energy are still required.

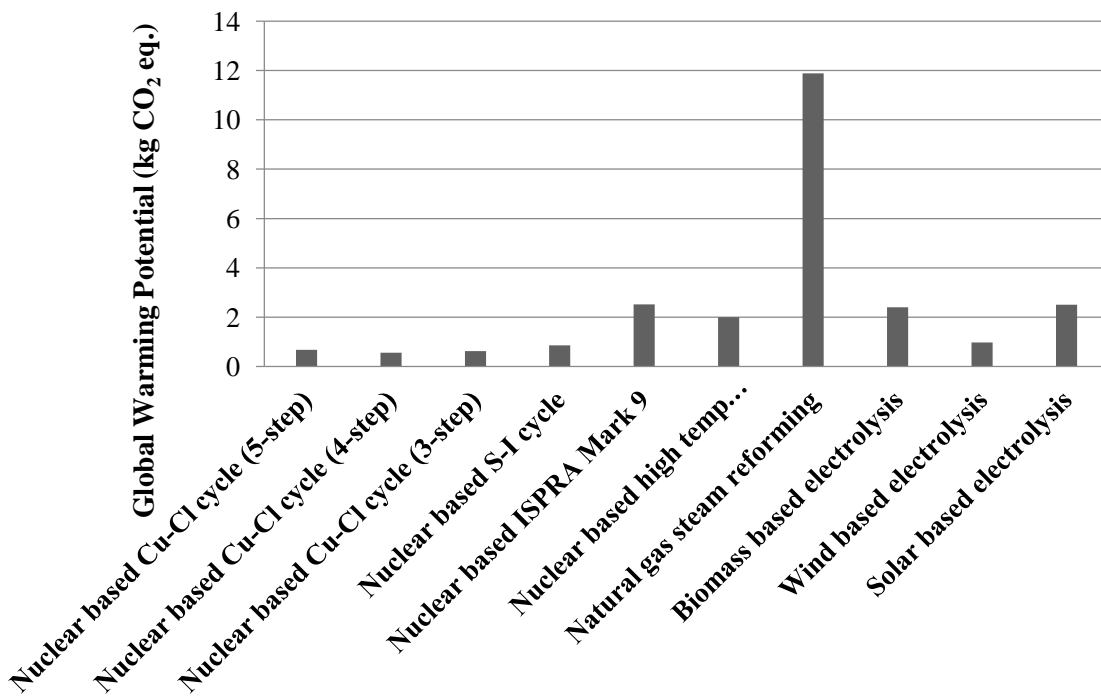


Fig. 1.1. Global warming potential of different hydrogen production systems (modified from Ozbilen et al. [2]).

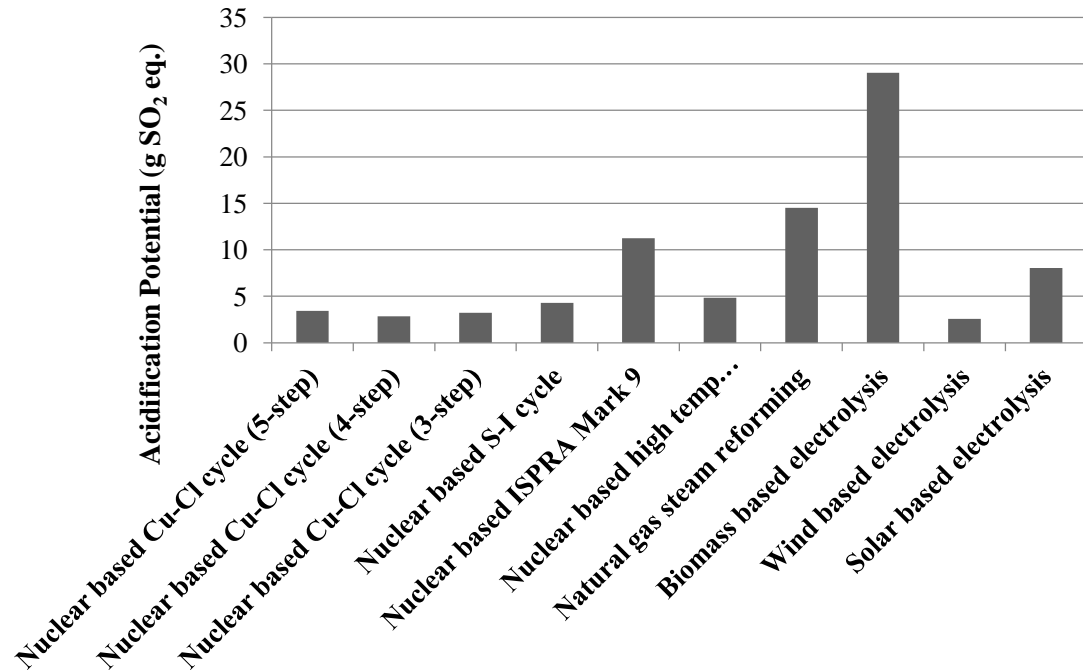


Fig. 1.2. Acidification potential of different hydrogen production systems (modified from Ozbilen et al. [2]).

To reduce the dependence of thermochemical water splitting cycles on electrical energy, researchers have introduced a new kind of hydrogen production reactor known as a photocatalytic hydrogen production reactor that relies more on solar light than a conventional electrolyzer to produce hydrogen. In the reactor, solar light is used to activate the catalyst, which alongside electricity, drives the chemical reaction and produces hydrogen.

1.4 Motivation

The extensive use of fossil fuels has led to numerous negative environmental consequences. The time has come to develop sustainable and environmentally benign energy sources capable of replacing fossil fuels. One such energy carrier is hydrogen. The major drawback of hydrogen is that it is not freely available in the atmosphere. Traditional hydrogen production systems rely on fossil fuel conversion into hydrogen, which does not help mitigate greenhouse gas emissions. A thermochemical water splitting cycle (TWSC) is one such system that can produce hydrogen using recovered heat in an environmentally benign manner. The four-stage Cu-Cl cycle studied at the

University of Ontario Institute of Technology is one possible TWSC that has shown great potential to be a leading hydrogen production system in the near future. The electrolyzer component of the Cu-Cl cycle is undergoing a thorough evaluation to make it more dependent on solar rather than electrical energy. This is the motivation behind the current research, which is to conduct detailed energy and exergy analyses of an integrated solar-based four-step Cu-Cl cycle and develop hybrid photocatalytic hydrogen production reactor.

1.5 Objectives

The current technologies available for hydrogen production are not considered sustainable for a carbon-free society due to their dependence on fossil fuels. Steam methane reforming (SMR) is utilized by many hydrogen production plants but depends on non-renewable methane resources. In addition, water electrolysis requires electricity, which is largely fossil-based in most parts of the world, to break apart water molecules into hydrogen and oxygen. The thermochemical water splitting cycle is a technology that can generate hydrogen on a large scale with minimum or no dependence on fossil fuels. The thermochemical water splitting cycles are mostly heat driven cycles and their heat requirement can be fulfilled by high-temperature solar systems such as a solar heliostat field. Although, the amount of electrical energy required by the thermochemical water splitting cycle is small compared to conventional water electrolysis, it is not negligible. The introduction of hybrid photocatalytic hydrogen production reactor inside the Cu-Cl cycle paves the way for this TWSC to be completely non-dependent on fossil fuels.

The main objectives of this thesis study are to conduct experimental studies on hybrid photocatalytic hydrogen production reactor and to study solar-based integrated Cu-Cl systems for hydrogen production. The specific objectives of the present study are given as follows:

- a) To develop an electrochemical model of hybrid photocatalytic reactor for hydrogen production:

An electrochemical model of hybrid photocatalytic hydrogen production reactor for the Cu-Cl cycle is developed to better understand the energy needs of the hybrid reactor. This

electrochemical model incorporates concentrations of CuCl and HCl in anode half-cells, concentrations of ZnS, Na₂S and NaOH in cathode half-cells and the energy input required to excite these chemicals for hydrogen production.

- b) To design and build a prototype of hybrid photocatalytic reactor for hydrogen production:

A lab-scale experimental set-up is designed and built to conduct the required experiments. The prototype makes use of solar light intensity and the properties of photocatalysts ZnS and TiO₂ to produce hydrogen when induced with solar light, which reduces the need for electrical energy in hydrogen production step of Cu-Cl cycle.

- c) To perform experiments on the developed photocatalytic reactor:

The experimental study is carried out in two steps. First, photocatalytic experiments are carried out to investigate the effects of different operating parameters such as solar light intensity and mass or concentrations of CuCl and ZnS on the hydrogen production rate. Second, photo-electrocatalytic experiments are performed, where graphite and titanium are used as electrodes and voltage, solar light intensity and mass or concentrations of CuCl and ZnS are varied to witness their effects on the hydrogen production rate. In the final step of the experimental study, TiO₂ is added to the anode solution. The utilization of TiO₂ as a photocatalyst in an anolyte solution reduces the electrical dependency of the hydrogen production reactor due to its property of providing an electric charge in the solution in the presence of solar light. The parameters varied during the experiments are determined based on a literature review and research meetings.

- d) To conduct energy and exergy analyses of a hybrid photocatalytic reactor and integrated systems:

The energy and exergy analyses of the studied systems are performed to better understand the energy needs of the systems. The energy and exergy efficiencies of the studied systems are also presented to show how efficient each of the studied systems is from both energy and exergy perspective.

- e) To perform parametric studies of a hybrid photocatalytic hydrogen production reactor and integrated systems:

The parametric studies are undertaken for the hybrid photocatalytic reactor to study the effects of current density, reactor temperature, ambient temperature, CuCl concentration, and distance of electrodes from the membrane on the hydrogen production rate, energy and exergy efficiencies and cost of hydrogen production. For the integrated systems, the effects of solar light intensity, view factor, mass fraction of hydrochloric acid, mass flow rate of zinc sulfide, concentration ratio, electrolyzer pressure, molten salt inlet temperature and ambient temperature on the hydrogen production rate, energy and exergy efficiencies and exergy destruction rate are studied.

- f) To perform an exergoeconomic analysis of the hybrid photocatalytic reactor for hydrogen production:

An exergoeconomic model of the hybrid photocatalytic hydrogen production reactor is developed to relate exergy with the cost rate associated with the reactor. The exergoeconomic model takes into consideration equipment, chemical, operational and costs related to exergy destruction. In the present study, exergy terms are replaced with mass flow rates as suggested in the literature for systems with more unknowns than equations.

- g) To perform a multi-objective optimization study of the hybrid photocatalytic hydrogen production reactor and the integrated system:

An optimization study is performed to find the operating parameters that provide maximum hydrogen production, maximum exergy efficiency and minimum cost of hydrogen production for the hybrid photocatalytic reactor. The objective functions for the optimization study of the hybrid reactor are constrained by the voltage, concentration of Cu-Cl, concentration of zinc sulfide, temperature of the reactor and ambient temperature. The optimization study of the integrated system attempts to maximize exergy efficiency and minimize cost of hydrogen production. The objective functions for the optimization study of the integrated system are constrained by the solar light intensity, view factor, mass fraction of hydrochloric acid, mass flow rate of zinc sulfide, concentration ratio, electrolyzer pressure, molten salt inlet temperature and ambient temperature.

1.6 Summary of Approach and Rationale

The present research focuses on the development of hybrid photocatalytic hydrogen production reactor. The electrochemical, energy, exergy and exergoeconomic models of the hybrid reactors are also developed. Energy and exergy analyses of the solar heliostat field based integrated systems for hydrogen production is also performed to study the effect of different operating parameters on the performance of the systems.

In the first phase of the present research, novel hybrid photocatalytic hydrogen production reactor for the Cu-Cl cycle is developed. The hybrid reactors developed here are then utilized to produce hydrogen using an aqueous solution of CuCl and HCl on the anode side and an aqueous solution of ZnS, Na₂S and NaOH on the cathode side. In the first part of the research, photocatalytic experiments are performed to study the effect of solar light intensity, mass or concentration of CuCl and mass or concentration of ZnS on the hydrogen production rate. In the second phase, photo-electrocatalytic experiments using a titanium electrode as the cathode and a graphite electrode as the anode are performed to study the effects of variation in voltage, mass or concentration of CuCl, mass or concentration of ZnS and solar light intensity on the hydrogen production rate. At the end of the experimental study, titanium dioxide is added to the anolyte compartment to study the effect of a photocatalyst in the anolyte solution. After performing the experiments, electrochemical, energy, exergy and exergoeconomic models of the hybrid photocatalytic reactor are developed to study the effects of several operating parameters on the performance of the reactor. An optimization study is also carried out to determine the optimum operating conditions for the best possible reactor performance.

In the second phase of the thesis research, energy and exergy models of the solar heliostat field based integrated systems for hydrogen production are developed. Two integrated systems, namely (a) solar heliostat field system integrated with Cu-Cl cycle and Kalina cycle (system 1) and (b) solar heliostat field system integrated with Cu-Cl cycle, Kalina cycle and photocatalytic reactor are considered in this study. The energy and exergy results of both systems are compared to show the effect of further integration on the overall performance of the system. The operating conditions varied during the parametric

study are solar light intensity, view factor, mass fraction of HCl, mass flow rate of ZnS, concentration ratio, electrolyzer pressure, molten salt inlet temperature and ambient temperature.

Chapter 2: Literature Review

Increased emissions of greenhouse gases and other air pollutants due to extensive use of fossil fuels require a new approach to energy production in the future. One way of responding to this challenge is by developing hydrogen as an energy carrier [3-5]. Argun and Kargi [6] used bio-fermentation techniques to produce hydrogen. Ratlamwala et al. [7] performed a thermodynamic analysis of solar-assisted hydrogen production and showed that hydrogen can renewably be generated. Dincer and Ratlamwala [8] performed a comparative study of different hydrogen production systems to demonstrate a more sustainable way of producing hydrogen for the future. Turner [9] discussed how hydrogen can be sustainably produced to meet future energy demand. Studies conducted by researchers [10-15] showed that hydrogen is a contender for becoming a leading energy carrier in the future for sustainable development. Leighty [16] discussed the topic of transmission lines for hydrogen transport and geological hydrogen storage methods. Abbasi and Abbaso [17] studied the prospects and challenges faced by the hydrogen economy. The major benefit of using hydrogen as an energy carrier compared to fossil fuels is the reduction in greenhouse gas emissions. The role of hydrogen will become more prominent in the future as the world shifts from an era of fossil fuels to cleaner fuels [18-24]. Smitkova et al. [25] presented a life cycle assessment of systems used for hydrogen production to illustrate the effect of hydrogen production on environmental considerations. Although hydrogen can be an environmentally benign energy carrier it is not freely available in the atmosphere. Hydrogen can be produced using several systems that include but are not limited to (a) steam methane reforming (SMR), (b) water electrolysis, (c) coal gasification, (d) thermochemical cycles and (e) fermentation of biomass [26-33]. Dufour et al. [34] stated that at present, 96% of hydrogen is produced using SMR, which has the disadvantage of releasing CO₂. On the other hand, electrolyzers require electrical power to produce hydrogen through dissociation of water molecules. Burman [35] reported that to produce an amount of hydrogen capable of yielding 1,000 Joules of energy requires an input of 1,600 Joules. To address the shortcomings of the dominant methods of hydrogen production, researchers have developed emerging and promising technologies. The proposed systems are: (a) direct

production using sunlight and semiconductors, (b) nuclear/solar thermochemical cycles, and (c) biological and bio-inspired systems.

2.1 Cu-Cl Cycle for Hydrogen Production

Thermochemical water-splitting cycles (TWSCs) appear to have advantages as a carbon-free option for hydrogen production powered by alternative (carbon-free) energy sources [36, 37]. Giaconia et al. [38] performed a thermodynamic analysis of a sulfur-based thermochemical water splitting cycle for hydrogen production. Abandes et al. [39] studied a novel two-step SnO_2/SnO water-splitting cycle for solar thermochemical production of hydrogen. Xiao et al. [40] presented the overview of advances in solar hydrogen production via two-step water-splitting thermochemical cycles based on metal redox reactions. Gokon [41] performed a thermochemical study of a two-step water splitting cycle by monoclinic ZrO_2 -supported NiFe_2O_4 and Fe_3O_4 powders and ceramic foam devices. A thermochemical cycle is a process consisting of a closed loop of thermally driven chemical reactions, where water is decomposed into hydrogen and oxygen, while all other intermediate compounds are recycled [42, 43]. According to Ozbilen et al. [2] many TWSCs have been studied and evaluated, but very few of these technologies have made it to the level of elaborative research and pilot plants. At present, some major hindrances to vast scale hydrogen production using TWSCs are high temperature requirements and high production costs.

Although there are many thermochemical cycles available in the literature, the Cu-Cl cycle holds an edge in terms of temperature requirements and handling. The studies carried out by several researchers [44-46] show that the lower operating temperature requirements of the Cu-Cl cycle (around 530°C) has reduced the material and maintenance costs compared to other thermochemical cycles. Ferrandon et al. [47] studied the key step of hydrolyzing CuCl_2 to Cu_2OCl_2 and HCl using a spray reactor, which has the highest temperature requirement for the Cu-Cl cycle. The major benefit of the Cu-Cl cycle is that it offers one of the highest efficiencies among all TWSCs and requires lower operating temperatures. Orhan et al. [48] presented the design of systems for hydrogen production based on the Cu-Cl thermochemical water decomposition cycle and studied the performance of these systems at different configurations. Studies

conducted by several researchers [49, 50] showed that the Cu-Cl cycle efficiency can reach up to 55%, depending on operating and design conditions. Apart from the Cu-Cl cycle, another heavily studied TWSC and considered for potential applications is the hybrid sulfur (HyS) cycle. The hybrid sulfur cycle, also known as the Westinghouse cycle, was initially studied in detail by Soliman et al. [51] and Brecher et al. [52]. Jomard et al. [53] performed numerical modeling for the preliminary design of the hydrogen production electrolyzer in the Westinghouse hybrid cycle. Hinkley et al. [54] studied the prospects of integrating the hybrid sulfur cycle with solar-based systems for stand-alone hydrogen production. A hydrogen production system based on an integrated solar and hybrid sulfur cycle was studied by Corgnal and Summers [55]. Ratlamwala et al. [56] performed energy and exergy analyses of integrated hybrid sulfur cycles capable of recovering the majority of waste heat to enhance performance. The negative attribute associated with the HyS cycle is that it needs high operating temperatures in the range of 1050 K as reported by several researchers [57-59]. This high-temperature requirement of the HyS cycle as compared to the Cu-Cl cycle makes it less favorable in comparison.

In Japan, some bench-scale tests have been performed to show the hydrogen production capabilities of sulfur cycles, requiring heat at 900°C, with an energy efficiency of about 50% based on the higher heating value of hydrogen [60]. Uhrig [60] stated that inorganic separation membranes can reduce the operating temperature of the sulfur cycle to a more realistic and practical level of 700°C. Nuclear reactors having different operating temperatures such as conventional light-water reactors, high-temperature gas-cooled reactors, liquid metal-cooled fast reactors, very high temperature reactors (VHTRs), the generator IV concept reactor, and the advanced high-temperature reactor (AHTR) are considered. Forsberg [61] conducted a detailed study of nuclear hydrogen production using AHTR. Brown et al. [62] carried out a detailed literature survey of published TWSCs (approx. 100 cycles) to identify the most promising thermochemical water splitting cycles based on efficiency, cost-effectiveness and large-scale hydrogen production utilizing high-temperature heat from an advanced nuclear power station. These researchers found that the Adiabatic UT-3 cycle and the sulfur cycle were the most promising ones and the sulfur cycle was selected for further development.

Until today, the major problem associated with TWSCs is that they require high-temperature heat. Forsberg et al. [61] focused on lowering the operating temperature of sulfur cycles for hydrogen production to make them more feasible. The research conducted by Forsberg et al. [61] was motivated by the fact that most TWSCs required high-temperature heat (850°C or higher) to produce hydrogen which cannot be provided by the present nuclear reactors. However, heat to the TWSCs can be provided if the peak temperature requirements are brought down by 100°C or more. Apart from these high-temperature TWSCs based mostly on sulfur, some researchers have focused on finding alternative TWSCs that can operate at much lower temperatures. In this regard, research has been carried out in North America and the Cu-Cl cycle has been proposed as a new TWSC by the researchers as it requires heat at approximately 550°C [61-63].

There are several nuclear hydrogen production technologies being proposed but the two most promising are (a) sulfur cycles and (b) the Cu-Cl cycle. Apart from the thermodynamic advantages of these cycles, it is also important to look at the economic benefits associated with these cycles. Table 2.1 summarizes the production cost of both the sulfur and Cu-Cl cycles having different production capacities. The cost data for the sulfur cycles is obtained from Brown [62] and from Orhan [63] for the Cu-Cl cycle. From a cost perspective, the sulfur cycles have a clear advantage over the Cu-Cl cycles at lower hydrogen production rates. This advantage diminishes as the production capacity of the Cu-Cl cycle increases. At higher production rates, the Cu-Cl cycle is a better option compared to the sulfur cycle because of its lower temperature requirements and higher efficiency.

2.2 Photocatalytic Hydrogen Production

Photocatalytic hydrogen production methods have recently gained in interest due to the potential of converting solar energy into electrical and chemical energy. Researchers in the past have focused on the development of a two half-cell reactor separated by a membrane. This two half-cell reactor uses a photocatalyst (supramolecular catalyst) and a sacrificial or non-sacrificial electron donor to produce hydrogen or any other gas. The photocatalysts used in photocatalytic processes are divided into two categories: (a) homogenous and (b) heterogeneous photocatalysts.

Table 2.1 Cost comparison of TWSCs hydrogen production methods

Process	Total Annual Cost (C\$)	Annual Production (tonnes)	Cost (C\$/kg)
PH-MHR [62]	406,697,000	201,982	2.01
H ₂ -MHR [62]	468,562,000	250,073	1.87
Cu-Cl [63]	3,495,000	1080	3.24
Cu-Cl [63]	4,606,000	1800	2.56
Cu-Cl [63]	5,548,000	2520	2.20

The homogenous photocatalysts work on the principle of supramolecular complexes in which there are different sections. A typical homogenous supramolecular catalyst is divided into three different sections; namely (a) the light absorbing unit also known as the terminal ligand, (b) the electron relay unit also known as the bridging ligand and (c) the electron collector unit [64-66]. All these units have a specific task to produce the eventual end product. The process starts when the terminal ligand receives an electron from the electron donor, which is then transferred to the electron collector unit with the help of the bridging ligand. The water is then introduced into the solution at the electron collector unit to reduce its bond to hydrogen gas and hydroxyl ion [67]. Schulz et al. [68] studied the role of the bridging ligand in photocatalytic supramolecular assemblies for the reduction of protons and carbon dioxide. An important characteristic of homogenous photocatalysts is that they allow light to pass through, which can then be used for other purposes. Prussin et al. [68] studied photochemical methods to examine DNA photocleavage using supercoiled pUC18 DNA and LED or xenon arc lamp excitation. Synthesis, characterization, and study of the photophysics and photocatalytic properties of the photoinitiated electron collector were performed by White et al. [70]. Rangan et al. [71] performed a solar energy conversion study using photochemical molecular devices for photocatalytic hydrogen production from water using mixed metal supramolecular complexes. Arachchige et al. [72] studied design considerations for a photocatalytic hydrogen production from water system by employing mixed-metal photochemical molecular devices for photoinitiated electron collection. However, homogenous photocatalysts are too expensive and are currently limited to lab-scale use only.

A relatively new homogenous supramolecular catalyst consisting of ruthenium (Ru) and rhodium (Rh) was introduced by Brewer and Elvington [73] for photocatalytic hydrogen

production. In this new homogenous supramolecular catalyst, several terminal legends such as 2, 2'-bipyridine (bpy), 2,2',6',2''-terpyridine(tpy) and 1,10-phenanthroline(Phen) and two bridging ligands such as 2, 3'-bis(2-pyridyl) pyrazine (dpp) and 2, 2'-bipyrimidine (bpm) are used to facilitate photocatalytic hydrogen production [73]. Spectroscopic, electrochemical, and spectro-electrochemical investigations of mixed-metal osmium(II)/ruthenium(II) bimetallic complexes incorporating polypyridyl bridging ligands was performed by Ritcher et al. [74]. In this relatively new homogenous supramolecular catalyst, dimethylamine (DMA) is used as an electron donor and dimethylformamide (DMF) and acetonitrile are used as the solvent [75]. Elvington and Brewer [76] studied the electron collection on a metal in a rhodium-centered mixed-metal supramolecular complex by photoinitiating the process using light intensity.

The heterogeneous photocatalysts show the characteristics of a solid photocatalyst, which can be used either as a powder or a solid electrode. In heterogeneous photocatalysts, the catalyst exists in a different phase as that of the reactant. These catalysts act as semiconductor devices consisting of valence and conduction band. When solar or other forms of light carrying energy greater than that of the energy gap between the valence and conduction band is focused on such photocatalysts, it excites the electrons carried by the valence band of the photocatalysts. These excited electrons then travel from the valence band to the conduction band where they react with water to produce hydrogen and hydroxyl ions.

A study conducted by Kamiya et al. [77] investigated the energy requirements of the photocatalytic hydrogen production reactor. Another study carried out by Buehler et al. [78] looked at the possible deposition of platinum on cadmium sulfide (CdS) microcrystal and found that by doing so an active solar hydrogen production photocatalyst can be obtained. Reber et al. [79] found that by irradiating suspensions for platinized CdS in the solutions of the sulfur or sulfide ions, an effective photocatalytic hydrogen production can be achieved. Li et al. [80] prepared heterogeneous bi-nuclear complexes in which the polypyridil ruthenium photosensitizer and cobaloxime catalysts are connected via conjugated or unconjugated bridges; these complexes prepared by Li et al. [80] can be used for photocatalytic hydrogen production.

A feasibility study to investigate the suitability of using zinc sulfide suspensions in photocatalytic hydrogen production was conducted by Reber and Meier [81]. In this study it was concluded that effective hydrogen production can be achieved by suspending ZnS in multiple electrolyte solutions such as Sz, So-, S2O-, and H₂PO. Working on the principal of Reber and Meier [81], Xing et al. [82] studied photocatalytic hydrogen production by splitting water molecules in the presence of a band-controlled cadmium-zinc sulfide solution and found that hydrogen production was achieved under visible and ultraviolet light irradiation. Another study conducted by Amouyal et al. [83] solidified the claim of Xing et al. [82] that photocatalytic hydrogen production can be achieved by visible light. The major difference between the catalyst presented by Brewer and Evington [73] and ZnS is that the quantum yield of Brewer and Evington catalyst is approximately 0.01 [74] as opposed to 0.9 [82] for ZnS based catalyst.

Another form of catalyst group available in the literature is SrTiO₃ based catalysts. Kang et al. [84] used co-doping schemes to enhance hydrogen evolution under visible light irradiation over SrTiO₃:Ni/M catalyst. Yu et al. [85] performed studies on visible light driven photocatalytic hydrogen production over Cr/N-Codoped SrTiO₃ to investigate the effectiveness of such photocatalyst under visible light. Kang et al. [86] also evaluated the performance of an organic-inorganic composite of g-C₃N₄-SrTiO₃:Rh photocatalyst for hydrogen production under visible light. Tantalum oxide based catalysts are another set of photocatalysts that can be used in solar hydrogen production systems. Leilei et al. [87] studied photocatalytic activity of well-dispersed heterostructured In₂O₃/Ta₂O₅ composites for photochemical hydrogen production. A photocatalyst capable of working under visible light for hydrogen production was prepared by Xu et al. [88] by crystallizing mesoporous CdS/Ta₂O₅ composite assisted by silica reinforcement. Khan and Qureshi [89] performed a study to determine the effectiveness of tantalum doped BaZrO₃ for photocatalytic hydrogen production by water splitting. Kanhere et al. [90] presented photophysical properties of Bi₃D doped NaTaO₃ capable of producing hydrogen under visible light. Yang et al. [91] performed a study in which they used cadmium sulfide based photocatalysts for photocatalytic hydrogen production and found out that these photocatalysts have high quantum efficiency. A visible light driven Ag-doped Mn-Cd sulfide photocatalyst for hydrogen production was studied by Ikeue and Shinmura [92].

Macias-Sanchez et al. [93] presented structural features and photocatalytic activity of visible light driven $\text{Cd}_{1-x}\text{Zn}_x\text{S}$ based photocatalyst. Wanga et al. [94] carried out a study to enhance the photocatalytic hydrogen production capability of cadmium sulfide nano-crystals by surface loading them with nickel, copper and carbon monoxide. An enhancement study of solar hydrogen production using modified photochemical Pt/CdS photocatalyst was conducted by Yao et al. [95].

The titanium dioxide based catalysts are another group of catalysts which can be very useful in producing hydrogen using photocatalytic hydrogen production systems. Wu et al. [96] used a Pd-Gardenia- TiO_2 photocatalyst for solar driven hydrogen production. A comparative study that focused on studying the effect of Ag-, Ni-, and Cu-loaded mesoporous assembled TiO_2 - ZrO_2 mixed oxide nano-crystal photocatalysts on the rate of hydrogen production was conducted by Onsuratoom et al. [97]. Parayil et al. [98] in their study showed that carbon modified TiO_2 composite materials can enhance the photocatalytic water splitting capability of titanium dioxide based photocatalysts. An improved hydrogen production rate by using TiO_2 - ZnO mixed oxides photocatalysts was achieved by Perez-Larios et al. [99]. A study carried out by Matos et al. [100] showed that titanium dioxide based catalysts can also be used to produce hydrogen in visible light if these catalysts are prepared to form an Au- TiO_2 activated carbon photocatalyst. The advantages and disadvantages associated with different types of catalyst categories are summarized in Table 2.2.

This thesis investigates hybrid photocatalytic hydrogen production reactor, which are developed as part of the research. The hybrid photocatalytic hydrogen production reactor developed is used to produce hydrogen using CuCl, hydrochloric acid, zinc sulfide, sodium sulfide, sodium hydroxide and water solution. Experiments are performed to study the effect of different operating parameters such as voltage, mass of zinc sulfide, mass or concentration of CuCl and solar light intensity on the hydrogen production rate. Comparative energy and exergy analyses of two solar-based integrated systems are also performed to analyze the importance of integration on system performance. In the end, the results obtained from the research are presented and discussed thoroughly.

Table 2.2 Advantages and disadvantages associated with different photocatalysts category.

Catalyst	Advantages	Disadvantages
SrTiO ₃	<ul style="list-style-type: none"> • Chemically stable. • Suitable for supporting the accommodation space for a wide range of cations and valences 	<ul style="list-style-type: none"> • Wide band gap (3.2 eV). • Active only under UV light.
TiO ₂	<ul style="list-style-type: none"> • Environmentally friendly. • Chemically stable. • Cost effective. 	<ul style="list-style-type: none"> • Low photocatalytic efficiency. • Wide band gap (3.2 eV). • Mostly active under UV light. • Hazardous to health.
ZnS	<ul style="list-style-type: none"> • High energy conversion efficiency. • Reasonable band gap. • Active in visible light. 	<ul style="list-style-type: none"> • Expensive. • Not environmentally friendly.
Ta/O	<ul style="list-style-type: none"> • High photocatalytic performance. • Robust structure. 	<ul style="list-style-type: none"> • Rarely studied. • Limited practical application.
CdS	<ul style="list-style-type: none"> • High photocatalytic performances. • Reasonable band gap. • Rapid generation of electron-hole pairs. 	<ul style="list-style-type: none"> • Expensive. • Not environmentally friendly. • Unstable. • Photocorrosion.
Ru	<ul style="list-style-type: none"> • Transparent solution. • Works in visible light range. 	<ul style="list-style-type: none"> • Low quantum yield. • Lack of data. • Expensive.

Chapter 3: Experimental Setup and Procedure

3.1 Reactor Design

A promising alternative to conventional hydrogen production techniques is thermochemical water splitting cycles. The Cu-Cl cycle poses the best value in terms of its impact on the environment as it re-circulates the near-maximum amount of chemicals used within the cycle. However, like any other electrolysis-based process, the electrolyzer inside the Cu-Cl cycle requires some significant inputs of electrical energy to produce hydrogen. This problem can be overcome by hybridizing the current electrolysis cell of the Cu-Cl cycle with a photocatalytic process that makes use of solar light intensity to generate enough potential to produce hydrogen. The hybrid photocatalytic reactor developed as part of the present research is divided into two half-cells (anode half-cell and cathode half-cell) separated by a cation exchange membrane. The process flow diagram of the experimental setup is shown in Fig. 3.1. The experimental setup used in the present research is made of glass to allow solar light to come in contact with the catalyst as shown in Fig. 3.2. The anode-side compartment produces electrons and positively-charged hydrogen ions by dissociating the aqueous solution of CuCl and HCl. The electrons and positively-charged ions then pass through the electrodes and cation exchange membrane, respectively, to enter the cathode half-cell of the reactor. In the cathode half-cell of the reactor, water molecules are dissociated into hydrogen and hydroxyl ion. The hydrogen produced is then collected using a collection chamber fitted with a pressure sensor. At first, the photocatalytic experiments are performed to investigate the effect of variation in solar light intensity, mass or concentration of CuCl and concentration of ZnS on hydrogen production rate. In the second phase of the experiment, the photo-electrocatalytic experiments are carried out with a voltage applied through an external power supply to simulate the conditions of using titanium dioxide as an electron donor.

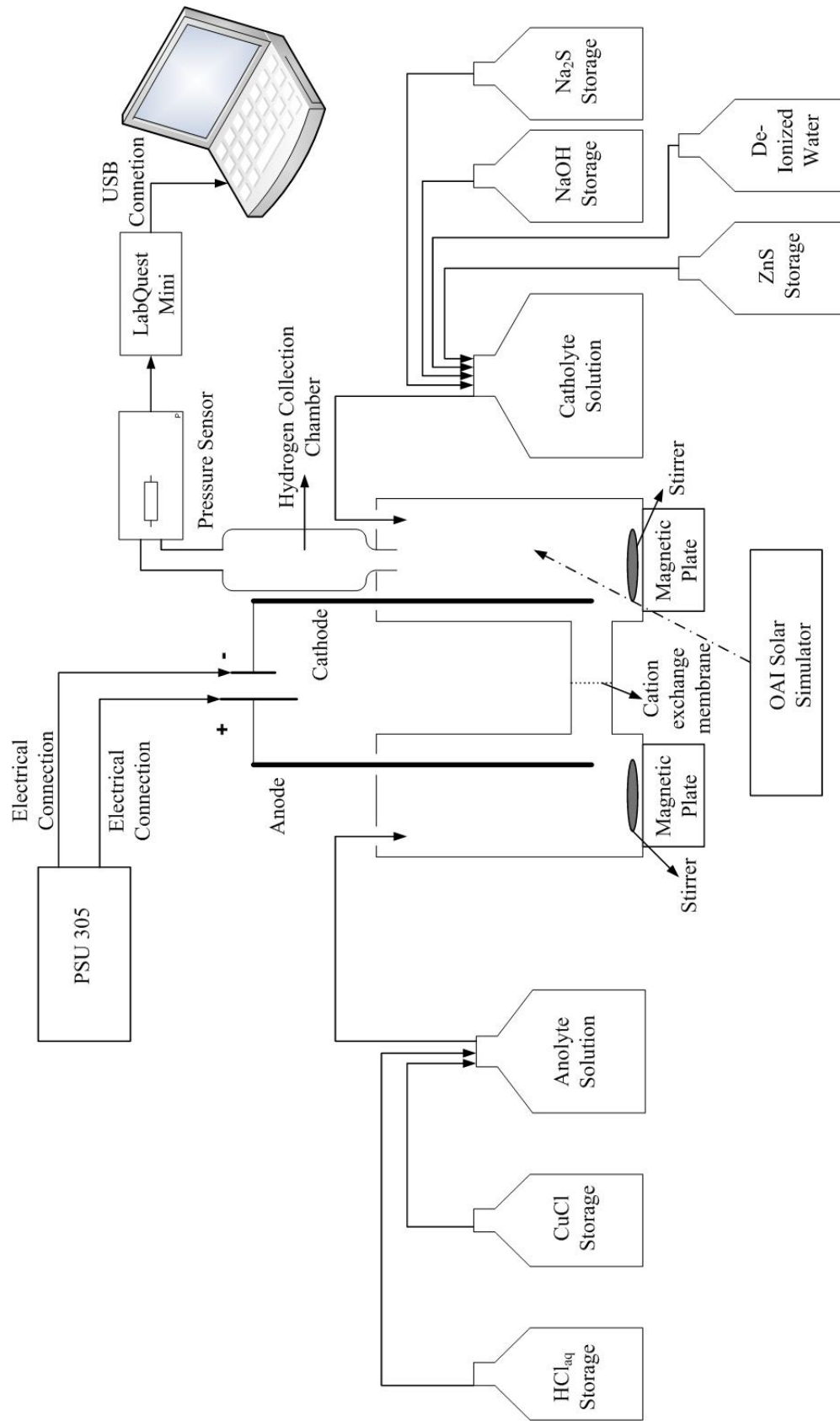


Fig. 3.1. Process flow diagram of the hybrid photocatalytic hydrogen production reactor.

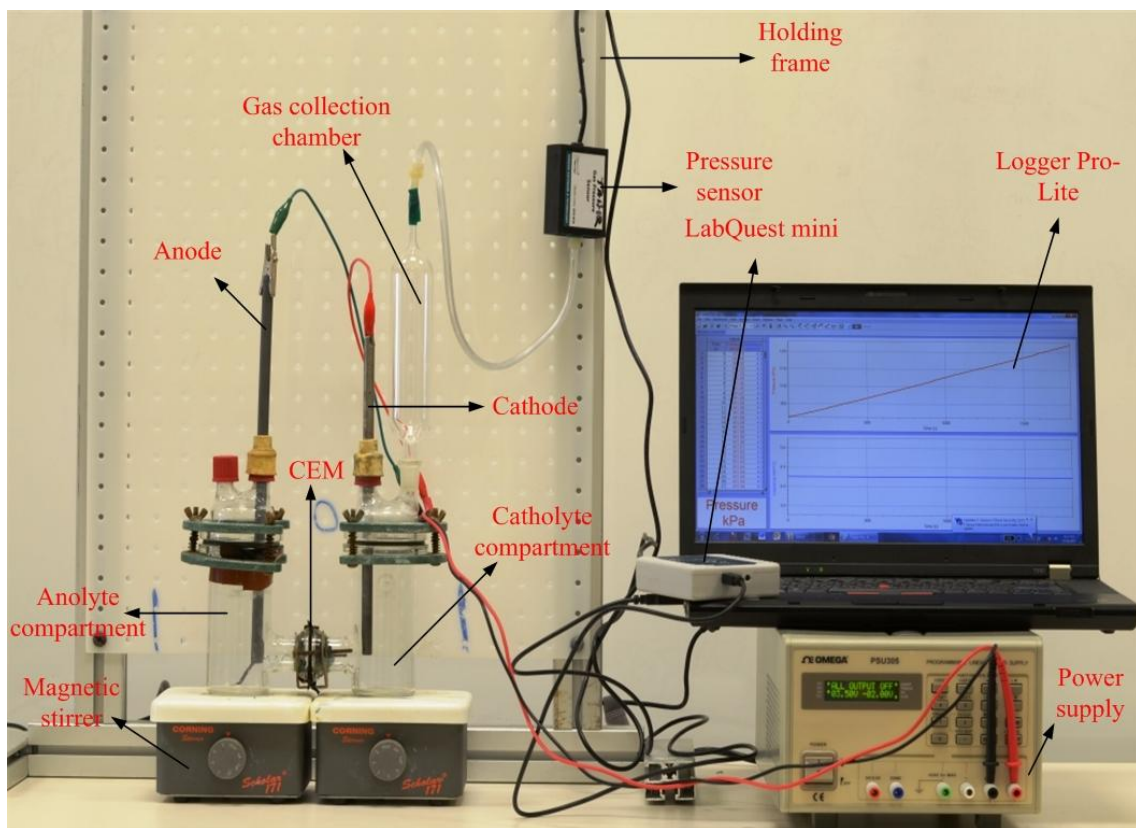


Fig. 3.2. Experimental setup.

Several parameters in different combinations are varied to observe the effects of different operating parameters on the desired output of the system. The design of the experiment, also known as factorial design technique, helps in selecting the repeatability criteria by varying the operating parameters in different combinations to ensure that the number of experiments conducted satisfies the repeatability criteria selected. The benefit of using the design of experiment method is that it allows (a) varying one input parameter with several combinations of other input parameters and (b) applying analysis of variance technique to find the correlation between the input parameters and the desired output. The number of experiments suggested by factorial design depends on the repeatability criteria selected for each operating parameter being varied. In the photocatalytic experiments, zinc sulfide is used as a photocatalyst alongside sodium hydroxide, which acts as an electrolyte, and sodium sulfide, which acts as a hole scavenger in the cathode half-cell. During the photocatalytic experiment, the effects of three parameters on the hydrogen production rate are studied. The three parameters varied are (a) solar light intensity, (b)

mass or concentration of CuCl and (c) mass or concentration of ZnS while the concentration of sodium hydroxide and sodium sulfide are kept constant at 0.033 and 0.22 g/mL, respectively in the cathode half-cell based on research conducted by Rabbani [75]. The solar light intensity is varied at three different levels from 400 to 500 W/m² with an interval of 50 W/m². Such a range for solar light intensity is selected for experimental investigation, due to the limitation of the solar simulator, which is only able to provide solar light intensity up to 500 W/m². The mass or concentration of CuCl is varied at three different levels from 5 to 10 g or 0.033 to 0.066 g/mL with an interval of 2.5 g or 0.016 g/mL in aqueous hydrochloric acid solution. The mass or concentration of ZnS is varied at three different levels from 2 to 4 g or 0.013 to 0.027 g/mL with an interval of 1 g or 0.006 g/mL in the cathode solution. The mass or concentration of CuCl and ZnS are experimentally varied based on the ranges suggested by Aghahosseini [43] and Rabbani [75]. The advantage of using three degree of repeatability in factorial design is that it gives a better indication of the effects of varying parameters on the desired output, such as hydrogen production rate. The software developed by Stat-Ease [101] The Design-Expert 8.1.6 is used for designing the experiments based on the factorial design theory. The numbers of experiments designed by factorial design are based on the multiplication of repeatability of each parameter being varied. For the photocatalytic experiments, the numbers of experiments done are 27 and each experiment is conducted for 30 minutes. Table 3.1 tabulates the combination of parameters which are varied during the experiments.

3.2 Design of Experiments

The photo-electrocatalytic experiments are performed in the second phase of the experimental study as shown in Fig. 3.3. In photo-electrocatalytic experiments, a hybrid unit is constructed by combining electrolysis and photocatalytic experiments. These experiments are performed to show the amount of hydrogen that can be produced if external power input is replaced by titanium dioxide on the anode side of the experiment. In photo-electrocatalytic experiments, four parameters are varied each with an interval of three. In these experiments the voltage is varied from 2.5 to 3.5 V with an interval of 0.5 V, the solar light intensity is varied from 400 to 500 W/m² with an interval of 50 W/m²,

the mass or concentration of CuCl is varied from 5 to 10 g or 0.033 to 0.066 g/mL with an interval of 2.5 g or 0.0166 g/mL in aqueous hydrochloric acid solution and the mass or concentration of ZnS is varied from 2 to 4 g or 0.013 to 0.027 g/mL with an interval of 1 g or 0.006 g/mL in the cathode solution. The concentration of sodium hydroxide and sodium sulfide are kept constant at 0.033 and 0.22 g/mL, respectively in the cathode half-cell.

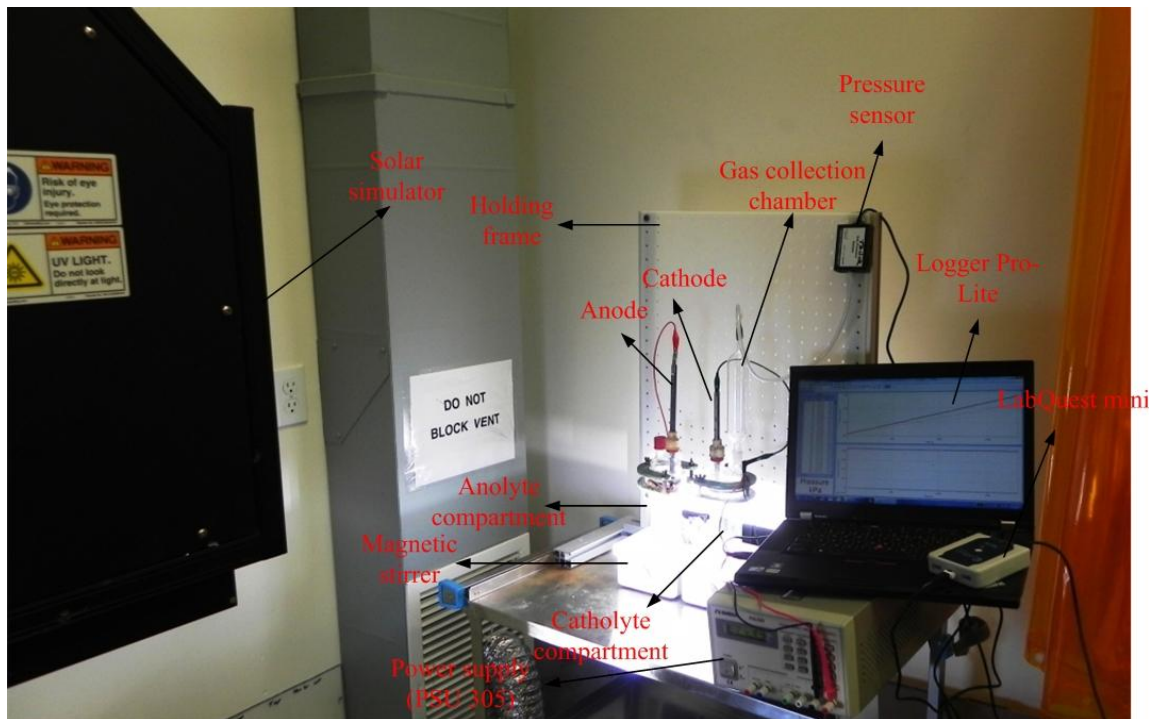


Fig. 3.3. Experimental setup for photocatalytic experiments.

For the photo-electrocatalytic experiments, a total 81 experiments are carried out, and each experiment is conducted for 30 minutes. Table 3.2 tabulates the combination of parameters that were varied during the experiments.

3.3 Experimental Setup

The experimental apparatus is manufactured based on a control volume process, where the total volume of the system remains constant. However, with the production of hydrogen, the pressure at the cathode side increases as gas requires more space than liquid. To measure the pressure of the hydrogen gas, a pressure sensor manufactured by Vernier is used as shown in Fig. 3.4. This pressure sensor is capable of measuring

pressure in the range of 0 to 210 kPa with a resolution of 0.06 kPa, accuracy of $\pm 0.25\%$ and response time of 100 μs [102]. The pH values of both cathode and anode solutions are measured using the pH sensor manufactured by Vernier, as shown in Fig. 3.5. The sensor is capable of measuring the pH of a solution in the range of 0 to 14 with a resolution of 0.005 and response time of 1 s [103].

Table 3.1. Factorial design of experiments for photocatalytic experiments

Experiment	Solar Light Intensity (W/m^2)	Mass of ZnS (g)/ Concentration of ZnS (g/mL)	Mass of CuCl (g) / Concentration of CuCl (g/mL)
1	400	2 / 0.013	5 / 0.033
2	450	2 / 0.013	5 / 0.033
3	500	2 / 0.013	5 / 0.033
4	400	3 / 0.020	5 / 0.033
5	450	3 / 0.020	5 / 0.033
6	500	3 / 0.020	5 / 0.033
7	400	4 / 0.027	5 / 0.033
8	450	4 / 0.027	5 / 0.033
9	500	4 / 0.027	5 / 0.033
10	400	2 / 0.013	7.5 / 0.050
11	450	2 / 0.013	7.5 / 0.050
12	500	2 / 0.013	7.5 / 0.050
13	400	3 / 0.020	7.5 / 0.050
14	450	3 / 0.020	7.5 / 0.050
15	500	3 / 0.020	7.5 / 0.050
16	400	4 / 0.027	7.5 / 0.050
17	450	4 / 0.027	7.5 / 0.050
18	500	4 / 0.027	7.5 / 0.050
19	400	2 / 0.013	10 / 0.066
20	450	2 / 0.013	10 / 0.066
21	500	2 / 0.013	10 / 0.066
22	400	3 / 0.020	10 / 0.066
23	450	3 / 0.020	10 / 0.066
24	500	3 / 0.020	10 / 0.066
25	400	4 / 0.027	10 / 0.066
26	450	4 / 0.027	10 / 0.066
27	500	4 / 0.027	10 / 0.066

The cation exchange membrane is obtained from Ion Power Inc. The membrane that is used is Nafion 115 with an active area of 12 x 12 cm, thickness of 127 microns, weight of 250 g/m² and electrical conductivity of 0.1 S/cm [104]. For projection of the solar light, the OAI TriSol 208 mm × 208 mm, Class AAA 1 Sun solar simulator is used as shown in Fig. 3.6. This solar simulator is capable of providing solar light intensity equal to that of one full sun and covers the complete spectrum of solar light with an accuracy of ±2% [105]. The electrical input to the reactor is provided by a power supply manufactured by OMEGA (PSU 305) as shown in Fig. 3.7 [106].

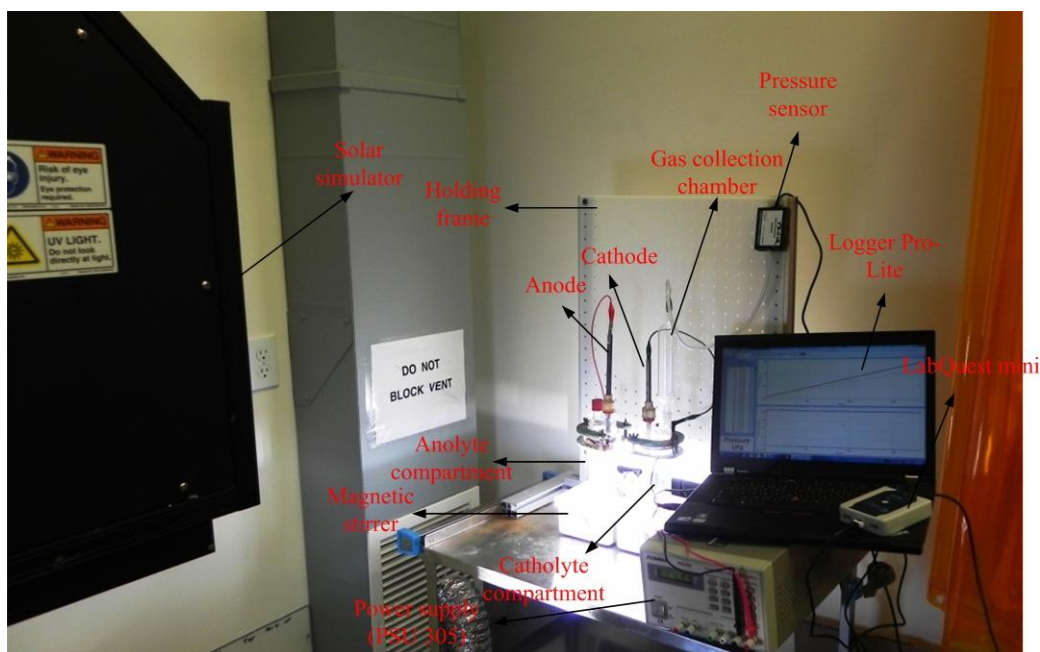


Fig. 3.4. Experimental setup for photo-electrocatalytic experiments.

Table 3.2. Factorial design of experiments for photo-electrocatalytic experiments

Experiment	Voltage (V)	Solar Light Intensity (W/m ²)	Mass of ZnS (g)/ Concentration of ZnS (g/mL)	Mass of CuCl (g)/ Concentration of CuCl (g/mL)
1	2.5	400	2 / 0.013	5 / 0.033
2	2.5	450	2 / 0.013	5 / 0.033
3	2.5	500	2 / 0.013	5 / 0.033
4	2.5	400	3 / 0.020	5 / 0.033
5	2.5	450	3 / 0.020	5 / 0.033
6	2.5	500	3 / 0.020	5 / 0.033
7	2.5	400	4 / 0.027	5 / 0.033
8	2.5	450	4 / 0.027	5 / 0.033
9	2.5	500	4 / 0.027	5 / 0.033

10	2.5	400	2 / 0.013	7.5 / 0.050
11	2.5	450	2 / 0.013	7.5 / 0.050
12	2.5	500	2 / 0.013	7.5 / 0.050
13	2.5	400	3 / 0.020	7.5 / 0.050
14	2.5	450	3 / 0.020	7.5 / 0.050
15	2.5	500	3 / 0.020	7.5 / 0.050
16	2.5	400	4 / 0.027	7.5 / 0.050
17	2.5	450	4 / 0.027	7.5 / 0.050
18	2.5	500	4 / 0.027	7.5 / 0.050
19	2.5	400	2 / 0.013	10 / 0.066
20	2.5	450	2 / 0.013	10 / 0.066
21	2.5	500	2 / 0.013	10 / 0.066
22	2.5	400	3 / 0.020	10 / 0.066
23	2.5	450	3 / 0.020	10 / 0.066
24	2.5	500	3 / 0.020	10 / 0.066
25	2.5	400	4 / 0.027	10 / 0.066
26	2.5	450	4 / 0.027	10 / 0.066
27	2.5	500	4 / 0.027	10 / 0.066
28	3	400	2 / 0.013	5 / 0.033
29	3	450	2 / 0.013	5 / 0.033
30	3	500	2 / 0.013	5 / 0.033
31	3	400	3 / 0.020	5 / 0.033
32	3	450	3 / 0.020	5 / 0.033
33	3	500	3 / 0.020	5 / 0.033
34	3	400	4 / 0.027	5 / 0.033
35	3	450	4 / 0.027	5 / 0.033
36	3	500	4 / 0.027	5 / 0.033
37	3	400	2 / 0.013	7.5 / 0.050
38	3	450	2 / 0.013	7.5 / 0.050
39	3	500	2 / 0.013	7.5 / 0.050
40	3	400	3 / 0.020	7.5 / 0.050
41	3	450	3 / 0.020	7.5 / 0.050
42	3	500	3 / 0.020	7.5 / 0.050
43	3	400	4 / 0.027	7.5 / 0.050
44	3	450	4 / 0.027	7.5 / 0.050
45	3	500	4 / 0.027	7.5 / 0.050
46	3	400	2 / 0.013	10 / 0.066
47	3	450	2 / 0.013	10 / 0.066
48	3	500	2 / 0.013	10 / 0.066
49	3	400	3 / 0.020	10 / 0.066
50	3	450	3 / 0.020	10 / 0.066
51	3	500	3 / 0.020	10 / 0.066
52	3	400	4 / 0.027	10 / 0.066
53	3	450	4 / 0.027	10 / 0.066
54	3	500	4 / 0.027	10 / 0.066

55	3.5	400	2 / 0.013	5 / 0.033
56	3.5	450	2 / 0.013	5 / 0.033
57	3.5	500	2 / 0.013	5 / 0.033
58	3.5	400	3 / 0.020	5 / 0.033
59	3.5	450	3 / 0.020	5 / 0.033
60	3.5	500	3 / 0.020	5 / 0.033
61	3.5	400	4 / 0.027	5 / 0.033
62	3.5	450	4 / 0.027	5 / 0.033
63	3.5	500	4 / 0.027	5 / 0.033
64	3.5	400	2 / 0.013	7.5 / 0.050
65	3.5	450	2 / 0.013	7.5 / 0.050
66	3.5	500	2 / 0.013	7.5 / 0.050
67	3.5	400	3 / 0.020	7.5 / 0.050
68	3.5	450	3 / 0.020	7.5 / 0.050
69	3.5	500	3 / 0.020	7.5 / 0.050
70	3.5	400	4 / 0.027	7.5 / 0.050
71	3.5	450	4 / 0.027	7.5 / 0.050
72	3.5	500	4 / 0.027	7.5 / 0.050
73	3.5	400	2 / 0.013	10 / 0.066
74	3.5	450	2 / 0.013	10 / 0.066
75	3.5	500	2 / 0.013	10 / 0.066
76	3.5	400	3 / 0.020	10 / 0.066
77	3.5	450	3 / 0.020	10 / 0.066
78	3.5	500	3 / 0.020	10 / 0.066
79	3.5	400	4 / 0.027	10 / 0.066
80	3.5	450	4 / 0.027	10 / 0.066
81	3.5	500	4 / 0.027	10 / 0.066



Fig. 3.5. The pressure sensor used for experimental measurements [102].

The power supply has 12-bit digital to analogue converter, numeric keyboard for direct setting and three channels with two adjustable and one fixed output. The maximum

output power supplied by PSU 305 is 165 W with output voltage ranging from -30 to 30 V with a difference of ± 20 mV and current ranging from -2.5 to 2.5 A with a difference of ± 5 mA [106]. The benefit of using this power supply is that it is highly stable even when the load fluctuates due to its load management system and also has a response time of 200 μ s. A pyranometer manufactured by Vernier (Fig. 3.8) is used to measure the amount of solar light reaching the experimental setup. The pyranometer is capable of handling an irradiance range of 0 to 1100 W/m² with an accuracy of $\pm 5\%$ and resolution of 0.3 W/m² [107]. In the experiments, de-ionized water from Canadian Tire, having a pH of approximately seven is used to ensure that the solution prepared does not receive any impurities from the water. The aqueous hydrochloric acid used in all of the experiments is obtained from Fisher Scientific with a molarity of 11 mol/L. To record the data from the experiments in an automatic manner, sensors interface namely the LabQuest mini [108] as shown in Fig. 3.9 and data logger software namely Pro-lite developed by Vernier are used [109].



Fig. 3.6. The sensor utilized to record the pH reading of the solutions [103].

3.4 Experimental Procedure

The experimental study performed during the course of the research is carried out in the Clean Energy Research Lab located at the University of Ontario Institute of Technology. The apparatus used during the experimental study are presented in earlier sections. For the photocatalytic experiment, the anode solution is prepared by adding different mass or concentration of CuCl to the aqueous hydrochloric acid. The cathode solution is prepared by mixing different mass or concentration of zinc sulfide, sodium hydroxide and sodium sulfide in 150 mL of de-ionized water. For the photo-electrocatalytic experiments the

anode and cathode solutions are prepared in the same way as that of the photocatalytic experiments. In the photocatalytic and the photo-electrocatalytic experiments, titanium is used as the cathode and graphite is used as the anode. Graphite is selected as an anode due to its high resistivity to the corrosion and cheaper acquiring cost. For the purpose of demonstrating the working principal of a titanium dioxide catalyst, a titanium dioxide anode is used instead of graphite for a small number of photocatalytic experiments. The titanium dioxide anode is prepared by screen printing titanium dioxide onto conductive glass, which can stay stable in an 11 mol/L hydrochloric acid. The hydrogen production rate is measured by a gas collection chamber and pressure sensor. The pressure sensor is connected to the computer with the help of LabQuest mini to automatically record the pressure change in the reactor after every second.



Fig. 3.7. The solar simulator used in the experiments.



Fig. 3.8. The power supply employed in the experiments [106].



Fig. 3.9. The pyranometer used to measure the solar light intensity during the experiments [107].



Fig. 3.10. The sensors interface used to record experimental values digitally [108].

3.5 Experimental Errors and Measurement Uncertainties

Any quantity measured through an experiment contains errors associated with the measured data. A quantity measured can differ slightly or greatly from its true value depending on the errors associated with the measurements. Measurement errors can arise due to several factors, such as illegitimate errors, systematic errors and random errors [110].

Illegitimate errors occur when a mistake is made in measurement or reporting a particular measurement. This type of error can be easily avoided by carefully performing and repeating the experiments and by making sure that measurements are reported in the correct units. In the present experimental work, these types of errors are avoided by using the automatic data logger LabQuest min.

Systematic errors are usually caused by mishandling the instrument used to measure the required quantity [111]. A non-calibrated instrument can result in systematic errors or

one can make a mistake in their measurement because of the way one reads the instrument. Some examples of mistakes that can lead to bias errors are not taking into account the presence of meniscus when reading the liquid level, or when the reaction time is ignored while measuring the duration of an event. The calibration errors can be avoided by using automatic calibration system for the pressure sensor and by calibrating the electronic weighing scale every time before use.

Random errors in measurement are introduced by the precision of the measuring device used and the precision of reading the measurements. These types of errors can be estimated by taking into account the precision of the measuring instrument, which is most often provided by the manufacturer.

An error in an experiment can be evaluated by using either of the two techniques that are the direct evaluation of the experimental errors and the statistical evaluation of the experimental errors.

Direct evaluation of experimental errors is used if an experimenter knows the precision of the instrument being used and if the instrument is being used optimally such that no usage error or reading error occurs. The experimental error should then be equal to the precision of the instruments being used [112]. For example, if a balance with a precision of 0.005 g is used, then the error associated with the measurement of the mass will be ± 0.005 g.

Statistical evaluation of an experimental errors method is used if an experimental error is random and not systematic. Repeating the experiments and measuring the required value several times can result in slightly different values and by averaging these values one can obtain a value close to the real value. To estimate the random error, one can calculate the standard deviation of a series of values and if the number of values is very large then one can use the standard error method, which is simply the standard deviation divided by the square root of the number of values being measured. For experimental data dealing with several varying parameters it is recommended to use more complicated methods such as analysis of variance (ANOVA), which is a refinement of methods discussed earlier [110, 113].

When reporting the errors, it is important to mention whether the errors presented are in the form of accuracy or precision. Accuracy refers to how close the measurement of the quantity is to the actual value of that particular quantity. Accuracy of a reading is affected by all three types of errors, which are illegitimate, systematic and random errors. On the other hand, precision of a measurement refers to how close a particular measurement is to the average value obtained for that quantity. Precision of a measurement is only affected by the random errors and not by the illegitimate or systematic errors.

Analysis of variance (ANOVA) is used in statistics to assess the variations in the experimental data. The ANOVA analysis assumes that the total variation in an experimental data is no greater than the combined variation of individual parameters and errors in measurements [114]. In other words, it is a statistical tool used to find the significance of the varied parameters on the desired output from the experiments [115]. The ANOVA method has five components: (a) degree of freedom, (b) sum of squares, (c) mean square value, (d) F_{value} and (e) p-value.

Here, the degree of freedom corresponds to the minimum number of values that should be obtained to identify all data point in a particular sample. The N number of data points requires N number of degrees of freedom and if the mean of the data is known then the degree of freedom is defined as N-1 [115].

For any model, the total degree of freedom (Df) is defined as

$$Df_{tot} = Df_{MT} + Df_R \quad (3.1)$$

where Df_{tot} , Df_{MT} and Df_R represent total degree of freedom, degree of freedom associated with model term and degree of freedom associated with residual, respectively.

The degree of freedom associated with the residual term is defined as

$$Df_R = Df_{LOF} + Df_{PE} \quad (3.2)$$

where Df_{LOF} and Df_{PE} represent degree of freedom based on lack of fit and degree of freedom based on pure error.

The total sum of squares for any given model is defined as the summation of the squared deviation from the mean of a data due to the effect of an individual term and the interaction between two terms [116]. The sum of squares is defined as

$$SS_{tot} = SS_{MT} + SS_R \quad (3.3)$$

where SS_{tot} , SS_{MT} and SS_R represent total sum of squares, sum of squares associated with model term and sum of squares associated with residual, respectively.

The sum of squares associated with the residual is defined as

$$SS_R = SS_{LOF} + SS_{PE} \quad (3.4)$$

where SS_{LOF} and SS_{PE} represent sum of squares for lack of fit and pure error, respectively.

Here, the SS_{LOF} term represents the residual caused by the model term not fitting the data. It takes into consideration the sum of squared deviations occurring between the mean responses at each factor level along with its corresponding fitted value. However, the errors associated with the repeatability in the data are represented by the sum of squares due to pure error. It consists of the corrected sum of squares of the repeated observations at each level of input combined with overall input levels [75].

The mean square value denoted by MV represents the ratio of the sum of squares to the degree of freedom and is defined as

$$MV = SS/Df \quad (3.5)$$

The test which compares variance related to a particular term with the residual term is known as F_{value} . It is the ratio between the mean square value for the term and the mean square value for error [117]. It is defined as

$$F_{value} = \frac{\frac{SS_{term}}{Df_{term}}}{\frac{SS_{residual}}{Df_{residual}}} \quad (3.6)$$

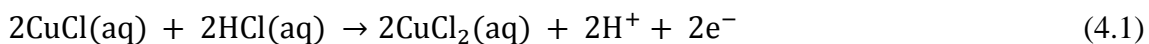
The p-value represents the probability of having certain F_{value} for the parameter based on the effect of the parameter on the system response. On the basis of 95% confidence level,

a parameter having a p-value less than 0.05 is considered significant and one having p-value larger than 0.10 is considered insignificant [118].

Chapter 4: Integrated System Development and Description

4.1 Hybrid Photo-electrocatalytic Hydrogen Production Reactor

The use of solar energy in producing hydrogen comes with the benefits of low greenhouse gas emissions and low operation cost. The hybrid photo-electrocatalytic hydrogen production reactor studied in this research is shown in Fig. 4.1. The hybrid photo-electrocatalytic hydrogen production reactor consists of two half-cells. The first half-cell is the anode side of the reactor and the second half-cell is the cathode. A mixture of CuCl, HCl and water is fed to the anode half-cell. Voltage is then applied to the circuit, which helps in breaking the mixture into CuCl₂, water and positive hydrogen ions. As a result of this breaking of bonds, two electrons and positive hydrogen ion are released. The positive hydrogen ions and electrons pass through the membrane and electrical circuit, respectively, then enter the second half-cell of the hybrid photo-electrocatalytic hydrogen production reactor (cathode side). The reaction taking place at the anode side of the hybrid photo-electrocatalytic hydrogen production reactor is given below:



The protons and electrons released by the mixture on the anode side enter the cathode side, where they come in contact with water. The two electrons combine with two water molecules to produce hydrogen and two hydroxyl ions. The hydrogen produced is collected from the reactor.

In this reactor, ZnS is used as a photocatalyst due to its positive attributes as explained in the earlier chapter. The Na₂S is used as an electron donor/hole scavenger to provide necessary electrons to the cell and to keep the catalyst active for a longer time. The NaOH is used as an electrolyte to facilitate the reaction. The cathode side of the hydrogen production reactor is driven by solar light.

The heterogeneous photocatalyst (ZnS) used in the present study is a semi-conductor device with the valence and conduction bands. When a photon of light having energy equal or larger than the band gap between the valence and conduction bands of the ZnS is induced on the ZnS, the electrons from the valence band jump into the conduction band and form a hole in the valence band. The electrons in the conduction band then combine

with water molecule to form hydrogen and hydroxyl ions. The reactions occurring at the cathode side of the reactor are given below:

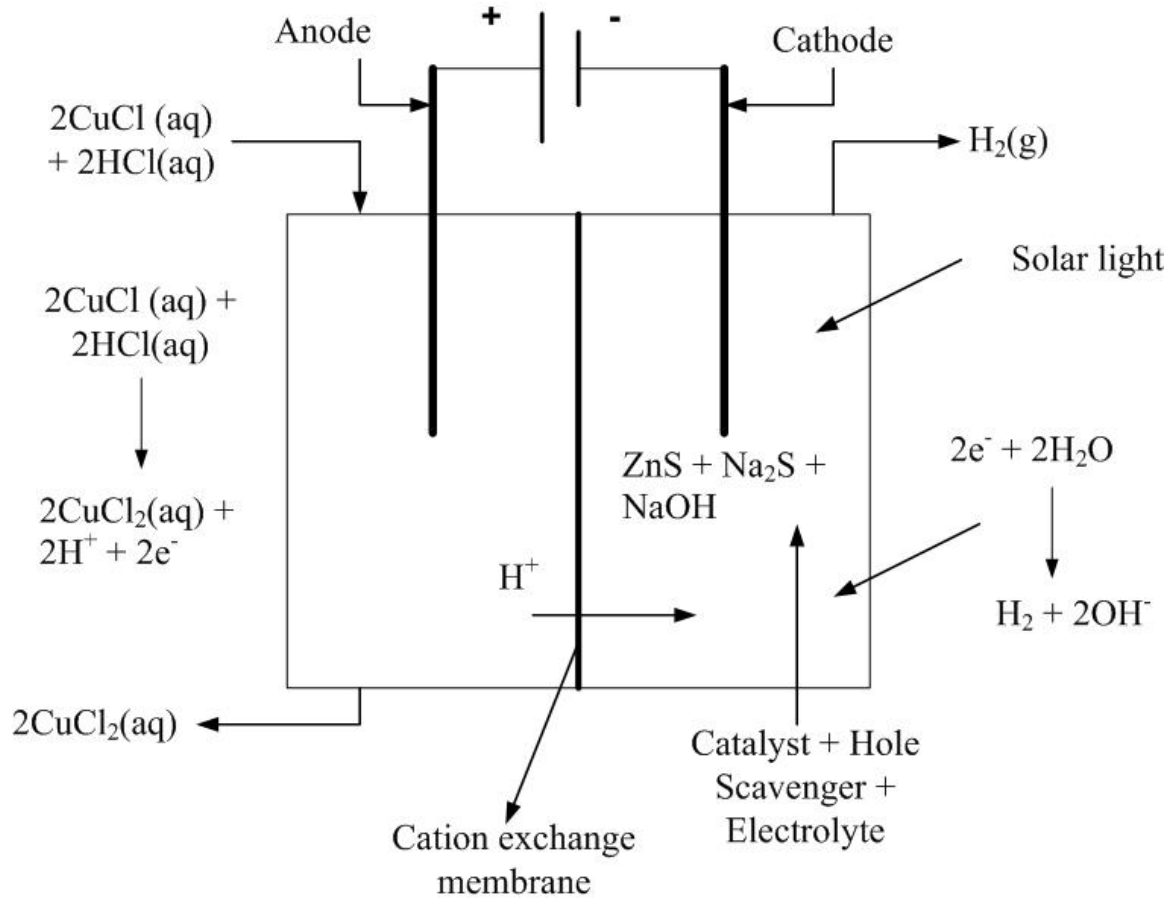


Fig. 4.1. Schematic of the hybrid photocatalytic hydrogen production reactor.

In the second part of the study, the anolyte compartment is also fed with the photocatalyst to remove the electrical input requirement of the reactor for hydrogen production. The heterogeneous photocatalyst titanium dioxide is used in the anolyte solution to provide necessary potential for the chemical reaction to take place. The electrons generated in the anolyte compartment are then circulated to the catholyte compartment with the help of electrodes. The overall reaction of the second experimental setup remains the same, because titanium dioxide provides the necessary potential to the cell which was earlier

done with the help of power supply. These types of hybrid systems are expected to pave the way to hydrogen production technologies which are more dependent on alternative/renewable energy sources that are environmental friendly compared to conventional fossil fuel based technologies. The hybrid photocatalytic hydrogen production reactor presented in this research can further be modified to produce other useful gases or chemicals that at present are achieved through fossil fuels.

4.2 Integrated Solar Thermal, Cu-Cl Cycle and Photocatalytic Reactor System

Although the thermochemical water splitting cycles provide an attractive solution to the conventional hydrogen production methods, they come with a drawback of high-temperature heat requirement. An attractive renewable energy system that has a capability of providing high temperature heat to the Cu-Cl cycle is the solar heliostat field system. Solar heliostat field systems have operating temperatures in the range of 150 to 2000°C as mentioned by Kalogirou [119]. The two integrated systems studied are shown in Fig. 4.2. In both integrated systems, a heliostat solar system is used to supply the required heat to the system. Heliostat mirrors reflect solar light to the central receiver. Molten salt passes through the central receiver and gains energy from the reflected sunlight that raises its temperature. This high-temperature molten salt then enters the high-temperature heat exchanger, where it releases heat to the water returning from the Kalina cycle. The superheated steam leaving the high-temperature heat exchanger is supplied to the Cu-Cl cycle to meet the heat requirement of the cycle. After releasing heat at different stages in the Cu-Cl cycle, steam enters the Kalina cycle. This steam then releases heat to the ammonia-water working fluid of the Kalina cycle to be supplied back to the high-temperature heat exchanger. The power produced by the Kalina cycle is supplied to the Cu-Cl cycle. For the second integrated system, the solar light reflected by the central receiver of the heliostat field system is directed to the photocatalytic hydrogen production process as shown in Fig. 4.2b. The photocatalytic reactor is made of glass, which contains the solution of ZnS, Na₂S and NaOH. The solution of these chemicals makes it possible to produce hydrogen using solar light, thus eliminating the need for electrical input to the system. The function of ZnS is to act as a catalyst while breaking

the bond of water molecules to produce hydrogen. The Na₂S is used as hole scavengers to keep the catalyst active for a longer period of time by recirculating sulfur ions in the solution. The NaOH acts as an electrolyte, which increases the hydrogen production rate. The energy requirement of this photocatalytic reactor is fulfilled by supplying the solar light reflected by the central receiver of the heliostat field to the reactor.

The four-step Cu-Cl cycle studied in this research is shown in Fig. 4.3. The cycle is divided into following four steps: (a) hydrolysis, (b) oxygen production, (c) hydrogen production and (d) drying.

In the hydrolysis step, the high-temperature steam at approximately 400°C is brought in contact with solid CuCl₂. The reaction takes place and the products coming out of the hydrolysis section are aqueous HCl and solid Cu₂OCl₂. The overall reaction is presented below.

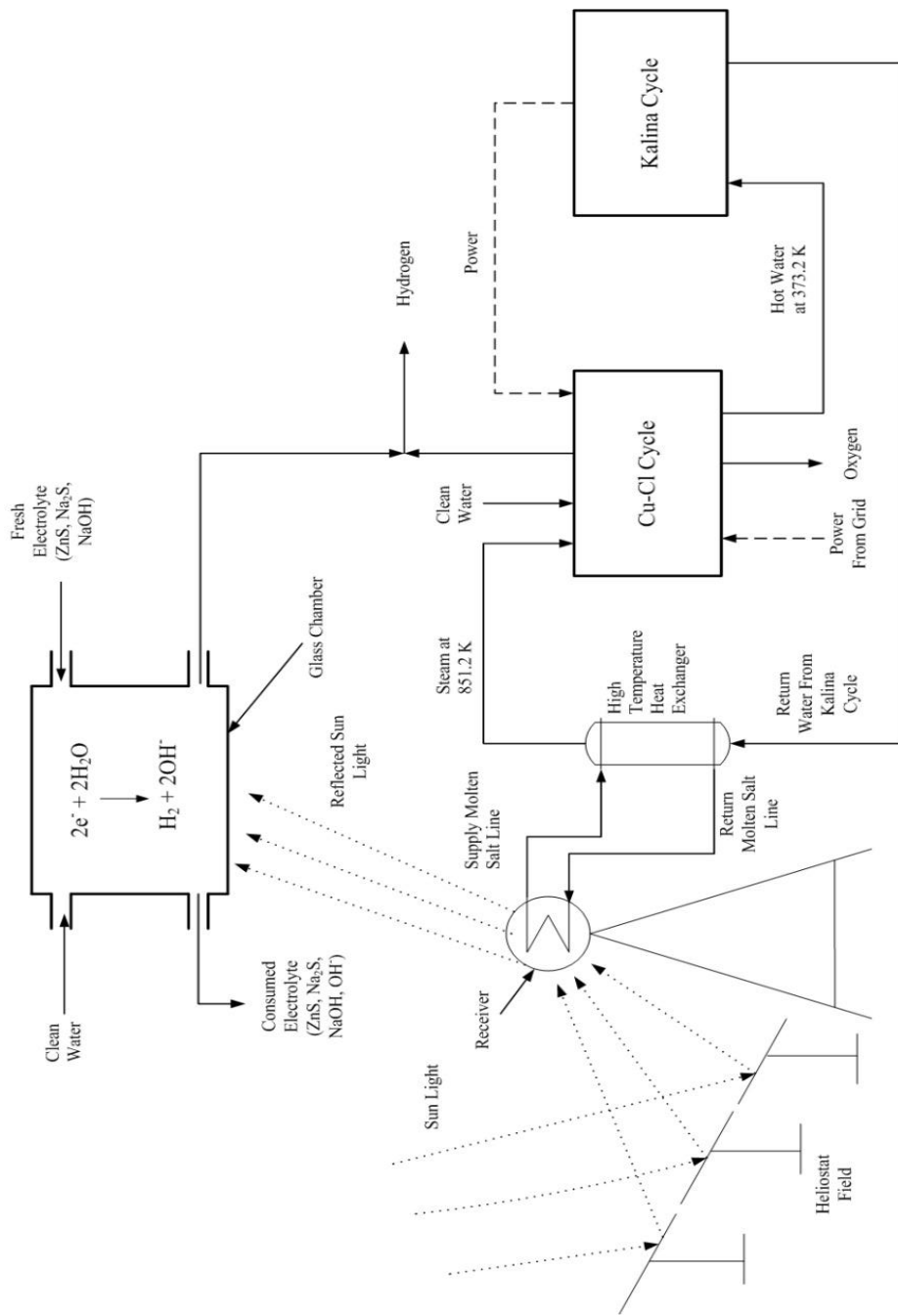


The second reaction is oxygen production, which is the most energy consuming step of the cycle since the temperature required for oxygen production is approximately 500°C. The Cu₂OCl₂ solution is passed through two heat exchangers before it reaches the second separator denoted by SEP2. In this separator Cu₂OCl₂ is broken into CuCl and oxygen. The gaseous oxygen produced is passed through several heat exchangers where its temperature is brought down to make it available for later use.

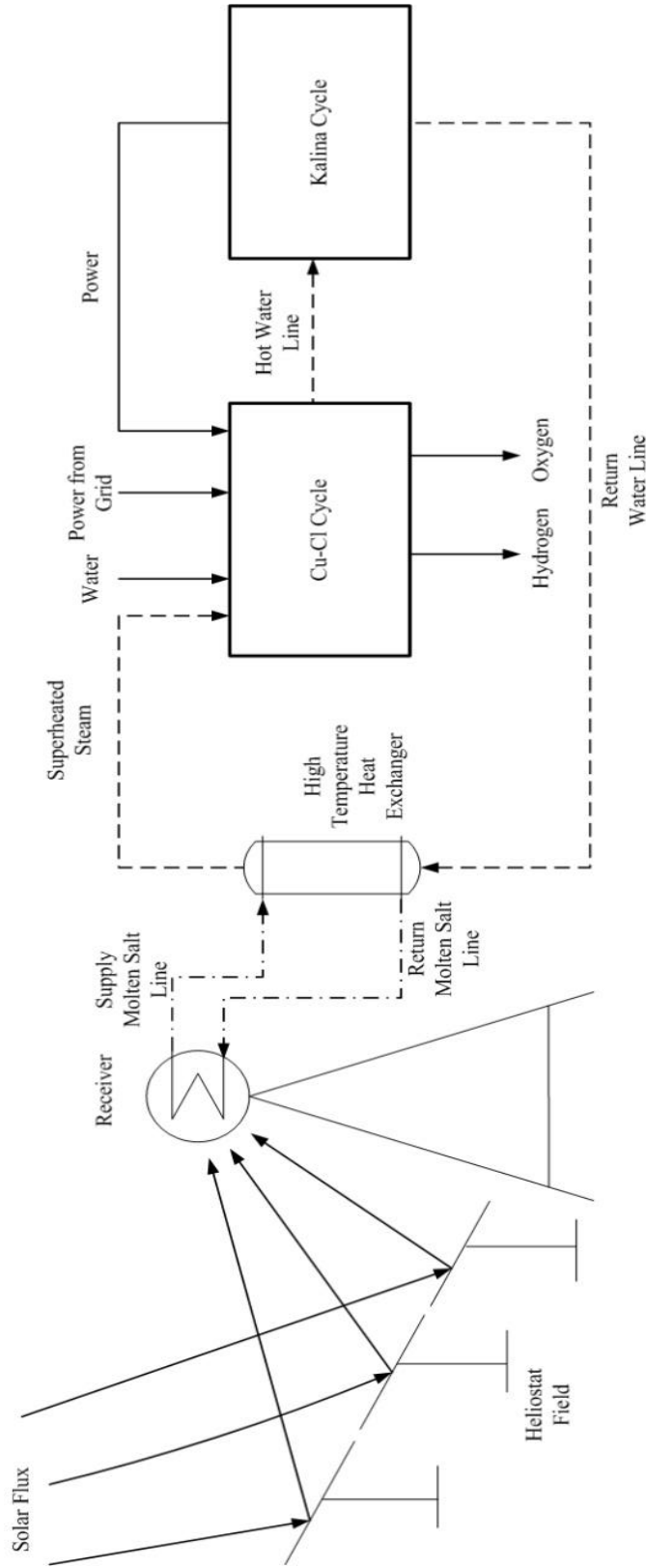
The CuCl produced passes through several heat exchangers, where it is cooled down, to mix with water and HCl. The separation reaction which takes place in this step is written as follows:



The third step in the four-step Cu-Cl cycle is hydrogen production. This step takes place at a temperature lower than 100°C. In this step aqueous CuCl and HCl from mixture enter the electrolyzer. In the electrolyzer, electrical energy is provided to dissociate CuCl and HCl into aqueous CuCl₂ and H₂. The hydrogen produced is sent to the storage tank whereas aqueous CuCl₂ produced is passed through the heat exchanger network where its temperature is increased to separate water from the solution.



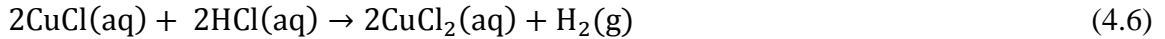
(a)



(b)

Fig. 4.2. Schematic diagram of the integrated systems. (a) system 1 and (b) system 2.

The reaction taking place in this step is given below:



The final step is drying, where water is removed from the aqueous CuCl_2 . The dried CuCl_2 in solid form is then passed through the heat exchangers to enter the hydrolysis section. The water separated from the aqueous CuCl_2 is pumped to the pressure of the mixture and is passed through the heat exchanger to bring down its temperature to that of the mixture.



Most of the heat requirement of the four-step Cu-Cl cycle is met by recycling the waste heat within the cycle using a heat exchanger network as shown in Fig. 4.4. This heat exchanger network recovers the maximum amount of heat within the cycle to reduce the energy demand of the cycle and enhance its efficiency. The steam at 851.2 K is supplied to the heat exchanger network to match the temperature requirement of the Cu-Cl cycle, which requires temperatures as high as 773 K. In this network, steam from the energy source at state hw_1 is supplied to HE6 to heat the fluid running through it from 755.2 to 773.2 K to meet the high temperature requirement of the cycle. The steam then enters HE5-C at state hw_2 where it releases heat to raise the temperature of the fluid from 673.2 to 755.2 K. The steam at state hw_3 enters HE5-H where it gains heat from the fluid running in the heat exchanger and reduces its temperature from 773.2 to 585.2 K. The steam at state hw_4 then enters HE10-H where it gains heat from the flowing solution to cool it down from 773.2 to 690.2 K. The steam at state hw_5 then enters HE4-C where it releases heat to raise the temperature of the flowing solution from 651.2 to 673.4 K.

The relatively lower temperature steam then enters HE9-H at state hw_6 , where it gains heat from the flowing solution to cool it from 690.2 to 585.4 K. After gaining heat in HE9-H, the steam at state hw_7 enters HE4-H to gain heat from the flowing solution to drop its temperature from 696.2 to 682.2 K. The steam then enters HE3-C at state hw_8 , where it releases heat to raise the temperature of the flowing solution from 353.2 to 651.2 K. The relatively lower temperature steam then enters HE8-H at state hw_9 to gain heat from the solution flowing through it to drop its temperature from 682.2 to 298.2 K.

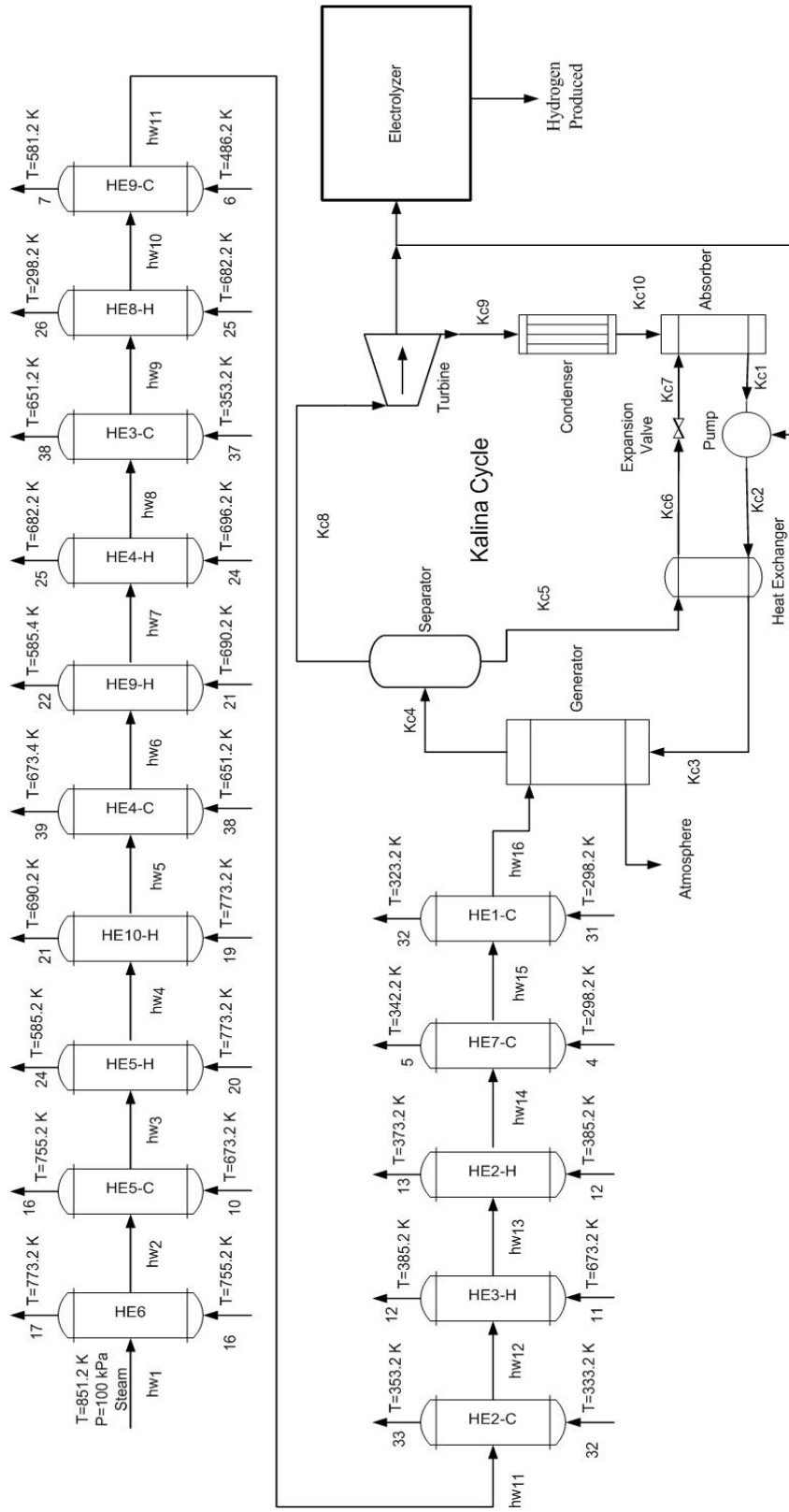


Fig. 4.4. Schematic diagram of heat exchanger network and integrated Kalina cycle.

The steam then enters HE9-C at state hw_{10} and releases heat to raise the temperature of flowing solution from 486.2 to 581.2 K. After releasing heat in HE9-C, the steam at state hw_{11} enters HE2-C, where it is used to raise the temperature of the flowing solution from 333.2 to 353.2 K. The steam then enters HE3-H at state hw_{12} to bring down the temperature of flowing solution from 673.2 to 385.2 K. The steam then enters HE2-H at state hw_{13} so that the temperature of the flowing solution can be brought down from 385.2 to 373.2 K. After gaining heat, the steam at state hw_{14} enters HE7-C to release heat to the flowing solution to raise its temperature from 298.2 to 342.2 K. After releasing heat, the steam at state hw_{15} enters HE1-C to release heat to the flowing solution to raise its temperature from 298.2 to 323.2 K. The steam leaving HE1-C at state hw_{16} then enters the generator of Kalina cycle, where it releases heat to ammonia-water mixture before leaving the generator at ambient temperature.

The steam coming out of the heat exchanger network of the Cu-Cl cycle is at approximately 373 K and can be further used for power generation using the Kalina cycle. In the Kalina cycle, heat is supplied to the generator by a waste heat recovery network of Cu-Cl cycle. In the generator, a strong solution of ammonia-water enters at state Kc3, which is then heated to leave at a higher temperature at state Kc4. The strong solution of ammonia-water leaving at state Kc4 then enters the separator where ammonia-water vapor is removed at state Kc8 and the weak ammonia-water solution is removed at state Kc5. The ammonia-water vapor is then expanded in the turbine and power is produced. The expanded ammonia-water leaves the turbine at state Kc9 to enter the condenser, where its temperature is brought down before it enters the absorber at state Kc10. The weak solution leaving the separator passes through the heat exchanger where it releases heat to the incoming strong solution at state Kc2. After releasing heat in the heat exchanger, the weak solution passes through the expansion valve where its pressure is brought down to that of the absorber. In the absorber, the weak solution at state Kc7 and ammonia-water vapor at state Kc10 mix together to leave at state Kc1 as a strong solution in the liquid form.

Chapter 5: Analyses and Optimization

In this chapter, the electrochemical and exergoeconomic modeling of the hybrid photocatalytic hydrogen production reactor is presented. Also presented is the energy and exergy modeling of the integrated solar based hydrogen production system. The software developed by Klein [120], namely Engineering Equation solver (EES), is used to run the energy, exergy, electrochemical and exergoeconomic models. EES is selected as the simulation software due to its capability of providing thermo-physical properties of large amount of liquids and gases as it contains a vast directory of thermo-physical and thermo-fluid properties. Also, EES contains built-in multi-objective optimization tools and it develops mathematical models for optimization based on user requirement by itself.

5.1 Electrochemical Modeling

In this section detailed electrochemical modeling of the hybrid photocatalytic hydrogen production reactor is provided. The electrochemical model is obtained from the models presented by [75, 121].

The overall voltage balance equation of the reactor is written as

$$V = E^0 + V_A + V_{sol1} + V_{CEM} + V_{sol2} + V_C \quad (5.1)$$

where V represents overall voltage, E^0 represents the open circuit voltage, V_A represents voltage drop across the anode electrode, V_{sol1} represents voltage drop in the anode side solution (i.e. solution of $\text{CuCl}(\text{aq})$ and $\text{HCl}(\text{aq})$), V_{CEM} represents the voltage drop across the cation exchange membrane, V_{sol2} represents voltage drop across cathode side solution (i.e. solution of catalyst and water), and V_C represents voltage drop across the cathode electrode.

The open circuit cell voltage is defined on the basis of Nernst equation and is written as

$$E^0 = E_0 + \frac{R_u \times T_{elec}}{n \times F} \ln \left(\frac{\gamma_{\text{CuCl}_2} \times P_{\text{H}_2}^{0.5}}{\gamma_{\text{CuCl}} \times \gamma_{\text{HCl}}} \right) \quad (5.2)$$

where R_u , T_{elec} , F , γ , n and P represent universal gas constant, temperature of the process, Faraday's constant, activity coefficient, number of electrons exchanged and pressure of the process, respectively. For the Cu-Cl cycle activity coefficients of CuCl

and CuCl_2 are not available in the literature. For the processes whose activity coefficients are unknown a modified equation is presented by Liu [122] which is written as

$$E^0 = E_0 + \frac{3 \times R_u \times T_{elec}}{2 \times n \times F} \ln(P_{elec}) \quad (5.3)$$

with

$$E_0 = \Delta h^0 - T_{elec} \times \Delta S^0$$

where ΔH and ΔS represent change in specific enthalpy and change in specific entropy, respectively.

The voltage drop across the anode electrode is calculated as

$$V_A = c_A \log\left(\frac{i}{i_{oA}}\right) \quad (5.4)$$

where V_A represents voltage drop across the anode electrode, c_A represents the electrode constant, i represents the current density and i_{oA} represents the exchange current density of the anode electrode.

The voltage drop that occurs in the $\text{CuCl}(\text{aq})$ and $\text{HCl}(\text{aq})$ solution is written as

$$V_{sol1} = \left(\frac{i \times d_{AM}}{k_{sol1}}\right) \quad (5.5)$$

where k_{sol1} is found using experiment and the correlation obtained after performing experiment is

$$k_{sol1} = \left(\frac{(-4 \times 10^{-5} \times m_{CuCl}^4) + (0.0040 \times m_{CuCl}^3) + (0.0016 \times m_{CuCl}^2) - (-0.0496 \times m_{CuCl} + 29.22)}{10}\right)$$

Here, V_{sol1} , i , d_{AM} , k_{sol1} and m_{CuCl} represent the voltage drop across the first solution, the current density, the distance between the anode and the membrane, the electrical conductivity of the first solution and the mass of CuCl , respectively.

The voltage drop occurring across the cation exchange membrane can be defined as

$$V_{CEM} = \left(\frac{i \times \sigma_{CEM}}{k_{CEM}}\right) \quad (5.6)$$

where V_{CEM} represents the voltage drop across the cation exchange membrane, i represents the current density, σ_{CEM} represents the thickness of the cation exchange membrane, and k_{CEM} represents the electrical conductivity of the cation exchange membrane.

The voltage drop occurring in the solution of ZnS, Na₂S, NaOH and the water can be written as

$$V_{sol2} = \left(\frac{i \times d_{CM}}{k_{sol2}} \right) \quad (5.7)$$

where k_{sol2} is a combination of k_{ZnS} , k_{Na_2S} and k_{NaOH} which are obtained from Rabbani [75] and are calculated as follows:

$$\begin{aligned} k_{ZnS} = & \left(-2.18 + 30.55143 \times m_{ZnS} + 0.031319 \times \bar{U}_{water} - 0.12323 \times \bar{U}_{water} \right. \\ & \times m_{ZnS} - 1.82857 \times m_{ZnS}^2 + 2.14857 \times 10^{-4} \times \bar{U}_{water}^2 + 0.016168 \\ & \times \bar{U}_{water} \times m_{ZnS}^2 + 3.24694 \times 10^{-5} \times \bar{U}_{water}^2 \times m_{ZnS} - 4.43333 \\ & \times 10^{-7} \times \bar{U}_{water}^3 - 2.47449 \times 10^{-5} \times \bar{U}_{water}^2 \times m_{ZnS}^2 + 1.91667 \\ & \left. \times 10^{-7} \times \bar{U}_{water}^3 \times m_{ZnS} \right) \times 10^{-4} \end{aligned}$$

$$\begin{aligned} \log_{10}(k_{Na_2S}) = & 4.0 - 4.74 \times 10^{-3} \times \bar{U}_{water} + 0.6 \times m_{Na_2S} + 5.4 \times 10^{-4} \times \bar{U}_{water} \\ & \times m_{Na_2S} + 3.9 \times 10^{-6} \times \bar{U}_{water}^2 - 0.13 \times m_{Na_2S}^2 + 2.9 \\ & \times 10^{-4} \times \bar{U}_{water} \times m_{Na_2S}^2 - 2.5 \times 10^{-9} \times \bar{U}_{water}^3 - 0.03 \times m_{Na_2S}^3 \end{aligned}$$

$$\begin{aligned} k_{NaOH} = & 2.6 + 40.9 \times \frac{M_{NaOH} \times \rho_{NaOH}}{1000 + 40 \times MW_{NaOH}} - 4.03 \times \left(\frac{M_{NaOH} \times \rho_{NaOH}}{1000 + 40 \times M_{NaOH}} \right)^2 \\ & + 0.13 \times \left(\frac{M_{NaOH} \times \rho_{NaOH}}{1000 + 40 \times M_{NaOH}} \right)^3 \end{aligned}$$

Here, V_{sol2} , i and d_{CM} represent voltage drop across the second solution, the current density and the distance between the cathode electrode and the membrane, respectively. k_{sol2} , k_{ZnS} , k_{Na_2S} and k_{NaOH} represent the electrical conductivity of the second solution, the electrical conductivity of the ZnS, the electrical conductivity of the Na₂S and the

electrical conductivity of the NaOH, respectively. \bar{U}_{water} , m_{ZnS} , m_{Na_2S} , M_{NaOH} , ρ_{NaOH} represent volume of water, mass of ZnS, mass of Na₂S, molarity of NaOH and density of NaOH, respectively.

The voltage drop occurring across the cathode electrode can be calculated as

$$V_c = c_c \log\left(\frac{i}{i_{oc}}\right) \quad (5.8)$$

where V_c represents voltage drop across the cathode, c_c represents electrode constant, i represents the current density, and i_{oc} represents the exchange current density of the cathode electrode.

The parameters of the photocatalytic hydrogen production reactor are presented in Table 5.1.

Table 5.1. Parameters of photocatalytic hydrogen production reactor.

Parameter	Symbol	Value
Universal gas constant	R_u	8.314 J/mol K [123]
Faraday's constant	F	96485 C/mol [123]
Electron exchange	n	2
Constant for anode (graphite electrode)	c_A	0.4528
Exchange current density at anode (graphite electrode)	i_{oA}	0.0125 A/m ² [75]
Constant for cathode (titanium electrode)	c_c	0.0344
Exchange current density at cathode (titanium electrode)	i_{oc}	0.003 A/m ² [124]
Membrane thickness	σ_{CEM}	0.000125 m [86]
Membrane electrical conductivity	k_{CEM}	0.1 S/cm [86]

5.2 Energy and Exergy Analyses

The general energy and exergy balance equations for the integrated four-step Cu-Cl cycle are presented in this section. The energy and exergy models are developed based on the thermodynamic principals introduced by Cengel and Boles [123] and Dincer and Rosen [125].

The specific enthalpy at any given state is calculated as

$$h_i = \sum_{m=1}^k m f_m h_m \quad (5.9)$$

where h represents specific enthalpy, and mf represents mass fraction.

The specific entropy at any given state is calculated as

$$s_i = \sum_{m=1}^k mf_m s_m \quad (5.10)$$

where s represents specific entropy, and mf represents mass fraction.

The mass fraction of a substance is found by

$$mf_m = y_m \frac{MW_m}{MW_i} \quad (5.11)$$

with $MW_i = \sum_{m=1}^k y_m MW_m$

where mf represents mass fraction, y represents mole fraction, and M represents molar weight.

The exergy rate at any given state is defined as

$$\dot{E}x_i = \dot{m}_i [(h_i - h_0) - T_0(s_i - s_0) + ex_{ch}] \quad (5.12)$$

where $\dot{E}x$ represents exergy flow rate, \dot{m} represents mass flow rate, h represents specific enthalpy, T represents temperature, s represents specific entropy, and ex_{ch} represents specific chemical exergy.

The thermal exergy rate is defined as

$$\dot{E}x_{th_i} = \left(1 - \frac{T_0}{T_i}\right) \dot{Q}_i \quad (5.13)$$

where $\dot{E}x_{th}$ represents thermal exergy rate, T represents temperature, and \dot{Q} represents rate of heat flowing in or out of the system.

The power required by a pump is written as

$$\dot{W}_{p_i} = \dot{m}_i (h_i - h_{i-1}) \quad (5.14)$$

where \dot{W}_p represents power required by the pump, \dot{m} represents mass flow rate, and h represents specific enthalpy.

The exergy destruction rate in any component of the integrated system studied is calculated as

$$\sum \dot{E}x_{in} = \sum \dot{E}x_{out} + \dot{E}x_{dest} \quad (5.15)$$

where $\sum \dot{E}x_{in}$, $\sum \dot{E}x_{out}$ and $\dot{E}x_{dest}$ represent exergy rate carried by all the streams entering the component, exergy rate carried by all the streams leaving the component and exergy destruction rate in the system.

In general, energy and exergy efficiencies are defined as

$$\eta_{en} = \frac{\dot{E}n_{out,des}}{\dot{E}n_{in,req}} \quad (5.16)$$

$$\eta_{ex} = \frac{\dot{E}x_{out,des}}{\dot{E}x_{in,req}} \quad (5.17)$$

where η_{en} represents energy efficiency, $\dot{E}n_{out,des}$ represents the rate of energy associated with the desired outputs, $\dot{E}n_{in,req}$ represents the rate of energy associated with the required inputs, η_{ex} represents exergy efficiency, $\dot{E}x_{out,des}$ represents the rate of exergy associated with the desired outputs, and $\dot{E}x_{in,req}$ represents the rate of exergy associated with the required inputs.

The energy and exergy efficiencies of the hybrid photocatalytic hydrogen production unit are defined as

$$\eta_{en} = \frac{\dot{m}_{H_2} \times HHV_{H_2}}{\dot{W}_{solar}} \quad (5.18)$$

$$\eta_{ex} = \frac{\dot{E}x_{H_2}}{\dot{E}x_{solar}} \quad (5.19)$$

where

$$\dot{E}x_{H_2} = \dot{m}_{H_2} [ex_{H_2,ch} + ex_{H_2,ph}]$$

$$ex_{H_2,ch} = \frac{235.153 \times 1000}{M_{H_2}}$$

$$ex_{H_2,ph} = [(h_{H_2} - h_0) - T_0(s_{H_2} - s_0)]$$

Here, $ex_{H_2,ch}$ represents chemical exergy content of hydrogen, $ex_{H_2,ph}$ represents physical exergy content of the hydrogen, and M_{H_2} represents the molecular weight of the hydrogen. The constant 235.15 kJ/g-mol represents exergy content of the hydrogen.

5.3 Integrated System

The heliostat field energy model is adopted from the model presented by Xu et al. [126]. The rate of heat received by the solar light intensity is calculated as

$$\dot{Q}_s = I \times A_{field} \quad (5.20)$$

where \dot{Q}_s , I and A_{field} represent rate of heat carried by solar light intensity, solar light intensity and heliostat field area, respectively.

The rate of heat received by the central receiver is defined as

$$\eta_H = \frac{\dot{Q}_{rec}}{\dot{Q}_s} \quad (5.21)$$

where η_H and \dot{Q}_{rec} represent heliostat efficiency and rate of heat received by the central receiver, respectively.

The average central receiver emissivity is calculated as

$$\varepsilon_{avg} = \frac{\varepsilon_w}{\varepsilon_w + (1 - \varepsilon_w)F_r} \quad (5.22)$$

where ε_{avg} , ε_w and F_r represent average emissivity, emissivity of the wall and view factor, respectively

The inner side temperature of the central receiver is defined as

$$T_{insi} = \frac{T_{rec,surf} + T_0}{2} \quad (5.23)$$

where T_{insi} , $T_{rec,surf}$ and T_0 represent inside temperature of the central receiver, surface temperature of the central receiver and ambient temperature, respectively.

The receiver surface area is calculated as

$$A_{rec,surf} = \frac{A_{field}}{C \times F_r} \quad (5.24)$$

where $A_{rec,surf}$ and C represent central receiver area and concentration ratio, respectively.

The rate of heat lost due to emissivity in the central receiver is defined as

$$\dot{Q}_{rec,em} = \frac{\varepsilon_{avg} \times \sigma (T_{rec,surf}^4 - T_0^4) A_{field}}{C} \quad (5.25)$$

where $\dot{Q}_{rec,em}$ represent rate of heat lost from the central receiver due to emissivity.

The rate of heat lost due to reflection in the central receiver is calculated as

$$\dot{Q}_{rec,ref} = \dot{Q}_{rec} \times \rho \times \frac{F_r}{A_{field}} \quad (5.26)$$

where $\dot{Q}_{rec,ref}$ and ρ represent rate of heat lost from the central receiver due to reflection and density, respectively.

The rate of heat lost due to convection in receiver is found using

$$\dot{Q}_{rec,conv} = \frac{(h_{air,fc,insu} \times (T_{rec,surf} - T_0) + h_{air,nc,insu} \times (T_{rec,surf} - T_0)) A_{field}}{C \times F_r} \quad (5.27)$$

where $\dot{Q}_{rec,conv}$ and h represent rate of heat lost from the central receiver due to convection and specific enthalpy, respectively.

The rate of heat lost due to conduction in receiver is calculated as

$$\dot{Q}_{rec,cond} = \frac{(T_{rec,surf} - T_0) A_{field}}{\left(\frac{\partial_{insu}}{\lambda_{insu}} + \frac{1}{h_{air,o}} \right) C \times F_r} \quad (5.28)$$

where $\dot{Q}_{rec,cond}$, ∂_{insu} and λ_{insu} represent rate of heat lost from the receiver due to conduction, thickness of insulation and thermal conductivity of the insulation, respectively.

The rate of heat absorbed by molten salt passing through the receiver is found using

$$\dot{Q}_{rec,abs} = \dot{m}_{ms} c_p (T_{ms,o} - T_{ms,in}) \quad (5.29)$$

where $\dot{Q}_{rec,abs}$, \dot{m}_{ms} and c_p represent rate of heat absorbed by the molten salt flowing through the central receiver, mass flow rate of molten salt and specific heat capacity of molten salt, respectively.

The total rate of heat received by the receiver is defined as

$$\dot{Q}_{rec} = \dot{Q}_{rec,abs} + \dot{Q}_{rec,em} + \dot{Q}_{rec,ref} + \dot{Q}_{rec,conv} + \dot{Q}_{rec,cond} \quad (5.30)$$

The receiver surface temperature is found using

$$\frac{\dot{Q}_{rec}}{A_{field} F_r C} = \frac{T_{rec,surf} - T_{ms}}{\frac{d_o}{d_i h_{ms}} + d_o \frac{\ln \frac{d_o}{d_i}}{2 \lambda_{tube}}} \quad (5.31)$$

where d_o and d_i represent outer diameter and inner diameter, respectively.

The exergy rate carried by the solar flux is calculated as

$$\dot{E}x_s = \left(1 - \frac{T_0}{T_{sun}}\right) \dot{Q}_s \quad (5.32)$$

where $\dot{E}x_s$ represents rate of exergy carried by solar light intensity.

The exergy rate carried by the molten salt is calculated as

$$\dot{E}x_{rec,abs} = \left(1 - \frac{T_0}{T_{ms,o}}\right) \dot{Q}_{rec,abs} \quad (5.33)$$

where $\dot{E}x_{rec,abs}$ represents rate of exergy carried by the molten salt flowing through the central receiver.

The mass balance equation for the seventh cold heat exchanger of the Cu-Cl cycle is written as

$$\dot{m}_4 = \dot{m}_5 \quad (5.34)$$

where \dot{m} represents mass flow rate.

The rate of heat required by the seventh cold heat exchanger of the Cu-Cl cycle is calculated as

$$\dot{Q}_{HE7-C} = \dot{m}_4 (h_5 - h_4) \quad (5.35)$$

where \dot{Q}_{HE7-C} represents rate of heat required by the seventh cold heat exchanger of the Cu-Cl cycle and h represents specific enthalpy.

The exergy balance equation for the seventh cold heat exchanger of the Cu-Cl cycle is written as

$$\dot{E}x_4 + \left(1 - \frac{T_0}{\frac{T_4 + T_5}{2}}\right) \dot{Q}_{HE7-C} = \dot{E}x_{dest,HE7-C} + \dot{E}x_5 \quad (5.36)$$

where $\dot{E}x_{dest,HE7-C}$ represents exergy destruction rate of the seventh cold heat exchanger of the Cu-Cl cycle.

The mass balance equation for the cold heat exchanger (HE8-C) of the Cu-Cl cycle is written as

$$\dot{m}_5 = \dot{m}_6 \quad (5.37)$$

The rate of heat required by the eight cold heat exchanger of the Cu-Cl cycle is defined as

$$\dot{Q}_{HE8-C} = \dot{m}_5(h_6 - h_5) \quad (5.38)$$

where \dot{Q}_{HE8-C} represents the rate of heat required by the eighth cold heat exchanger of the Cu-Cl cycle.

The exergy balance equation for the eighth cold heat exchanger of the Cu-Cl cycle is written as

$$\dot{E}x_5 + \left(1 - \frac{T_0}{\frac{T_5+T_6}{2}}\right) \dot{Q}_{HE8-C} = \dot{E}x_{dest,HE8-C} + \dot{E}x_6 \quad (5.39)$$

where $\dot{E}x_{dest,HE8-C}$ represents exergy destruction rate of the eight cold heat exchanger of the Cu-Cl cycle.

The mass balance equation for the ninth cold heat exchanger of the Cu-Cl cycle is written as

$$\dot{m}_6 = \dot{m}_7 \quad (5.40)$$

The rate of heat required by the ninth cold heat exchanger of the Cu-Cl cycle is calculated as

$$\dot{Q}_{HE9-C} = \dot{m}_6(h_7 - h_6) \quad (5.41)$$

where \dot{Q}_{HE9-C} represents rate of heat required by the ninth cold heat exchanger of the Cu-Cl cycle.

The exergy balance equation for the ninth cold heat exchanger of the Cu-Cl cycle is written as

$$\dot{E}x_6 + \left(1 - \frac{T_0}{\frac{T_7+T_6}{2}}\right) \dot{Q}_{HE9-C} = \dot{E}x_{dest,HE9-C} + \dot{E}x_7 \quad (5.42)$$

where $\dot{E}x_{dest,HE9-C}$ represents exergy destruction rate of the ninth cold heat exchanger of the Cu-Cl cycle.

The mass balance equation for the tenth cold heat exchanger of the Cu-Cl cycle is written as

$$\dot{m}_7 = \dot{m}_8 \quad (5.43)$$

The rate of heat required by the tenth cold heat exchanger of the Cu-Cl cycle is found using

$$\dot{Q}_{HE10-C} = \dot{m}_7(h_8 - h_7) \quad (5.44)$$

where \dot{Q}_{HE10-C} represents rate of heat required by the tenth cold heat exchanger of the Cu-Cl cycle.

The exergy balance equation for the tenth cold heat exchanger of the Cu-Cl cycle is written as

$$\dot{E}x_7 + \left(1 - \frac{T_0}{\frac{T_7+T_8}{2}}\right) \dot{Q}_{HE10-C} = \dot{E}x_{dest,HE10-C} + \dot{E}x_8 \quad (5.45)$$

where $\dot{E}x_{dest,HE10-C}$ represents exergy destruction rate of the tenth cold heat exchanger of the Cu-Cl cycle.

The mass balance equation for the S1 of the Cu-Cl cycle is written as

$$\dot{m}_8 + \dot{m}_{39} = \dot{m}_9 \quad (5.46)$$

The rate of heat required by the S1 of the Cu-Cl cycle is defined as

$$\dot{Q}_{S1} = \dot{m}_9(h_9) - \dot{m}_8(h_8) - \dot{m}_{39}(h_{39}) \quad (5.47)$$

where \dot{Q}_{S1} represents rate of heat required by the S1 of the Cu-Cl cycle.

The exergy balance equation for the S1 of the Cu-Cl cycle is written as

$$\dot{E}x_8 + \dot{E}x_{39} + \left(1 - \frac{T_0}{\frac{T_8+T_{39}+T_9}{3}}\right) \dot{Q}_{S1} = \dot{E}x_{dest,S1} + \dot{E}x_9 \quad (5.48)$$

where $\dot{E}x_{dest,S1}$ represents exergy destruction rate of the S1 of the Cu-Cl cycle.

The mass balance equation for the fifth cold heat exchanger of the Cu-Cl cycle is written as

$$\dot{m}_{10} = \dot{m}_{16} \quad (5.49)$$

The rate of heat required by the fifth cold heat exchanger of the Cu-Cl cycle is calculated as

$$\dot{Q}_{HE5-C} = \dot{m}_{10}(h_{16} - h_{10}) \quad (5.50)$$

where \dot{Q}_{HE5-C} represents rate of heat required by the fifth cold heat exchanger of the Cu-Cl cycle.

The exergy balance equation for the fifth cold heat exchanger of the Cu-Cl cycle is written as

$$\dot{E}x_{10} + \left(1 - \frac{T_0}{\left(\frac{T_{10}+T_{16}}{2}\right)}\right) \dot{Q}_{HE5-C} = \dot{E}x_{dest,HE5-C} + \dot{E}x_{16} \quad (5.51)$$

where $\dot{E}x_{dest,HE5-C}$ represents exergy destruction rate of the fifth cold heat exchanger of the Cu-Cl cycle.

The mass balance equation for the sixth heat exchanger of the Cu-Cl cycle is written as

$$\dot{m}_{16} = \dot{m}_{17} \quad (5.52)$$

The rate of heat required by the sixth heat exchanger of the Cu-Cl cycle is defined as

$$\dot{Q}_{HE6} = \dot{m}_{16}(h_{17} - h_{16}) \quad (5.53)$$

where \dot{Q}_{HE6} represents rate of heat required by the sixth heat exchanger of the Cu-Cl cycle.

The exergy balance equation for the sixth heat exchanger of the Cu-Cl cycle is written as

$$\dot{E}x_{16} + \left(1 - \frac{T_0}{\left(\frac{T_{16}+T_{17}}{2}\right)}\right) \dot{Q}_{HE6} = \dot{E}x_{dest,HE6} + \dot{E}x_{17} \quad (5.54)$$

where $\dot{E}x_{dest,HE6}$ represents exergy destruction rate of the sixth heat exchanger of the Cu-Cl cycle.

The mass balance equation for the S2 of the Cu-Cl cycle is written as

$$\dot{m}_{17} = \dot{m}_{18} \quad (5.55)$$

The rate of heat required by the S2 of the Cu-Cl cycle is found using

$$\dot{Q}_{S2} = \dot{m}_{18}(h_{18}) - \dot{m}_{17}(h_{17}) \quad (5.56)$$

where \dot{Q}_{S2} represents rate of heat required by the S2 of the Cu-Cl cycle.

The exergy balance equation for the S2 of the Cu-Cl cycle is written as

$$\dot{E}x_{17} + \left(1 - \frac{T_0}{\left(\frac{T_{17}+T_{18}}{2}\right)}\right) \dot{Q}_{S2} = \dot{E}x_{dest,S2} + \dot{E}x_{18} \quad (5.57)$$

where $\dot{E}x_{dest,S2}$ represents exergy destruction rate of the S2 of the Cu-Cl cycle.

The mass balance equation for the third hot heat exchanger of the Cu-Cl cycle is written as

$$\dot{m}_{11} = \dot{m}_{12} \quad (5.58)$$

The rate of heat rejected by the third hot heat exchanger of the Cu-Cl cycle is defined as

$$\dot{Q}_{HE3-H} = \dot{m}_{11}(h_{11} - h_{12}) \quad (5.59)$$

where \dot{Q}_{HE3-H} represents rate of heat rejected by the third hot heat exchanger of the Cu-Cl cycle.

The exergy balance equation for the third hot heat exchanger of the Cu-Cl cycle is written as

$$\dot{E}x_{11} = \dot{E}x_{dest,HE3-H} + \left(1 - \frac{T_0}{\left(\frac{T_{11}+T_{12}}{2}\right)}\right) \dot{Q}_{HE3-H} + \dot{E}x_{12} \quad (5.60)$$

where $\dot{E}x_{dest,HE3-H}$ represents exergy destruction rate of the third hot heat exchanger of the Cu-Cl cycle.

The mass balance equation for the second hot heat exchanger of the Cu-Cl cycle is written as

$$\dot{m}_{12} = \dot{m}_{13} \quad (5.61)$$

The rate of heat rejected by the second hot heat exchanger of the Cu-Cl cycle is calculated as

$$\dot{Q}_{HE2-H} = \dot{m}_{12}(h_{12} - h_{13}) \quad (5.62)$$

where \dot{Q}_{HE2-H} represents rate of heat rejected by the second hot heat exchanger of the Cu-Cl cycle.

The exergy balance equation for the second hot heat exchanger of the Cu-Cl cycle is written as

$$\dot{E}x_{12} = \dot{E}x_{dest,HE2-H} + \left(1 - \frac{T_0}{\left(\frac{T_{12}+T_{13}}{2}\right)}\right)\dot{Q}_{HE2-H} + \dot{E}x_{13} \quad (5.63)$$

where $\dot{E}x_{dest,HE2-H}$ represents exergy destruction rate of the second hot heat exchanger of the Cu-Cl cycle.

The mass balance equation for the seventh hot heat exchanger of the Cu-Cl cycle is written as

$$\dot{m}_{13} = \dot{m}_{14} \quad (5.64)$$

The rate of heat rejected by the seventh hot heat exchanger of the Cu-Cl cycle is defined as

$$\dot{Q}_{HE7-H} = \dot{m}_{13}(h_{13} - h_{14}) \quad (5.65)$$

where \dot{Q}_{HE7-H} represents the rate of heat rejected by the seventh hot heat exchanger of the Cu-Cl cycle.

The exergy balance equation for the seventh hot heat exchanger of the Cu-Cl cycle is written as

$$\dot{E}x_{13} = \dot{E}x_{dest,HE7-H} + \left(1 - \frac{T_0}{\left(\frac{T_{13}+T_{14}}{2}\right)}\right)\dot{Q}_{HE7-H} + \dot{E}x_{14} \quad (5.66)$$

where $\dot{E}x_{dest,HE7-H}$ represents exergy destruction rate of the seventh hot heat exchanger of the Cu-Cl cycle.

The mass balance equation for the tenth hot heat exchanger of the Cu-Cl cycle is written as

$$\dot{m}_{19} = \dot{m}_{21} \quad (5.67)$$

The rate of heat rejected by the tenth hot heat exchanger of the Cu-Cl cycle is found using

$$\dot{Q}_{HE10-H} = \dot{m}_{19}(h_{19} - h_{21}) \quad (5.68)$$

where \dot{Q}_{HE10-H} represents the rate of heat rejected by the tenth hot heat exchanger of the Cu-Cl cycle.

The exergy balance equation for the tenth hot heat exchanger of the Cu-Cl cycle is written as

$$\dot{E}x_{19} = \dot{E}x_{dest,HE10-H} + \left(1 - \frac{T_0}{\left(\frac{T_{19}+T_{21}}{2}\right)}\right)\dot{Q}_{HE10-H} + \dot{E}x_{21} \quad (5.69)$$

where $\dot{E}x_{dest,HE10-H}$ represents exergy destruction rate of the seventh hot heat exchanger of the Cu-Cl cycle.

The mass balance equation for the ninth hot heat exchanger of the Cu-Cl cycle is written as

$$\dot{m}_{21} = \dot{m}_{22} \quad (5.70)$$

The rate of heat rejected by the ninth hot heat exchanger of the Cu-Cl cycle is defined as

$$\dot{Q}_{HE9-H} = \dot{m}_{21}(h_{21} - h_{22}) \quad (5.71)$$

where \dot{Q}_{HE9-H} represents the rate of heat rejected by the ninth hot heat exchanger of the Cu-Cl cycle.

The exergy balance equation for the ninth hot heat exchanger of the Cu-Cl cycle is written as

$$\dot{E}x_{21} = \dot{E}x_{dest,HE9-H} + \left(1 - \frac{T_0}{\left(\frac{T_{22}+T_{21}}{2}\right)}\right)\dot{Q}_{HE9-H} + \dot{E}x_{22} \quad (5.72)$$

where $\dot{E}x_{dest,HE9-H}$ represents exergy destruction rate of the ninth hot heat exchanger of the Cu-Cl cycle.

The mass balance equation for the fifth hot heat exchanger of the Cu-Cl cycle is written as

$$\dot{m}_{20} = \dot{m}_{24} \quad (5.73)$$

The rate of heat rejected by the fifth hot heat exchanger of the Cu-Cl cycle is calculated as

$$\dot{Q}_{HE5-H} = \dot{m}_{20}(h_{20} - h_{24}) \quad (5.74)$$

where \dot{Q}_{HE5-H} represents rate of heat rejected by the fifth hot heat exchanger of the Cu-Cl cycle.

The exergy balance equation for the fifth hot heat exchanger of the Cu-Cl cycle is written as

$$\dot{E}x_{20} = \dot{E}x_{dest,HE5-H} + \left(1 - \frac{T_0}{\frac{T_{20}+T_{24}}{2}}\right) \dot{Q}_{HE5-H} + \dot{E}x_{24} \quad (5.75)$$

where $\dot{E}x_{dest,HE5-H}$ represents exergy destruction rate of the fifth hot heat exchanger of the Cu-Cl cycle.

The mass balance equation for the fourth hot heat exchanger of the Cu-Cl cycle is written as

$$\dot{m}_{24} = \dot{m}_{25} \quad (5.76)$$

The rate of heat rejected by the fourth hot heat exchanger of the Cu-Cl cycle is defined as

$$\dot{Q}_{HE4-H} = \dot{m}_{24}(h_{24} - h_{25}) \quad (5.77)$$

where \dot{Q}_{HE4-H} represents rate of heat rejected by the fourth hot heat exchanger of the Cu-Cl cycle.

The exergy balance equation for the fourth hot heat exchanger of the Cu-Cl cycle is written as

$$\dot{E}x_{24} = \dot{E}x_{dest,HE4-H} + \left(1 - \frac{T_0}{\frac{T_{25}+T_{24}}{2}}\right) \dot{Q}_{HE4-H} + \dot{E}x_{25} \quad (5.78)$$

where $\dot{E}x_{dest,HE4-H}$ represents exergy destruction rate of the fourth hot heat exchanger of the Cu-Cl cycle.

The mass balance equation for the eighth hot heat exchanger of the Cu-Cl cycle is written as

$$\dot{m}_{26} = \dot{m}_{25} \quad (5.79)$$

The rate of heat rejected by the eight hot heat exchanger of the Cu-Cl cycle is calculated as

$$\dot{Q}_{HE8-H} = \dot{m}_{25}(h_{25} - h_{26}) \quad (5.80)$$

where \dot{Q}_{HE8-H} represents rate of heat rejected by the eight hot heat exchanger of the Cu-Cl cycle.

The exergy balance equation for the eighth hot heat exchanger of the Cu-Cl cycle is written as

$$\dot{E}x_{25} = \dot{E}x_{dest,HE8-H} + \left(1 - \frac{T_0}{\left(\frac{T_{25}+T_{26}}{2}\right)}\right)\dot{Q}_{HE8-H} + \dot{E}x_{26} \quad (5.81)$$

where $\dot{E}x_{dest,HE8-H}$ represents exergy destruction rate of the eight hot heat exchanger of the Cu-Cl cycle.

The mass balance equation for the third pump of the Cu-Cl cycle is written as

$$\dot{m}_{28} = \dot{m}_{23} \quad (5.82)$$

The power required by the third pump of the Cu-Cl cycle is defined as

$$\dot{W}_{P3} = \dot{m}_{28}(h_{23} - h_{28}) \quad (5.83)$$

where \dot{W}_{P3} represents power required by the third pump of the Cu-Cl cycle.

The exergy balance equation for the third pump of the Cu-Cl cycle is written as

$$\dot{E}x_{28} + \dot{W}_{P3} = \dot{E}x_{dest,P3} + \dot{E}x_{23} \quad (5.84)$$

where $\dot{E}x_{dest,P3}$ represents exergy destruction rate of the third pump of the Cu-Cl cycle.

The mass balance equation for the second pump of the Cu-Cl cycle is written as

$$\dot{m}_{35} = \dot{m}_{36} \quad (5.85)$$

The power required by the second pump of the Cu-Cl cycle is calculated as

$$\dot{W}_{P2} = \dot{m}_{35}(h_{36} - h_{35}) \quad (5.86)$$

where \dot{W}_{P2} represents power required by the second pump of the Cu-Cl cycle.

The exergy balance equation for the second pump of the Cu-Cl cycle is written as

$$\dot{E}x_{35} + \dot{W}_{P2} = \dot{E}x_{dest,P2} + \dot{E}x_{36} \quad (5.87)$$

where $\dot{E}x_{dest,P2}$ represents exergy destruction rate of the second pump of the Cu-Cl cycle.

The mass balance equation for the first pump of the Cu-Cl cycle is written as

$$\dot{m}_2 = \dot{m}_3 \quad (5.88)$$

The power required by the first pump of the Cu-Cl cycle is defined as

$$\dot{W}_{P1} = \dot{m}_2(h_3 - h_2) \quad (5.89)$$

where \dot{W}_{P1} represents power required by the first pump of the Cu-Cl cycle.

The exergy balance equation for the first pump of the Cu-Cl cycle is written as

$$\dot{E}x_2 + \dot{W}_{P1} = \dot{E}x_{dest,P1} + \dot{E}x_3 \quad (5.90)$$

where $\dot{E}x_{dest,P1}$ represents exergy destruction rate of the first pump of the Cu-Cl cycle.

The mass balance equation for the first hot heat exchanger of the Cu-Cl cycle is written as

$$\dot{m}_{34} = \dot{m}_{35} \quad (5.91)$$

The rate of heat rejected by the first hot heat exchanger of the Cu-Cl cycle is calculated as

$$\dot{Q}_{HE1-H} = \dot{m}_{34}(h_{34} - h_{35}) \quad (5.92)$$

where \dot{Q}_{HE1-H} represents rate of heat rejected by the first hot heat exchanger of the Cu-Cl cycle.

The exergy balance equation for the first hot heat exchanger of the Cu-Cl cycle is written as

$$\dot{E}x_{34} = \dot{E}x_{dest,HE1-H} + \left(1 - \frac{T_0}{\left(\frac{T_{34}+T_{35}}{2}\right)}\right) \dot{Q}_{HE1-H} + \dot{E}x_{35} \quad (5.93)$$

where $\dot{E}x_{dest,HE1-H}$ represents exergy destruction rate of the first hot heat exchanger of the Cu-Cl cycle.

The mass balance equation for the first cold heat exchanger of the Cu-Cl cycle is written as

$$\dot{m}_{31} = \dot{m}_{32} \quad (5.94)$$

The rate of heat required by the first cold heat exchanger of the Cu-Cl cycle is defined as

$$\dot{Q}_{HE1-C} = \dot{m}_{31}(h_{32} - h_{31}) \quad (5.95)$$

where \dot{Q}_{HE1-C} represents rate of heat required by the first cold heat exchanger of the Cu-Cl cycle.

The exergy balance equation for the first cold heat exchanger of the Cu-Cl cycle is written as

$$\dot{E}x_{31} + \left(1 - \frac{T_0}{\left(\frac{T_{31}+T_{32}}{2}\right)}\right) \dot{Q}_{HE1-C} = \dot{E}x_{dest,HE1-C} + \dot{E}x_{32} \quad (5.96)$$

where $\dot{E}x_{dest,HE1-C}$ represents exergy destruction rate of the first cold heat exchanger of the Cu-Cl cycle.

The mass balance equation for the second cold heat exchanger of the Cu-Cl cycle is written as

$$\dot{m}_{32} = \dot{m}_{33} \quad (5.97)$$

The rate of heat required by the second cold heat exchanger of the Cu-Cl cycle is found using

$$\dot{Q}_{HE2-C} = \dot{m}_{32}(h_{33} - h_{32}) \quad (5.98)$$

where \dot{Q}_{HE2-C} represents rate of heat required by the second cold heat exchanger of the Cu-Cl cycle.

The exergy balance equation for the second cold heat exchanger of the Cu-Cl cycle is written as

$$\dot{E}x_{32} + \left(1 - \frac{T_0}{\left(\frac{T_{32}+T_{33}}{2}\right)}\right) \dot{Q}_{HE2-C} = \dot{E}x_{dest,HE2-C} + \dot{E}x_{33} \quad (5.99)$$

where $\dot{E}x_{dest,HE2-C}$ represents exergy destruction rate of the second cold heat exchanger of the Cu-Cl cycle.

The mass balance equation for the third cold heat exchanger of the Cu-Cl cycle is written as

$$\dot{m}_{37} = \dot{m}_{38} \quad (5.100)$$

The rate of heat required by the third cold heat exchanger of the Cu-Cl cycle is defined as

$$\dot{Q}_{HE3-C} = \dot{m}_{37}(h_{38} - h_{37}) \quad (5.101)$$

where \dot{Q}_{HE3-C} represents rate of heat required by the third cold heat exchanger of the Cu-Cl cycle.

The exergy balance equation for the third cold heat exchanger of the Cu-Cl cycle is written as

$$\dot{E}x_{37} + \left(1 - \frac{T_0}{\left(\frac{T_{37}+T_{38}}{2}\right)}\right) \dot{Q}_{HE3-C} = \dot{E}x_{dest,HE3-C} + \dot{E}x_{38} \quad (5.102)$$

where $\dot{E}x_{dest,HE3-C}$ represents exergy destruction rate of the third cold heat exchanger of the Cu-Cl cycle.

The mass balance equation for the fourth cold heat exchanger of the Cu-Cl cycle is written as

$$\dot{m}_{38} = \dot{m}_{39} \quad (5.103)$$

The rate of heat required by the fourth cold heat exchanger of the Cu-Cl cycle is calculated as

$$\dot{Q}_{HE4-C} = \dot{m}_{38}(h_{39} - h_{38}) \quad (5.104)$$

where \dot{Q}_{HE4-C} represents rate of heat required by the fourth cold heat exchanger of the Cu-Cl cycle.

The exergy balance equation for the fourth cold heat exchanger of the Cu-Cl cycle is written as

$$\dot{E}x_{38} + \left(1 - \frac{T_0}{\left(\frac{T_{38}+T_{39}}{2}\right)}\right) \dot{Q}_{HE4-C} = \dot{E}x_{dest,HE4-C} + \dot{E}x_{39} \quad (5.105)$$

where $\dot{E}x_{dest,HE4-C}$ represents exergy destruction rate of the fourth cold heat exchanger of the Cu-Cl cycle.

The mass balance equation for the generator of the Kalina cycle is written as

$$\dot{m}_{Kc3} = \dot{m}_{Kc4} \quad (5.106)$$

The heat required by the generator of the Kalina cycle is defined as

$$\dot{Q}_g = \dot{m}_{hw}(h_{hw_{16}} - h_{hw_0}) \quad (5.107)$$

where \dot{Q}_g represents rate of heat required by the generator of the Kalina cycle.

The exergy balance equation for the generator of the Kalina cycle is written as

$$\dot{E}x_{Kc3} + \left(1 - \frac{T_0}{\left(\frac{T_{Kc3}+T_{Kc4}}{2}\right)}\right) \dot{Q}_g = \dot{E}x_{dest,g} + \dot{E}x_{Kc4} \quad (5.108)$$

where $\dot{E}x_{dest,g}$ represents exergy destruction rate by the generator of the Kalina cycle.

The mass balance equation for the turbine of the Kalina cycle is written as

$$\dot{m}_{Kc8} = \dot{m}_{Kc9} \quad (5.109)$$

The power that can be obtained from the turbines of the Kalina cycle is calculated as

$$\dot{W}_{turb} = \dot{m}_{Kc8}(h_{Kc8} - h_{Kc9}) \quad (5.110)$$

where \dot{W}_{turb} represents power produced by the turbine.

The exergy balance equation for the turbine of the Kalina cycle is written as

$$\dot{E}x_{Kc8} + \dot{W}_{turb} = \dot{E}x_{dest,turb} + \dot{E}x_{Kc9} \quad (5.111)$$

where $\dot{E}x_{dest,g}$ represents exergy destruction rate by the generator of the Kalina cycle.

In the model, parasitic losses are also considered. The percentage of parasitic losses is assumed to be 20% [8]. The parasitic losses are defined as

$$\dot{W}_{parasitic} = 0.2(\dot{W}_{turb} - \dot{W}_{p_{Kc}}) \quad (5.112)$$

where $\dot{W}_{parasitic}$, \dot{W}_{turb} , and $\dot{W}_{p_{Kc}}$ represent power lost due to parasitic losses, power produced by the turbine, and power consumed by the pump of the Kalina cycle, respectively.

The actual net power output that can be obtained from the Kalina cycle is

$$\dot{W}_{net_{Kc}} = \dot{W}_{turb} - \dot{W}_{p_{Kc}} - \dot{W}_{parasitic} \quad (5.113)$$

where $\dot{W}_{net_{Kc}}$ represents net power produced by the Kalina cycle.

It is assumed that only about 80% of total solar light reflected by the central receiver is directed to the photocatalytic hydrogen production process. The reason behind this assumption is that 20% of the solar light intensity reflected by the central receiver is non-recoverable because of reflection from the edges of the central receiver and reflection by dust and water particles in the air. The rate of heat supplied to the photocatalytic reactor is given by

$$\dot{Q}_{PC} = 0.8 \times \dot{Q}_{rec,ref} \quad (5.114)$$

where \dot{Q}_{PC} represents rate of heat received by the photocatalytic reactor.

The total voltage required by the photocatalytic reactor is defined as

$$V_{PC} = V_{rev} + V_{sol} \quad (5.115)$$

where

$$V_{rev} = 1.229 - 8.5 \times 10^{-4}(T_{PC} - 298.15) + 4.3085 \times 10^{-5} \times T_{PC} \left[\ln(p_{H_2}) + 12 \ln p_{O_2} \right]$$

$$V_{sol} = \frac{i}{k_{sol}}$$

where V_{PC} , V_{rev} and V_{sol} represent voltage required by the reactor, reversible voltage of the reactor and voltage drop due to catalyst based solution, respectively. T_{PC} , p_{H_2} , i and

p_{O_2} represent temperature of the reactor, partial pressure of hydrogen, current density and partial pressure of oxygen, respectively. k_{sol} represents electrical conductivity of the solution and is calculated in the same manner as electrical conductivity of the second solution in electrochemical modeling section of the report.

The rate of exergy carried by the hydrogen produced is defined as

$$\dot{E}x_{H_2} = \dot{m}_{H_2} [ex_{H_2,ch} + ex_{H_2,ph}] \quad (5.116)$$

$$\text{where } ex_{H_2,ch} = \frac{235.153 \times 1000}{M_{H_2}} \text{ and } ex_{H_2,ph} = [(h_{H_2} - h_0) - T_0(s_{H_2} - s_0)].$$

The exergy destruction ratio of system 1 is calculated as

$$E_x R_{s-sys1} = \frac{\dot{E}x_{dest,s,sys1}}{\dot{E}x_{in}} \quad (5.117)$$

where $E_x R_{s-sys1}$, $\dot{E}x_{dest,s,sys1}$ and $\dot{E}x_{in}$ represent exergy destruction ratio of system 1, exergy destruction rate of system 1, and total exergy input to the overall system, respectively.

The exergy destruction ratio of system 2 is calculated as

$$E_x R_{s-sys2} = \frac{\dot{E}x_{dest,s,sys2}}{\dot{E}x_{in}} \quad (5.118)$$

where $E_x R_{s-sys2}$ and $\dot{E}x_{dest,s,sys2}$ represent exergy destruction ratio of system 2 and exergy destruction rate of system 2, respectively.

The exergy destruction ratio of first cold heat exchanger of the Cu-Cl cycle is found using

$$E_x R_{HE1-C} = \frac{\dot{E}x_{dest,HE1-C}}{\dot{E}x_{in}} \quad (5.119)$$

where $E_x R_{HE1-C}$ and $\dot{E}x_{dest,HE1-C}$ represent exergy destruction ratio of first cold heat exchanger of the Cu-Cl cycle and exergy destruction rate of first cold heat exchanger of the Cu-Cl cycle, respectively.

The exergy destruction ratio of second cold heat exchanger of the Cu-Cl cycle is defined as

$$E_x R_{HE2-C} = \frac{Ex_{dest,HE2-C}}{\dot{Ex}_{in}} \quad (5.120)$$

where $E_x R_{HE2-C}$ and $\dot{Ex}_{dest,HE2-C}$ represent exergy destruction ratio of second cold heat exchanger of the Cu-Cl cycle and exergy destruction rate of second cold heat exchanger of the Cu-Cl cycle, respectively.

The exergy destruction ratio of the third cold heat exchanger of the Cu-Cl cycle is defined as

$$E_x R_{HE3-C} = \frac{\dot{Ex}_{dest,HE3-C}}{\dot{Ex}_{in}} \quad (5.121)$$

where $E_x R_{HE3-C}$ and $\dot{Ex}_{dest,HE3-C}$ represent exergy destruction ratio of the third cold heat exchanger and exergy destruction rate of third cold heat exchanger of the Cu-Cl cycle, respectively.

The exergy destruction ratio of the fourth cold heat exchanger of the Cu-Cl cycle is defined as

$$E_x R_{HE4-C} = \frac{\dot{Ex}_{dest,HE4-C}}{\dot{Ex}_{in}} \quad (5.122)$$

where $E_x R_{HE4-C}$ and $\dot{Ex}_{dest,HE4-C}$ represent exergy destruction ratio of fourth cold heat exchanger of the Cu-Cl cycle and exergy destruction rate of fourth cold heat exchanger of the Cu-Cl cycle, respectively.

The exergy destruction ratio of the fifth cold heat exchanger of the Cu-Cl cycle is defined as

$$E_x R_{HE5-C} = \frac{\dot{Ex}_{dest,HE5-C}}{\dot{Ex}_{in}} \quad (5.123)$$

where $E_x R_{HE5-C}$ and $\dot{Ex}_{dest,HE5-C}$ represent exergy destruction ratio of the fifth cold heat exchanger of the Cu-Cl cycle and exergy destruction rate of fifth cold heat exchanger of the Cu-Cl cycle, respectively.

The exergy destruction ratio of seventh cold heat exchanger of the Cu-Cl cycle is defined as

$$E_x R_{HE7-C} = \frac{\dot{Ex}_{dest,HE7-C}}{\dot{Ex}_{in}} \quad (5.124)$$

where $E_x R_{HE7-C}$ and $\dot{E}x_{dest,HE7-C}$ represent exergy destruction ratio of seventh cold heat exchanger of the Cu-Cl cycle and exergy destruction rate of seventh cold heat exchanger of the Cu-Cl cycle, respectively.

The exergy destruction ratio of eight cold heat exchanger of the Cu-Cl cycle is defined as

$$E_x R_{HE8-C} = \frac{\dot{E}x_{dest,HE8-C}}{\dot{E}x_{in}} \quad (5.125)$$

where $E_x R_{HE8-C}$ and $\dot{E}x_{dest,HE8-C}$ represent exergy destruction ratio of eight cold heat exchanger of the Cu-Cl cycle and exergy destruction rate of eight cold heat exchanger of the Cu-Cl cycle, respectively.

The exergy destruction ratio of ninth cold heat exchanger of the Cu-Cl cycle is defined as

$$E_x R_{HE9-C} = \frac{\dot{E}x_{dest,HE9-C}}{\dot{E}x_{in}} \quad (5.126)$$

where $E_x R_{HE9-C}$ and $\dot{E}x_{dest,HE9-C}$ represent exergy destruction ratio of ninth cold heat exchanger of the Cu-Cl cycle and exergy destruction rate of ninth cold heat exchanger of the Cu-Cl cycle, respectively.

The exergy destruction ratio of tenth cold heat exchanger of the Cu-Cl cycle is calculated as

$$E_x R_{HE10-C} = \frac{\dot{E}x_{dest,HE10-C}}{\dot{E}x_{in}} \quad (5.127)$$

where $E_x R_{HE10-C}$ and $\dot{E}x_{dest,HE10-C}$ represent exergy destruction ratio of tenth cold heat exchanger of the Cu-Cl cycle and exergy destruction rate of tenth cold heat exchanger of the Cu-Cl cycle, respectively.

The exergy destruction ratio of first separator in the Cu-Cl cycle is defined as

$$E_x R_{S1} = \frac{\dot{E}x_{dest,S1}}{\dot{E}x_{in}} \quad (5.128)$$

where $E_x R_{S1}$ and $\dot{E}x_{dest,S1}$ represent exergy destruction ratio of first separator in the Cu-Cl cycle and exergy destruction rate of first separator in the Cu-Cl cycle, respectively.

The exergy destruction ratio of second separator in the Cu-Cl cycle is calculated as

$$E_x R_{S2} = \frac{\dot{E}x_{dest,S2}}{\dot{E}x_{in}} \quad (5.129)$$

where $E_x R_{S2}$ and $\dot{E}x_{dest,S2}$ represent exergy destruction ratio of second separator in the Cu-Cl cycle and exergy destruction rate of second separator in the Cu-Cl cycle, respectively.

The exergy destruction ratio of fourth separator in the Cu-Cl cycle is calculated as

$$E_x R_{S4} = \frac{\dot{E}x_{dest,S4}}{\dot{E}x_{in}} \quad (5.130)$$

where $E_x R_{S4}$ and $\dot{E}x_{dest,S4}$ represent exergy destruction ratio of fourth separator in the Cu-Cl cycle and exergy destruction rate of fourth separator in the Cu-Cl cycle, respectively.

The exergy destruction ratio of first hot heat exchanger of the Cu-Cl cycle is defined as

$$E_x R_{HE1-H} = \frac{\dot{E}x_{dest,HE1-H}}{\dot{E}x_{in}} \quad (5.131)$$

where $E_x R_{HE1-H}$ and $\dot{E}x_{dest,HE1-H}$ represent exergy destruction ratio of first hot heat exchanger of the Cu-Cl cycle and exergy destruction rate of first hot heat exchanger of the Cu-Cl cycle, respectively.

The exergy destruction ratio of second hot heat exchanger of the Cu-Cl cycle is found using

$$E_x R_{HE2-H} = \frac{\dot{E}x_{dest,HE2-H}}{\dot{E}x_{in}} \quad (5.132)$$

where $E_x R_{HE2-H}$ and $\dot{E}x_{dest,HE2-H}$ represent exergy destruction ratio of second hot heat exchanger of the Cu-Cl cycle and exergy destruction rate of second hot heat exchanger of the Cu-Cl cycle, respectively.

The exergy destruction ratio of third hot heat exchanger of the Cu-Cl cycle is found using

$$E_x R_{HE3-H} = \frac{\dot{E}x_{dest,HE3-H}}{\dot{E}x_{in}} \quad (5.133)$$

where $E_x R_{HE3-H}$ and $\dot{E}x_{dest,HE3-H}$ represent exergy destruction ratio of third hot heat exchanger of the Cu-Cl cycle and exergy destruction rate of third hot heat exchanger of the Cu-Cl cycle, respectively.

The exergy destruction ratio of fourth hot heat exchanger of the Cu-Cl cycle is defined as

$$E_x R_{HE4-H} = \frac{\dot{E}x_{dest,HE4-H}}{\dot{E}x_{in}} \quad (5.134)$$

where $E_x R_{HE4-H}$ and $\dot{E}x_{dest,HE4-H}$ represent exergy destruction ratio of fourth hot heat exchanger of the Cu-Cl cycle and exergy destruction rate of fourth hot heat exchanger of the Cu-Cl cycle, respectively.

The exergy destruction ratio of fifth hot heat exchanger of the Cu-Cl cycle is calculated as

$$E_x R_{HE5-H} = \frac{\dot{E}x_{dest,HE5-H}}{\dot{E}x_{in}} \quad (5.135)$$

where $E_x R_{HE5-H}$ and $\dot{E}x_{dest,HE5-H}$ represent exergy destruction ratio of fifth hot heat exchanger of the Cu-Cl cycle and exergy destruction rate of fifth hot heat exchanger of the Cu-Cl cycle, respectively.

The exergy destruction ratio of seventh hot heat exchanger of the Cu-Cl cycle is found using

$$E_x R_{HE7-H} = \frac{\dot{E}x_{dest,HE7-H}}{\dot{E}x_{in}} \quad (5.136)$$

where $E_x R_{HE7-H}$ and $\dot{E}x_{dest,HE7-H}$ represent exergy destruction ratio of seventh hot heat exchanger of the Cu-Cl cycle and exergy destruction rate of seventh hot heat exchanger of the Cu-Cl cycle, respectively.

The exergy destruction ratio of eight hot heat exchanger of the Cu-Cl cycle is calculated as

$$E_x R_{HE8-H} = \frac{\dot{E}x_{dest,HE8-H}}{\dot{E}x_{in}} \quad (5.137)$$

where $E_x R_{HE8-H}$ and $\dot{E}x_{dest,HE8-H}$ represent exergy destruction ratio of eight hot heat exchanger of the Cu-Cl cycle and exergy destruction rate of eight hot heat exchanger of the Cu-Cl cycle, respectively.

The exergy destruction ratio of ninth hot heat exchanger of the Cu-Cl cycle is found using

$$E_x R_{HE9-H} = \frac{\dot{E}x_{dest,HE9-H}}{\dot{E}x_{in}} \quad (5.138)$$

where $E_x R_{HE9-H}$ and $\dot{E}x_{dest,HE9-H}$ represent exergy destruction ratio of ninth hot heat exchanger of the Cu-Cl cycle and exergy destruction rate of ninth hot heat exchanger of the Cu-Cl cycle, respectively.

The exergy destruction ratio of tenth hot heat exchanger of the Cu-Cl cycle is defined as

$$E_x R_{HE10-H} = \frac{\dot{E}x_{dest,HE10-H}}{\dot{E}x_{in}} \quad (5.139)$$

where $E_x R_{HE10-H}$ and $\dot{E}x_{dest,HE10-H}$ represent exergy destruction ratio of tenth hot heat exchanger of the Cu-Cl cycle and exergy destruction rate of tenth hot heat exchanger of the Cu-Cl cycle, respectively.

The exergy destruction ratio of sixth heat exchanger of the Cu-Cl cycle is defined as

$$E_x R_{HE6} = \frac{\dot{E}x_{dest,HE6}}{\dot{E}x_{in}} \quad (5.140)$$

where $E_x R_{HE6}$ and $\dot{E}x_{dest,HE6}$ represent exergy destruction ratio of sixth heat exchanger of the Cu-Cl cycle and exergy destruction rate of sixth heat exchanger of the Cu-Cl cycle, respectively.

The exergy destruction ratio of first pump of the Cu-Cl cycle is calculated as

$$E_x R_{P1} = \frac{\dot{E}x_{dest,P1}}{\dot{E}x_{in}} \quad (5.141)$$

where $E_x R_{P1}$ and $\dot{E}x_{dest,P1}$ represent exergy destruction ratio of first pump of the Cu-Cl cycle and exergy destruction rate of first pump of the Cu-Cl cycle, respectively.

The exergy destruction ratio of second pump of the Cu-Cl cycle is calculated as

$$E_x R_{P2} = \frac{\dot{Ex}_{dest,P2}}{\dot{Ex}_{in}} \quad (5.142)$$

where $E_x R_{P2}$ and $\dot{Ex}_{dest,P2}$ represent exergy destruction ratio of second pump of the Cu-Cl cycle and exergy destruction rate of second pump of the Cu-Cl cycle, respectively.

The exergy destruction ratio of third pump of the Cu-Cl cycle is calculated as

$$E_x R_{P3} = \frac{\dot{Ex}_{dest,P3}}{\dot{Ex}_{in}} \quad (5.143)$$

where $E_x R_{P3}$ and $\dot{Ex}_{dest,P3}$ represent exergy destruction ratio of third pump of the Cu-Cl cycle and exergy destruction rate of third pump of the Cu-Cl cycle, respectively.

The exergy destruction ratio of generator of the Kalina cycle is defined as

$$E_x R_{g,Kc} = \frac{\dot{Ex}_{dest,g,Kc}}{\dot{Ex}_{in}} \quad (5.144)$$

where $E_x R_{g,Kc}$ and $\dot{Ex}_{dest,g,Kc}$ represent exergy destruction ratio of generator of the Kalina cycle and exergy destruction rate of generator of the Kalina cycle, respectively.

The exergy destruction ratio of heat exchanger of the Kalina cycle is calculated as

$$E_x R_{HE,Kc} = \frac{\dot{Ex}_{dest,HE,Kc}}{\dot{Ex}_{in}} \quad (5.145)$$

where $E_x R_{HE,Kc}$ and $\dot{Ex}_{dest,HE,Kc}$ represent exergy destruction ratio of heat exchanger of the Kalina cycle and exergy destruction rate of heat exchanger of the Kalina cycle, respectively.

The exergy destruction ratio of separator of the Kalina cycle is found using

$$E_x R_{s,Kc} = \frac{\dot{Ex}_{dest,s,Kc}}{\dot{Ex}_{in}} \quad (5.146)$$

where $E_x R_{s,Kc}$ and $\dot{Ex}_{dest,s,Kc}$ represent exergy destruction ratio of separator of the Kalina cycle and exergy destruction rate of separator of the Kalina cycle, respectively.

The exergy destruction ratio of absorber of the Kalina cycle is defined as

$$E_x R_{abs,Kc} = \frac{\dot{Ex}_{dest,abs,Kc}}{\dot{Ex}_{in}} \quad (5.147)$$

where $E_x R_{abs,Kc}$ and $\dot{E}x_{dest,abs,Kc}$ represent exergy destruction ratio of absorber of the Kalina cycle and exergy destruction rate of absorber of the Kalina cycle, respectively.

The exergy destruction ratio of condenser of the Kalina cycle is calculated as

$$E_x R_{con,Kc} = \frac{\dot{E}x_{dest,con,Kc}}{\dot{E}x_{in}} \quad (5.148)$$

where $E_x R_{con,Kc}$ and $\dot{E}x_{dest,con,Kc}$ represent exergy destruction ratio of condenser of the Kalina cycle and exergy destruction rate of condenser of the Kalina cycle, respectively.

The exergy destruction ratio of turbine of the Kalina cycle is found using

$$E_x R_{turb,Kc} = \frac{\dot{E}x_{dest,turb,Kc}}{\dot{E}x_{in}} \quad (5.149)$$

where $E_x R_{turb,Kc}$ and $\dot{E}x_{dest,turb,Kc}$ represent exergy destruction ratio of turbine of the Kalina cycle and exergy destruction rate of turbine of the Kalina cycle, respectively.

The exergy destruction ratio of turbine of the Kalina cycle is defined as

$$E_x R_{p,Kc} = \frac{\dot{E}x_{dest,p,Kc}}{\dot{E}x_{in}} \quad (5.150)$$

where $E_x R_{p,Kc}$ and $\dot{E}x_{dest,p,Kc}$ represent exergy destruction ratio of pump of the Kalina cycle and exergy destruction rate of pump of the Kalina cycle, respectively.

The exergy destruction ratio of photocatalytic reactor is calculated as

$$E_x R_{PC} = \frac{\dot{E}x_{dest,PC}}{\dot{E}x_{in}} \quad (5.151)$$

where $E_x R_{PC}$ and $\dot{E}x_{dest,PC}$ represent exergy destruction ratio of photocatalytic reactor and exergy destruction rate of photocatalytic reactor, respectively.

The energy and exergy efficiencies of system 1 are defined as

$$\eta_{en_{sys1}} = \left(\frac{\dot{m}_{29} HHV_{H_2} + \dot{m}_{22} h_{22}}{\dot{Q}_{in} + \dot{m}_1 h_1 + \frac{(\dot{W}_{elec} - \dot{W}_{net,Kc} + \dot{W}_{p1} + \dot{W}_{p2} + \dot{W}_{p3} + \dot{W}_{p4})}{\eta_{convr}}} \right) \quad (5.152)$$

where $\dot{Q}_{in} = \dot{Q}_{HE8-C} + \dot{Q}_{HE10-C} + \dot{Q}_{S1} + \dot{Q}_{S2} + \dot{Q}_{S4} + \dot{Q}_S$.

Here, $\eta_{en_{sys1}}$ represents energy efficiency of system 1, \dot{m} represents the mass flow rate, HHV_{H_2} represents higher heating value of hydrogen, h represents specific enthalpy, \dot{Q}_{HE8-C} represents the rate of heat required by the eighth heat exchanger, \dot{Q}_{HE10-C} represents the rate of heat required by the tenth heat exchanger. \dot{Q}_{S1} , \dot{Q}_{S2} , and \dot{Q}_{S4} represent the rate of heat required by the first, second and fourth separator, respectively. \dot{Q}_S represents the rate of heat carried by the solar light. \dot{W}_{elec} , \dot{W}_{p1} , \dot{W}_{p2} , \dot{W}_{p3} , and \dot{W}_{p4} represent power input required by the electrolyzer, pump one, pump two, pump three and pump four, respectively. \dot{W}_{net_k} represents the net power produced by the Kalina cycle and η_{convr} represents heat to power conversion efficiency which is assumed to be 40% [50].

$$\eta_{ex_{sys1}} = \left(\frac{\dot{Ex}_{H_2} + \dot{Ex}_{22}}{\dot{Ex}_{in} + \frac{(\dot{W}_{elec} - \dot{W}_{net_{kc}} + \dot{W}_{p1} + \dot{W}_{p2} + \dot{W}_{p3} + \dot{W}_{p4})}{\eta_{convr}}} \right) \quad (5.153)$$

where $\dot{Ex}_{in} = \dot{Ex}_{HE8-C} + \dot{Ex}_{HE10-C} + \dot{Ex}_{S1} + \dot{Ex}_{S2} + \dot{Ex}_{S4} + \dot{Ex}_1 + \dot{Ex}_S$.

Here, $\eta_{ex_{sys1}}$ represents exergy efficiency of system 1, \dot{Ex}_{H_2} represents exergy content of hydrogen, \dot{Ex}_{HE8-C} represents exergy rate of eighth heat exchanger, \dot{Ex}_{HE10-C} represents exergy rate of tenth heat exchanger. \dot{Ex}_{S1} , \dot{Ex}_{S2} and \dot{Ex}_{S4} represent exergy rate of first, second and fourth separator, respectively. \dot{Ex}_S represents exergy rate of the solar light.

The energy and exergy efficiencies of system 2 are defined as

$$\eta_{en_{sys2}} = \left(\frac{\dot{m}_{29} HHV_{H_2} + \dot{m}_{22} h_{22} + \dot{m}_{H_2 PC} HHV_{H_2}}{\dot{Q}_{in} + \dot{m}_1 h_1 + \frac{(\dot{W}_{elec} - \dot{W}_{net_{kc}} + \dot{W}_{p1} + \dot{W}_{p2} + \dot{W}_{p3} + \dot{W}_{p4})}{\eta_{convr}}} \right) \quad (5.154)$$

where $\dot{Q}_{in} = \dot{Q}_{HE8-C} + \dot{Q}_{HE10-C} + \dot{Q}_{S1} + \dot{Q}_{S2} + \dot{Q}_{S4} + \dot{Q}_S$.

Here, $\eta_{en_{sys2}}$ represents energy efficiency of system 2 and $\dot{m}_{H_2 PC}$ represents mass flow rate of hydrogen produced by the photocatalytic reactor.

$$\eta_{ex_{sys2}} = \left(\frac{\dot{Ex}_{H_2} + \dot{Ex}_{22} + \dot{Ex}_{H_2 PC}}{\dot{Ex}_{in} + \frac{(\dot{W}_{elec} - \dot{W}_{net_{kc}} + \dot{W}_{p1} + \dot{W}_{p2} + \dot{W}_{p3} + \dot{W}_{p4})}{\eta_{convr}}} \right) \quad (5.155)$$

where $\dot{Ex}_{in} = \dot{Ex}_{HE8-C} + \dot{Ex}_{HE10-C} + \dot{Ex}_{S1} + \dot{Ex}_{S2} + \dot{Ex}_{S4} + \dot{Ex}_1 + \dot{Ex}_S$.

Here, $\eta_{ex_{sys2}}$ and $\dot{E}x_{H_2PC}$ represent exergy efficiency of system 2 and rate of exergy carried by hydrogen produced by the photocatalytic reactor.

The assumptions made during the modeling are presented in Table 5.2. The thermodynamic properties of the Cu-Cl cycle at a sample simulating conditions are tabulated in Table 5.3.

5.4 Exergoeconomic Analysis

Exergoeconomic analysis relates cost to thermodynamics. The exergoeconomic analysis of the hybrid photocatalytic reactor is presented in this section. The exergoeconomic equation for a hybrid photocatalytic reactor is written as

$$\dot{C}_{CuCl} + \dot{C}_{HCl} + \dot{C}_{ZnS} + \dot{C}_{Na_2S} + \dot{C}_{NaOH} + \dot{Z}_{eq} = \dot{C}_{H_2} \quad (5.156)$$

where

$$\dot{C}_{CuCl} = c_{CuCl} \times \dot{E}x_{CuCl}$$

$$\dot{C}_{HCl} = c_{HCl} \times \dot{E}x_{HCl}$$

$$\dot{C}_{ZnS} = c_{ZnS} \times \dot{E}x_{ZnS}$$

$$\dot{C}_{Na_2S} = c_{Na_2S} \times \dot{E}x_{Na_2S}$$

$$\dot{C}_{NaOH} = c_{NaOH} \times \dot{E}x_{NaOH}$$

$$\dot{C}_{H_2} = c_{H_2} \times \dot{E}x_{H_2}$$

$$\dot{Z}_{eq} = \dot{C}_{glassware} + \dot{C}_{electrode} + \dot{C}_{energy}$$

Here, c represents cost, $\dot{E}x$ represent exergy rate and \dot{Z}_{eq} represents cost rate associated with the equipments.

So the above equation can be written as

$$(c \times \dot{E}x)_{CuCl} + (c \times \dot{E}x)_{HCl} + (c \times \dot{E}x)_{ZnS} + (c \times \dot{E}x)_{Na_2S} + (c \times \dot{E}x)_{NaOH} + \dot{Z}_{eq} = (c \times \dot{E}x)_{H_2} \quad (5.157)$$

In its present form the above-mentioned equation cannot be solved as it has more unknowns than equations. The exergoeconomic analysis, which faces these types of

problems, can be re-written in terms of mass flow rate [75]. Replacing exergy rate by mass flow rate in Eq. 5.157 will give us

$$(c \times \dot{m})_{CuCl} + (c \times \dot{m})_{HCl} + (c \times \dot{m})_{ZnS} + (c \times \dot{m})_{NaS} + (c \times \dot{m})_{NaOH} + \dot{Z}_{eq} = (c \times \dot{m})_{H_2} \quad (5.158)$$

The cost of hydrogen can then be calculated by rearranging the Eq. 5.158 and re-writing it as

$$c_{H_2} = \frac{(c \times \dot{m})_{CuCl} + (c \times \dot{m})_{HCl} + (c \times \dot{m})_{ZnS} + (c \times \dot{m})_{NaS} + (c \times \dot{m})_{NaOH} + \dot{Z}_{eq}}{\dot{m}_{H_2}} \quad (5.159)$$

The cost values used in the study are presented in Table 5.4.

5.5 Optimization Study

After conducting the experiments and developing an electrochemical model of the photocatalytic hydrogen production reactor, an optimization study is conducted to attain the best possible operating parameters. The optimization study is based on multi-objective optimization theory, which helps in finding the best possible set of design values that are needed to attain the pre-set objectives. The multi-objective optimization technique used in the present study is the genetic algorithm technique. This method is selected as it can provide the best possible result of any desired output based on several inputs. The genetic method is a robust optimization algorithm that is designed to reliably locate a global optimum even in the presence of local minima/maxima. The genetic method intends to mimic the processes occurring in biological evolution. Initially, sample points are chosen at random from the range specified by the bounds of the independent variables. The sample points are then surveyed to determine the values of the objective function as quantified by the value of the variable that is to be minimized or maximized. A new generation of sample points is then generated in a stochastic manner by combining selected points of the current sample points. The characteristics of a point that are passed on to the next generation are represented by encoded values of its independent variables. The probability that a point out of the current sample point will be selected for breeding the next generation is an increasing function of its value. This process continues till the best points are recorded [120].

Table 5.2. The parameters assumed for integrated systems.

Parameter	Symbol	Assumed value
Ambient temperature	T_0	298.15 K
Ambient pressure	P_0	101 kPa
Sun temperature	T_{sun}	4500 K
Heliostat efficiency	η_H	75% [126]
Heliostat field area	A_{field}	2000 m ²
View factor	Fr	0.8 [126]
Emissivity	ε_w	0.8 [126]
Thickness of insulation	∂_{insu}	0.07 m [126]
Concentration ratio	C	1000 [126]
Isentropic turbine efficiency	η_{turb}	80% [8]
Isentropic pump efficiency	η_p	80% [8]
Power lost due to parasitic losses	$\dot{W}_{parasitic}$	20% [8]
Heat to power conversion efficiency	η_{convr}	40% [50]
Low pressure of the Kalina cycle	P_{Kc1}	250 kPa
High pressure of the Kalina cycle	P_{Kc2}	400 kPa
Ammonia-water concentration of the strong solution	x_{Kc4}	0.6 kg/kg
Ammonia-water concentration of the weak solution	x_{Kc5}	0.4 kg/kg
Ammonia-water vapor concentration	x_{Kc8}	0.9 kg/kg

The software developed by Klein [120] is used to carry out optimization study. For multi-objective optimization study, the objectives function considered are the hydrogen production rate (to be maximized), the exergy efficiency (to be maximized) and the total cost rate (to be minimized) of the hybrid photocatalytic hydrogen production reactor. The aim of this optimization study is to obtain the best possible hydrogen production rate and exergy efficiency at minimum total cost for the given independent variables. The independent variables, also known as constraints, selected in this study are the voltage, the concentration of the ZnS, the concentration of the CuCl, the temperature of the reactor and the ambient temperature. The constraints of optimization study of hybrid photocatalytic reactor are presented in Table 5.5.

The first objective function which aims at maximizing the hydrogen production rate of the hybrid photocatalytic reactor is defined as follows:

$$\dot{m}_{H_2} = \frac{i}{2F} \times M_{H_2} \quad (5.160)$$

where \dot{m}_{H_2} denotes the hydrogen production rate, i represents current density, F represents Faraday's constant and M_{H_2} represents molecular weight of hydrogen.

Table 5.3. Thermodynamic properties of the Cu-Cl Cycle at sample running conditions.

State	Pressure (kPa)	Temperature (K)	Mass flow rate (kg/s)	Specific enthalpy (kJ/kg)	Specific entropy (kJ/kg K)
1	101.3	298.2	0.001802	104.8	0.3669
2	23.08	298.2	0.003156	104.8	0.3669
3	101.3	298.2	0.003156	104.9	0.367
4	101.3	298.2	0.004957	104.9	0.367
5	101.3	342.2	0.004957	288.9	0.9427
6	101.3	486.2	0.004957	2900	7.881
7	101.3	581.2	0.004957	3090	8.237
8	101.3	673.2	0.004957	3278	8.537
9	101.3	673.2	0.07156	2336	4.069
10	101.3	673.2	0.05578	3316	3.429
11	101.3	673.2	0.01578	-1128	6.507
12	101.3	385.2	0.01578	-1428	5.926
13	101.3	373.2	0.01578	-1441	5.894
14	101.3	298.2	0.01578	-2004	4.249
15	101.3	298.2	0.01578	-2004	4.249
16	101.3	755.2	0.05578	3352	3.48
17	101.3	773.2	0.05578	3360	3.49
18	101.3	773.2	0.05578	3521	3.277
19	6.977	773.2	0.001302	467.6	8.03
20	94.35	773.2	0.05448	3594	3.189
21	6.977	690.2	0.001302	381.6	7.913
22	6.977	585.2	0.001302	275	7.745
23	94.35	298.2	0.01262	-2493	5.142
24	94.35	696.2	0.05448	3564	3.147
25	94.35	682.2	0.05448	3558	3.139
26	94.35	298.2	0.05448	3408	2.816
27	101.3	298.2	0.01628	-1822	5.968
28	45.61	298.2	0.01262	-2532	5.308
29	32.63	298.2	0.0004993	3931	58.05
31	101.3	298.2	0.06859	2440	2.823
32	101.3	323.2	0.06859	2453	2.865
33	101.3	353.2	0.06859	2535	3.113
34	18.42	353.2	0.001983	2648	8.057
35	18.42	298.2	0.001983	104.8	0.3669

36	94.35	298.2	0.001983	104.8	0.3669
37	101.3	353.2	0.06661	2532	2.966
38	101.3	651.2	0.06661	2658	3.224
39	101.3	673.2	0.06661	2667	3.238
41	94.35	298.2	0.06909	266	2.844
42	94.35	298.2	0.06909	266	2.844
43	101.3	298.2	0.06909	266	2.836

Table 5.4. Cost of material of hybrid photocatalytic reactor.

Material	Cost [127]
CuCl	0.0820 C\$/g
ZnS	0.7314 C\$/g
Na ₂ S	0.1211 C\$/g
NaOH	0.0161 C\$/g
HCl	0.005076 C\$/g
Titanium electrode	17 C\$/foot
Graphite electrode	4.33 C\$/foot
Glassware	1200 C\$/m ²

Table 5.5. Constraints associated with the optimization study of hybrid photocatalytic reactor.

Parameter	Minimum Value	Maximum Value
T_{reac}	290 K	340 K
T_0	280 K	320 K
M_{CuCl}	0.1 mol/L	1.0 mol/L
M_{ZnS}	0.1 mol/L	1.0 mol/L
V	2.0 V	3.5 V

The second objective function, the exergy efficiency of the hybrid photocatalytic hydrogen production reactor is defined as

$$\eta_{ex} = \frac{\dot{E}x_{H_2}}{\dot{W}_{in}} \quad (5.161)$$

The third objective function, the total cost rate of hydrogen production by the hybrid photocatalytic reactor is defined as

The cost of hydrogen can then be calculated by rearranging the Eq. 5.158 and re-writing it as

$$C_{H_2} = \frac{(c \times \dot{m})_{CuCl} + (c \times \dot{m})_{HCl} + (c \times \dot{m})_{ZnS} + (c \times \dot{m})_{Na_2S} + (c \times \dot{m})_{NaOH} + \dot{Z}_{eq}}{\dot{m}_{H_2}} \quad (5.162)$$

The temperature constraints are selected in such a way that they satisfy the normal operating temperature. Increasing the temperature of the hybrid reactor above a certain point can result in permanent damage to the membrane and a higher voltage drop in the system. The ambient temperature range is selected keeping in mind normal ambient conditions. The constraints of concentration of CuCl and zinc sulfide are selected based on research meetings. The voltage is constrained within the given limit to avoid supply of higher overpotential to the system, which can result in a higher corrosion rate in the anolyte compartments and can result in permanent damage to the membrane.

An optimization study of the second integrated system is also performed to determine the best operating conditions for the system. In this optimization study, exergy efficiency of the system and the cost of hydrogen production is selected as objective functions. These objective functions are then constrained by solar light intensity, view factor, concentration ratio, mass fraction of HCl, mass flow rate of ZnS, electrolyzer pressure and ambient temperature.

The first objective function, which aims at maximizing the exergy efficiency of the second integrated system, is defined as follows:

$$\eta_{ex_{sys2}} = \left(\frac{\dot{E}x_{H_2} + \dot{E}x_{22} + \dot{E}x_{H_2PC}}{\dot{E}x_{in} + \frac{(\dot{W}_{elec} - \dot{W}_{net_{KC}} + \dot{W}_{p1} + \dot{W}_{p2} + \dot{W}_{p3} + \dot{W}_{p4})}{\eta_{convr}}} \right) \quad (5.163)$$

The second objective function, the cost of hydrogen production for the second integrated system is calculated as

$$\frac{c_a}{c_b} = \left(\frac{\dot{V}_a}{\dot{V}_b} \right)^n \quad (5.164)$$

where c_a and c_b represent cost of hydrogen production by system a and b, respectively. \dot{V}_a and \dot{V}_b represent hydrogen production rate by system a and b, respectively. The n represents a factor which is taken as 0.6 [2]. This cost and hydrogen production relation is known as six-tenth rule and is obtained from Ozbilen [2]. The constraints of optimization study of hybrid photocatalytic reactor are presented in Table 5.6.

In the present multi-objective optimization study, all of the variables are given equal importance to avoid subjectivity in the analysis.

Table 5.6. Constraints associated with the optimization study of integrated systems.

Parameter	Minimum Value	Maximum Value
$T_{ms,in}$	550 K	700 K
T_0	290 K	330 K
mf_{HCl}	0.7	0.9
\dot{m}_{ZnS}	0.45 kg/s	0.7 kg/s
C	300	1500
I_s	600 W/m ²	1200 W/m ²
F_r	0.5	0.9
P_{elec}	100 kPa	1000 kPa

The linear programming technique for multidimensional analysis of preference (LINMAP) [130] is used to find a single best optimization point by placing a point on the Pareto frontier in such a way that it is closest to the ideal operating conditions where all specific objectives are optimized.

Chapter 6: Results and Discussion

This section of the report presents and discusses results from experiments, electrochemical and thermodynamic analyses of a hybrid photocatalytic reactor and energy and exergy analyses of integrated systems considered during the course of the research.

6.1 Experimental Results of Photo-electrocatalytic Hydrogen Production

After performing experiments, a statistical technique known as analysis of variance is used to find the effects of different operating parameters such as voltage, light intensity, mass or concentration of CuCl and mass or concentration of ZnS on hydrogen production rate using the sixth model technique. The results obtained from analysis of variance are presented in Table 6.1. The F_{value} of 1112.20 for the model shows that the model is significant. There is a slight chance of 0.01% that F_{value} this large can occur due to noise. In present analysis, A, B, C, D, AC, AD, CD, B², C², D², ABC, ACD, BCD, A²B, A²D, AC², AD², B²C, B²D, BC², CD², ABCD, A²C², A²D², AB²D, ABC², ACD², B²CD, B²D², C²D², AB²C², AB²D², ABC²D, ABCD², AC²D², B²C²D, B²CD², BC²D², A²B²CD, A²B²D², AB²CD², ABC²D², B²C²D² are significant model terms. Here, A, B, C, and D represent voltage, light intensity, mass or concentration of ZnS and mass or concentration of CuCl, respectively. Adeq Precision method, which is used to measure the signal to noise ratio, shows that for the present model its value is 112, which is greater than 4 and assures that the model obtained is adequate. The correlation obtained between the rate of hydrogen production and voltage, light intensity, mass or concentration of CuCl and mass or concentration of ZnS for the hybrid photo-electrocatalytic hydrogen production process after conducting regression analysis is presented below. In this experiment, the voltage is applied to simulate the condition in which the necessary overpotential is generated by the titanium dioxide catalyst. It is not suitable to perform many experiments using titanium dioxide due to health risks as well as cost restrictions; therefore, applied voltage is used to simulate the conditions. For photo-electrocatalytic experimental analysis the uncertainty in the result is obtained to be 2%.

$$\begin{aligned}
\dot{m}_{H_2} = & 560.58282 + 5.36628(V) - 2.76072(I) - 62.94273(\dot{m}_{ZnS}) - 337.57834(\dot{m}_{CuCl}) \\
& + 0.17914(V)(I) - 230.91922(V)(\dot{m}_{ZnS}) + 100.96386(V)(\dot{m}_{CuCl}) \\
& + 0.36406(I)(\dot{m}_{ZnS}) + 1.57769(I)(\dot{m}_{CuCl}) + 86.5993(\dot{m}_{ZnS})(\dot{m}_{CuCl}) - 8.15218(V^2) \\
& + 3.41738 \times 10^{-3}(I^2) + 53.71443(\dot{m}_{ZnS}^2) + 34.89607(\dot{m}_{CuCl}^2) \\
& + 0.95357(V)(I) (\dot{m}_{ZnS}) - 0.50207(V)(I) (\dot{m}_{CuCl}) + 31.93752(V) (\dot{m}_{ZnS})(\dot{m}_{CuCl}) \\
& - 0.41136(I) (\dot{m}_{ZnS})(\dot{m}_{CuCl}) + 0.015684(V^2)(I) + 35.36307(V^2)(\dot{m}_{ZnS}) \\
& - 13.29970(V^2)(\dot{m}_{CuCl}) - 4.19544 \times 10^{-4}(V) (I^2) + 8.59612(V)(\dot{m}_{ZnS}^2) \\
& - 14.00534(V)(\dot{m}_{CuCl}^2) - 5.53006 \times 10^{-4}(I^2)(\dot{m}_{ZnS}) - 1.85460 \\
& \times 10^{-3}(I^2)(\dot{m}_{CuCl}) - 0.25242(I)(\dot{m}_{ZnS}^2) - 0.16048(I)(\dot{m}_{CuCl}^2) \\
& - 19.66366(\dot{m}_{ZnS}^2)(\dot{m}_{CuCl}) - 9.98586(\dot{m}_{ZnS})(\dot{m}_{CuCl}^2) \\
& - 0.12278(V)(I)(\dot{m}_{ZnS})(\dot{m}_{CuCl}) + 1.30741 \times 10^{-6}(V^2)(I^2) \\
& - 0.15377(V^2)(I)(\dot{m}_{ZnS}) + 0.063389(V^2)(I)(\dot{m}_{CuCl}) - 0.068506(V^2)(\dot{m}_{ZnS}^2) \\
& - 5.27244(V^2)(\dot{m}_{ZnS})(\dot{m}_{CuCl}) + 2.08504(V^2)(\dot{m}_{CuCl}^2) - 9.69311 \\
& \times 10^{-4}(V)(I^2)(\dot{m}_{ZnS}) + 6.17118 \times 10^{-4}(V)(I^2)(\dot{m}_{CuCl}) - 0.027032(V)(I)(\dot{m}_{ZnS}^2) \\
& + 0.065794(V)(I)(\dot{m}_{CuCl}^2) - 1.60988(V)(\dot{m}_{ZnS}^2)(\dot{m}_{CuCl}) \\
& - 0.026449(V)(\dot{m}_{ZnS})(\dot{m}_{CuCl}^2) + 3.04052 \times 10^{-4}(I^2)(\dot{m}_{ZnS}^2) + 5.05476 \\
& \times 10^{-4}(I^2)(\dot{m}_{ZnS})(\dot{m}_{CuCl}) + 1.84955 \times 10^{-4}(I^2)(\dot{m}_{CuCl}^2) \\
& + 0.092100(I)(\dot{m}_{ZnS}^2)(\dot{m}_{CuCl}) + 0.046375(I)(\dot{m}_{ZnS})(\dot{m}_{CuCl}^2) \\
& + 1.47855(\dot{m}_{ZnS}^2)(\dot{m}_{CuCl}^2) + 1.68167 \times 10^{-4}(V^2)(I^2)(\dot{m}_{ZnS}) - 7.43304 \\
& \times 10^{-5}(V^2)(I^2)(\dot{m}_{CuCl}) + 0.023286(V^2)(I)(\dot{m}_{ZnS})(\dot{m}_{CuCl}) - 9.51988 \\
& \times 10^{-3}(V^2)(I)(\dot{m}_{CuCl}^2) + 1.67000 \times 10^{-5}(V)(I^2)(\dot{m}_{ZnS}^2) + 1.10033 \\
& \times 10^{-4}(V)(I^2)(\dot{m}_{ZnS})(\dot{m}_{CuCl}) - 7.67902 \times 10^{-5}(V)(I^2)(\dot{m}_{CuCl}^2) + 3.94700 \\
& \times 10^{-3}(V)(I)(\dot{m}_{ZnS}^2)(\dot{m}_{CuCl}) - 1.20582 \times 10^{-3}(V)(I)(\dot{m}_{ZnS})(\dot{m}_{CuCl}^2) \\
& + 0.11408(V)(\dot{m}_{ZnS}^2)(\dot{m}_{CuCl}^2) - 1.10757 \times 10^{-4}(I^2)(\dot{m}_{ZnS}^2)(\dot{m}_{CuCl}) \\
& - 5.48951 \times 10^{-5}(I^2)(\dot{m}_{ZnS})(\dot{m}_{CuCl}^2) - 6.92953 \times 10^{-3}(I)(\dot{m}_{ZnS}^2)(\dot{m}_{CuCl}^2) \\
& - 2.55778 \times 10^{-5}(V^2)(I^2)(\dot{m}_{ZnS})(\dot{m}_{CuCl}) + 1.07639 \times 10^{-5}(V^2)(I^2)(\dot{m}_{CuCl}^2) \\
& + 3.08889 \times 10^{-6}(V)(I^2)(\dot{m}_{ZnS})(\dot{m}_{CuCl}^2) - 2.77733 \\
& \times 10^{-4}(V)(I)(\dot{m}_{ZnS}^2)(\dot{m}_{CuCl}^2) + 8.30696 \times 10^{-6}(I^2)(\dot{m}_{ZnS}^2)(\dot{m}_{CuCl}^2)
\end{aligned} \tag{6.1}$$

After performing experiments and completing the ANOVA analysis, a normal plot of residuals is analyzed to check the linearity of interactions between the operating variables and the desired output. This normal probability plot shows whether the trend followed by residuals is based on normal distribution or not as shown in Fig 6.1. These residuals are calculated by taking the difference between the actual responses obtained from experiments with the predicted response created by ANOVA.

Table 6.1. Analysis of variance for rate of hydrogen production by photo-electrocatalytic experiments

Source	Sum of Squares	Degree of Freedom	Mean Square	F_{value}	p-value
Model	12.01585246	67	0.179341	1112.203	< 0.0001
A-Voltage [V]	0.012152009	1	0.012152	75.36202	< 0.0001
B-Intensity [W/m ²]	0.000945216	1	0.000945	5.861861	0.0308
C- m_{ZnS} [g]	0.025972236	1	0.025972	161.0697	< 0.0001
D- m_{CuCl} [g]	0.830293553	1	0.830294	5149.157	< 0.0001
AB	0.000250694	1	0.000251	1.554709	0.2344
AC	0.003179707	1	0.00318	19.7193	0.0007
AD	0.014598006	1	0.014598	90.53114	< 0.0001
BC	0.000607039	1	0.000607	3.764618	0.0744
BD	0.000295595	1	0.000296	1.833165	0.1988
CD	0.001736111	1	0.001736	10.76668	0.0060
A ²	6.93554E-05	1	6.94E-05	0.430115	0.5234
B ²	0.002693444	1	0.002693	16.70369	0.0013
C ²	0.00354512	1	0.003545	21.98545	0.0004
D ²	0.006442474	1	0.006442	39.95371	< 0.0001
ABC	0.003803858	1	0.003804	23.59004	0.0003
ABD	2.8534E-06	1	2.85E-06	0.017696	0.8962
ACD	0.001320409	1	0.00132	8.188661	0.0134
BCD	0.002917631	1	0.002918	18.09401	0.0009
A ² B	0.00109267	1	0.001093	6.776312	0.0219
A ² C	1.238E-05	1	1.24E-05	0.076776	0.7861
A ² D	0.001967087	1	0.001967	12.1991	0.0040
AB ²	8.06667E-06	1	8.07E-06	0.050026	0.8265
AC ²	0.000792067	1	0.000792	4.912089	0.0451
AD ²	0.001496669	1	0.001497	9.281754	0.0094
B ² C	0.012857824	1	0.012858	79.73921	< 0.0001
B ² D	0.015507314	1	0.015507	96.17032	< 0.0001
BC ²	0.011025	1	0.011025	68.37275	< 0.0001
BD ²	0.000274649	1	0.000275	1.703267	0.2145
C ² D	0.000147128	1	0.000147	0.91243	0.3569
CD ²	0.00547326	1	0.005473	33.94302	< 0.0001
ABCD	0.001215297	1	0.001215	7.536798	0.0167
A ² B ²	0.000245339	1	0.000245	1.521496	0.2392
A ² BC	0.00023272	1	0.000233	1.443241	0.2510
A ² BD	0.000306969	1	0.000307	1.903703	0.1909
A ² C ²	0.001173274	1	0.001173	7.276187	0.0183
A ² CD	0.000734581	1	0.000735	4.555583	0.0524

A2D2	0.001203707	1	0.001204	7.464919	0.0171
AB2C	0.000611163	1	0.000611	3.790192	0.0735
AB2D	0.000835951	1	0.000836	5.18424	0.0404
ABC2	0.006519342	1	0.006519	40.43041	< 0.0001
ABD2	0.000507227	1	0.000507	3.145623	0.0995
AC2D	9.8E-05	1	9.8E-05	0.607758	0.4496
ACD2	0.002088593	1	0.002089	12.95264	0.0032
B2C2	0.000714449	1	0.000714	4.430734	0.0553
B2CD	0.00169456	1	0.001695	10.509	0.0064
B2D2	0.022210701	1	0.022211	137.7421	< 0.0001
BC2D	0.000176302	1	0.000176	1.093359	0.3148
BCD2	0.000580521	1	0.000581	3.600166	0.0802
C2D2	0.004926752	1	0.004927	30.55379	< 0.0001
A2B2C	0.000583449	1	0.000583	3.618324	0.0795
A2B2D	0.000703364	1	0.000703	4.361992	0.0570
A2BCD	0.00036729	1	0.000367	2.277792	0.1552
A2BD2	0.000457109	1	0.000457	2.834814	0.1161
AB2C2	0.001162042	1	0.001162	7.206529	0.0187
AB2CD	0.000438021	1	0.000438	2.716434	0.1233
AB2D2	0.001407261	1	0.001407	8.727286	0.0112
ABC2D	0.000999187	1	0.000999	6.196571	0.0271
ABCD2	0.001107414	1	0.001107	6.867749	0.0212
AC2D2	0.003092749	1	0.003093	19.18002	0.0007
B2C2D	0.01997403	1	0.019974	123.8711	< 0.0001
B2CD2	0.011557407	1	0.011557	71.67453	< 0.0001
BC2D2	0.021369507	1	0.02137	132.5253	< 0.0001
A2B2CD	0.002839508	1	0.00284	17.60952	0.0010
A2B2D2	0.001571459	1	0.001571	9.745574	0.0081
AB2CD2	0.00103529	1	0.001035	6.420466	0.0249
ABC2D2	0.003347908	1	0.003348	20.76242	0.0005
B2C2D2	0.014975181	1	0.014975	92.87023	< 0.0001
Residual	0.00209623	13	0.000161		

It can be seen in this figure that the residuals follow an s-shape pattern, which is non-linear, therefore indicating that the correlation between the hydrogen production rate and operating parameters is non-linear. The effects of experimental run order on residuals are presented in Fig. 6.2. This figure clearly shows which values of the analytical model have the greatest effect. The randomness of points in this figure shows that there is no hidden

parameter affecting the response and provide insurance against the trends which otherwise may affect the analysis.

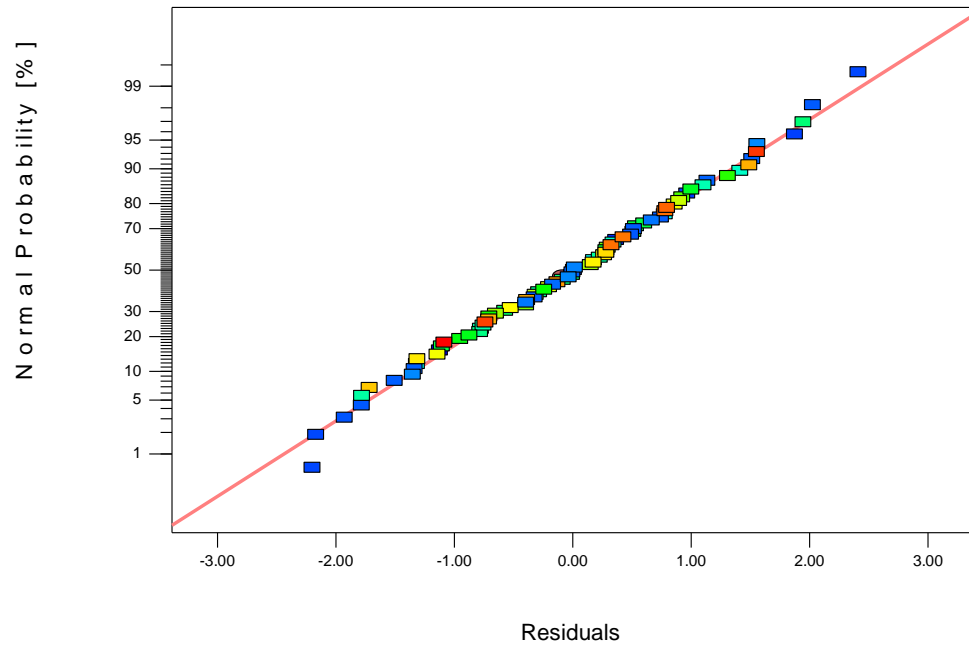


Fig. 6.1. Normal probability distribution of residuals for photo-electrocatalytic hydrogen production process.

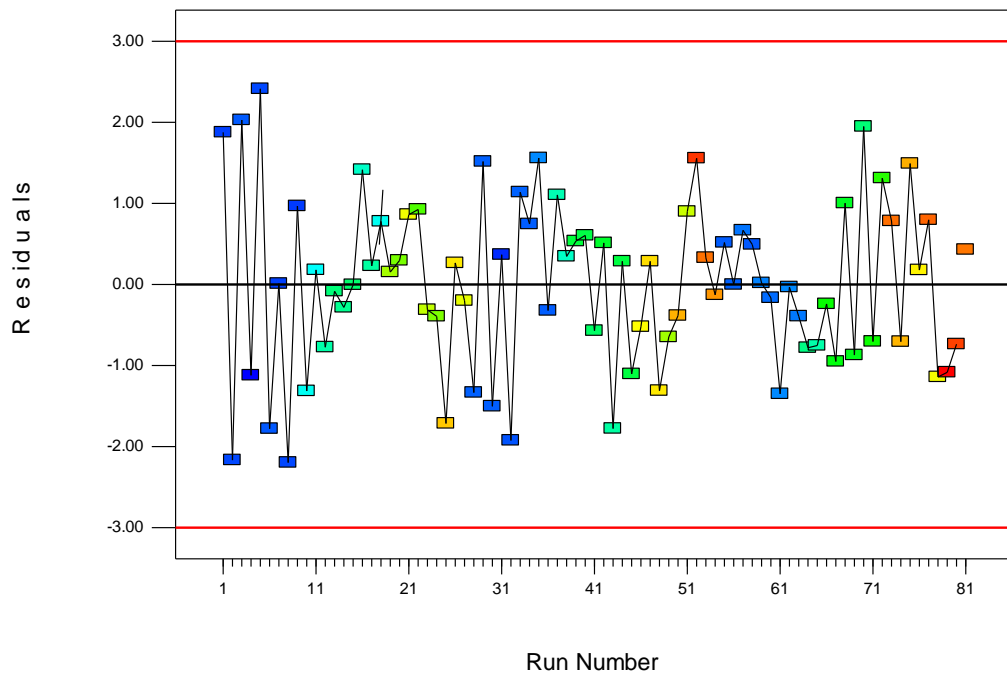


Fig. 6.2. Effects of run number on residuals for photo-electrocatalytic hydrogen production process.

The Box-Cox plot technique is used by the experimenters to find the correct power law transformation for their experimental results. The recommended model transformation of the photocatalytic hydrogen production process is 0.74 as shown in Fig 6.3. This value is obtained based on the best power value, which can be attained at the absolute minimum of the curve generated by the natural log of the sum of squares of the residuals. In this figure, green line, blue line and the red line represent best power value, current value and 95% confidence interval surrounding the best value, respectively. Figure 6.4 shows the accuracy of the predicted response versus the actual response. This figure indicates that there is a high accuracy between the predicted response and actual response obtained from the experiments.

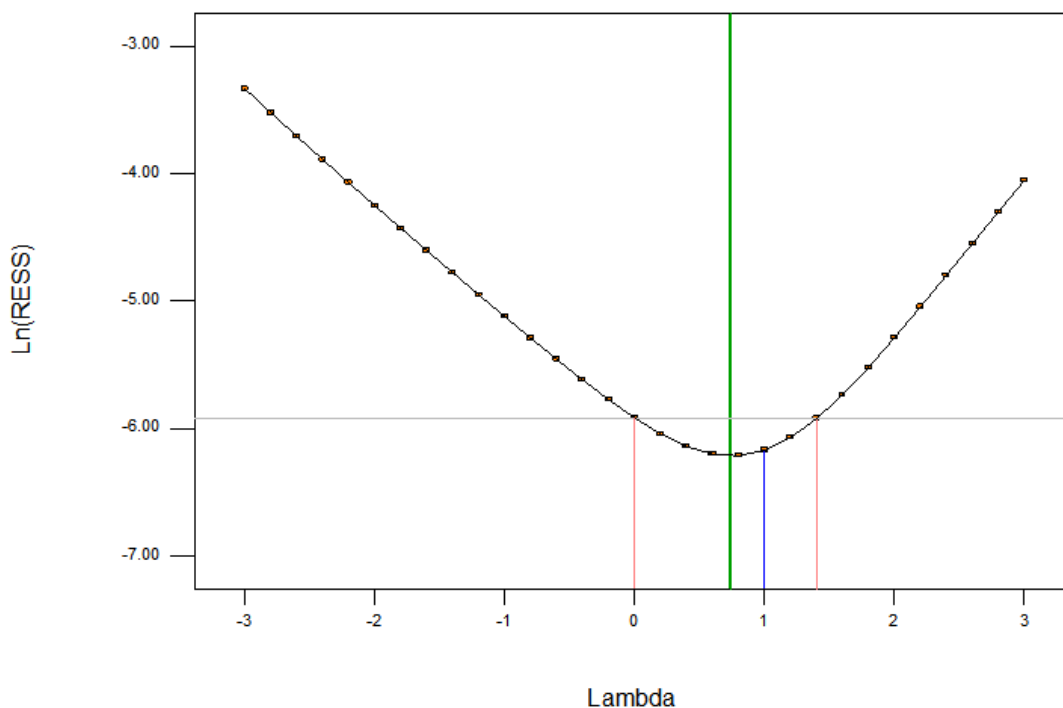


Fig. 6.3. Box-Cox plot for power transformation of photo-electrocatalytic hydrogen production process.

The effects of an increase in applied voltage, solar light intensity and mass or concentration of CuCl on the hydrogen production rate for fixed mass or concentration of ZnS of 2 g or 0.013 g/mL with a mass or concentration of CuCl of 5 g or 0.033 g/mL is shown in Fig. 6.5. The effects of an increase in applied voltage, solar light intensity and mass or concentration of CuCl on the hydrogen production rate for fixed mass or

concentration of ZnS of 2 g or 0.013 g/mL with a mass or concentration of CuCl of 8 g or 0.053 g/mL is shown in Fig. 6.6.

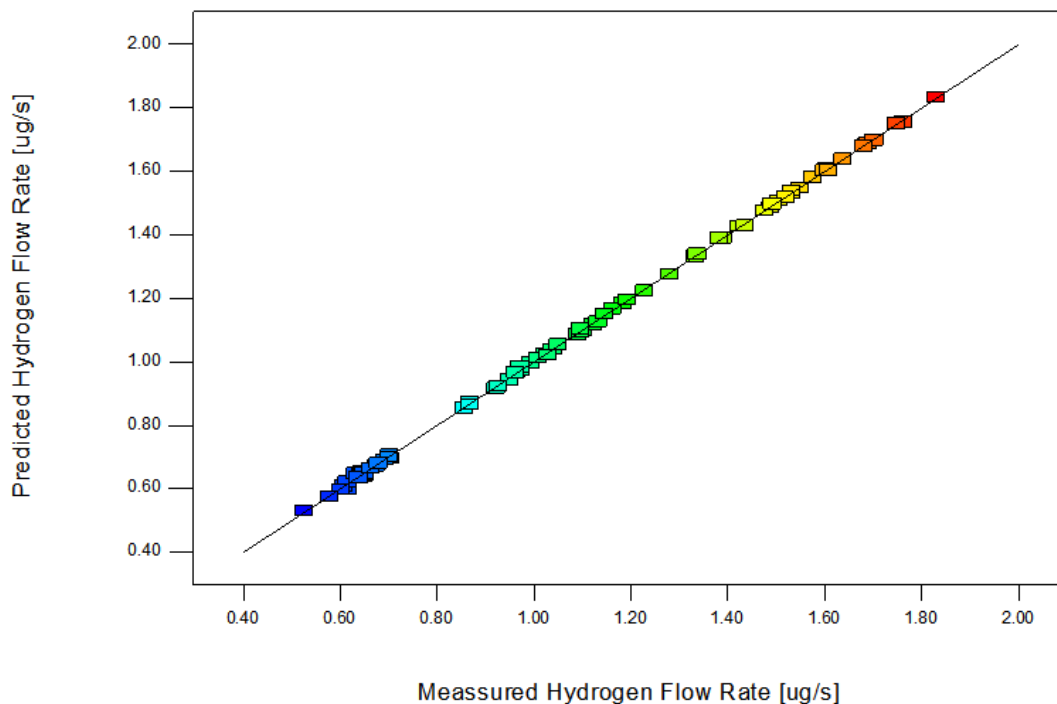


Fig. 6.4. Model prediction versus actual hydrogen production rate of photo-electrocatalytic hydrogen production process.

The effects of increase in applied voltage, solar light intensity and mass or concentration of CuCl on the hydrogen production rate for fixed mass or concentration of ZnS of 2 g or 0.013 g/mL with a mass or concentration of CuCl of 9 g or 0.06 g/mL is shown in Fig. 6.7. In these figures, solid black and red lines represent average hydrogen production rates for varying solar light intensity of 400 and 500 W/m², respectively. The dotted black and red lines denote the range in which the data is accurate. In other words, they represent an error associated with the data. The hydrogen production rate is observed to be increasing with an increase in applied voltage, solar light intensity and mass or concentration of CuCl. The increase in applied voltage results in a higher overpotential being developed in the hybrid reactor and as a result of this higher overpotential, the molecule breaking rate increases and the hydrogen production rate increases. The increase in the hydrogen production rate with an increase in solar light intensity follows the same concept as that of the applied voltage except that in photocatalytic process,

required photons are delivered by the solar light intensity. The increase in mass or concentration of CuCl helps to increase the hydrogen production rate because with an increase in mass more hydrochloric acid molecules are broken to produce hydrogen ions and copper chloride.

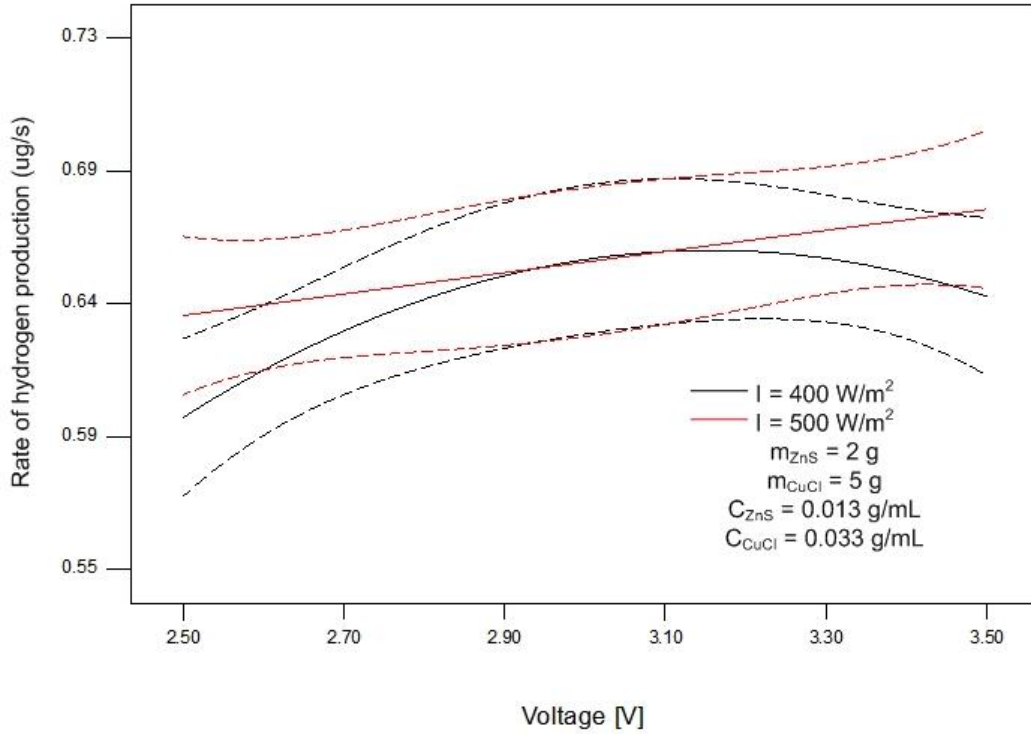


Fig. 6.5. Effects of applied voltage and solar light intensity on photo-electrocatalytic hydrogen production for mass or concentration of ZnS of 2 g or 0.013 g/mL and mass or concentration of CuCl of 5 g or 0.033 g/mL.

The effects of an increase in applied voltage, solar light intensity and mass or concentration of CuCl on the hydrogen production rate for fixed mass or concentration of ZnS of 3 g or 0.020 g/mL with a mass or concentration of CuCl of 5 g or 0.033 g/mL is shown in Fig. 6.8. The effects of increase in applied voltage, solar light intensity and mass or concentration of CuCl on the hydrogen production rate for fixed mass or concentration of ZnS of 3 g or 0.020 g/mL with a mass or concentration of CuCl of 8 g or 0.053 g/mL is shown in Fig. 6.9. The effects of an increase in applied voltage, solar light intensity and mass or concentration of CuCl on the hydrogen production rate for fixed mass or concentration of ZnS of 3 g or 0.020 g/mL with a mass or concentration of CuCl of 9 g or 0.06 g/mL is shown in Fig. 6.10.

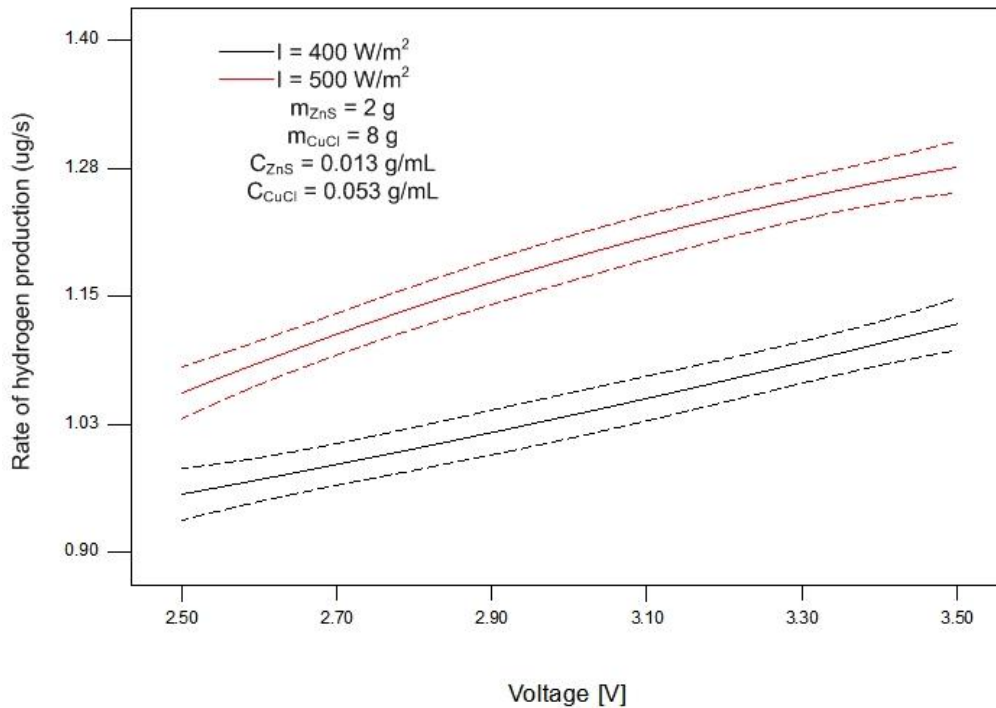


Fig. 6.6. Effects of applied voltage and solar light intensity on photo-electrocatalytic hydrogen production for mass or concentration of ZnS of 2 g or 0.013 g/mL and mass or concentration of CuCl of 8 g or 0.053 g/mL.

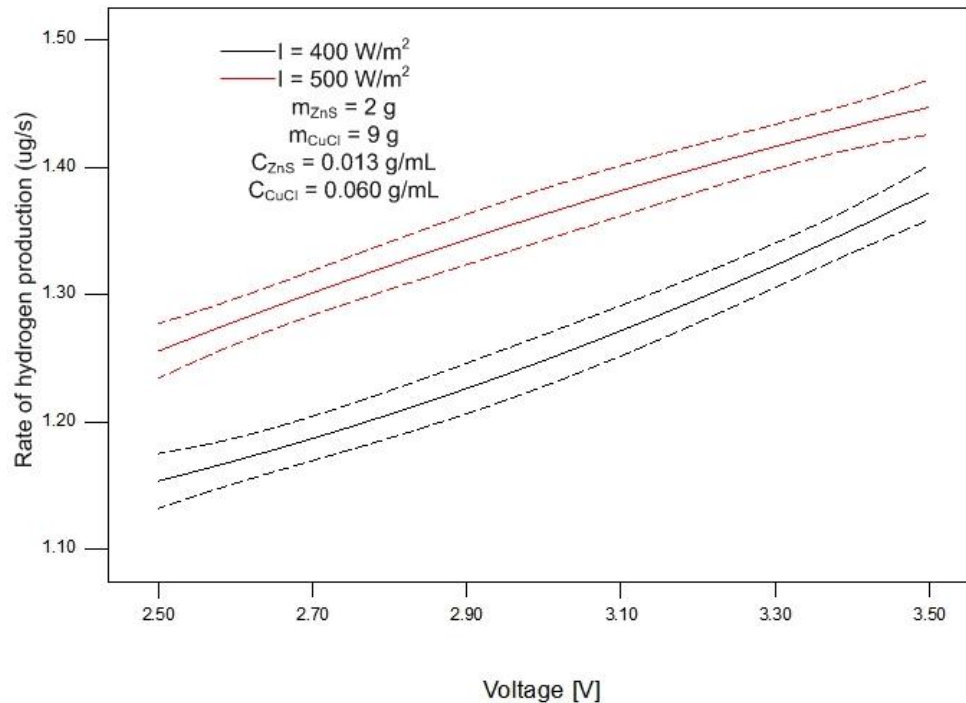


Fig. 6.7. Effects of applied voltage and solar light intensity on photo-electrocatalytic hydrogen production for mass or concentration of ZnS of 2 g or 0.013 g/mL and mass or concentration of CuCl of 9 g or 0.06 g/mL.

In these figures, the solid black and red lines represent the average hydrogen production rate for varying solar light intensity of 400 and 500 W/m², respectively. The dotted black and red lines denote the range in which the data is accurate in other words they represent an error associated with the date. The hydrogen production rate is observed to be increasing with increase in applied voltage, solar light intensity and mass or concentration of CuCl. However, an increase in mass or concentration of ZnS from 2 to 3 g or 0.013 to 0.020 g/mL shows a slight increase in hydrogen production rate. This increase in the hydrogen production rate is observed because in the present study, ZnS is used as a photocatalyst in the catholyte compartment of the reactor. An increase in the use of photocatalyst helps to increase the hydrogen production rate as it facilitates the photocatalytic hydrogen production process by generating additional electrons in the reactor to produce additional hydrogen by splitting water into hydrogen and oxygen.

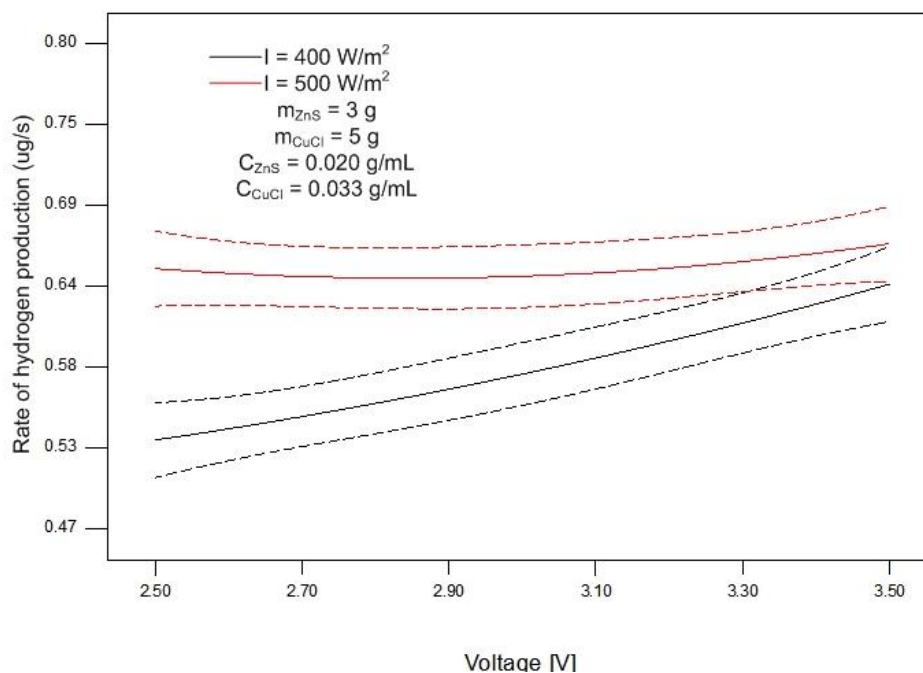


Fig. 6.8. Effects of applied voltage and solar light intensity on photo-electrocatalytic hydrogen production for mass or concentration of ZnS of 3 g or 0.020 g/mL and mass or concentration of CuCl of 5 g or 0.033 g/mL.

The effects of variation in applied voltage and mass CuCl on photo-electrocatalytic rate of hydrogen production is shown in Fig. 6.11. The results show that the rate of hydrogen production varies from 0.73 to 1.61 $\mu\text{g/s}$, with an increase in applied voltage and mass or

concentration of CuCl from 2.5 to 3.5 V and 5 to 10 g or 0.033 to 0.066 g/mL, respectively.

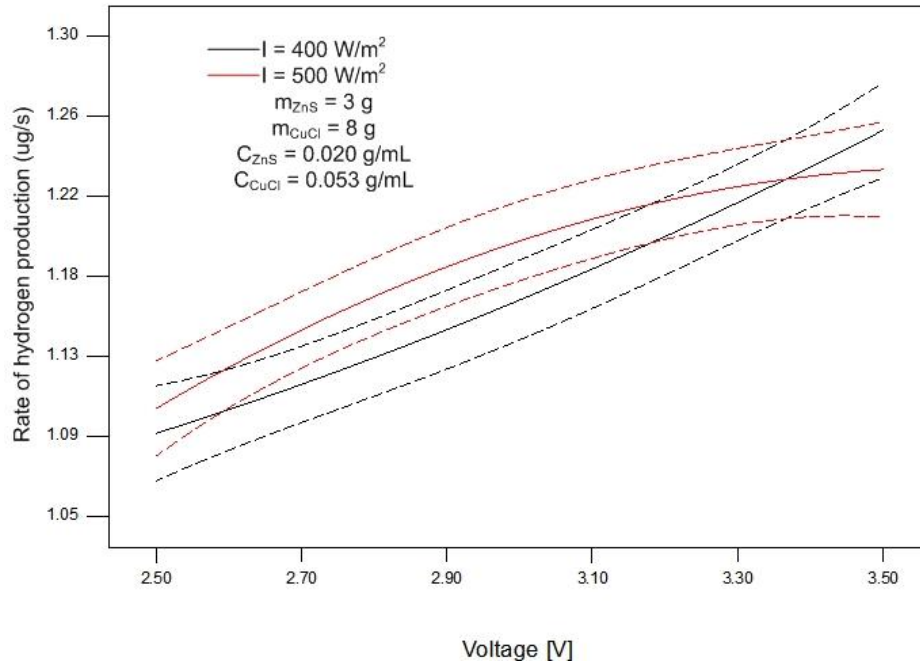


Fig. 6.9. Effects of applied voltage and solar light intensity on photo-electrocatalytic hydrogen production for mass or concentration of ZnS of 3 g or 0.020 g/mL and mass or concentration of CuCl of 8 g or 0.053 g/mL.

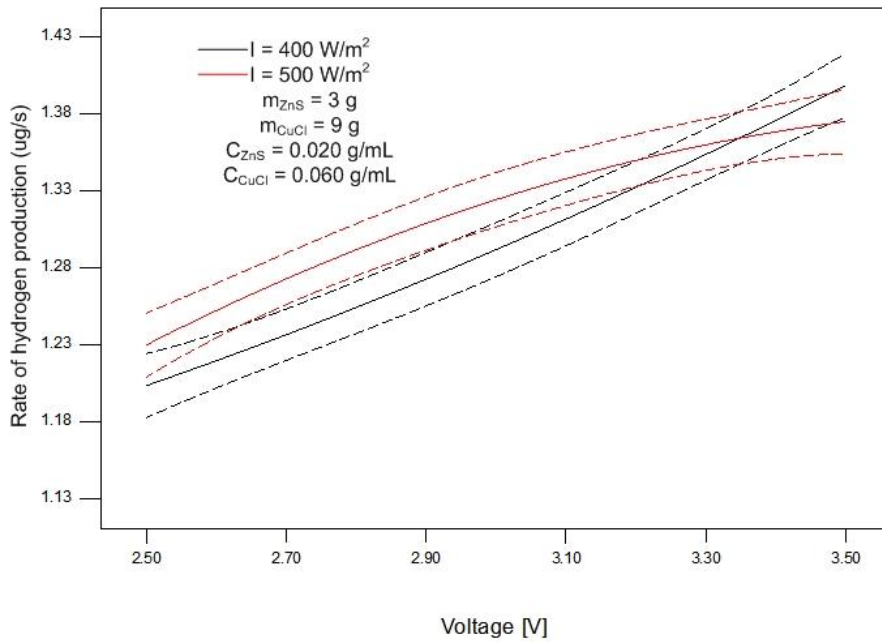


Fig. 6.10. Effects of applied voltage and solar light intensity on photo-electrocatalytic hydrogen production for mass or concentration of ZnS of 3 g or 0.020 g/mL and mass or concentration of CuCl of 9 g or 0.06 g/mL.

The increase in the hydrogen production rate with an increase in the applied voltage is observed because of the additional overpotential being provided to the reactor to help faster breaking of molecules to produce hydrogen. The increase in mass or concentration of CuCl has a positive impact on the hydrogen production rate because an increase in mass or concentration of CuCl pushes the HCl molecule to combine with it to form CuCl₂, therefore leaving behind positive hydrogen ions which travel to the catholytic solution to produce hydrogen at a faster rate.

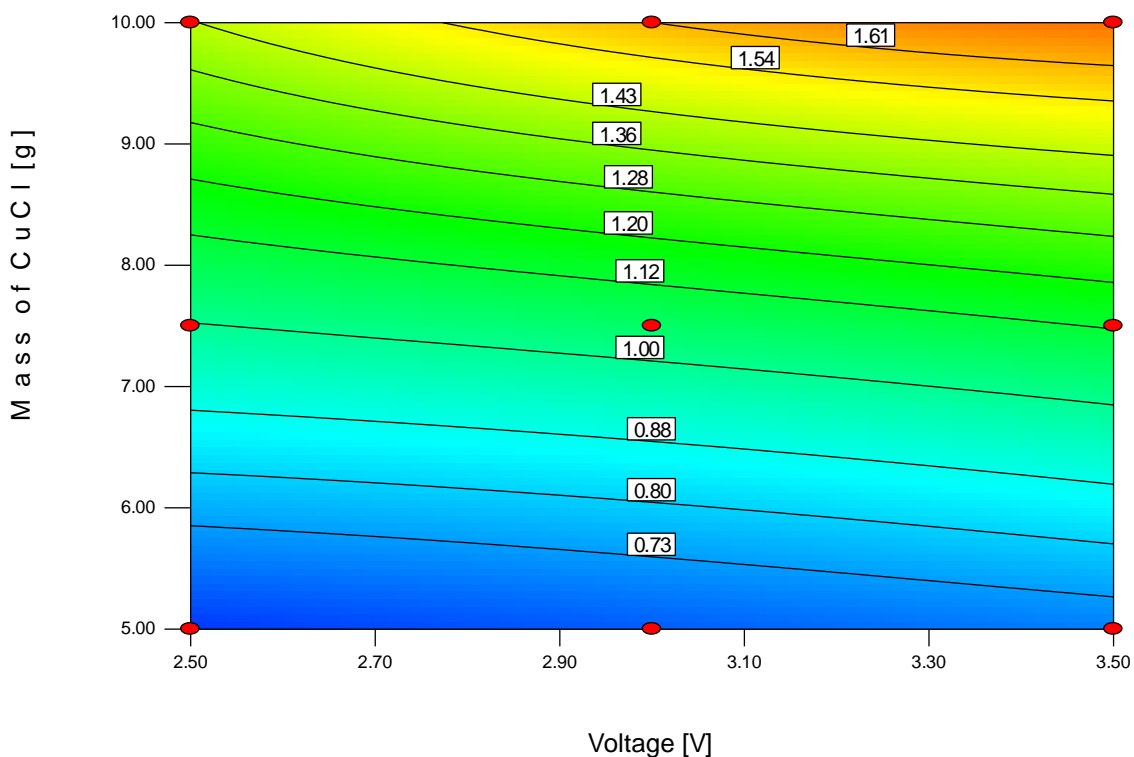


Fig. 6.11. Effects of applied voltage and mass of CuCl on photo-electrocatalytic hydrogen production rate.

The effects of variation in applied voltage and mass of ZnS on photo-electrocatalytic rate of hydrogen production is shown in Fig. 6.12. The rate of hydrogen production is observed to be varying from 1.37 to 1.64 $\mu\text{g/s}$ with an increase in applied voltage and mass or concentration of ZnS from 2.5 to 3.5 V and 2 to 4 g or 0.013 to 0.027 g/mL, respectively. Such trend is noticed because an increase in applied voltage helps in faster breaking of molecules to generate hydrogen at a faster rate. On the other hand, the rate of hydrogen production is noticed to be increasing with an increase in the mass or

concentration of ZnS because the higher availability of the photocatalyst in the solution helps to generate higher overpotential for breaking of water molecules to generate hydrogen.

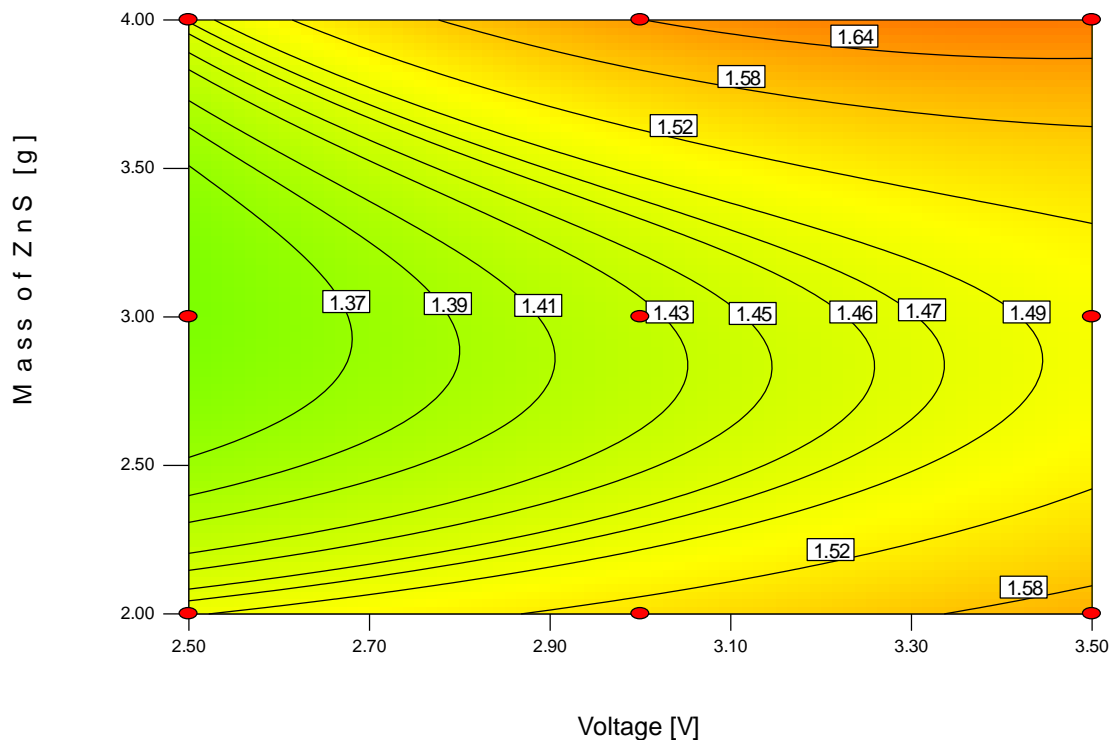


Fig. 6.12. Effects of applied voltage and mass of ZnS on photo-electrocatalytic hydrogen production rate.

Figure 6.13 demonstrates the effects of variation in the mass of ZnS and mass of CuCl on photo-electrocatalytic rate of hydrogen production. The hydrogen production rate is observed to be varying from 0.73 to 1.53 $\mu\text{g/s}$ with an increase in the mass or concentration of ZnS and the mass or concentration of CuCl from 2 to 4 g or 0.013 to 0.027 g/mL and 5 to 10 g or 0.033 to 0.066 g/mL, respectively. When a higher amount of photocatalyst such as ZnS is induced with solar light, the molecular activity in the solution in the form of faster breaking of water molecules increases and as a result the rate of hydrogen production increases. Moreover, an increase in the mass or concentration of CuCl has positive impact on hydrogen production rate because an increase in the mass or concentration of CuCl results in faster breaking of HCl molecule to generate positive hydrogen ions and CuCl_2 .

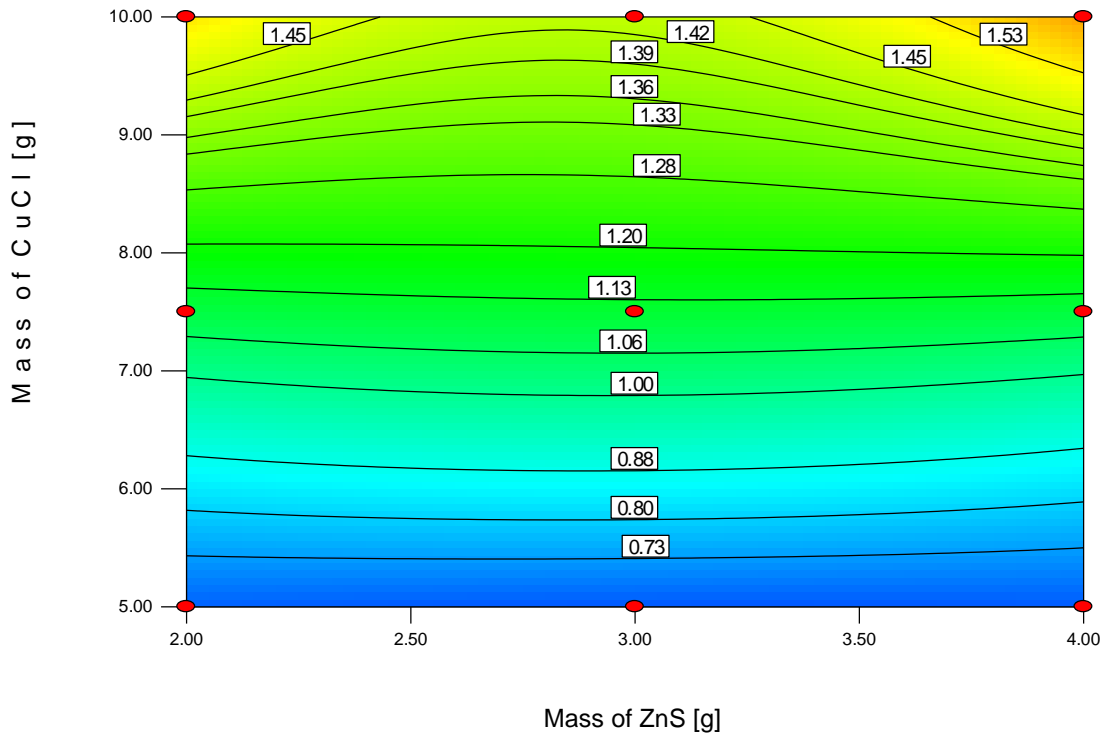


Fig. 6.13. Effects of mass of ZnS and mass of CuCl on photo-electrocatalytic hydrogen production rate.

6.2 Experimental Results of Photocatalytic Hydrogen Production

After performing experiments, a statistical technique known as analysis of variance is used to find the effects of different operating parameters such as voltage, light intensity, mass or concentration of CuCl and mass or concentration of ZnS on hydrogen production rate using the sixth model technique. The results obtained from the analysis of variance are presented in Table 6.2. The F_{value} of 140.74 for the model shows that the model becomes a significant one. There is a slight chance close to 0.01% that F_{value} this large can occur due to the presence of noise. In the present analysis, B, C, D, BC, BD, CD, B², C², D², B²C, B²D, BC², BD², C²D, CD², B²CD, B²D², BCD², B²C²D, B²CD² are significant model terms. Here, B, C, and D represent light intensity, mass or concentration of ZnS and mass or concentration of CuCl, respectively. For photocatalytic experimental analysis the uncertainty in the result is considered to be 9%.

In order to check for the linearity of interactions between the operating variables and the desired output, a normal plot of residuals is analyzed. This normal probability plot shows

whether the path followed by residuals is based on normal distribution or not as displayed in Fig 6.14. It can be seen in this figure that the residuals follow an s-shape pattern, which is non-linear therefore indicating that the correlation between the hydrogen production rate and operating parameters is non-linear.

Table 6.2. Analysis of variance for rate of hydrogen production by photocatalytic experiments

Source	Sum of Squares	Degree of Freedom	Mean Square	F_{value}	p-value
Model	0.735922	67	0.010984	140.7377	< 0.0001
B-Intensity [W/m^2]	0.004382	1	0.004382	56.14469	< 0.0001
C- m_{ZnS} [g]	0.012779	1	0.012779	163.7437	< 0.0001
D- m_{CuCl} [g]	0.050686	1	0.050686	649.4428	< 0.0001
BC	0.003576	1	0.003576	45.81551	< 0.0001
BD	0.00288	1	0.00288	36.90371	< 0.0001
CD	0.002566	1	0.002566	32.88169	< 0.0001
B ²	0.000798	1	0.000798	10.22564	0.0070
C ²	0.001841	1	0.001841	23.58991	0.0003
D ²	0.000707	1	0.000707	9.063005	0.0100
BCD	1.31E-06	1	1.31E-06	0.016768	0.8990
B ² C	0.003545	1	0.003545	45.42543	< 0.0001
B ² D	0.009113	1	0.009113	116.7648	< 0.0001
BC ²	0.000736	1	0.000736	9.43033	0.0089
BD ²	0.006208	1	0.006208	79.53986	< 0.0001
C ² D	0.000668	1	0.000668	8.559636	0.0118
CD ²	0.006451	1	0.006451	82.65506	< 0.0001
B ² C ²	5.5E-05	1	5.5E-05	0.705139	0.4162
B ² CD	0.003651	1	0.003651	46.77968	< 0.0001
B ² D ²	0.002854	1	0.002854	36.56539	< 0.0001
BC ² D	2.05E-06	1	2.05E-06	0.026277	0.8737
BCD ²	0.01526	1	0.01526	195.5215	< 0.0001
C ² D ²	3.67E-05	1	3.67E-05	0.470682	0.5047
B ² C ² D	0.001886	1	0.001886	24.1638	0.0003
B ² CD ²	0.007553	1	0.007553	96.7753	< 0.0001
BC ² D ²	0.000338	1	0.000338	4.327519	0.0578
Residual	0.001015	13	7.8E-05		

Figure 6.15 presents the effects of experimental run order on residuals. The randomness of points in the figure shows that there are no hidden parameters affecting the response. The recommended model transformation for photocatalytic hydrogen production process based on Box-Cox technique is 0.39 as shown in Fig 6.16. Here, the green line, blue line

and the red line represent best power value, current value and 95% confidence interval surrounding the best value, respectively. Figure 6.17 shows the accuracy of the predicted response versus the actual response. The figure indicates that there is a high accuracy between the predicted response and actual response obtained from the experiments.

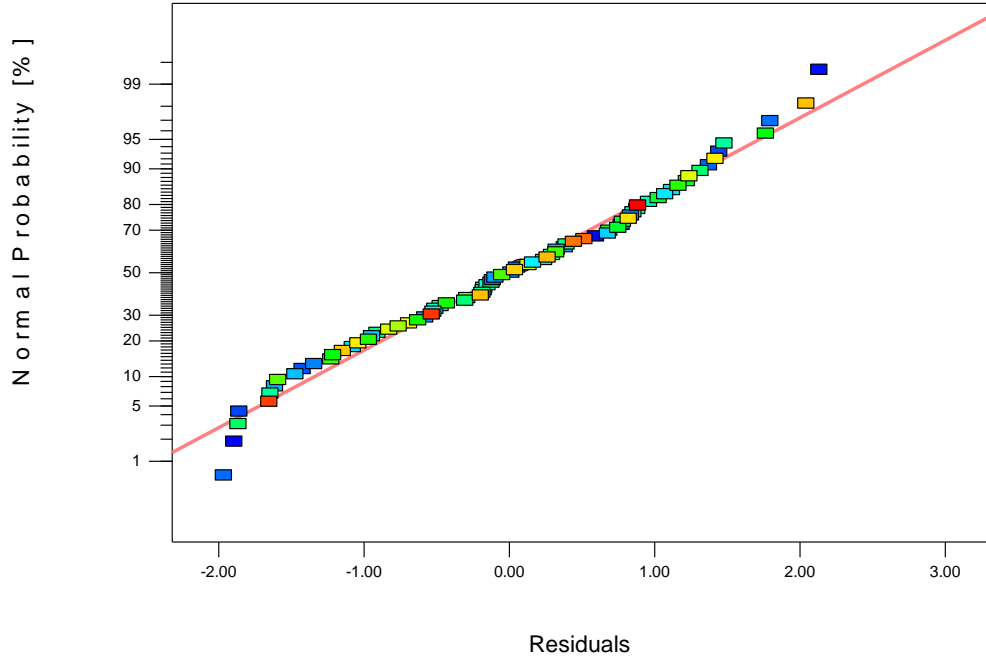


Fig. 6.14. Normal probability distribution of residuals for photocatalytic hydrogen production process.

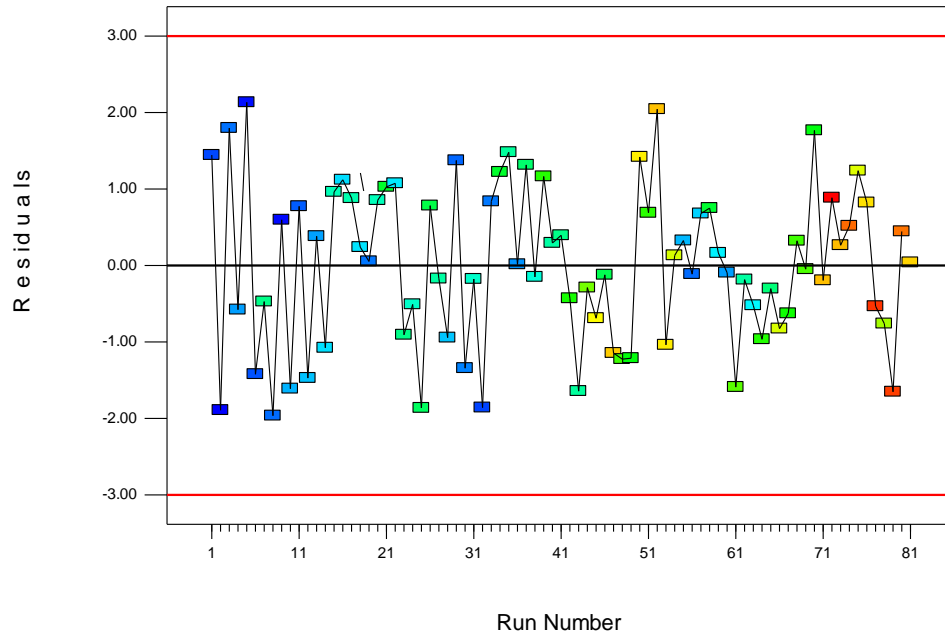


Fig. 6.15. Effects of run number on residuals for photocatalytic hydrogen production process.

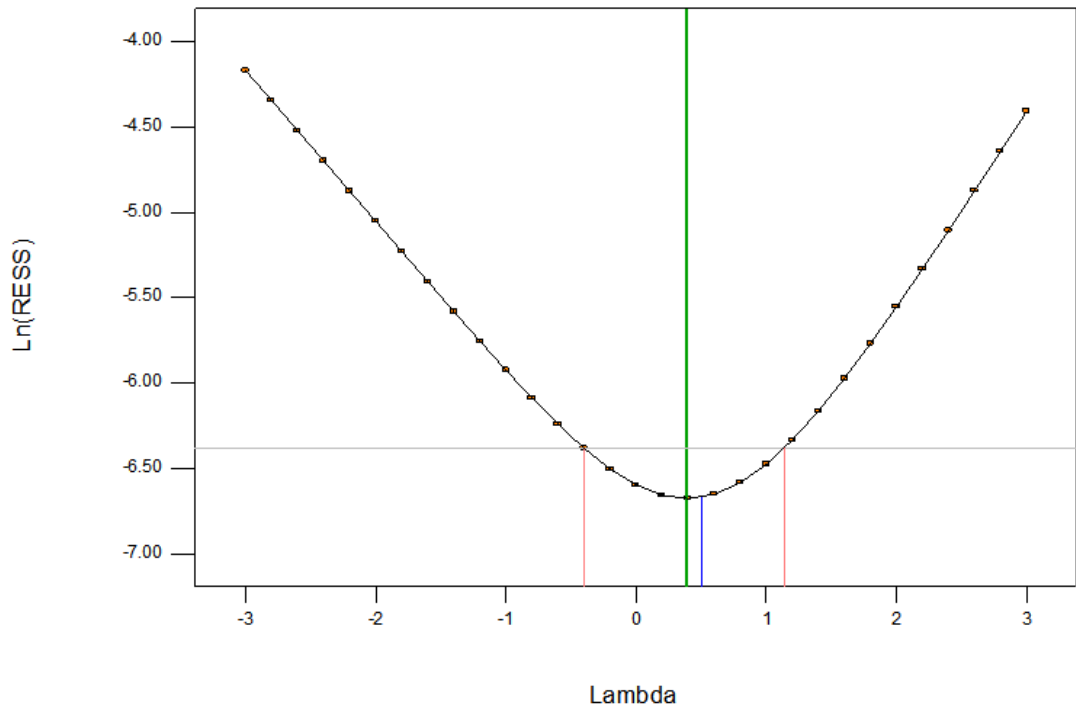


Fig. 6.16. Box-Cox plot for power transformation of photocatalytic hydrogen production process.

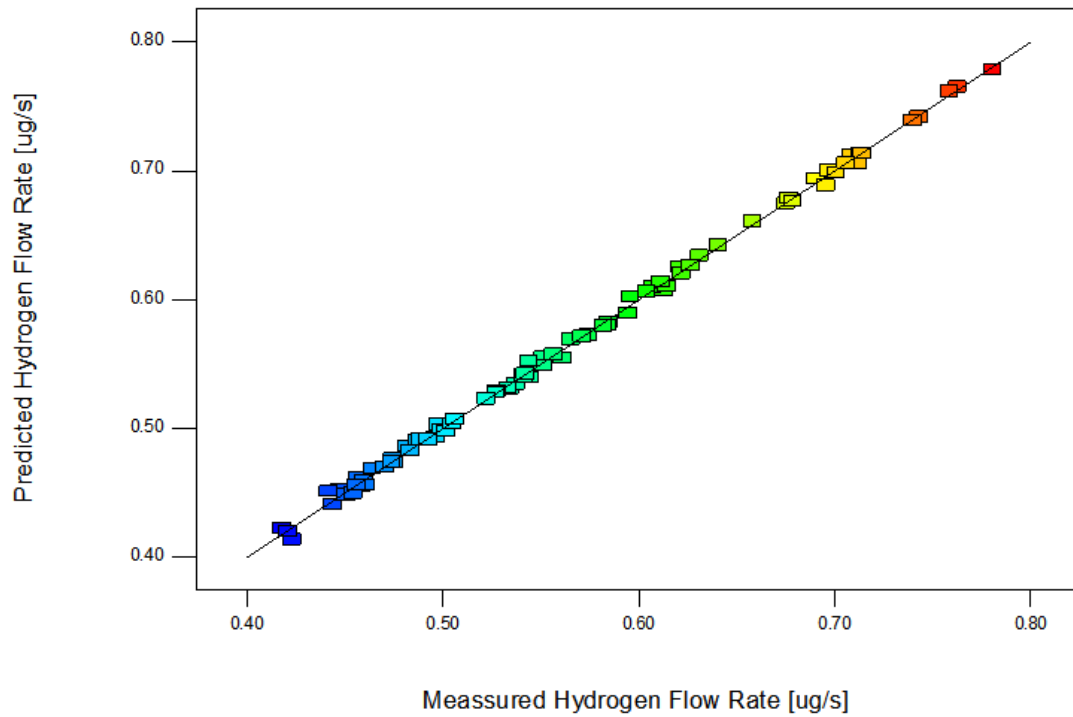


Fig. 6.17. Model prediction versus actual hydrogen production rate of photocatalytic hydrogen production process.

The effects of a rise in solar light intensity on the photocatalytic hydrogen production rate are shown in Fig 6.18. The photocatalytic hydrogen production rate is observed to vary from 0.28 to 0.36 $\mu\text{g/s}$, with a rise in solar light intensity from 400 to 500 W/m^2 at constant mass or concentration of ZnS of 3 g or 0.020 g/mL and constant mass or concentration of CuCl of 7.5 g or 0.05 g/mL. The dotted lines in the graph represent the confidence interval surrounding the actual value represented by the solid line. Such a trend is observed because a rise in solar light intensity brings with it higher number of photons, which then excite the photocatalyst to produce hydrogen at a faster rate. Figure 6.19 shows the effects of variation in the mass of CuCl on hydrogen photocatalytic production rate. The photocatalytic hydrogen production rate is noticed to be increasing from 0.2 to 0.49 $\mu\text{g/s}$ with an increase in the mass or concentration of CuCl from 5 to 10 g or 0.033 to 0.066 g/mL at constant solar light intensity of 450 W/m^2 and constant of ZnS of 3 g or 0.020 g/mL.

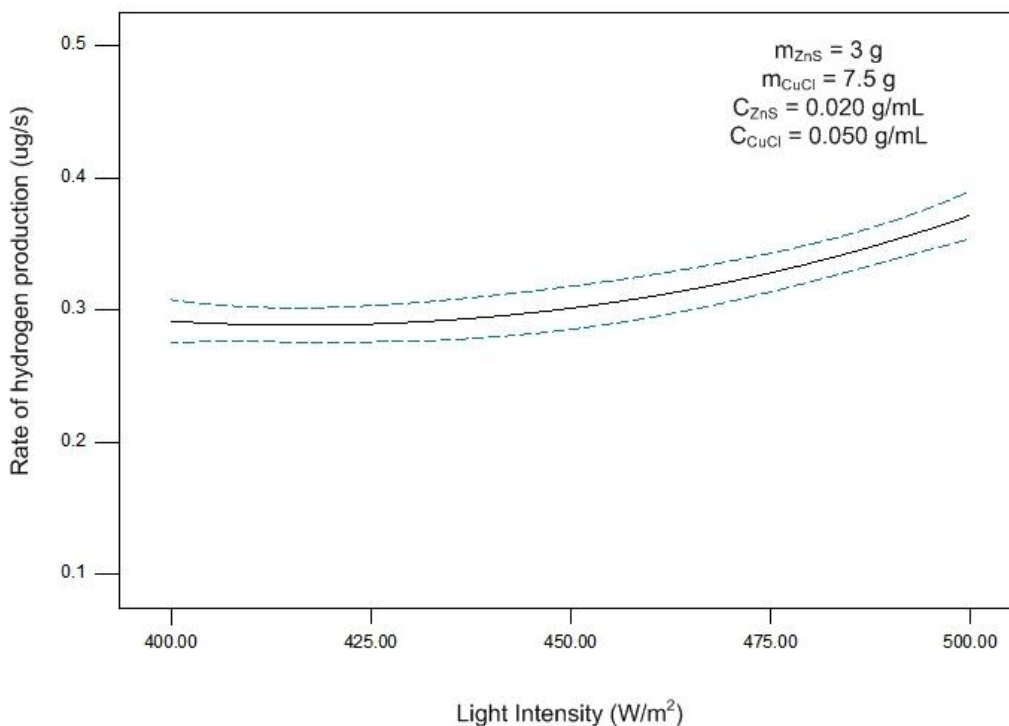


Fig. 6.18. Effects of solar light intensity on photocatalytic hydrogen production rate.

Such a trend of an increase in photocatalytic hydrogen production with an increase in the mass or concentration of CuCl is noticed because an increase in the mass or concentration of CuCl helps in faster breaking of the HCl molecule into hydrogen and chlorine ions.

The property of CuCl of getting excited when brought in contact with HCl to form CuCl₂ helps to increase the transfer of hydrogen ions from anolyte compartment to catholyte compartment via cation exchange membrane.

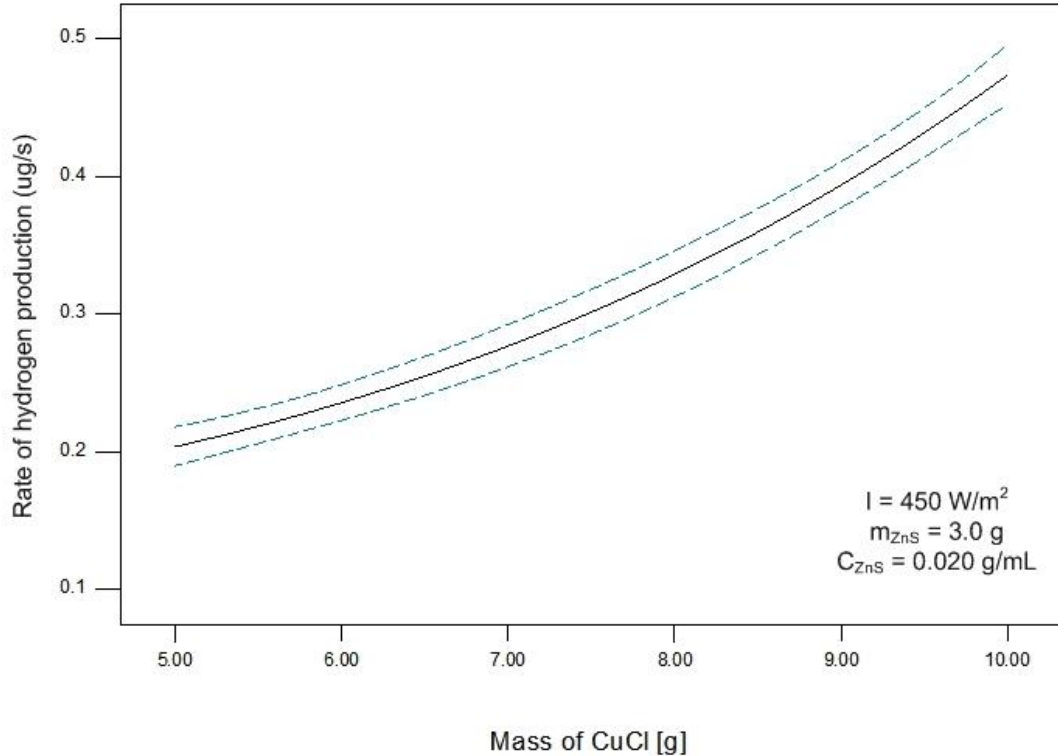


Fig. 6.19. Effects of mass of CuCl on photocatalytic hydrogen production rate.

Figure 6.20 shows the effects of an increase in the mass of photocatalyst ZnS on the rate of hydrogen production in photocatalytic reactor. The photocatalytic hydrogen production rate is observed to increase from 0.28 to 0.4 $\mu\text{g/s}$ with an increase in the mass or concentration of ZnS from 2 to 4 g or 0.013 to 0.027 g/mL at constant solar light intensity of 450 W/m^2 and constant mass or concentration of CuCl of 7.5 g or 0.05 g/mL. Increasing mass or concentration of ZnS in catholyte solution helps in increasing the photocatalytic hydrogen production rate because the extra availability of ZnS helps in a faster reaction between hole scavenger and photocatalyst to generate electrons at a faster rate to facilitate higher photocatalytic hydrogen production rate.

The effects of an increase in solar light intensity and mass of CuCl on the photocatalytic hydrogen production rate at mass or concentration of ZnS of 2 g or 0.013 g/mL is shown

in Fig. 6.21. The effects of an increase in solar light intensity and mass or concentration of CuCl on the photocatalytic hydrogen production rate at mass or concentration of ZnS of 3 g or 0.020 g/mL is shown in Fig. 6.22.

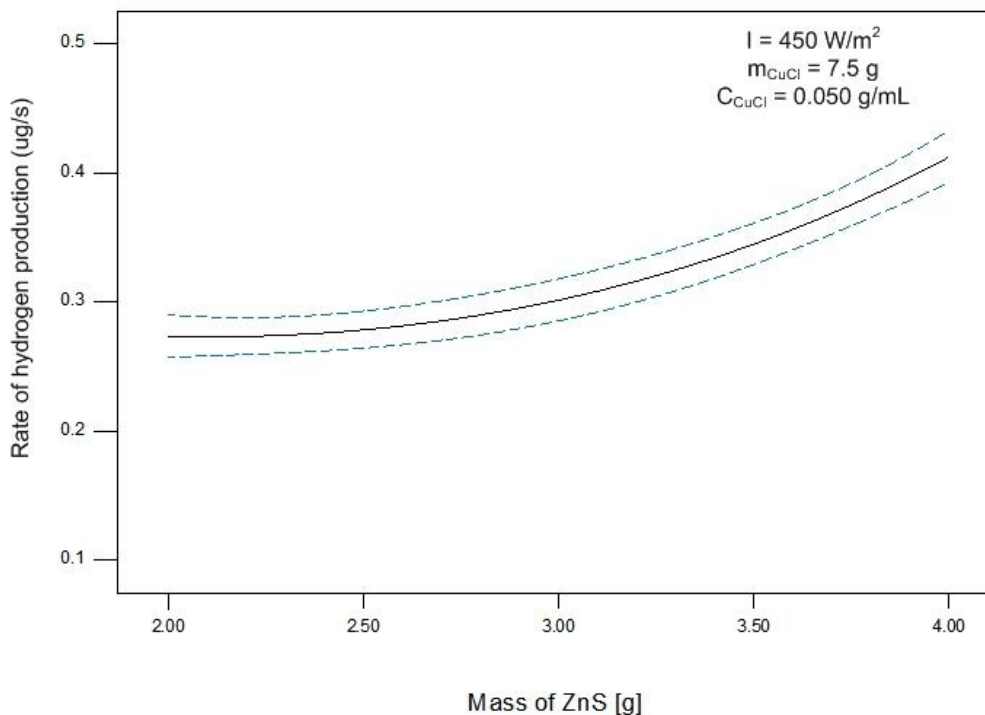


Fig. 6.20. Effects of mass of ZnS on photocatalytic hydrogen production rate.

The effects of an increase in solar light intensity and mass of CuCl on the photocatalytic hydrogen production rate at mass or concentration of ZnS of 4 g or 0.027 g/mL is shown in Fig. 6.23. The photocatalytic hydrogen production rate is observed to be varying from 0.21 $\mu\text{g/s}$ to 0.50 $\mu\text{g/s}$ with an increase in solar light intensity, mass or concentration of CuCl and mass or concentration of ZnS from 400 W/m^2 to 500 W/m^2 , 5 g to 10 g or 0.033 g/mL to 0.066 g/mL and 2 g to 4 g or 0.013 g/mL to 0.027 g/mL, respectively. The hydrogen production rate is observed to increase with an increase in solar light intensity because a higher solar light intensity means a higher amount of photons enter the photocatalytic cell, which help in generating relatively higher overpotential for the breaking of water molecule into hydrogen and oxygen. An increase in the mass or concentration of CuCl helps in increasing the hydrogen production rate because with an increase in mass or concentration, more hydrochloric acid molecules are broken to produce hydrogen ions and copper chloride. An increase in the hydrogen production rate

with an increase in the mass or concentration of ZnS is observed because in the present research ZnS is used as a photocatalyst in the catholyte compartment of the reactor. An increase in the use of photocatalyst helps in increasing the hydrogen production rate as it facilitates the photocatalytic hydrogen production process by generating additional electrons in the reactor to produce extra hydrogen by splitting water into hydrogen and oxygen.

The effects of an increase in the mass of CuCl and the mass of ZnS on the photocatalytic hydrogen production rate for solar light intensity of 400 W/m^2 is shown in Fig. 6.24. The effects of an increase in the mass of CuCl and the mass of ZnS on the photocatalytic hydrogen production rate for solar light intensity of 450 W/m^2 is shown in Fig. 6.25.

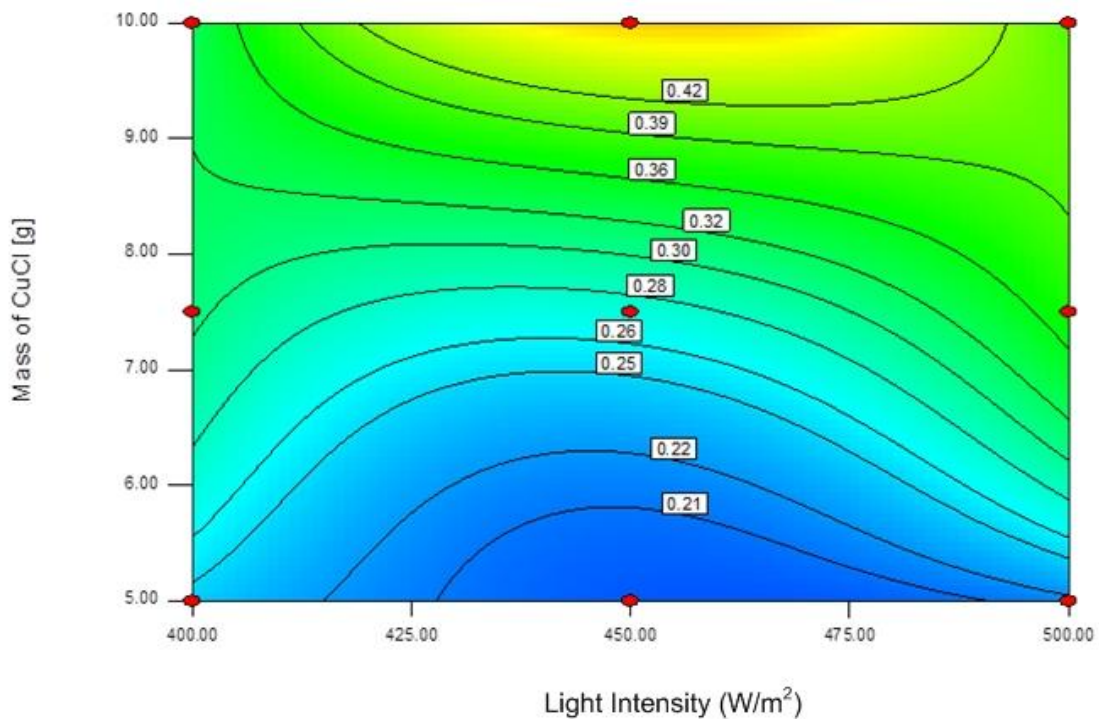


Fig. 6.21. Effects of solar light intensity and mass of CuCl on photocatalytic hydrogen production rate at mass or concentration of ZnS of 2 g or 0.013 g/mL.

The effects of an increase in the mass of CuCl and the mass of ZnS on photocatalytic hydrogen production rate for solar light intensity of 500 W/m^2 is shown in Fig. 6.26. The photocatalytic hydrogen production rate is observed to be varying from $0.21 \mu\text{g/s}$ to $0.49 \mu\text{g/s}$ with an increase in the mass or concentration of CuCl and the mass or concentration

of ZnS from 5 g to 10 g or 0.033 g/mL to 0.066 g/mL and 2 g to 4 g or 0.013 g/mL to 0.027 g/mL, respectively.

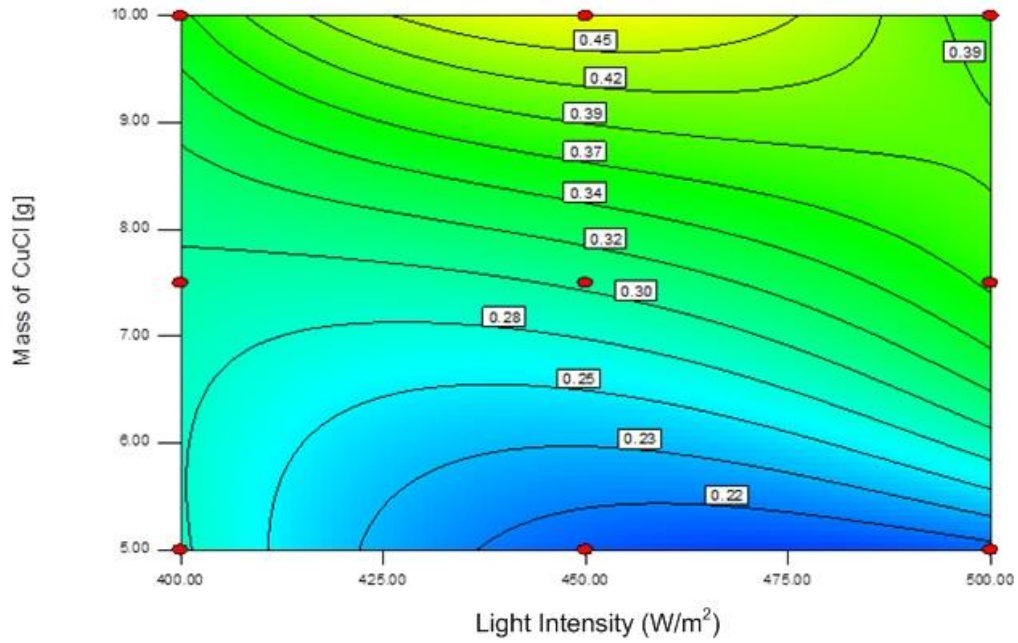


Fig. 6.22. Effects of solar light intensity and mass of CuCl on photocatalytic hydrogen production rate at mass or concentration of ZnS of 3 g or 0.020 g/mL.

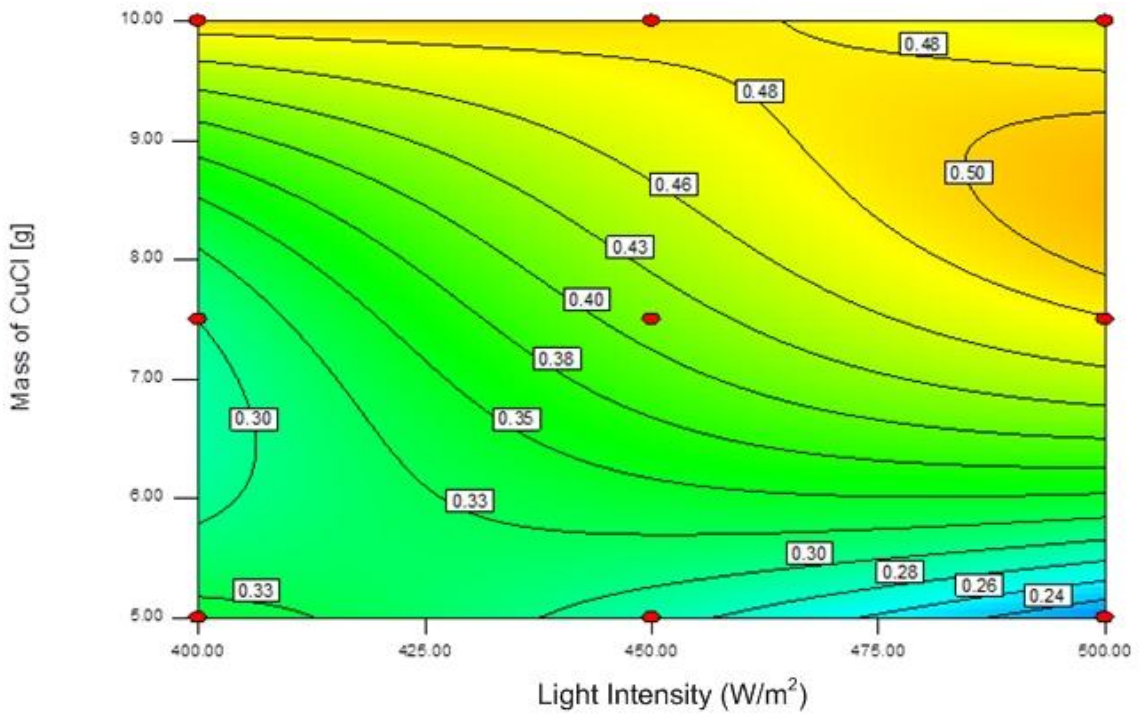


Fig. 6.23. Effects of solar light intensity and mass of CuCl on photocatalytic hydrogen production rate at mass or concentration of ZnS of 4 g or 0.027 g/mL.

The hydrogen production rate is observed to be increasing with an increase in the mass or concentration of CuCl because an increase in the mass or concentration of CuCl helps in increasing the hydrogen production rate due to chemical kinetics in which an increase in the mass or concentration of CuCl results in faster breaking of hydrochloric acid molecules to produce hydrogen ions and copper chloride. The increase in the hydrogen production rate with increase in the use of photocatalyst is observed because this increase helps in facilitating the photocatalytic hydrogen production process by generating additional electrons with the help of hole scavenger in the reactor to produce extra hydrogen by splitting water into hydrogen and oxygen.

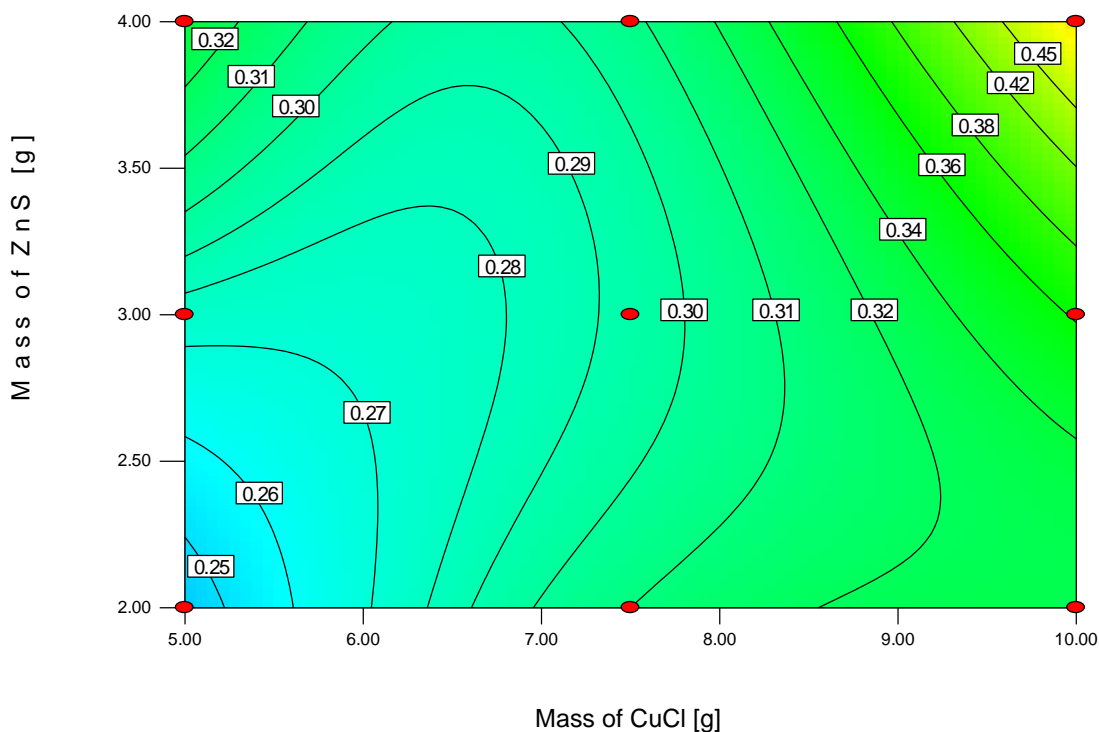


Fig. 6.24. Effects of mass of CuCl and mass of ZnS on photocatalytic hydrogen production rate at solar light intensity of 400 W/m^2 .

Figure 6.27 displays the effects of solar light intensity and mass of ZnS on photocatalytic hydrogen production rate. The rate of hydrogen production is noticed to be varying from $0.28 \mu\text{g/s}$ to $0.48 \mu\text{g/s}$ with an increase in solar light intensity and mass or concentration of ZnS from 400 W/m^2 to 500 W/m^2 and 2 g to 4 g or 0.013 g/mL to 0.027 g/mL , respectively.

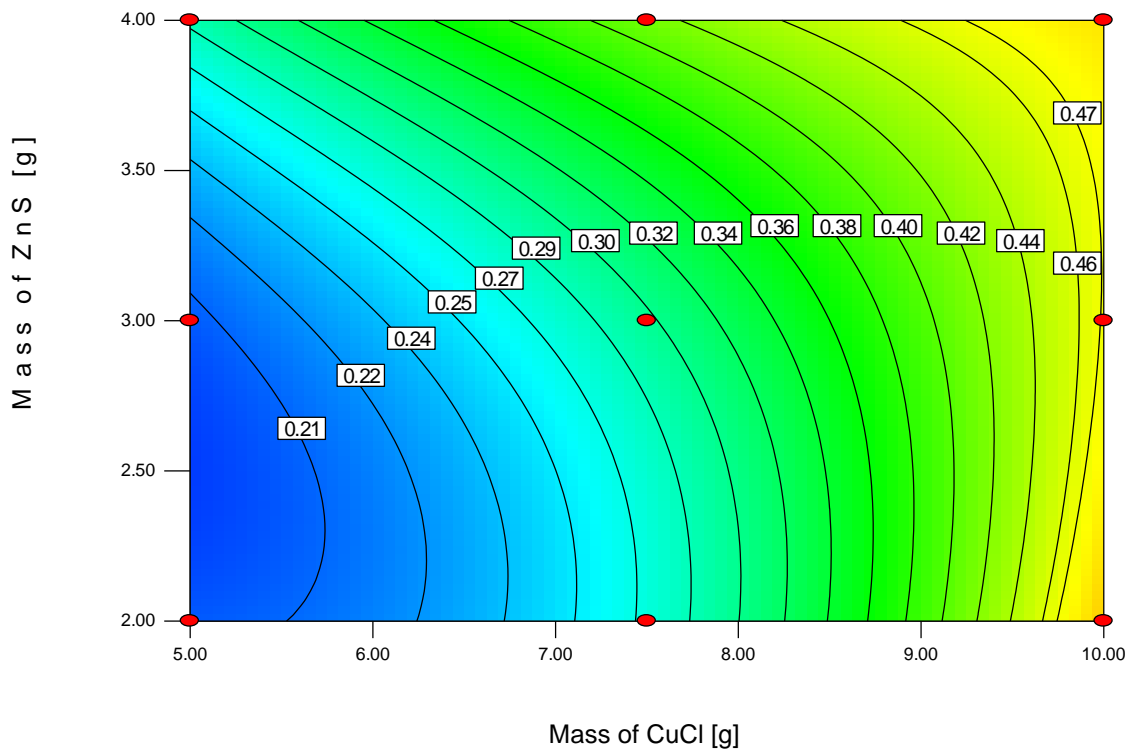


Fig. 6.25. Effects of mass of CuCl and mass of ZnS on photocatalytic hydrogen production rate at solar light intensity of 450 W/m².

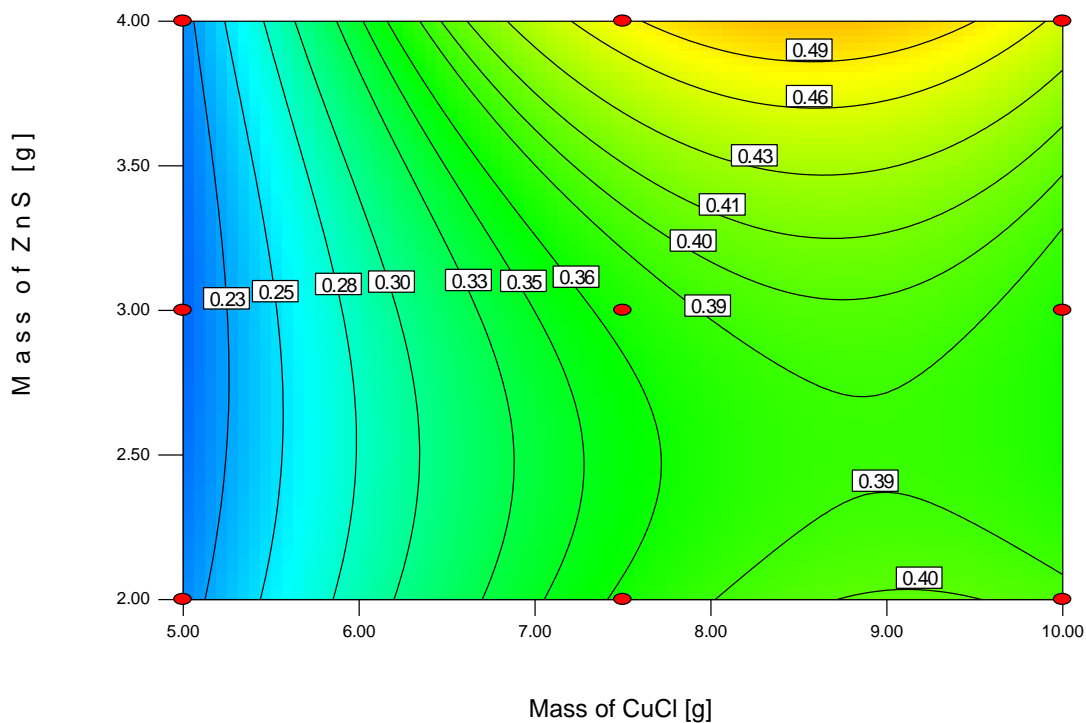


Fig. 6.26. Effects of mass of CuCl and mass of ZnS on photocatalytic hydrogen production rate at solar light intensity of 500 W/m².

The increase in solar light intensity for a specific mass or concentration of ZnS helps in the provision of extra photons to the solution which helps in faster breaking of water molecule and as a result the hydrogen production rate increases. However, an increase in the presence of photocatalyst such as ZnS in a solution for a specific solar light intensity helps in the provision of extra atoms to the hole scavenger such as Na₂S to react with it in order to generate additional electrons. These additional electrons then combine with water molecules to break their internal bonding in order to produce hydrogen at a faster rate.

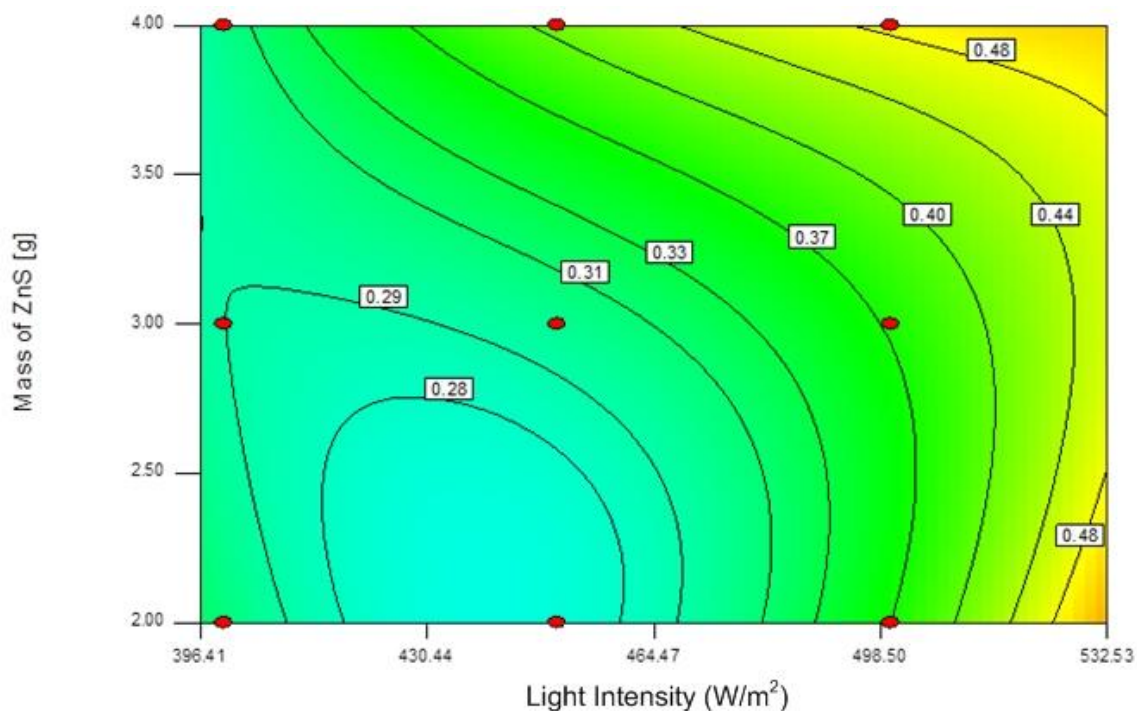


Fig. 6.27. Effects of solar light intensity and mass of ZnS on photocatalytic hydrogen production rate.

The effects of adding titanium dioxide in anolyte solution on the partial pressure of hydrogen developed in the hybrid reactor is shown in Fig. 6.28. It is observed that when titanium dioxide in amounts of 0.5 g is added to the anolyte solution, the partial pressure of hydrogen increases as compared to when no titanium dioxide is added to the anolyte solution. The experiment, involving titanium dioxide as a photocatalyst in the anolyte solution, is carried out at the solar light intensity of 400 W/m² with anolyte having 150 mL of 11 M hydrochloric acid and 5 g of CuCl while catholyte is made of 2 g ZnS, 5 g

sodium hydroxide and 33 g sodium sulfide in 150 mL de-ionized water. Figure 6.29 shows the effects of addition of titanium dioxide in the anolyte solution on hydrogen production. Higher hydrogen production is observed when titanium dioxide in amount of 0.5 g is added to the anolyte solution as compared to zero titanium dioxide in the anolyte solution. Such a trend is observed because when solar light is induced on titanium dioxide which is a photocatalyst, it releases electrons which help in breaking of hydrochloric acid molecules into hydrogen ions and chloride ions. The photocatalyst property of titanium dioxide thus helps in generating additional hydrogen. This experiment shows that titanium dioxide has the capability of decreasing the dependence of the hybrid photocatalytic hydrogen production reactor of the Cu-Cl cycle on external power.

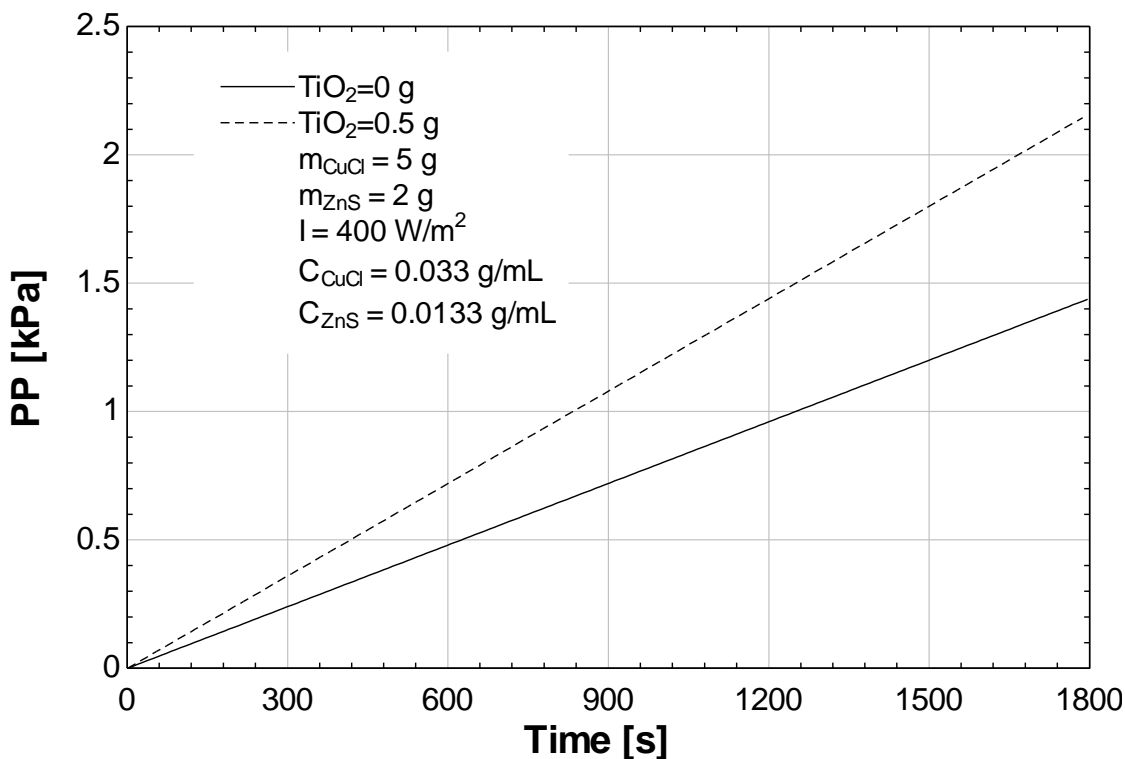


Fig. 6.28. Effects of titanium dioxide on partial pressure of hydrogen.

An experiment is also performed to find the relationship between the mass of titanium dioxide added to the anolyte compartment and voltage generated by the titanium dioxide photocatalyst and relationship between mass of CuCl and electrical conductivity of anolyte solution as shows in Fig. 6.30. In this experiment, the mass of titanium dioxide

was varied from 0.5 to 1.5 g in three intervals. Three sets of experiments were performed and the voltage values shown in the figure below represent the average value obtained from the experiment. The electrical conductivity of anolyte solution is observed to be decreasing with an increase in the mass of CuCl. Such behavior is observed because an increase in the presence of CuCl in the anolyte solution results in a higher voltage drop in the anolyte solution because of higher electrical resistance caused by the solution.

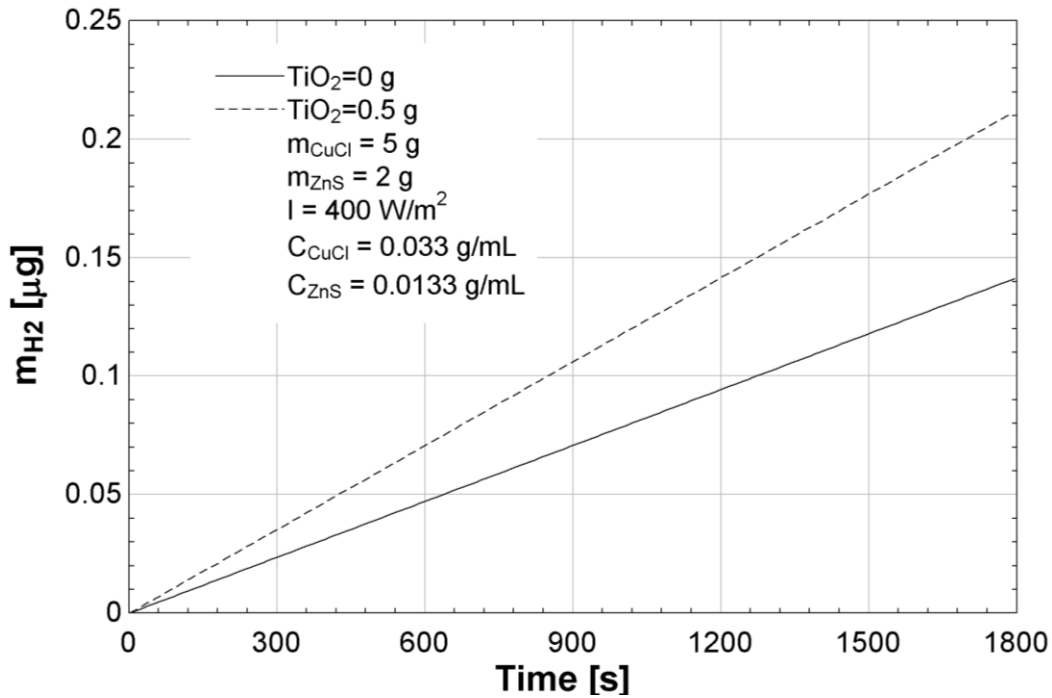


Fig. 6.29. Effects of titanium dioxide on hydrogen production.

6.3 Results of Hybrid Photocatalytic Hydrogen Production Reactor

In this section of the report, results obtained from electrochemical and thermodynamic analyses of the hybrid photocatalytic reactor are presented. The equations used during the modeling are presented in details in the earlier chapters. The parameters varied during this study are current density, temperature of the reactor, concentration of CuCl and ambient temperature.

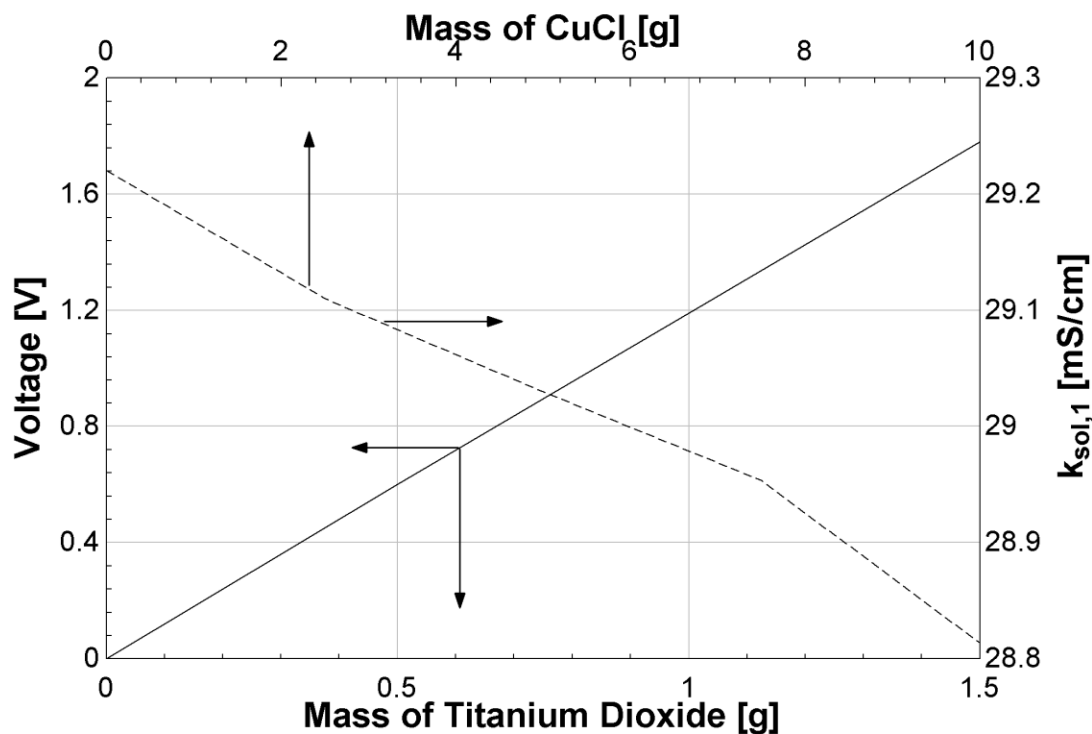


Fig. 6.30. Effects of mass of titanium dioxide on voltage and mass of CuCl on electrical conductivity of anolyte solution.

The current density plays an important role in the determination of the overall energy required by the system to produce the desired output. The effects of current density on the overall voltage required and voltage drop in anolyte solution (sol 1), catholyte solution (sol 2), anode, cathode and cation exchange membrane is presented in Fig. 6.31. The total voltage required by the system is observed to increase from 2.58 to 3.26 V with an increase in current density from 0.5 to 1.5 A/cm². The voltage drop across anolyte solution (sol 1), catholyte solution (sol 2), anode, cathode and cation exchange membrane is found to be increasing from 0.005 V to 0.016 V, 0.004 V to 0.013 V, 1.67 V to 2.168 V, 0.18 V to 0.22 V and 0.06 V to 0.19 V, respectively with an increase in current density. Such behavior is noticed because current density is related to the reaction kinetics and it acts as a driving force for the reaction. In an electrolytic cell the energy required by the overpotential is of greater quantity as compared to the thermodynamic potential to drive a reaction. The overpotential refers to the voltage difference between the half-reaction's reduction potential determined thermodynamically and the potential at which reduction and oxidation (red-ox) reaction occurs. The relationship between current

density and voltage can also be explained as the relationship between the temperature difference and heat transfer rate. In heat transfer problems, an increase in temperature difference results in a higher heat transfer rate because the temperature difference acts as a driving force. Considering the principle of heat transfer rate, an increase in the current density results in a higher voltage requirement in electrochemical processes.

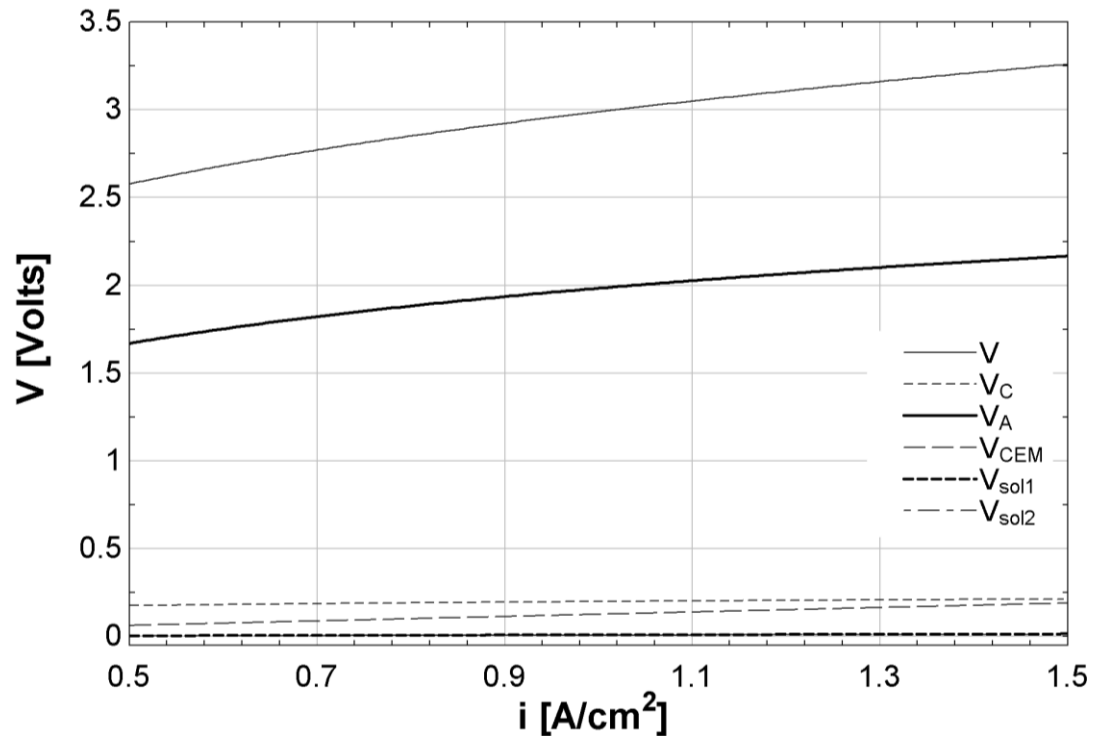


Fig. 6.31. Effects of current density on voltage requirement.

It is also noticed that the anode results in the largest voltage drop across the system because in the present experiment graphite is used as an anode due to its high resistivity to the corrosion but at the cost of very low electrical conductivity. The effects of current density on hydrogen production rate and the cost of hydrogen is displayed in Fig. 6.32. The hydrogen production rate is observed to increase from 0.68 to 2.1 L/s with an increase in current density from 0.5 to 1.5 A/cm^2 . The hydrogen production cost decreases from 6.8 to 2.3 C\$/kg with an increase in current density. Such a trend is seen because an increase in current density results in higher overpotential available to the process which in turn results in a much faster breaking of water molecule in hydrogen and oxygen as compared to the lower current density. This increase in overpotential also

impacts the cost of hydrogen production which is observed to be decreasing with an increase in current density. These phenomena are observed because an increase in current density results in a higher hydrogen production rate which in turns helps to reduce the production cost of hydrogen because from the same setup with a little extra energy input more hydrogen can be produced and sold in the market.

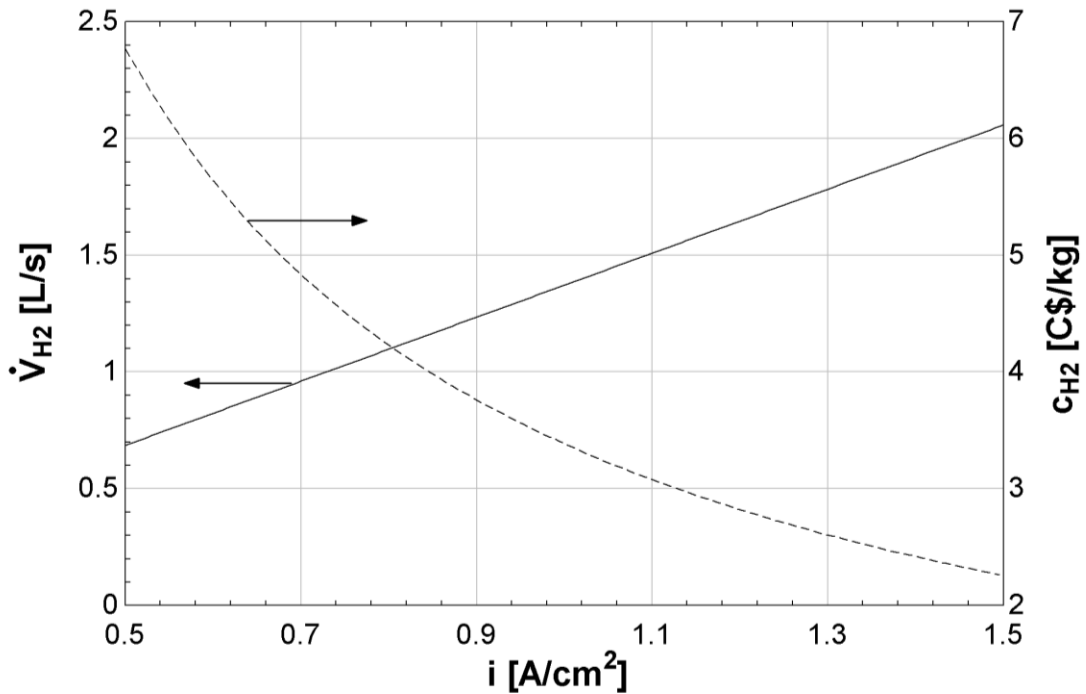


Fig. 6.32. Effects of current density on hydrogen production rate and cost of hydrogen production.

The effects of an increase in current density on energy and exergy efficiencies are displayed in Fig. 6.33. The energy and exergy efficiencies are observed to be decreasing from 5.74 to 4.54% and 5.11 to 4.04%, respectively with an increase in current density from 0.5 to 1.5 A/cm^2 . This trend is seen because an increase in current density results in a higher energy requirement of the system. The energy and exergy efficiency analyses show that despite an increase in current density has a positive effect on hydrogen production rate and the cost of hydrogen production, it fails to better utilize the energy supplied to the system. Another trend observed in efficiency analysis is that exergy efficiency is lower than energy efficiency. This difference between energy and exergy efficiencies is due to the fact that exergy analysis takes into consideration losses taking

place in the system due to friction and heat transfer; whereas, energy analysis does not take in consideration the losses which pushes energy efficiency above exergy efficiency. The energy and exergy efficiencies analyses demonstrate the importance of performing efficiency analysis because an increase in the desired output with an increase in the required input does not necessarily result in enhanced performance of the system.

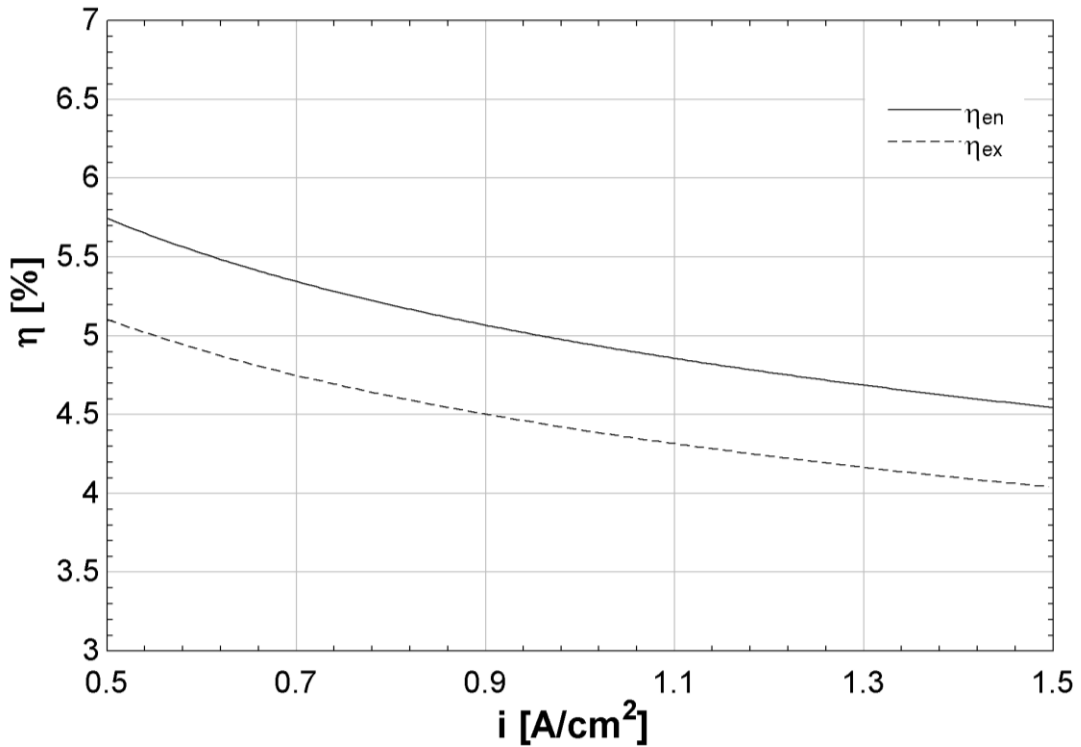


Fig. 6.33. Effects of current density on energy and exergy efficiencies.

The effects of reactor temperature on rate of hydrogen production and hydrogen production cost are presented in Fig. 6.34. The hydrogen production rate and cost of production is observed to increase from 1.28 to 1.47 L/s and 3.28 to 3.36 C\$/kg, respectively with a rise in reactor temperature from 290 to 340 K. This increasing behavior of the hydrogen production rate is observed because an increase in reactor temperature increases the vibration of molecules in the solution and also makes the system comparably unstable for the reactor working on low temperature. The rise in temperature can also be seen as an energy being provided to the system in the form of heat, which boosts the hydrogen production rate. The cost rate of hydrogen production is observed to increase with a rise in reactor temperature because of the rise in the energy

cost of the system. As the amount of energy supplied to the system increases, the cost required to run the system increases too.

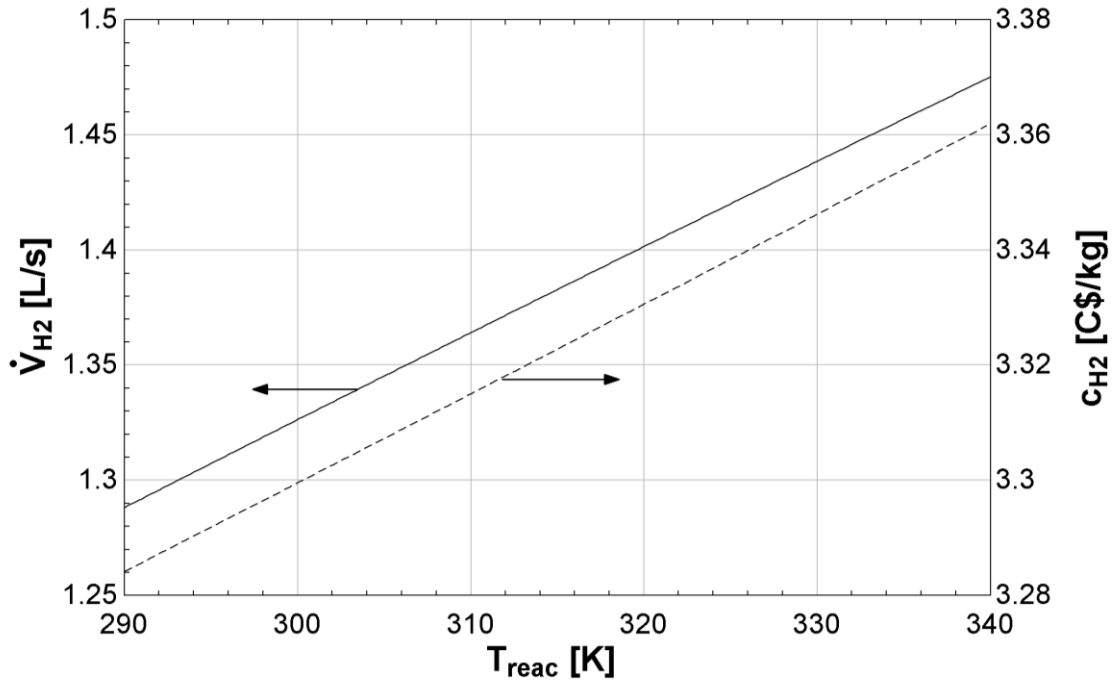


Fig. 6.34. Effects of reactor temperature on hydrogen production rate and cost of hydrogen production.

The effects of reactor temperature on energy and exergy efficiencies of the hybrid reactor are displayed in Fig. 6.35. The exergy efficiency of the reactor is observed to increase from 3.78 to 5.22% with a rise in reactor temperature. However, the energy efficiency of the system remains approximately constant at 4.94%. The exergy efficiency of the system is observed to increase because an increase in reactor temperature results in a higher hydrogen production rate and less exergy loss due to heat transfer from the reactor surface. The rise in reactor temperature has a negligible effect on energy efficiency because the current supplied to the systems dominates the definition of the energy efficiency; whereas, in exergy efficiency, the reactor temperature greatly affects the physical exergy of hydrogen and therefore changes the exergy efficiency with a change in reactor temperature. The effects of concentration of CuCl on hydrogen production rate and the cost of hydrogen production is presented in Fig. 6.36. The hydrogen production

rate is observed to decrease from 1.39 to 1.36 L/s with an increase in the concentration of CuCl from 0.1 to 1 mol/L.

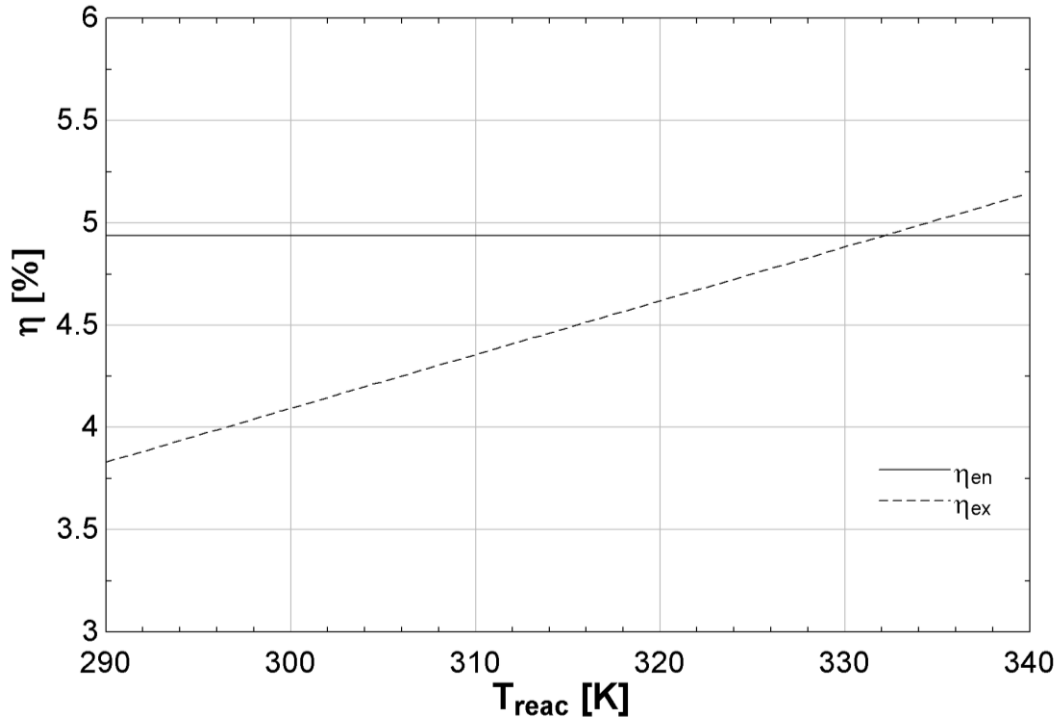


Fig. 6.35. Effects of reactor temperature on energy and exergy efficiencies.

The cost of hydrogen production is observed to increase from 3.25 to 3.75 C\$/kg with an increase in the concentration of CuCl. The decrease in the hydrogen production rate with an increase in the concentration of CuCl is observed because in an anolyte solution hydrochloric acid is responsible for supplying hydrogen ions, which pass through the membrane to the catholyte solution to form hydrogen. For a given concentration of hydrochloric acid in the solution a certain amount of CuCl can be added to ensure that the right amount of hydrochloric acid is converted to the CuCl (II). The provision of additional amount of CuCl than what is required by the system may result in clogging of the membrane, as extra CuCl provided cannot react with the hydrochloric acid present in the solution. This clogging at the membrane results in lower transportation of hydrogen ions from anolyte solution to the catholyte solution and as a result the hydrogen production rate decreases. The cost of hydrogen production is observed to increase because an increase in the concentration of CuCl brings with it the acquiring cost of the chemical and as a result running cost of the reactor increases. This increase in the running

cost at the expense of no extra production of hydrogen results in higher hydrogen production costs.

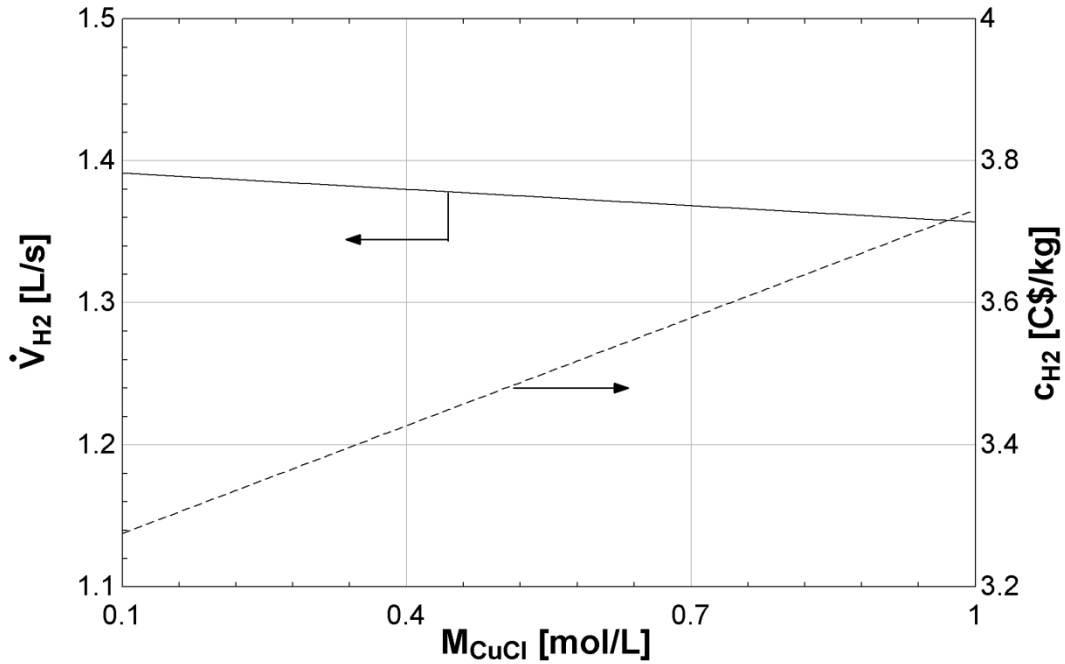


Fig. 6.36. Effects of concentration of CuCl on hydrogen production rate and cost of hydrogen production.

The variation in ambient temperature plays an important role in determining the performance of the system, especially for systems dependent on the temperature of the process. The effects of ambient temperature on energy and exergy efficiencies of the hybrid hydrogen production reactor are presented in Fig. 6.37. The energy efficiency is observed to remain constant at 4.94% with a rise in ambient temperature from 280 to 320 K. The exergy efficiency decreases from 5.25 to 3.9% with a rise in ambient temperature. The energy efficiency remains constant because energy analysis does not consider the losses occurring due to heat transfer and frictional losses in the system, which acts as a major flaw in the analysis of a system. The introduction of exergy analysis corrected this flaw by including exergy loss terms due to temperature differences and physical characteristics of the fluid. The exergy efficiency decreases with a rise in ambient temperature because of the larger temperature difference between the system boundary and the surroundings. Since temperature difference is the driving force of heat transfer, a higher rate of heat is lost from the system boundary to the surroundings.

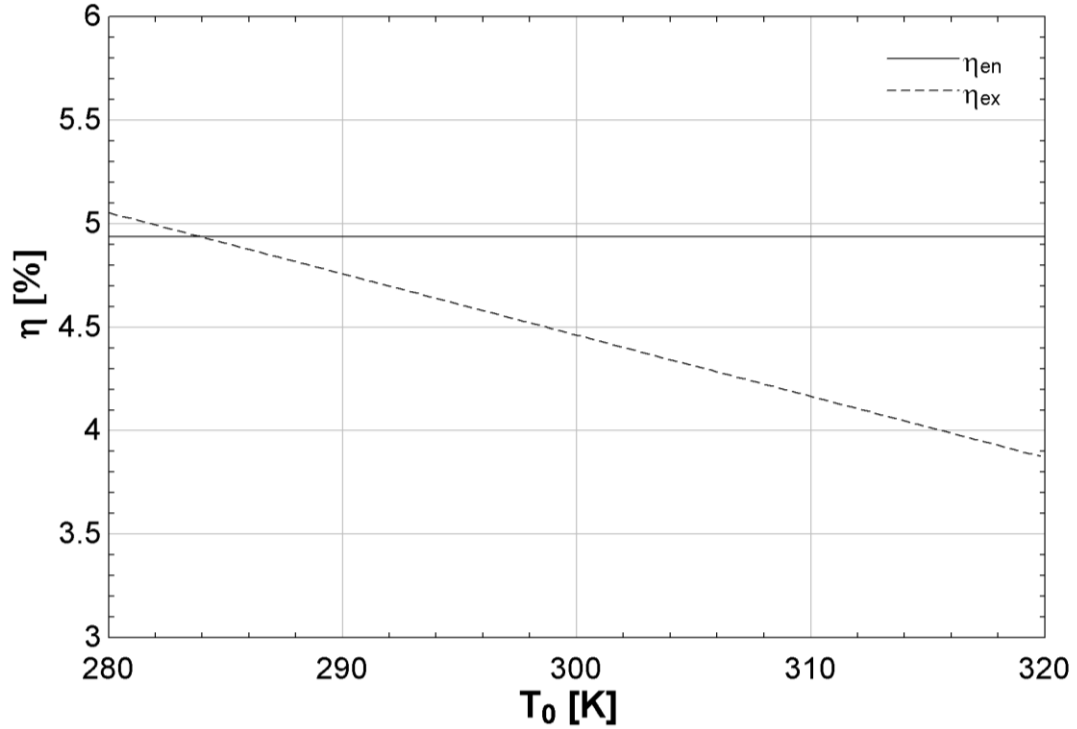


Fig. 6.37. Effects of ambient temperature on energy and exergy efficiencies.

The distance of electrodes from the membrane dictates how much of voltage drop takes place in the anolyte and catholyte solution. The effects of electrode's distance from the membrane on hydrogen production rate and the cost of hydrogen production is displayed in Fig. 6.38. The hydrogen production rate is observed to be decreasing from 1.42 to 1.31 L/s with an increase in the distance between electrode and membrane from 10 to 60 mm. The cost of hydrogen production is observed to be increasing from 3.26 to 3.55 C\$/kg with an increase in the distance from the electrode to the membrane. The decreasing behavior of hydrogen production is observed because increasing the distance of electrodes from the membrane results in a higher potential drop in the solution as electrons have to travel a longer distance to reach the membrane surface to create the necessary overpotential for the system to work. The hydrogen production cost increases because increasing the distance between the electrode and membrane results in higher energy requirements by the reactor to produce the desired amount of hydrogen. As the energy requirement of the reactor increases, the cost associated with the energy increases and as a result the hydrogen production cost increases.

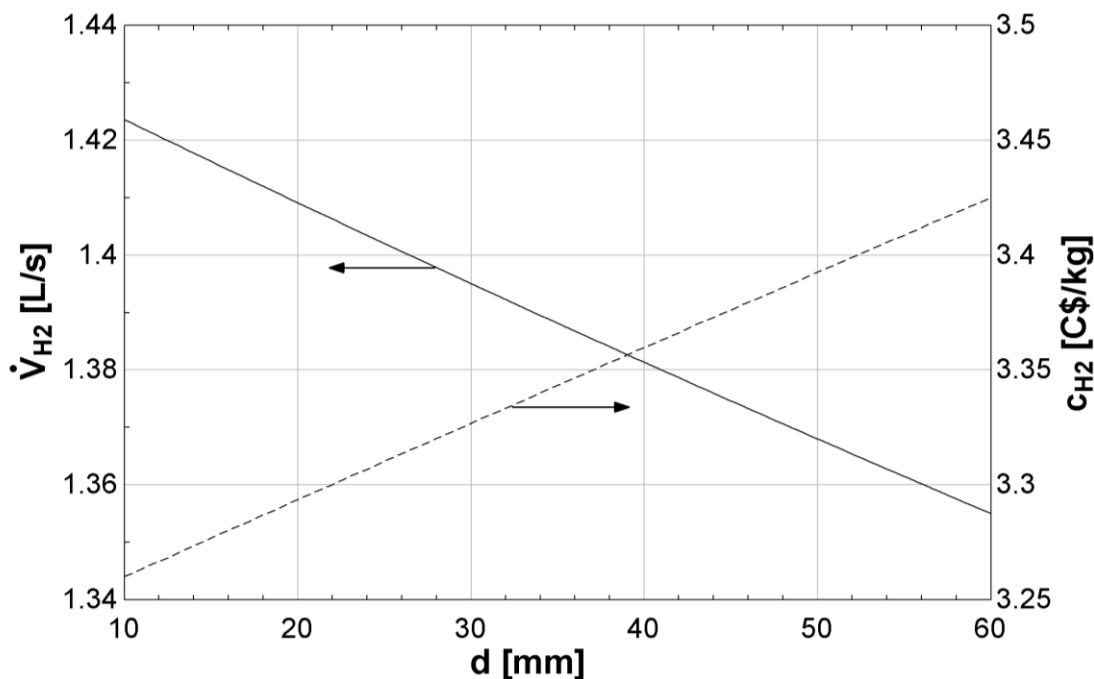


Fig. 6.38. Effects of electrode distance on hydrogen production rate and cost of hydrogen production.

A scale-up hydrogen production rate and cost analyses of the hybrid photocatalytic reactor is also carried out to make it suitable for integration with the solar based integrated systems studied in a later section. Figure 6.39 exhibits the effects of a rise in reactor temperature on the scale-up hydrogen production rate and cost of hydrogen production. The scale up hydrogen production rate and cost of hydrogen production increase from 113 to 117.5 L/s and 3.29 to 3.36 C\$/kg, respectively with rise in reactor temperature from 290 K to 340 K. The results obtained from the scale-up analysis are further utilized to enhance the performance of the solar assisted integrated hydrogen production systems studied in the next section. The concept of photocatalytic reactor tested during the experimental phase is used in the second part of the study to recover the reflected solar light intensity from the central receiver of the heliostat field. A cathode half-cell using ZnS catalyst is utilized in the second integrated system to produce additional hydrogen to further enhance the performance of the overall system.

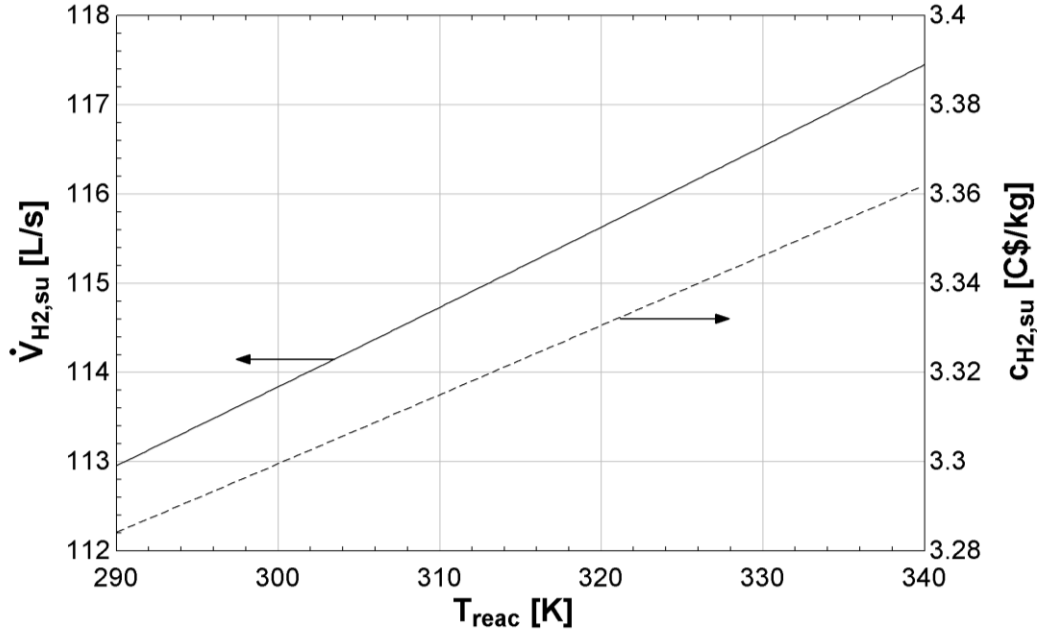


Fig. 6.39. Effects of reactor temperature on scale up hydrogen production rate and cost of hydrogen production.

6.4 Results of Integrated Systems

In this section of the report, the results of the energy and exergy analyses of the two integrated systems are discussed in details. Two integrated systems namely (a) solar heliostat field system integrated with Cu-Cl cycle and Kalina cycle (system 1) and (b) solar heliostat field system integrated with Cu-Cl cycle, Kalina cycle and photocatalytic reactor are considered in this study. The energy and exergy based results of both systems are compared to show the effects of further integration on the overall performance of the system. The parameters varied during the study are solar light intensity (600 to 1200 W/m^2), view factor (0.5 to 0.9), mass fraction of HCl (0.7 to 0.9), mass flow rate of ZnS (0.45 to 0.7 kg/s), inlet temperature of molten salt (550 to 700 K), electrolyzer pressure (100 to 1000 kPa), concentration ratio (300 to 1500) and ambient temperature (290 to 330 K). The operating range of solar light intensity is selected such that the results provided in this study can be used almost throughout the world as it can cater the need of the countries having low average solar light intensity such as Pakistan ($\sim 600 \text{ W}/\text{m}^2$) and the countries having high average solar light intensity ($\sim 1050 \text{ W}/\text{m}^2$) [128]. The operating ranges of view factor and concentration ratio are chosen based on the study conducted by Xu et al. [126]. The working ranges of mass fraction of HCl, mass flow rate of ZnS,

molten salt inlet temperature and electrolyzer pressure are selected based on the private communication [129].

It is aimed to ensure that the integrated system developed is correct as the results of individual systems were compared with data available in the literature. The heliostat field is modeled on the basis of the system studied by Xu et al. [126]. The energy efficiency of the heliostat field obtained in the present study is 80% as compared to 75% obtained by Xu et al. [126], which confirms that the present model is fairly accurate. The Kalina cycle is validated by comparing results with data presented by Bombarda et al. [132]. The predicted efficiency is calculated to be 19% as compared to 19.7% reported by Bombarda et al. [132]. The predictions of the Cu-Cl cycle are validated by comparing results with the data provided by Lewis et al. [50] and Zamfirescu et al. [133]. The predicted efficiency in this study is found to be 52% as compared to 55% reported by Lewis et al. [50] and Zamfirescu et al. [133].

In an integrated solar system, studying the effects of fluctuation in solar light intensity on the performance of the overall system is very important as solar light intensity is not constant throughout the day. The effects of a rise in solar light intensity on the rate of hydrogen production by system 1, photocatalytic reactor and system 2 are presented in Fig. 6.40. The rate of hydrogen produced by system 1, photocatalytic reactor and system 2 is found to increase from 126.9 to 289.4 L/s, 27.14 to 54.5 L/s and 154.1 to 343.9 L/s, respectively with a rise in solar light intensity from 600 to 1200 W/m². Such behavior is observed because a rise in solar light intensity results in a higher amount of light being reflected to the central receiver by the solar heliostats. As the intensity of light received by the central receiver increases, the heat generation capacity of the central receiver increases. In the present study, molten salt is used as a working fluid in solar heliostat system. Molten salt absorbs heat from the solar receiver due to its capabilities of absorbing large temperature ranges. With an increase in the rate of heat transfer by the molten salt solution coming from the central receiver to the Cu-Cl cycle steam supply, the amount of heat supplied to the Cu-Cl cycle increases. The ability of the Cu-Cl cycle to be largely heat dependent helps in recovering the excess heat supplied by the heliostat field system and therefore increases the hydrogen production rate of the system. It is also

noticed that system 2 produces more hydrogen compared to system 1 because in system 2, the solar light intensity reflected by the central receiver is directed to the photocatalytic reactor. The solar light intensity reaching the photocatalytic reactor comes in contact with the ZnS, which is a photocatalyst. The light falling on the photocatalyst generates the necessary potential to break water molecules into hydrogen and oxygen. The hydrogen production capacity of the photocatalytic reactor increases with an increase in the solar light intensity and as a result the overall hydrogen production capacity of system 2 increases. However, the hydrogen production rate should not be the only parameter to consider when comparing the two systems. Also important are the energy and exergy efficiencies of the system. Figure 6.41 shows the effects of variation in solar light intensity on total exergy destructions by systems 1 and 2. The total exergy destruction rate of both systems increases with a rise in solar light intensity. The total exergy destruction rates of systems 1 and 2 increase from 1495 to 3122 kW and 1238 to 2606 kW, respectively, with a rise in solar light intensity from 600 to 1200 W/m². This trend occurs because an increase in solar light intensity delivers additional energy to the surface of the earth, which is later used in the system to generate the required heat for the Cu-Cl cycle. This increase in energy results in additional heat production, which also contributes to the additional exergy destruction in the system. It is also noticed that system 2 displays lower total exergy destruction rate as compared to system 1 because system 2 utilizes reflected solar light from the central receiver of the heliostat field system in the photocatalytic reactor to generate additional hydrogen while using the same amount of energy as system 1.

Figure 6.42 shows the effects of rise in solar light intensity on the energy and exergy efficiencies of the two integrated systems studied. The energy efficiencies of systems 1 and 2 are found to be increasing from 37.42 to 39% and 54.3 to 56.01%, respectively with a rise in solar light intensity. The exergy efficiencies of the systems 1 and 2 are found to be increasing from 45.6 to 47.79% and 54.94 to 56.41%, respectively with a rise in solar light intensity. The increase in energy and exergy efficiencies with a rise in solar light intensity is noticed because with a rise in solar light intensity, the heat production capability of the heliostat system increases due to the higher temperature range which can be handled by the working fluid of the heliostat system.

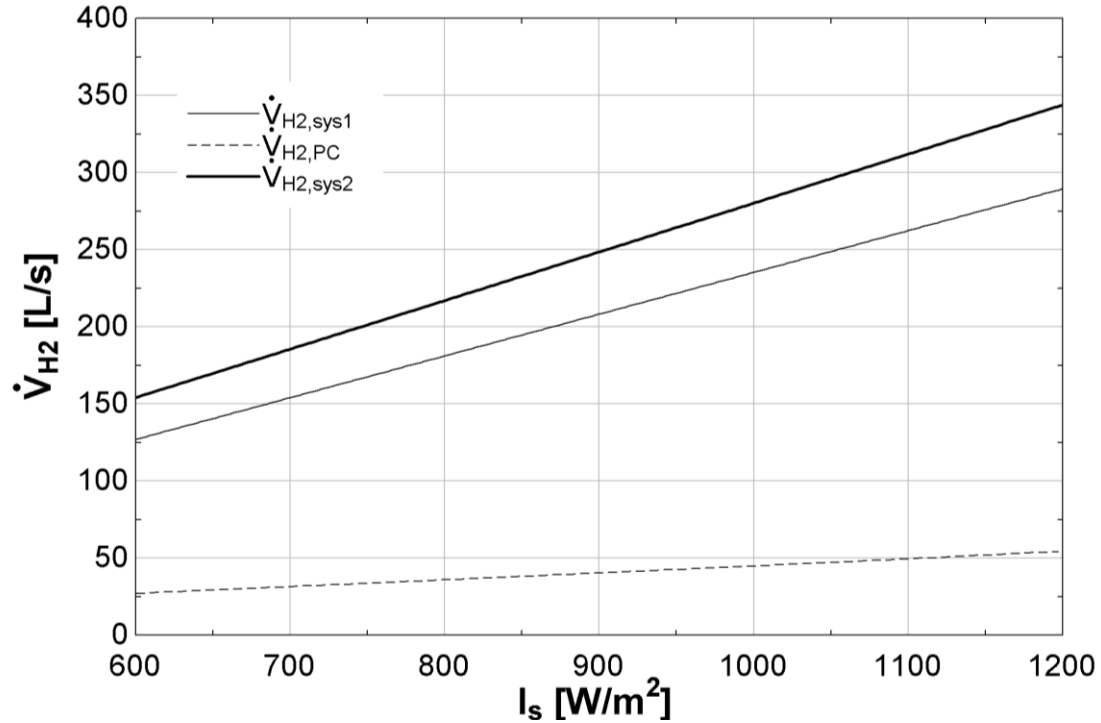


Fig. 6.40. Effects of solar light intensity on hydrogen production rates.

A rise in the solar light intensity also results in a larger amount of solar light being reflected from the central receiver to the photocatalytic reactor. As the heat production capacity of the heliostat system increases, the hydrogen production capacity of both the integrated systems increases. The increase in hydrogen production capacity is then reflected in terms of an increase in energy and exergy efficiencies. It is also noticed that system 2 performs better than system 1 because system 2 recovers the reflected solar light intensity to produce additional hydrogen. This additional hydrogen production from the same energy source results in higher energy and exergy efficiencies.

Studying the impact of view factor on the performance of the integrated system is important because this factor determines how often the solar light intensity is reflected from one surface to another. The effects of view factor on the rates of hydrogen production by systems 1 and 2 are shown in Fig. 6.43. The rates of hydrogen production by systems 1 and 2 decrease from 549.4 to 129 L/s and 577.6 to 179.8 L/s, respectively, with an increase in view factor from 0.5 to 0.9. The rate of hydrogen production by the photocatalytic reactor increases from 28.22 to 50.76 L/s with an increase in view factor.

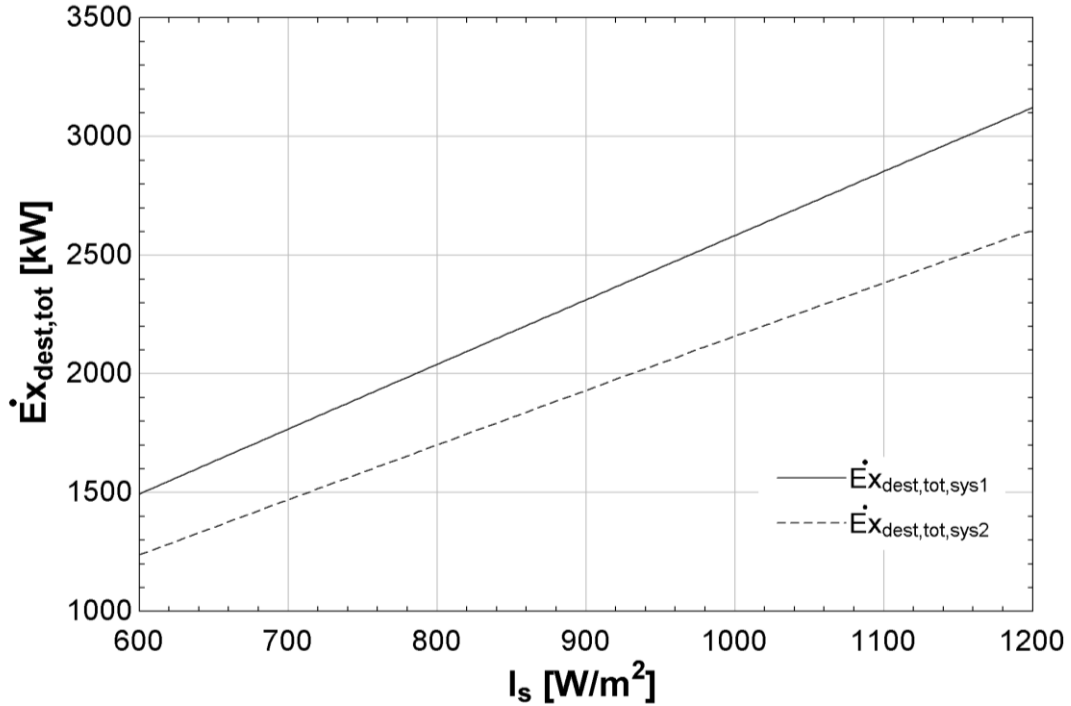


Fig. 6.41. Effects of solar light intensity on total exergy destruction rate.

The decreasing trends of hydrogen production rates of systems 1 and 2 are observed because an increase in view factor results in more solar light intensity being reflected from the surface of the central receiver to the photocatalytic reactor. The increase in reflection from the central receiver results in a lower amount of heat transferred to the working fluid of the heliostat field system. This decrease in heat transfer rate results in a lower rate of heat supplied to the Cu-Cl cycle, which in turn results in a lower amount of hydrogen being produced by the Cu-Cl system.

On the other hand, the increase in reflection of solar light intensity from the central receiver results in a better performance of system 2 as compared to system 1, due to the fact that in system 2 the solar light reflected from the central receiver is directed to the photocatalytic hydrogen production reactor. The reflected solar light is used to produce hydrogen with the help of zinc sulfide based photocatalyst. The additional hydrogen produced by the photocatalytic reactor by harnessing reflected solar light from the central receiver results in a higher rate of hydrogen production from system 2 as compared to system 1.

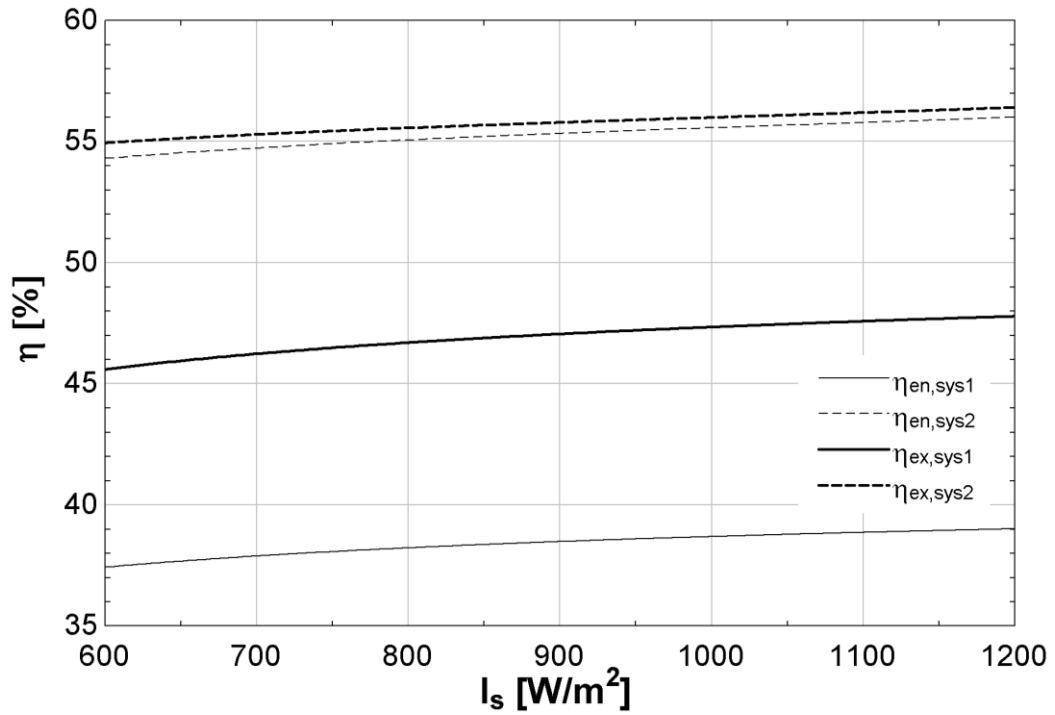


Fig. 6.42. Effects of solar light intensity on energy and exergy efficiencies.

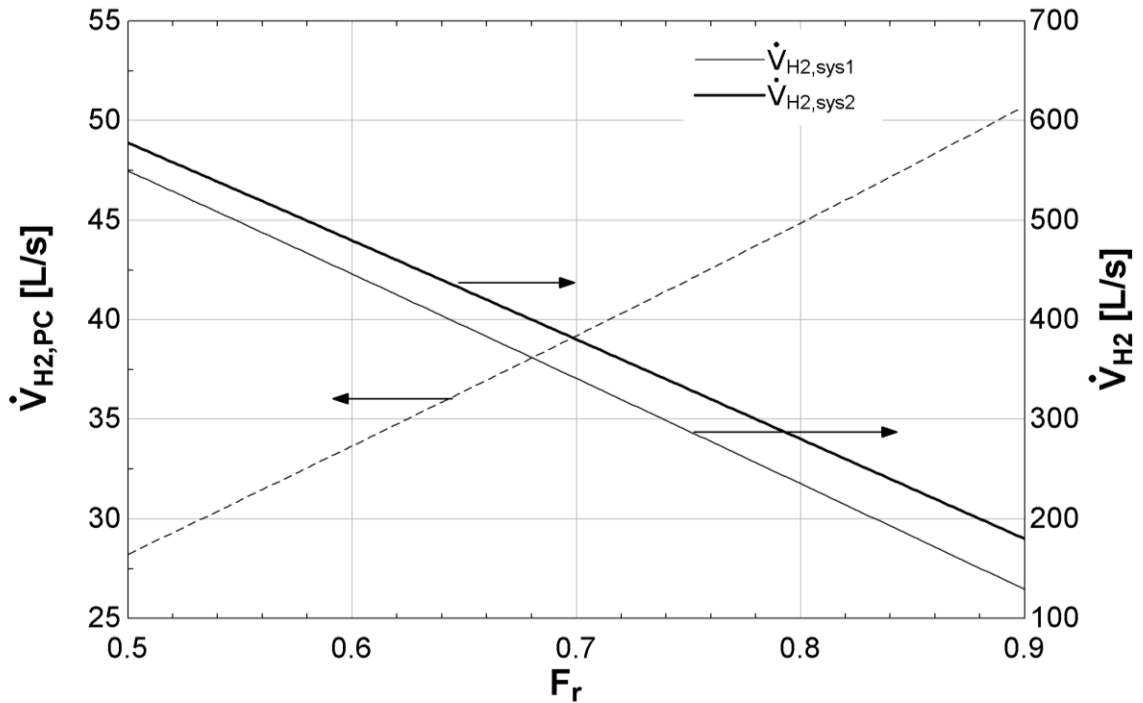


Fig. 6.43. Effects of view factor on hydrogen production rates.

Figure 6.44 shows the effects of an increase in view factor on total exergy destruction rates by systems 1 and 2. The rates of total exergy destruction by both systems decrease

with an increase in the view factor. The rates of total exergy destruction for systems 1 and 2 decrease from 3384 to 2209 kW and 3117 to 1728 kW, respectively, with an increase in view factor from 0.5 to 0.9. Such behavior is noticed because an increase in view factor results in less solar light being absorbed by the central receiver and less thermal exergy losses from the system.

Figure 6.45 displays the effects of an increase in view factor on energy and exergy efficiencies of systems 1 and 2. The energy efficiencies of systems 1 and 2 decrease from 48.5 to 30.71% and 64.4 to 49.11%, respectively, with an increase in view factor. The exergy efficiencies of systems 1 and 2 decrease from 61.57 to 36.57% and 64.61 to 50.37%, respectively, with an increase in view factor. The decreasing trend of energy and exergy efficiencies are observed because an increase in view factor results in less solar light intensity being converted to heat because with an increase in view factor the reflection from the central receiver increases. The energy and exergy efficiencies of system 2 are found to be better than system 1, because system 2 recovers the reflected solar light intensity by running a photocatalytic hydrogen production reactor to generate extra hydrogen in parallel with Cu-Cl cycle.

The effects of variation in the mass fraction of hydrochloric acid at state 11 on the hydrogen production rate by both the integrated systems are presented in Fig. 6.46. The rates of hydrogen production by systems 1 and 2 increase from 230.6 to 240.9 L/s and 275.4 to 285.7 L/s, respectively, with an increase in the mass fraction of hydrochloric acid at state 11 from 0.7 to 0.9. This behavior is noticed because an increase in mass fraction of hydrochloric acid results in higher amounts of availability of hydrogen ions in the solution entering the electrolyzer. As the availability of hydrogen ions entering the electrolyzer increases, the rate of hydrogen production also increases. Figure 6.47 illustrates the effects of an increase in mass fraction of hydrochloric acid at state 11 on energy and exergy efficiencies of the integrated systems studied. The energy efficiencies of the systems 1 and 2 decrease from 40.97 to 36.93% and 59.34 to 52.28%, respectively, with an increase in the mass fraction of hydrochloric acid at state 11. The exergy efficiencies of systems 1 and 2 decrease from 47.91 to 47.53% and 57.16 to 55.71%, respectively, with an increase in the mass fraction of hydrochloric acid at state 11. Such

behavior is observed because the mass fraction of hydrochloric acid plays a vital role during the hydrogen production process in the electrolyzer. The purpose of using hydrochloric acid in the Cu-Cl cycle is to provide hydrogen ions in the electrolyzer, as the mass fraction of hydrochloric acid changes its capability of providing hydrogen ions changes and thus the hydrogen production rate alters.

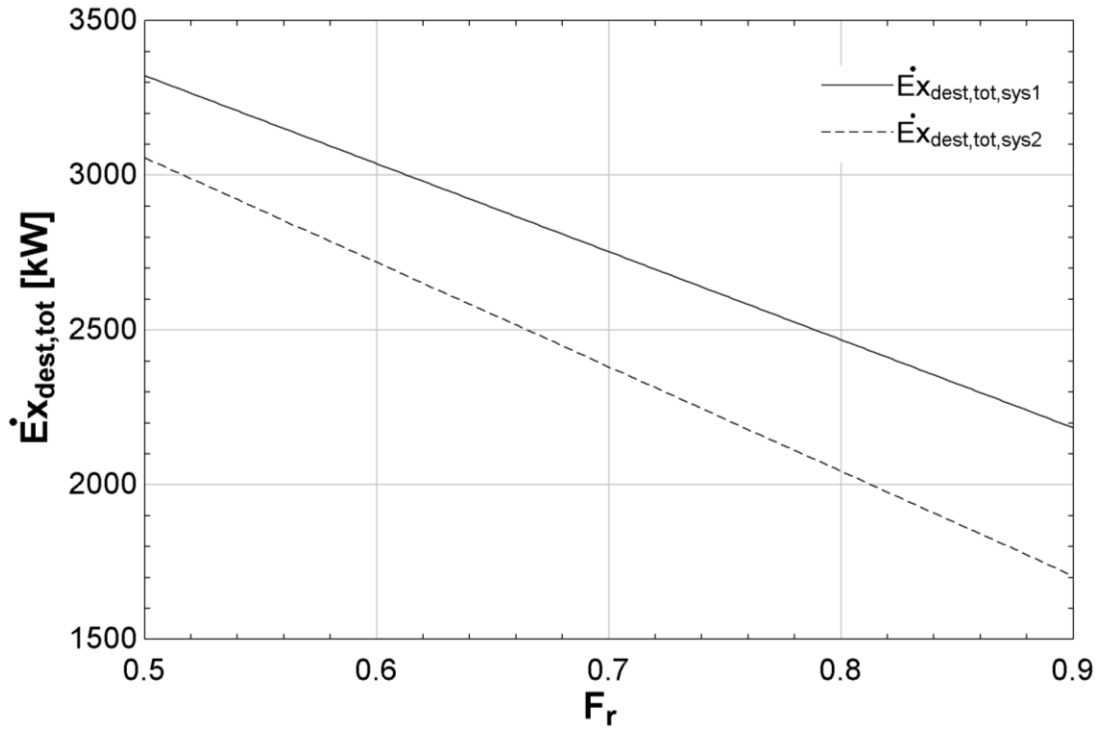


Fig. 6.44. Effects of view factor on total exergy destruction rate.

The energy and exergy efficiencies decrease with an increase in the mass fraction of hydrochloric acid because an increase in the mass fraction of hydrochloric acid results in higher energy requirement from the Cu-Cl cycle, therefore decreasing the overall energy and exergy efficiencies of the system.

The energy and exergy efficiencies of system 2 are observed to be higher than system 1 because system 2 makes use of reflected solar light intensity to generate additional hydrogen by utilizing photocatalytic hydrogen production technique. Although the mass fraction of hydrochloric acid has no effects on the photocatalytic hydrogen production reactor, reflected solar light directed towards the photocatalytic hydrogen production reactor pushes the energy and exergy efficiencies of system 2 above system 1. It is also

important to notice that maintaining enough water in the hydrochloric acid solution is very important as the concentrated hydrochloric acid is very acidic and harmful and may damage the equipment.

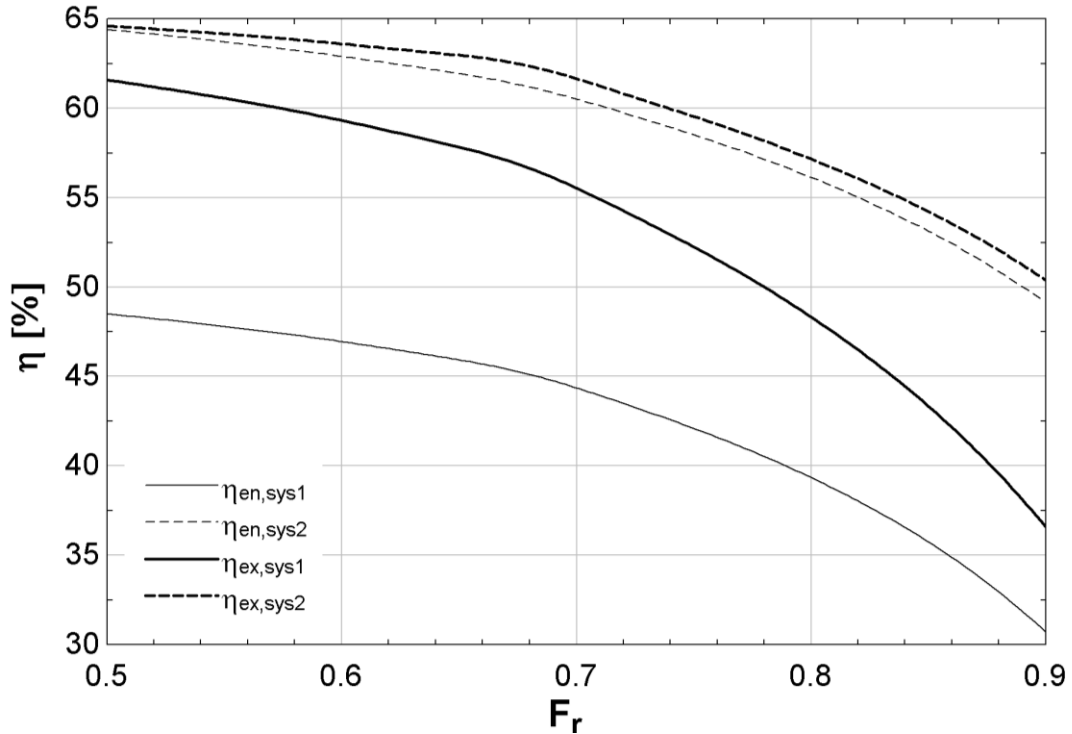


Fig. 6.45. Effects of view factor on energy and exergy efficiencies.

The mass flow rate of zinc sulfide plays an important role in the photocatalytic hydrogen production process as it determines how much voltage will be generated in the reactor to break subsequent water molecules. The effects of an increase in the mass flow rate of zinc sulfide on hydrogen production rates are shown in Fig. 6.48. The hydrogen production rates of photocatalytic reactor and system 2 decrease from 47.2 to 42.23 L/s and 282.5 to 277.5 L/s, respectively, with an increase in the mass flow rate of zinc sulfide from 0.45 to 0.70 kg/s. However, the hydrogen production rate of system 1 stays constant at 235.3 L/s. This decreasing behavior of hydrogen production rates with an increase in the mass flow rate of zinc sulfide shows that providing extra photocatalyst may not always be better for the system as extra photocatalyst supplied can deposit on the walls of the glassware, which stops solar light from falling onto the other molecules of zinc sulfide in the solution.

The effects of variation in mass flow rate of zinc sulfide on system performance are only observed for system 2 because system 2 utilized photocatalytic hydrogen production reactor to generate additional hydrogen by recovering reflected solar light from the central receiver. Figure 6.49 displays the effects of an increase in the mass flow rate of zinc sulfide on energy and exergy efficiencies of the integrated systems.

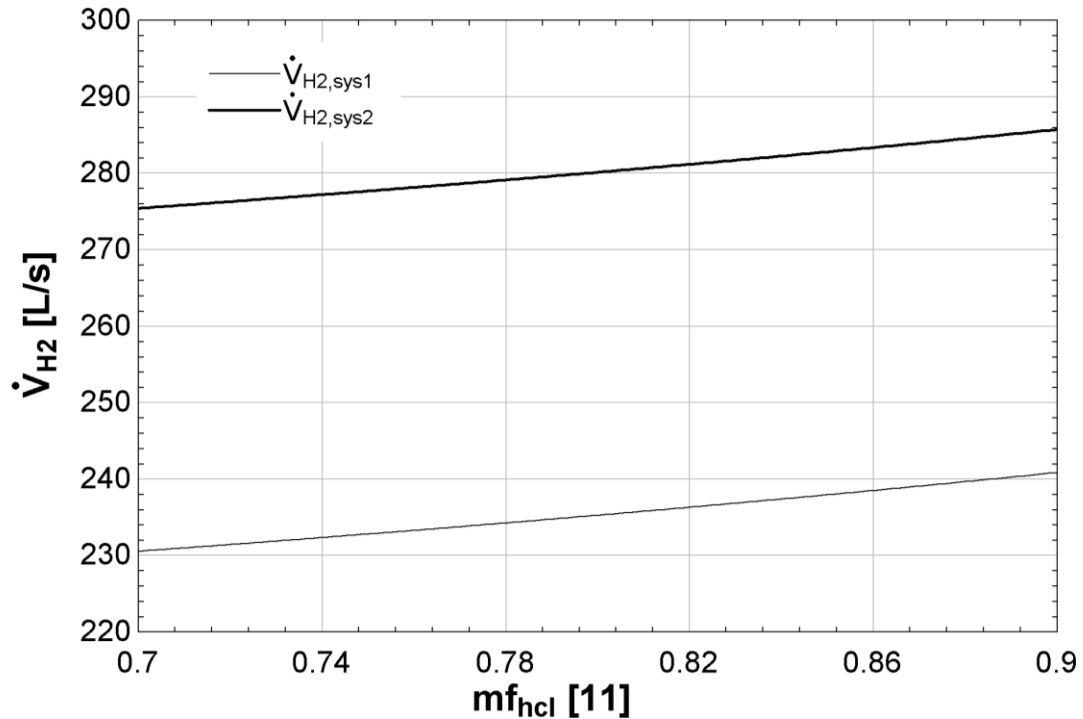


Fig. 6.46. Effects of mass fraction of hydrochloric acid at state 11 on hydrogen production rates.

The energy and exergy efficiencies of system 1 remain constant at 39.48% and 48.54%, respectively. The energy and exergy efficiencies of system 2 decrease from 57.86 to 51.64% and 57.87 to 56.89%, respectively with an increase in the mass flow rate of zinc sulfide. The decreasing trend of energy and exergy efficiencies of system 2 with an increase in the mass flow rate of zinc sulfide is observed, because for the studied system an increase in the mass of zinc sulfide may result in deposition of zinc sulfide on the walls of the reactor which will stop solar light from reaching other molecules of zinc sulfide floating in the solution. No effects of an increase in the mass flow rate of zinc sulfide on energy and exergy efficiencies of system 1 are noticed because system 1 does not utilize photocatalytic reactor to harness reflected solar light as compared to system 2.

The effects of Cu-Cl electrolyzer pressure on energy and exergy efficiencies of systems 1 and 2 are shown in Fig. 6.50. The energy efficiencies of systems 1 and 2 increase from 39.47 to 41.55% and 56.24 to 58.03%, respectively, with an increase in electrolyzer pressure from 100 to 1000 kPa. The exergy efficiencies of systems 1 and 2 increase from 48.51 to 52.64% and 57.38 to 62.31%, respectively, with an increase in electrolyzer pressure.

Note that the increase in electrolyzer pressure increases the energy and exergy efficiencies of both systems because the increase in pressure reduces the energy requirement of the electrolyzer by making the molecules of the chemical compound used in the electrolyzer unstable and increases the vibration within the molecule. This increase in molecular vibration results in lower energy requirement by the electrolyzer and better performance of the system.

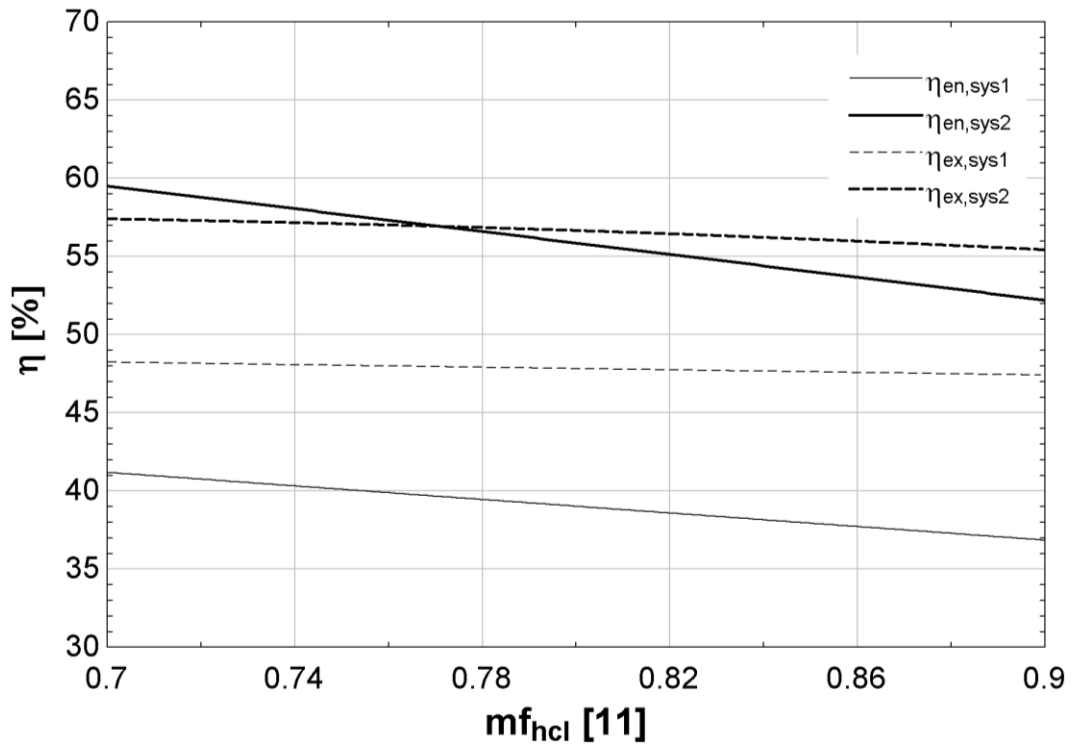


Fig. 6.47. Effects of mass fraction of hydrochloric acid at state 11 on energy and exergy efficiencies.

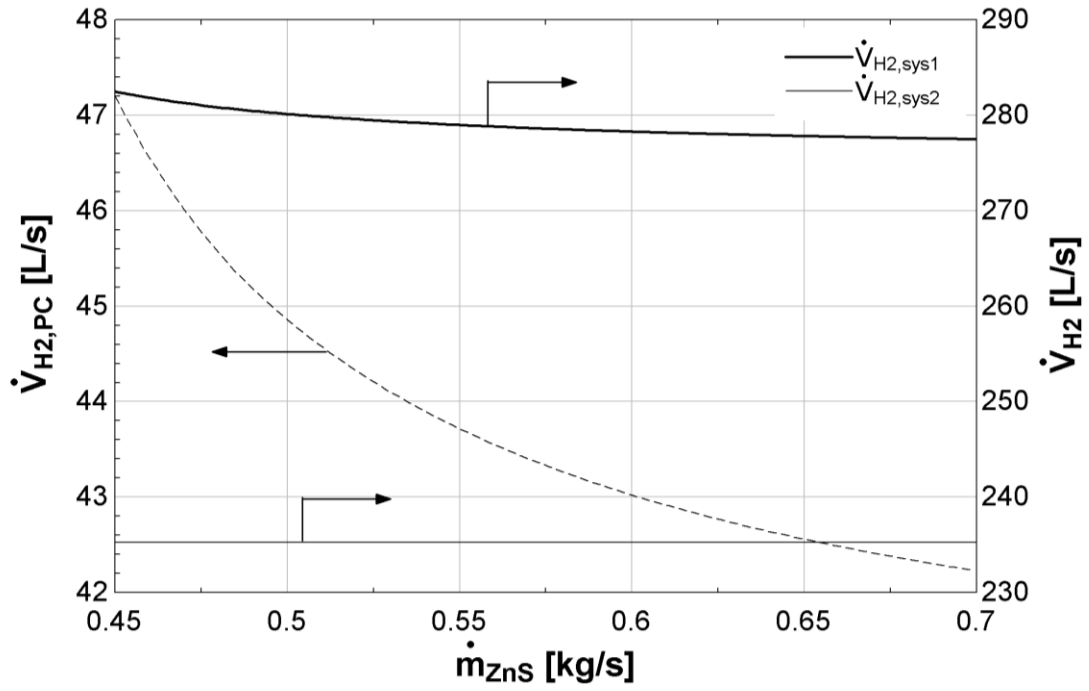


Fig. 6.48. Effects of mass flow rate of zinc sulfide on hydrogen production rates.

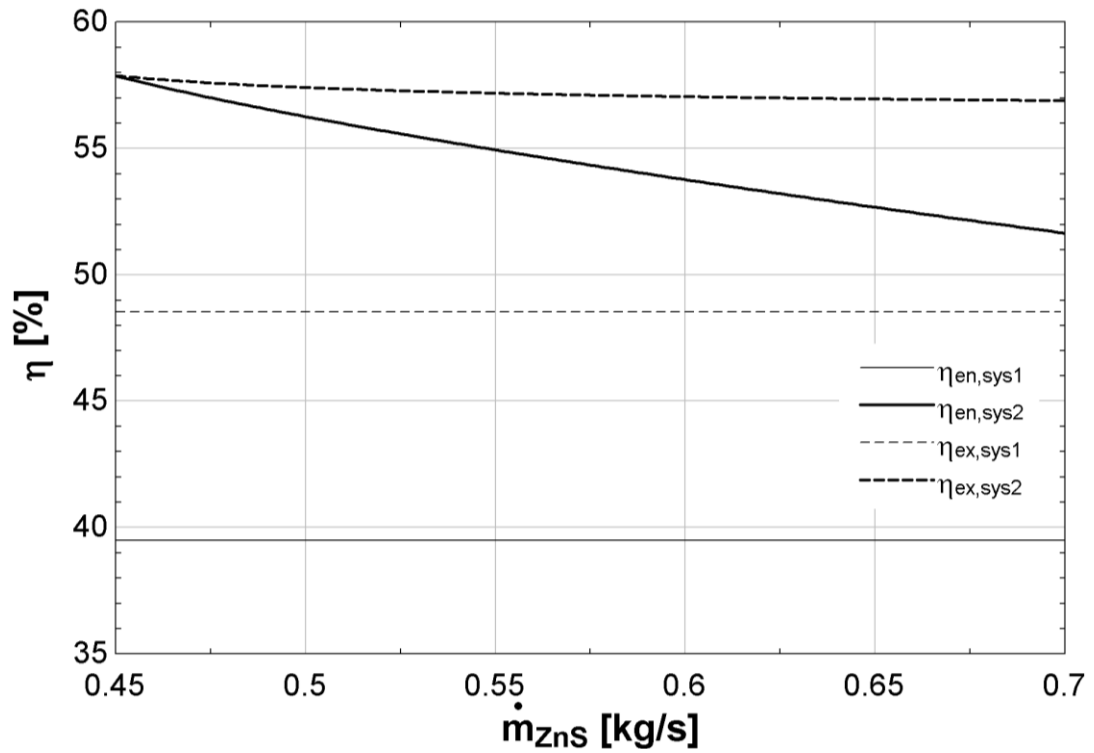


Fig. 6.49. Effects of mass flow rate of zinc sulfide on energy and exergy efficiencies.

It is important to note that the effects of varying the molten salt inlet temperature on the rate of hydrogen production for both systems are shown in Fig. 6.51. The rates of hydrogen production by systems 1 and 2 increase from 232.5 to 262.8 L/s and 277.6 to 305.6 L/s, respectively, with a rise in molten salt inlet temperature from 550 to 700 K. This occurs because an increase in molten salt inlet temperature leads to a higher mass flow rate of molten salt through the system to attain the required outlet temperature of molten salt. The increase in mass flow rate results in an increase in the rate of heat produced by the solar system.

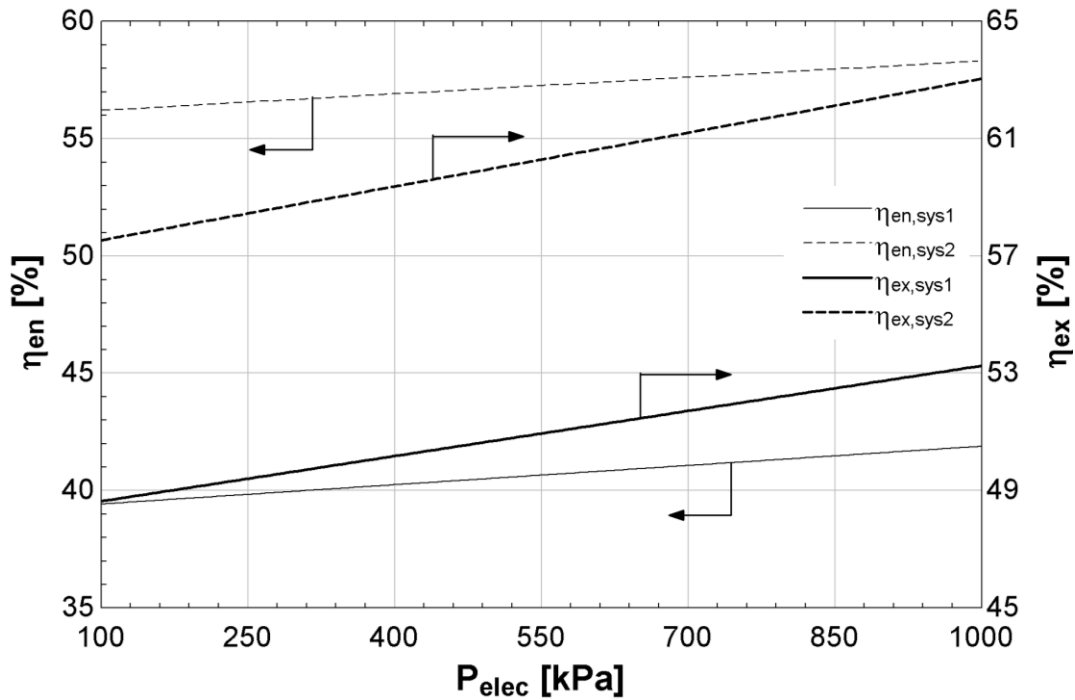


Fig. 6.50. Effects of electrolyzer pressure on energy and exergy efficiencies.

As the rate of heat produced by the solar system increases, the rate of heat supplied to the Cu-Cl cycle increases. With an increase in the rate of heat supplied to the Cu-Cl cycle, the rate of hydrogen production by the Cu-Cl cycle increases. The effects of variation in molten salt inlet temperature on energy and exergy efficiency of both systems are shown in Fig. 6.52. The energy efficiencies of systems 1 and 2 increase from 39.32 to 41.03% and 56.12 to 57.47%, respectively, with an increase in the molten salt inlet temperature. The exergy efficiencies of systems 1 and 2 increase from 48.3 to 50.73% and 57.28 to 58.65%, respectively, with an increase in the molten salt inlet temperature. This

increasing behavior of energy and exergy efficiencies is observed because an increase in molten salt inlet temperature results in a higher rate of hydrogen production. It is also noticed that system 2 performs better compared to system 1 because system 2 recovers additional energy reflected by the heliostat field central receiver in the photocatalytic reactor to produce extra hydrogen.

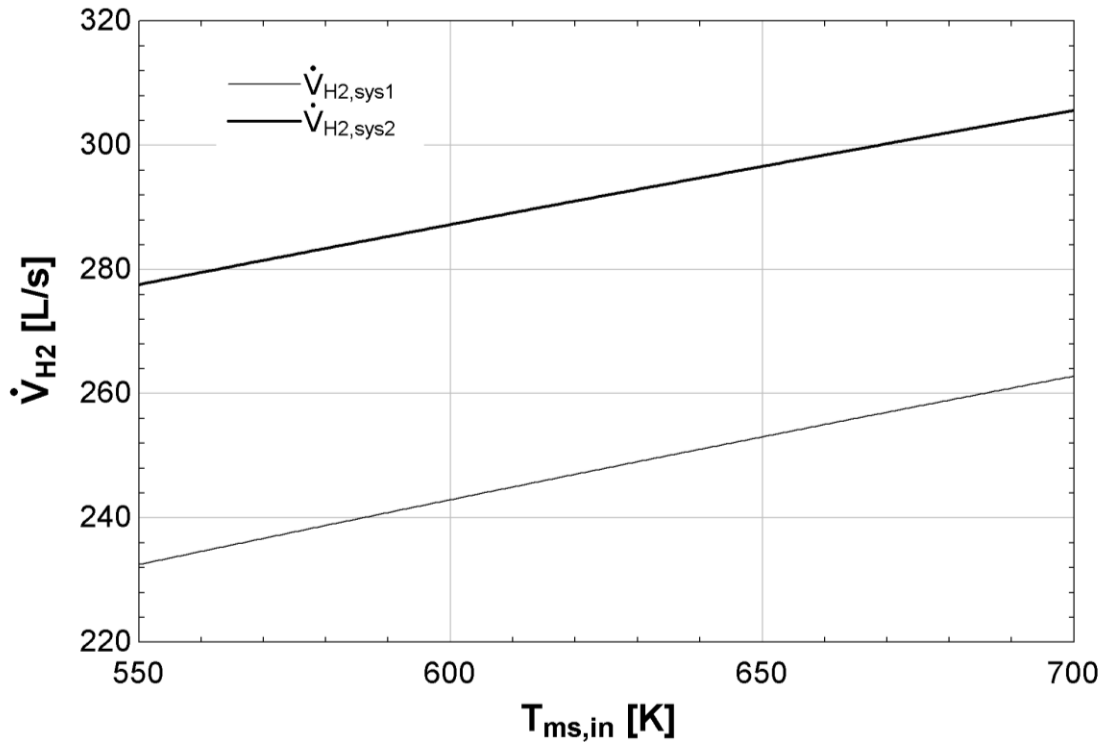


Fig. 6.51. Effects of molten salt inlet temperature on hydrogen production rates.

The concentration ratio of heliostat field mirror plays an important role in determining the amount of solar light being concentrated. The effects of concentration ratio of heliostat field system on the rate of hydrogen production by both systems are shown in Fig. 6.53. The rates of hydrogen production of systems 1 and 2 increase from 152.3 to 247.1 L/s and 197.2 to 292 L/s, respectively, with an increase in the concentration ratio of heliostat field system from 300 to 1500. The increase in the rate of hydrogen production with an increase in the concentration ratio is observed because an increase in concentration ratio results in a larger amount of solar light intensity, being reflected from heliostat field mirror to the central receiver. The increase in solar light intensity reaching the central receiver helps in generating additional heat, which is then supplied to the Cu-

Cl cycle and increases the hydrogen production rate. It is also noticed that system 2 produces a higher rate of hydrogen as compared to system 1 because system 2 makes use of solar light intensity being reflected by the central receiver in the photocatalytic reactor to produce excess hydrogen.

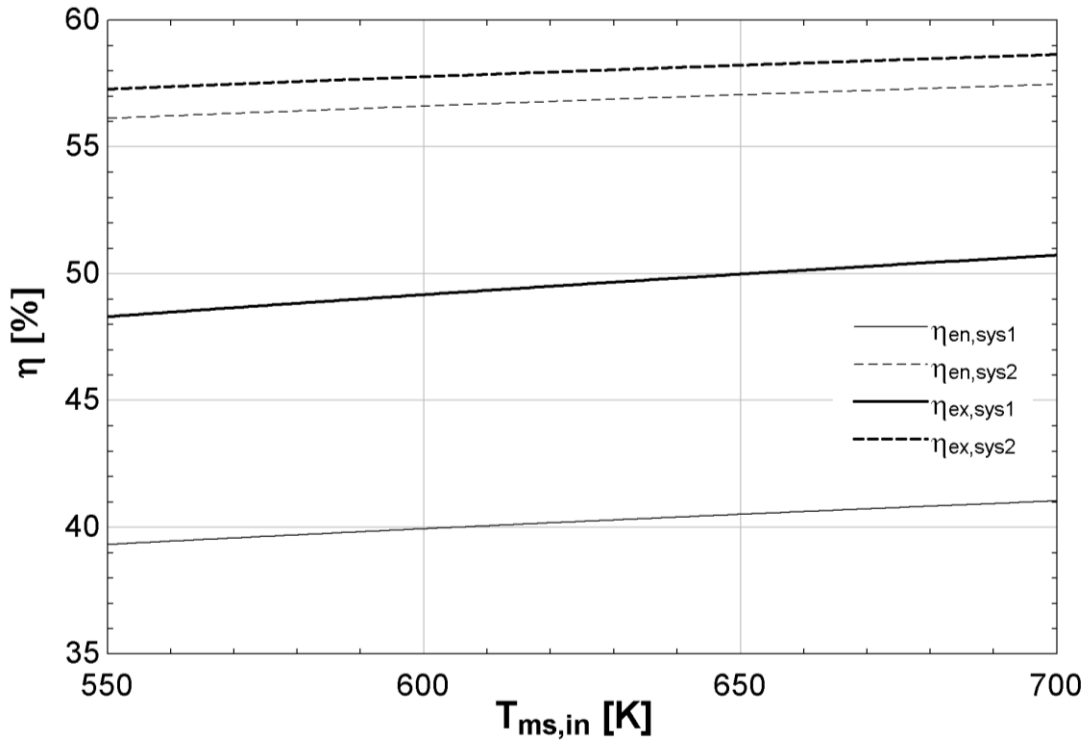


Fig. 6.52. Effects of molten salt inlet temperature on energy and exergy efficiencies.

The effects of an increase in the concentration ratio on exergy destruction rates of systems 1 and 2 are shown in Fig. 6.54. The exergy destruction rates of both systems increase with an increase in the concentration ratio. The exergy destruction rates of systems 1 and 2 increase from 2323 to 2620 kW and 1899 to 2196 kW, respectively, with an increase in the concentration ratio from 300 to 1500. This trend is observed because an increase in the concentration ratio results in a higher rate of solar light intensity being concentrated from the solar heliostats to the central receiver of the heliostat field system. The heat generation capacity of the central receiver increases with increase in the concentration of the solar light intensity received by the central receiver and as a result of this the exergy destruction rate increases. It is also observed that system 2 has a lower exergy destruction rate compared to system 1 because system 2 recovers the reflected

light from the central receiver in the photocatalytic hydrogen production reactor to generate additional hydrogen. This production of additional hydrogen by photocatalytic hydrogen production reactor while utilizing the same amount of exergy as that of system 1 reduces the exergy destruction rate of system 2. The effects of an increase in the concentration ratio on energy and exergy efficiencies of both systems are shown in Fig. 6.55. The energy efficiencies of systems 1 and 2 increase from 32.78 to 39.31% and 49.55 to 56.22%, respectively, with an increase in the concentration ratio of the heliostat field system. The exergy efficiencies of systems 1 and 2 increase from 39.29 to 48.21% and 50.38 to 56.6%, respectively, with an increase in the concentration ratio of the heliostat field system.

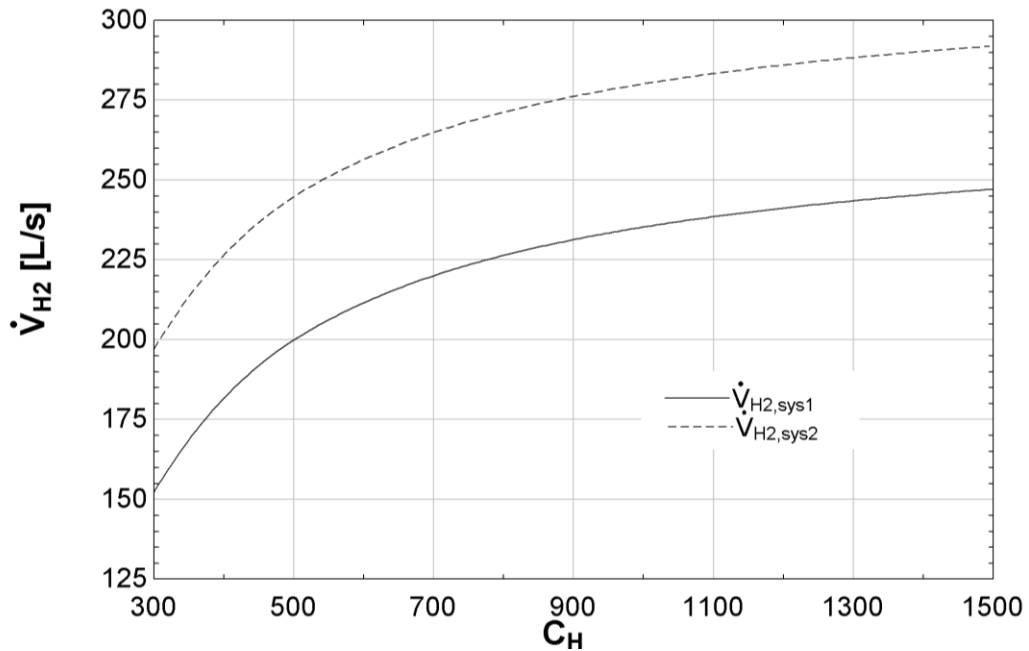


Fig. 6.53. Effects of concentration ratio of heliostat field system on hydrogen production rates.

This trend occurs because an increase in the concentration ratio results in better utilization of solar light intensity by the heliostat field system in the form of a higher rate of heat production and ultimately higher rate of hydrogen production. The results also show that system 2 performs better than system 1 because system 2 utilizes the solar light intensity in a superior manner by recovering the solar light intensity reflected by the heliostat field system.

The variation in ambient temperature plays an important role in performance determination of many systems such as the integrated systems studied because they are majorly heat dependent. Figure 6.56 illustrates the effects of a rise in the ambient temperature on hydrogen production rates.

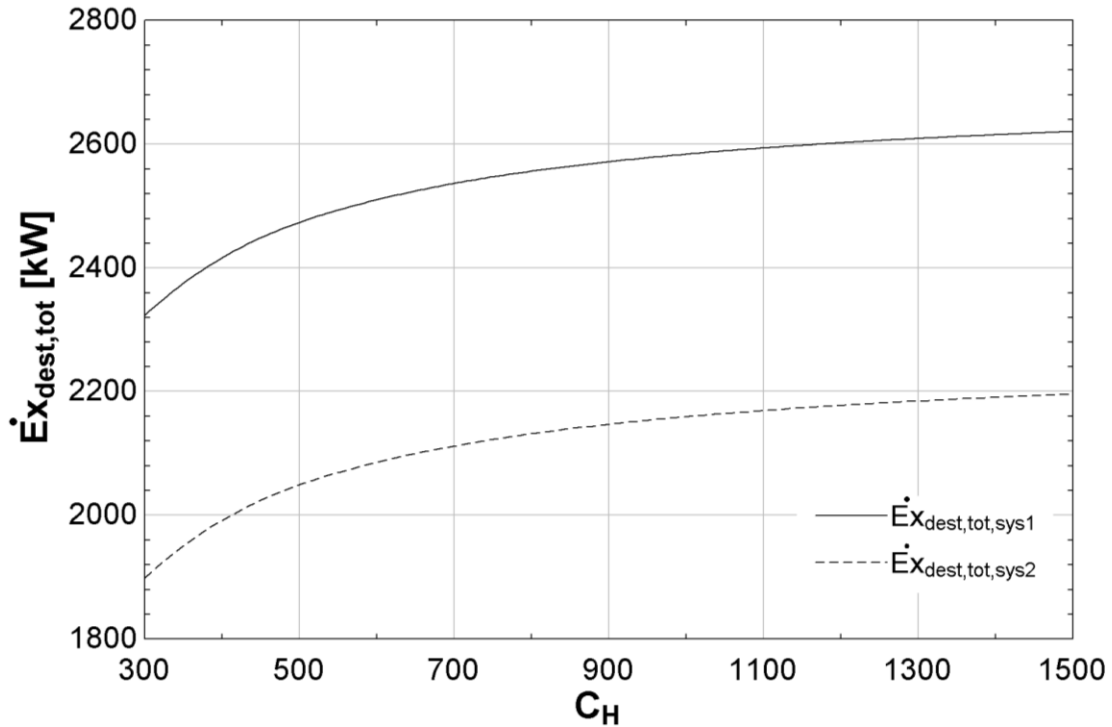


Fig. 6.54. Effects of concentration ratio of heliostat field system on total exergy destruction rate.

The hydrogen production rates of system 1, photocatalytic reactor and system 2 increase from 226.2 to 272.9 L/s, 43.63 to 49.65 and 269.8 L/s to 322.5 L/s, respectively, with a rise in ambient temperature from 290 to 330 K. This behavior is observed because the two integrated systems studied are mostly temperature driven systems. The change in ambient temperature results in fluctuation in heat loss to the environment and therefore results in fluctuating performance of the system. Figure 6.57 displays the effects of variation in ambient temperature on exergy destruction rates of systems 1 and 2. The exergy destruction rates of both systems decrease with a variation in ambient temperature. The exergy destruction rates of systems 1 and 2 decrease from 2486 to 2365 kW and 2061 to 1941 kW, respectively, with a rise in ambient temperature from 290 to

330 K. This trend occurs because an increase in ambient temperature leads to a lower temperature difference between the system studied and the surroundings.

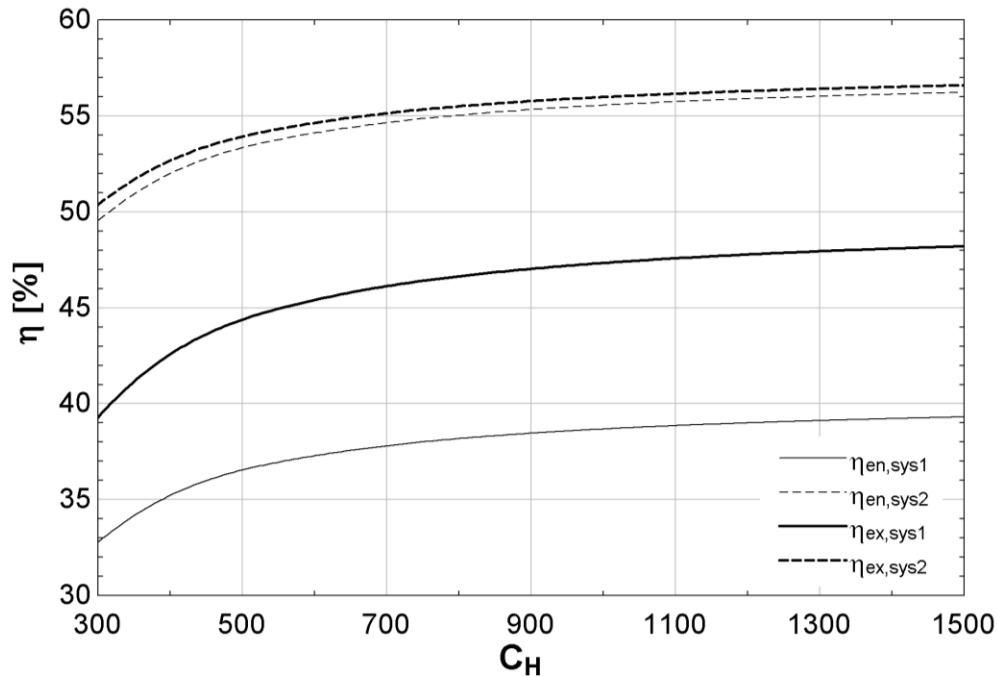


Fig. 6.55. Effects of concentration ratio of heliostat field system on energy and exergy efficiencies.

Note that the decrease in the temperature difference reduces both the heat transfer rate from the system boundary to the surroundings and the exergy destruction rate of both systems. It is also noticed that system 2 displays a lower exergy destruction rate than system 1 because system 2 better utilizes the input exergy by recovering the solar light intensity reflected by the central receiver in the photocatalytic hydrogen production reactor. The effects of a rise in ambient temperature on energy and exergy efficiencies are presented in Fig. 6.58. It is observed that the energy efficiency of both systems remains almost constant at 40 and 56.5%, respectively with a rise in ambient temperature. However, the exergy efficiencies of systems 1 and 2 increase from 47.98 to 50.82% and 56.87 to 59.64%, respectively, with a rise in ambient temperature. The almost constant value of energy efficiency with a variation in ambient temperature is obtained because the energy model accounts for no losses and irreversibilities in the analysis, while the exergy model considers such losses and irreversibilities. The increasing trend of exergy efficiencies with a rise in ambient temperature is observed because a rise in temperature

results in less heat loss due to the temperature difference between the system and the environment.

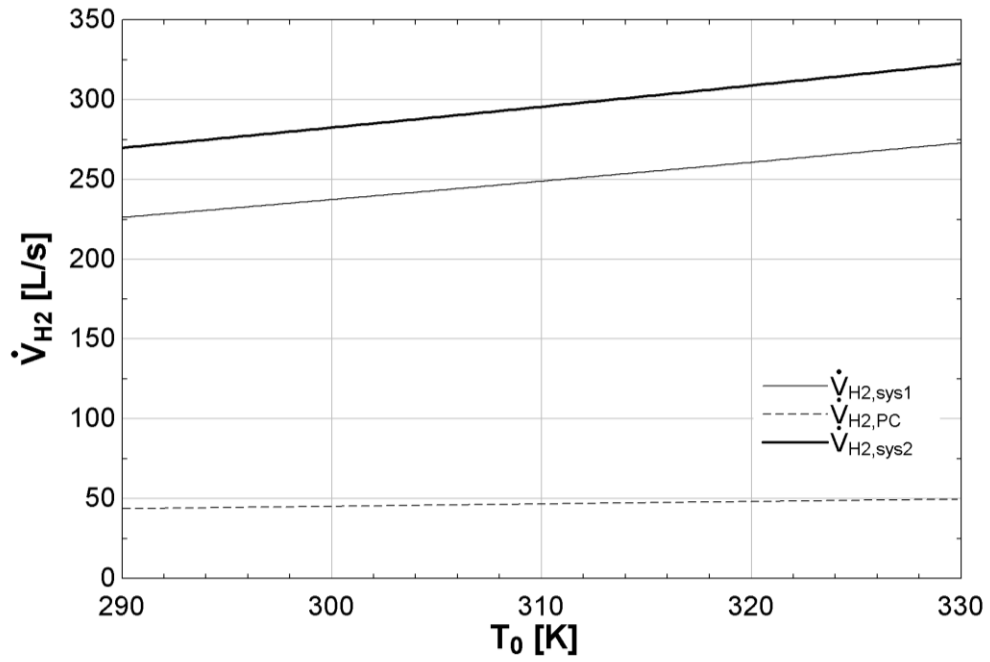


Fig. 6.56. Effects of ambient temperature on hydrogen production rates.

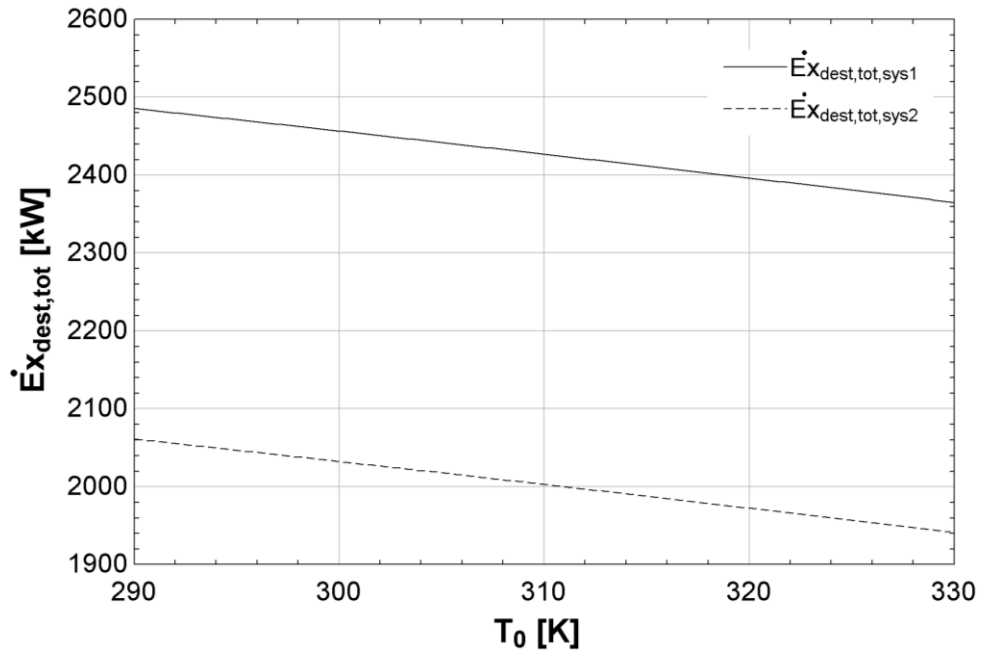


Fig. 6.57. Effects of ambient temperature on total exergy destruction rate.

The exergy destruction ratio for individual components of the integrated system studied in the present research is shown in Fig. 6.59. The exergy destruction ratio for each component is calculated by dividing the exergy destruction caused in the system by the total exergy input to the integrated system. The exergy destruction ratio figure is provided for a sample single run and shows that in the overall system the highest exergy destruction ratio is recorded by the heliostat field system for system 1 (0.35) followed by system 2 (0.22). For the Cu-Cl cycle, the highest exergy destruction ratio is found for S1 (0.14) followed by S2 (0.10), HE8-C (0.022), HE2-C (0.025), HE3-H (0.016), HE3-C (0.015), HE8-H (0.012), HE7-H (0.01), HE1-H (0.009), P3 (0.005), HE7-C (0.006), HE10-C (0.004), HE5-C (0.0026), HE1-C (0.0025) and HE2-H (0.001). The exergy destruction ratio of other components of the Cu-Cl cycle is closed to zero. The highest exergy destruction ratio in the Kalina cycle is recorded by the turbine (0.022) followed by heat exchanger (0.004) and absorber (0.002). The exergy destruction ratio for the photocatalytic reactor is calculated to be 0.04. The exergy destruction ratio analysis shows that improvement works should be concentrated on the heliostat field system to better utilize the solar light intensity and reduce the convection, conduction and emissivitive losses from the central receiver of the heliostat field system.

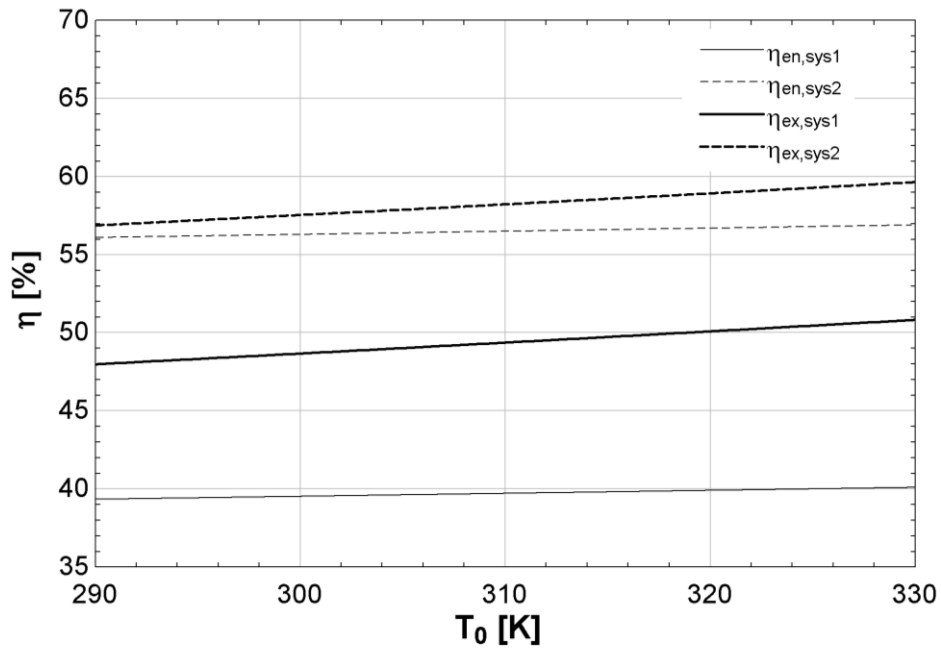


Fig. 6.58. Effects of ambient temperature on energy and exergy efficiencies.

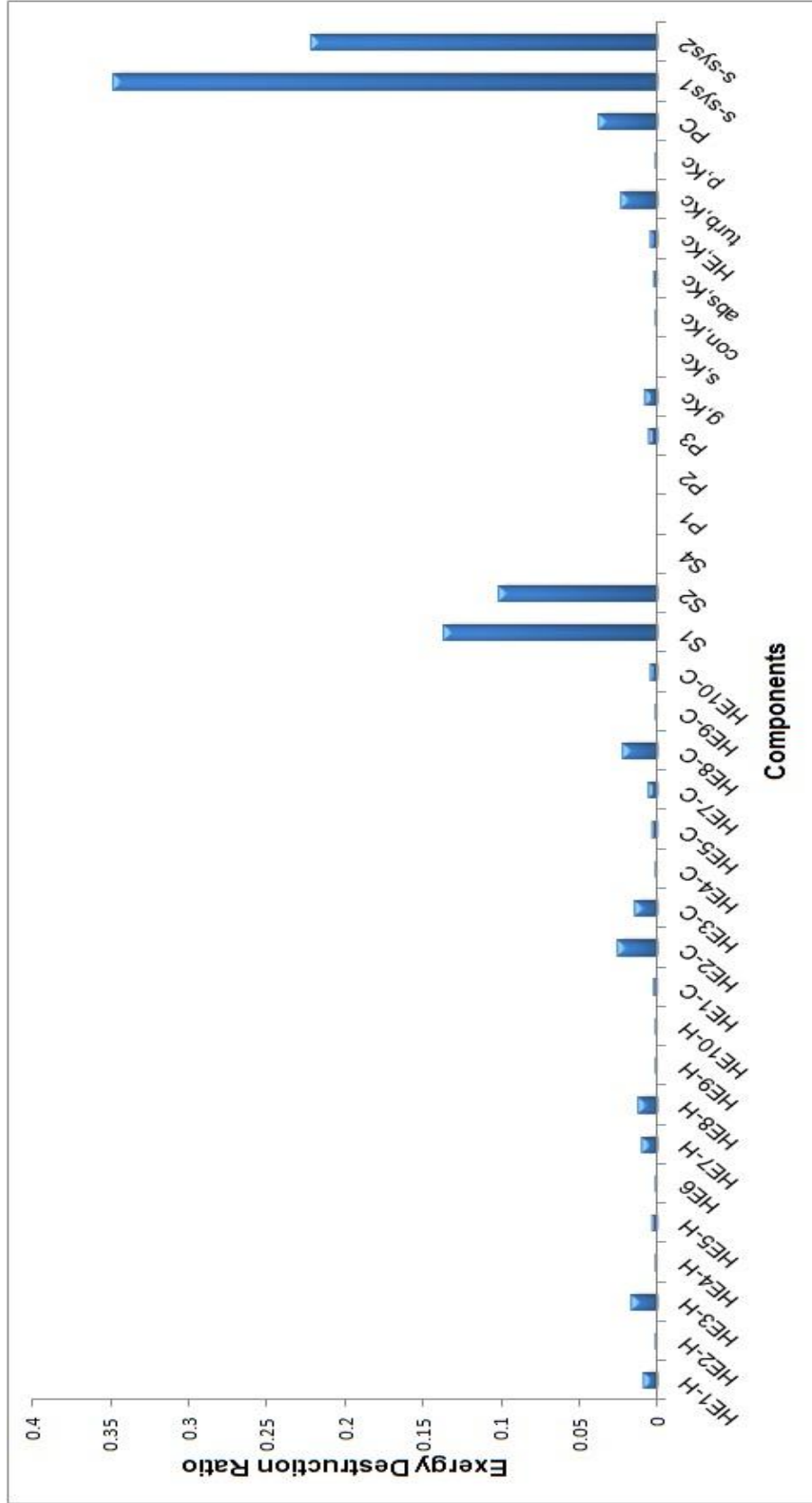


Fig. 6.59. Exergy destruction ratios for the components of the integrated systems.

6.5 Results of Optimization Study for Experimental System

A multi-objective optimization of the hybrid reactor consisting of three objective functions and five constraints with their specific ranges, as given in section 5.5, are presented in this section. The built-in genetic algorithm technique in the software developed by Klein [120] with 128 number of individuals, 2048 number of generations and 0.7 mutation rate is used to perform the multi-objective optimization. In the first multi-objective optimization study, hydrogen production rate (to be maximized) and cost of hydrogen production (to be minimized) are selected as the objective functions. In the second study, exergy efficiency (to be maximized) and cost of hydrogen production (to be minimized) are selected as the objective functions. For the first study, the optimum points obtained on the Pareto front are shown in Fig. 6.60. The optimization study shows that the highest hydrogen production rate achieved is 0.379 kg/hr and the lowest hydrogen production cost achieved is 3.25 C\$/kg for the given constraints. Although all points on the Pareto front are considered optimum, traditionally LINMAP technique is used to obtain the most desirable optimized points. The LINMAP technique helps in identifying a hypothetical point at which all the objective functions have their respective optimum point irrespective of other objective functions. Sayyadi and Babelahi [131] mention that although the point obtained by LINMAP technique is near impossible to achieve in reality, it helps in selecting the point on the Pareto frontier that it is closest to this hypothetical ideal point. This multi-objective optimization for first scenario shows that the hydrogen production rate is directly related to the cost of hydrogen production. The values of constraints for the optimized hydrogen production rate and the cost of hydrogen are listed in Table 6.3. For this optimization study hydrogen production rate is directly related to the cost of hydrogen production so the optimum points are the same.

Table 6.3. Constraints for multi-objective optimization of hybrid reactor with respect to hydrogen production rate and cost of hydrogen production.

Constraints	Value
T_{reac}	330.8 K
T_0	290.4 K
M_{CuCl}	0.1189 mol/L
M_{ZnS}	0.1022 mol/L
V	2.687 V

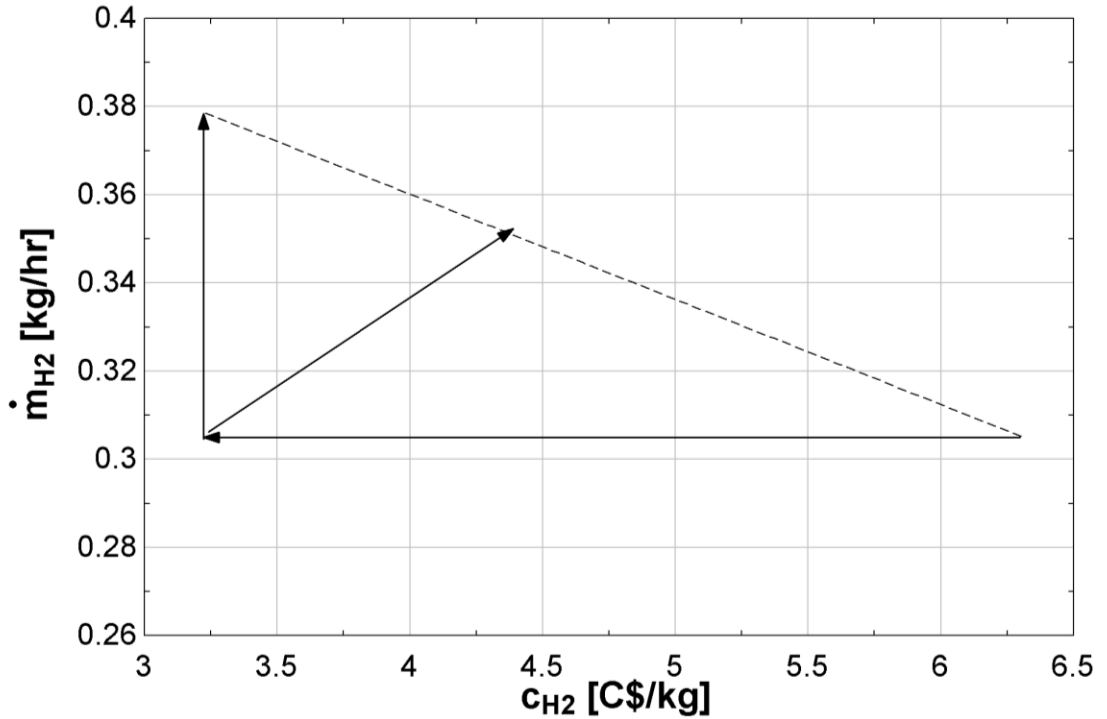


Fig. 6.60. Multi-objective optimization of the hybrid reactor with respect to hydrogen production rate and cost of hydrogen production.

The Pareto frontier obtained for the second multi-objective optimization study consisting of exergy efficiency and cost of hydrogen production is presented in Fig. 6.61. The optimization study shows that the highest exergy efficiency achieved is 8.5% and the lowest hydrogen production cost achieved is 6.4 C\$/kg for the given constraints. The values of constraints for the optimized exergy efficiency and cost of hydrogen are presented in Table 6.4.

Table 6.4. Constraints for multi-objective optimization of hybrid reactor with respect to exergy efficiency and cost of hydrogen production.

Constraints	Value
T_{reac}	340 K
T_0	280 K
M_{CuCl}	0.817 mol/L
M_{ZnS}	0.177 mol/L
V	2.43 V

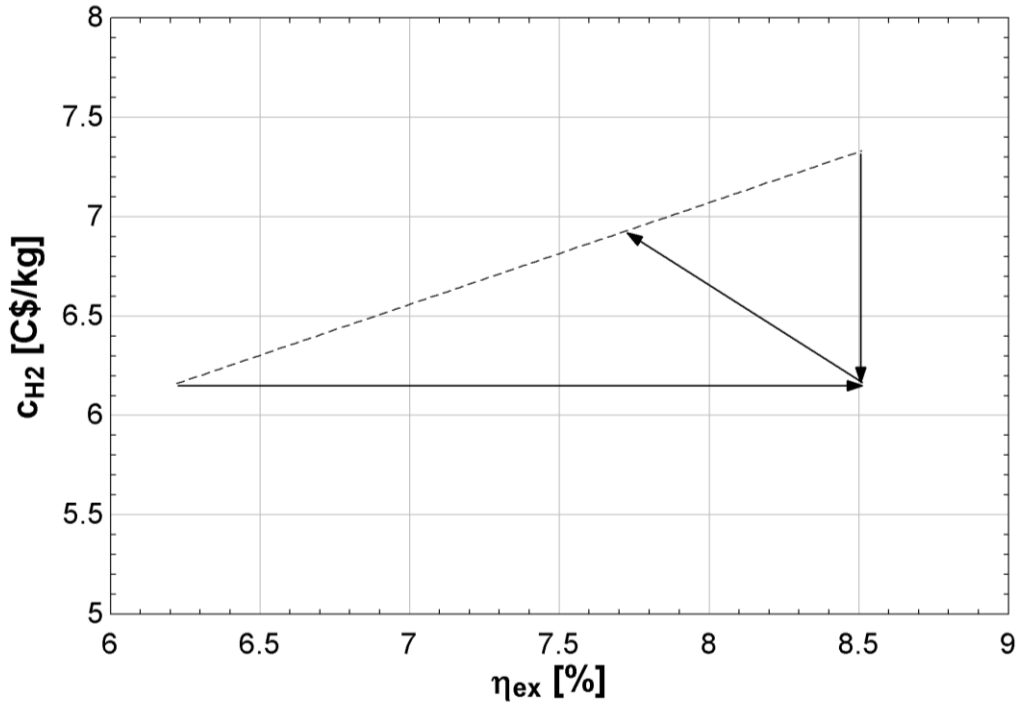


Fig. 6.61. Multi-objective optimization of the hybrid reactor with respect to exergy efficiency and cost of hydrogen production.

6.6 Results of Optimization Study for Integrated Systems

Multi-objective optimization of the second integrated system consisting of two objective functions and eight constraints with their specific ranges as given in earlier section are presented in this section. In the multi-objective optimization study, exergy efficiency (to be maximized) and cost of hydrogen production (to be minimized) are selected as the objective functions. For this multi-objective optimization study, the optimum points obtained on the Pareto front are shown in Fig. 6.62. The optimization study shows that the best exergy efficiency obtained is 77.85% and the lowest hydrogen production cost calculated is 3.75 C\$/kg for the given constraints. The LINMAP technique is utilized to identify a hypothetical point at which all the objective functions have their respective optimum point irrespective of other objective functions as shown in the figure. The values of constraints for the optimized exergy efficiency and cost of hydrogen production are presented in Table 6.5.

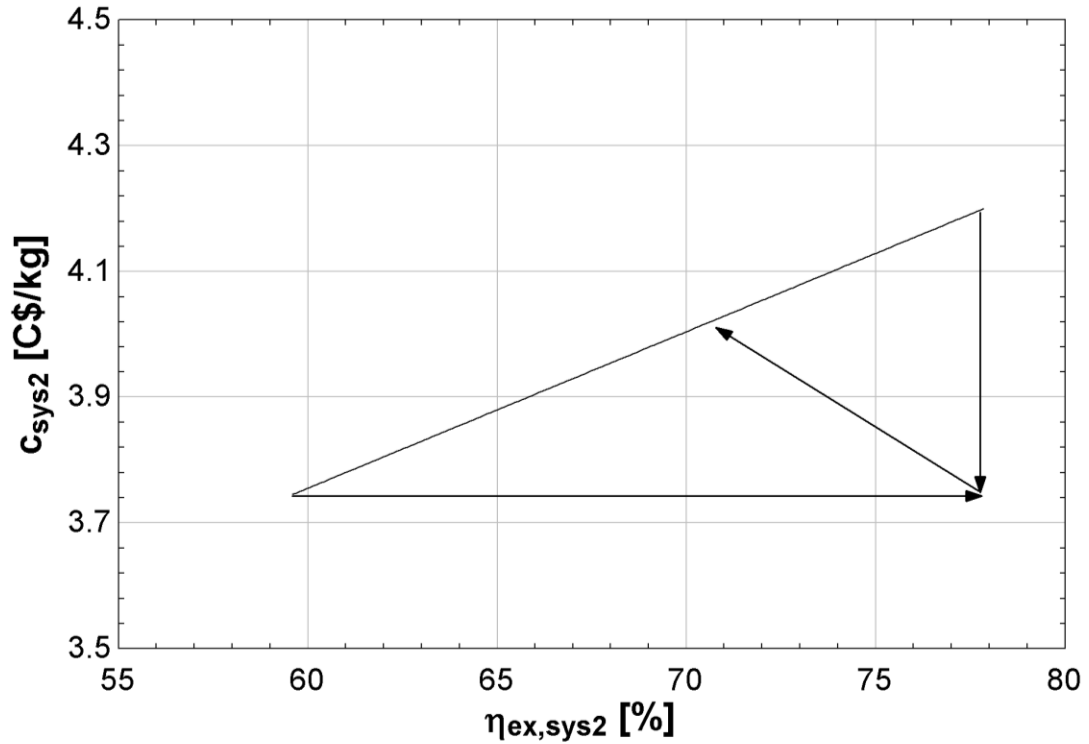


Fig. 6.62. Multi-objective optimization of the integrated system with respect to exergy efficiency and cost of hydrogen production.

Table 6.5. Constraints for multi-objective optimization of the integrated system with respect to exergy efficiency and cost of hydrogen production.

Constraints	Value
$T_{ms,in}$	551.5 K
T_0	316.4 K
$m_{f_{HCl}}$	0.7
\dot{m}_{znS}	0.467 kg/s
C	600.5
I_s	600 W/m ²
F_r	0.5016
P_{elec}	820.5 kPa

A cost comparison is performed to compare the cost of hydrogen production obtained for the hybrid reactor and integrated system with other hydrogen production systems as shown in Fig. 6.63. The cost comparison shows that the wind based systems have the highest production cost (C\$6.58) followed by, hybrid reactor analyzed in the present study (C\$6.40), geothermal based systems (C\$6.28), hydropower based systems

(C\$5.68), tidal based systems (C\$4.66), biomass based systems (C\$4.48), solar based systems (C\$4.43), second integrated system analyzed in the present study (C\$3.75), Cu-Cl cycle (C\$3.49) and SMR (C\$2.41). The high cost of hydrogen production for a hybrid reactor is obtained because this hydrogen production technology is relatively new and the running and manufacturing cost of the hybrid reactor is high. Moreover, when the hybrid reactor is added to the integrated system, the cost of hydrogen production decreases because the integration with the Cu-Cl cycle running on solar energy results in better utilization of input energy sources, which in turn boosts the hydrogen production rate. The cost comparison analysis shows that at present, hydrogen production by the hybrid reactor and the second integrated system is not as cost effective as compared to SMR. However, the extensive amount of research directed in the area of hybrid reactors could make the technology commercially viable in the future.

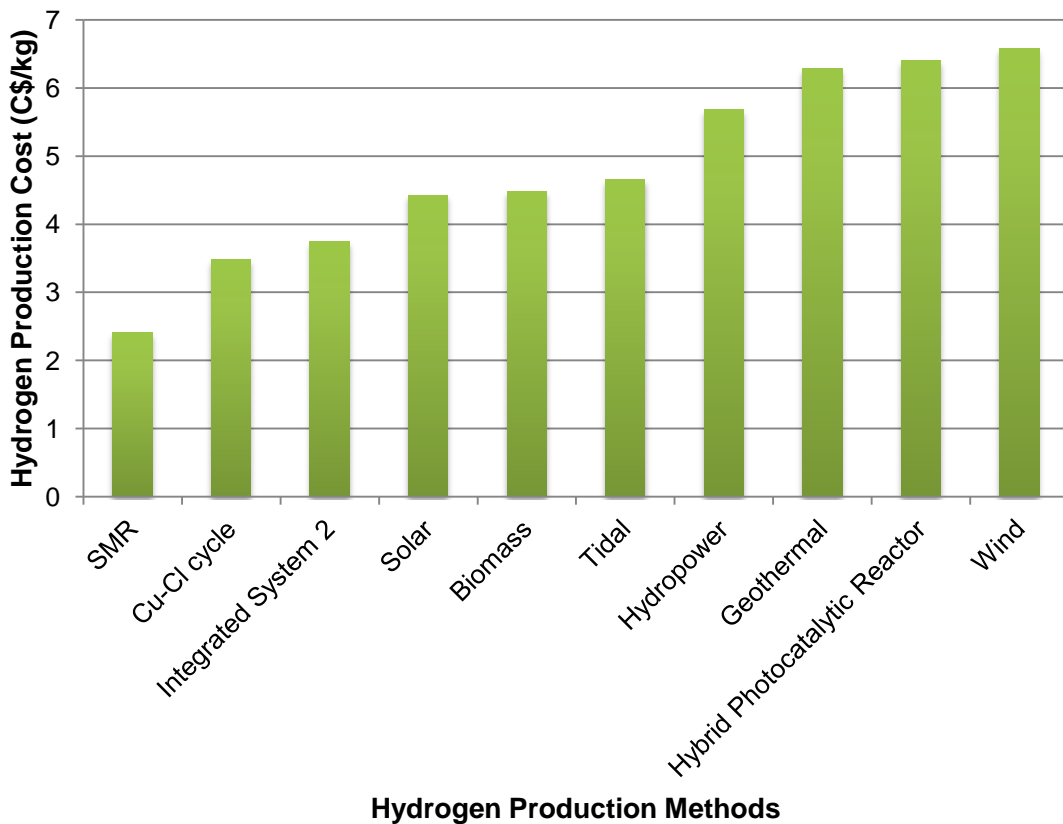


Fig. 6.63. Average hydrogen production cost of selected methods (Data from [134- 136]).

Chapter 7: Conclusions and Recommendations

7.1 Conclusions

The Cu-Cl thermochemical water splitting cycle appears to be a promising option to produce hydrogen in a relatively environmentally benign manner, compared to conventional technologies. Within the Cu-Cl cycle, the electrolyzer step consumes the majority of the total energy consumed by the cycle to break chemical bonds and produce hydrogen. The present research aims to contribute to the research being carried out in the field of Cu-Cl cycle by developing a lab-scale model of a photocatalytic hydrogen production reactor for the Cu-Cl cycle and by performing energy and exergy analyses of solar-based integrated Cu-Cl cycle systems. An experimental investigation is carried out on a lab-scale model of a photocatalytic hydrogen reactor capable of producing hydrogen by utilizing solar light intensity. The main objectives of the present research are to conduct an experimental study by designing and building a prototype of the hybrid photocatalytic hydrogen production reactor, perform electrochemical modeling of the hybrid photocatalytic hydrogen production reactor, carry out multi-objective optimization study of the hybrid photocatalytic hydrogen production reactor, analyze the solar-based integrated systems from energy and exergy perspectives and perform and assess the performance of the integrated systems by conducting parametric studies. The primary results of this study are summarized as follows:

- The photo-electrochemical hydrogen production rate increases as the applied voltage, solar light intensity and mass or concentration of CuCl and mass or concentration of ZnS increase.
- The rate of photo-electrochemical hydrogen production varies from 0.73 to 1.61 $\mu\text{g/s}$ with an increase in applied voltage and mass or concentration of CuCl from 2.5 to 3.5 V and 5 to 10 g or 0.033 to 0.066 g/mL, respectively.
- The rate of photo-electrochemical hydrogen production varies from 1.37 to 1.64 $\mu\text{g/s}$ with an increase in applied voltage and mass or concentration of ZnS from 2.5 to 3.5 V and 2 to 4 g or 0.013 to 0.027 g/mL, respectively.

- The photo-electrochemical hydrogen production rate increases from 0.73 to 1.53 $\mu\text{g/s}$ with an increase in the mass or concentration of ZnS and mass or concentration of CuCl from 2 to 4 g or 0.013 to 0.027 g/mL and 5 to 10 g or 0.033 to 0.066 g/mL, respectively.
- The photocatalytic hydrogen production rate increases from 0.21 to 0.50 $\mu\text{g/s}$ with an increase in solar light intensity, mass or concentration of CuCl and mass or concentration of ZnS from 400 to 500 W/m^2 , 5 to 10 g or 0.033 to 0.066 g/mL and 2 to 4 g or 0.013 to 0.027 g/mL, respectively.
- The rate of photocatalytic hydrogen production increases from 0.21 to 0.49 $\mu\text{g/s}$ with an increase in the mass or concentration of CuCl and mass or concentration of ZnS from 5 to 10 g or 0.033 to 0.066 g/mL and 2 to 4 g or 0.013 to 0.027 g/mL, respectively.
- The rate of photocatalytic hydrogen production increases from 0.28 to 0.48 $\mu\text{g/s}$ with an increase in solar light intensity and the mass or concentration of ZnS from 400 to 500 W/m^2 and 2 to 4 g or 0.013 to 0.027 g/mL, respectively.
- A higher hydrogen production rate is observed when 0.5 g of titanium dioxide is added to the anolyte solution, compared to zero titanium dioxide in the anolyte solution.
- The voltage generated by the titanium dioxide when induced with solar light intensity increases with an increase in the concentration of the titanium dioxide in the anolyte solution.
- The voltage drop across the anolyte solution (sol 1), catholyte solution (sol 2), anode, cathode and cation exchange membrane varies from 0.005 to 0.016 V, 0.004 to 0.013 V, 1.67 to 2.168 V, 0.18 to 0.22 V and 0.06 to 0.19 V, respectively with an increase in current density from 0.5 to 1.5 A/cm^2 .
- The energy and exergy efficiencies of the hybrid photocatalytic hydrogen production reactor decrease from 5.74 to 4.54% and 5.11 to 4.04%, respectively with an increase in current density.
- The hydrogen production rate and cost of hydrogen production from the hybrid photocatalytic hydrogen production reactor increase from 1.28 to 1.47 L/s and 3.28 to 3.36 C\$/kg, respectively, with a rise in the reactor temperature from 290 to 340 K.

- The exergy efficiency of the hybrid photocatalytic hydrogen production reactor increases from 3.78 to 5.22% with a rise in the reactor temperature.
- The hydrogen production rate from the hybrid photocatalytic hydrogen production reactor decreases from 1.39 to 1.36 L/s with an increase in the concentration of Cu-Cl from 0.1 to 1 mol/L.
- The cost of hydrogen production from the hybrid photocatalytic hydrogen production reactor increases from 3.25 to 3.75 C\$/kg with an increase in the concentration of CuCl.
- The exergy efficiency of the hybrid photocatalytic hydrogen production reactor decreases from 5.25 to 3.9% with a rise in ambient temperature.
- The cost of hydrogen production from the hybrid photocatalytic hydrogen production reactor increases from 3.26 to 3.55 C\$/kg with an increase in the distance from electrode to membrane.
- The highest hydrogen production rates is achieved as 0.379 kg/hr while the lowest hydrogen production cost becomes 3.25 C\$/kg for the specific constraints considered.
- The highest exergy efficiency is 8.5% while the lowest hydrogen production cost becomes 6.4 C\$/kg for the specific constraints considered.
- The rates of hydrogen produced by systems 1 and 2 increase from 126.9 to 289.4 L/s and 154.1 to 343.9 L/s, respectively with a rise in solar light intensity from 600 to 1200 W/m².
- The total exergy destruction rates of systems 1 and 2 increase from 1495 to 3122 kW, and 1238 to 2606 kW, respectively with a rise in solar light intensity.
- The energy efficiencies of systems 1 and 2 increase from 37.42 to 39% and 54.3 to 56.01%, respectively with a rise in solar light intensity.
- The exergy efficiencies of systems 1 and 2 increase from 45.6 to 47.79% and 54.94 to 56.41%, respectively with a rise in solar light intensity.
- The rates of hydrogen production by systems 1 and 2 decrease from 549.4 to 129 L/s and 577.6 to 179.8 L/s, respectively with an increase in view factor from 0.5 to 0.9.
- The rates of total exergy destruction for systems 1 and 2 decrease from 3384 to 2209 kW and 3117 to 1728 kW, respectively with an increase in view factor.

- The energy efficiencies of systems 1 and 2 decrease from 48.5 to 30.71% and 64.4 to 49.11%, respectively with an increase in view factor.
- The exergy efficiencies of systems 1 and 2 decrease from 61.57 to 36.57% and 64.61 to 50.37%, respectively with an increase in view factor.
- The hydrogen production rates by systems 1 and 2 increase from 230.6 to 240.9 L/s and 275.4 to 285.7 L/s, respectively with an increase in the mass fraction of hydrochloric acid at state 11 from 0.7 to 0.9.
- The energy efficiencies of systems 1 and 2 decrease from 40.97 to 36.93% and 59.34 to 52.28%, respectively with an increase in the mass fraction of hydrochloric acid at state 11.
- The exergy efficiencies of systems 1 and 2 decrease from 47.91 to 47.53% and 57.16 to 55.71%, respectively with an increase in the mass fraction of hydrochloric acid at state 11.
- The hydrogen production rates of the photocatalytic reactor and system 2 decrease from 47.2 to 42.23 L/s and 282.5 to 277.5 L/s, respectively with an increase in the mass flow rate of zinc sulfide from 0.45 to 0.70 kg/s.
- The energy and exergy efficiencies of system 2 decrease from 57.86 to 51.64% and 57.87 to 56.89%, respectively, with an increase in the mass flow rate of zinc sulfide.
- The energy efficiencies of systems 1 and 2 increase from 39.47 to 41.55% and 56.24 to 58.03%, respectively, with an increase in electrolyzer pressure from 100 to 1000 kPa.
- The exergy efficiencies of systems 1 and 2 increase from 48.51 to 52.64% and 57.38 to 62.31%, respectively, with an increase in electrolyzer pressure.
- The rates of hydrogen production by systems 1 and 2 increase from 232.5 to 262.8 L/s and 277.6 to 305.6 L/s, respectively, with a rise in molten salt inlet temperature from 550 to 700 K.
- The energy efficiencies of systems 1 and 2 increase from 39.32 to 41.03% and 56.12 to 57.47%, respectively, with an increase in molten salt inlet temperature.
- The exergy efficiencies of systems 1 and 2 increase from 48.3 to 50.73% and 57.28 to 58.65%, respectively, with an increase in molten salt inlet temperature.

- The rates of hydrogen production of systems 1 and 2 increase from 152.3 to 247.1 L/s and 197.2 to 292 L/s, respectively, with an increase in the concentration ratio of heliostat field system from 300 to 1500.
- The exergy destruction rates of systems 1 and 2 increase from 2323 to 2620 kW and 1899 to 2196 kW, respectively, with an increase in the concentration ratio.
- The energy efficiencies of systems 1 and 2 increase from 32.78 to 39.31% and 49.55 to 56.22%, respectively, with an increase in the concentration ratio of heliostat field system.
- The exergy efficiencies of systems 1 and 2 increase from 39.29 to 48.21% and 50.38 to 56.6%, respectively with an increase in concentration ratio of heliostat field system.
- The hydrogen production rates of systems 1 and 2 increase from 226.2 to 272.9 L/s and 269.8 to 322.5 L/s, respectively, with a rise in ambient temperature from 290 to 330 K.
- The exergy destruction rates of systems 1 and 2 decrease from 2486 to 2365 kW and 2061 to 1941 kW, respectively, with a rise in ambient temperature.
- The exergy efficiencies of systems 1 and 2 increase from 47.98 to 50.82% and 56.87 to 59.64%, respectively with a rise in ambient temperature.
- The highest exergy destruction ratios are obtained for system 1 as 0.35 and 0.22 for system 2.
- The costs of hydrogen production by the integrated system and the photocatalytic reactor are 3.75 and 6.4C\$/kg, respectively while the cost of hydrogen production through SMR is 2.41C\$/kg.

7.2 Recommendations

The electrochemical, energy and exergy analyses along with experimental studies carried out during the present research suggests numerous areas for future studies as summarized below:

- There is a need to perform a detailed electrochemical analysis of the hybrid reactor by taking in consideration the particle sizes of the chemicals used, to study their effects on the performance of the hybrid reactor.
- The problem of CuCl_2 oxidization should be resolved by inserting copper coils in the anolyte compartment to restrict oxidization of CuCl_2 , which can help improve the hydrogen production rate.
- A continuous flow hybrid reactor should be developed as an alternative to the batch reactor, to observe the effects of flow rates of CuCl , HCl and photocatalysts on the hydrogen production rate and energy and exergy efficiencies of the hybrid reactor.
- Some potential materials, other than graphite, should be employed to resist corrosion and provide high electrical conductivity and tested to improve the reactor performance.
- The larger electrode and membrane surface areas should be implemented to develop better crossing of hydrogen ions across the membrane and reduce the ohmic losses.
- Various potential photocatalysts, such as CdS and Ta/O , should be tested in the anolyte and catholyte solutions to better utilize the wide range of the solar light spectrum for splitting of HCl molecules into hydrogen and chlorine ions.
- A pilot-scale setup of the integrated system should be developed to observe the effects of different operating parameters and conditions on the performance of the integrated system.

References

- [1] Jefferson, M. Sustainable energy development: performance and prospects. *Renewable energy* 2006; 31: 571-82.
- [2] Ozbilen, AZ. Development, analysis and life cycle assessment of copper-chlorine (Cu-Cl) bases integrated systems for hydrogen production. Ph.D. thesis, FEAS, UOIT, 2012.
- [3] Gadalla, MA, Ratlamwala, TAH, Dincer, I., Kanoglu, M. Performance assessment of an integrated absorption cooling-hydrogen liquefaction system using geothermal energy. *International Journal of Exergy* 2013; 12 (2): 205-25.
- [4] Clark, WW, Rifkin, J, O'Connor, T, Swisher, J, Lipman, T, Rambach, G. Hydrogen energy stations: along the roadside to the hydrogen economy. *Utilities Policy* 2005; 13 (1): 41-50.
- [5] Ratlamwala, TAH, Dincer, I. Performance assessment of solar based integrated Cu-Cl systems for hydrogen production. *Solar Energy* 2013; 95: 345-56.
- [6] Argun, H, Kargi, F. Bio-hydrogen production by different operational modes of dark and photo-fermentation: An overview. *International Journal of Hydrogen Energy* 2011; 36 (13): 7443-59.
- [7] Ratlamwala, TAH, Dincer, I and Aydin, M. Energy and exergy analyses and optimization study of an integrated solar heliostat field system for hydrogen production. *International Journal of Hydrogen Energy* 2012; 37: 18704-12.
- [8] Dincer, I., Ratlamwala, TAH. Development of Novel Renewable Energy Based Hydrogen Production Systems: A Comparative Study. *Energy Conversion and Management* 2013; 72: 77-87.
- [9] Turner, JA. Sustainable hydrogen production. *Science* 2004; 305: 972-4.
- [10] Ratlamwala, TAH, Dincer, I. Development of a geothermal based integrated system for building multigenerational needs. *Energy and Buildings* 2013; 62: 496-506.
- [11] Moriarty, P, Honnery, D. Hydrogen's role in an uncertain energy future. *International Journal of Hydrogen Energy* 2009; 34: 31-9.
- [12] Bicakova, O, Straka, P. Production of hydrogen from renewable resources and its effectiveness, *International Journal of Hydrogen Energy* 2012; 37: 11563-78.
- [13] Dincer, I, Ratlamwala, TAH. Importance of exergy for analysis, improvement, design, and assessment. *Wiley Interdisciplinary Reviews: Energy and Environment* 2013; 2 (3): 335-49.
- [14] Dincer, I. Environmental and sustainability aspects of hydrogen and fuel cell systems. *International Journal of Energy Research* 2007; 31: 29-55.
- [15] Ratlamwala, TAH, Dincer, I, Gadalla, MA and Kanoglu, M. Thermodynamic analysis of a new renewable energy based hybrid system for hydrogen liquefaction. *International Journal of Hydrogen Energy* 2012; 37 (23): 18108-17.

- [16] Leighty, W. Running the world on renewable: Hydrogen transmission pipelines and firming geologic storage. *International Journal of Energy Research* 2008; 32: 408-26.
- [17] Abbasi, T, Abbaso, SA. ‘Renewable’ hydrogen: Prospects and challenges. *Renewable and Sustainable Energy Reviews* 2011; 15: 3034-40.
- [18] Gadalla, MA, Ratlamwala, TAH, Dincer, I. Energy and exergy analyses of an integrated fuel cell and absorption cooling system. *International Journal of Exergy* 2010; 7(6): 731-54.
- [19] Muradov, NZ, Veziroglu, TN. “Green” path from fossil-based to hydrogen economy: An overview of carbon-neutral technologies. *International Journal of Hydrogen Energy* 2008; 33: 6804-39.
- [20] Midilli, A, Dincer, I. Development of some exergetic parameters for PEM fuel cells for measuring environmental impact and sustainability. *International Journal of Hydrogen Energy* 2009; 34: 3858-72.
- [21] Ratlamwala, TAH, Dincer, I, Gadalla, MA. Performance analysis of a novel integrated geothermal-based system for multigeneration applications. *Applied Thermal Engineering* 2012; 40(1): 71-79.
- [22] Midilli, A, Dincer, I. Hydrogen as a renewable and sustainable solution in reducing global fossil fuel consumption. *International Journal of Hydrogen Energy* 2008; 33: 4209-22.
- [23] Mohammed, MAA, Salmiation, A, Wan-Azlina, WAKG, Amran, M, Faku’l-Razi, A, Taufiq-Yap, YH. Hydrogen rich gas from oil palm biomass as a potential source of renewable energy in Malaysia. *Renewable and Sustainable Energy Reviews* 2011; 15: 1258-70.
- [24] Ratlamwala, TAH, Dincer, I, Gadalla, MA. Thermodynamic analysis of a novel integrated geothermal based power generation-quadruple effect absorption cooling-hydrogen liquefaction system. *International Journal of Hydrogen Energy* 2012; 37 (7): 5840-49.
- [25] Smitkova, M, Janicek, F, Riccardi, J. Life cycle analysis of processes for hydrogen production. *International Journal of Hydrogen Energy* 2011; 36: 7844-51.
- [26] Abuadala, A, Dincer, I. A review on biomass-based hydrogen production and potential applications. *International Journal of Energy Research* 2012; 36: 415-55.
- [27] Ratlamwala, TAH, Dincer, I. Comparative efficiency assessment of novel multi-flash integrated geothermal systems for power and hydrogen production. *Applied Thermal Engineering* 201; 48: 359-66.
- [28] Abd-Alla, MH, Morsy, FM, El-Enany, AE. Hydrogen production from rotten dates by sequential three stages fermentation. *International Journal of Hydrogen Energy* 2011; 36: 13518-27.
- [29] Ratlamwala, TAH, Gadalla, MA, Dincer, I. Performance assessment of an integrated PV/T and triple effect cooling system for hydrogen and cooling production. *International Journal of Hydrogen Energy* 2011; 36(17): 11282-91.

- [30] Joshi, AS, Dincer, I, Reddy, BV. Exergetic assessment of solar hydrogen production methods. *International Journal of Hydrogen Energy* 2010; 35: 4901-8.
- [31] Ratlamwala, TAH, Gadalla, MA, Dincer, I. Thermodynamic analysis of an Integrated PEMFC-TEARS-geothermal system for sustainable buildings. *Energy and Buildings* 2012; 44(1): 73-80.
- [32] Tsuchiya, H. Innovative renewable energy solutions for hydrogen vehicles. *International Journal of Energy Research* 2008; 32: 427-35.
- [33] Ratlamwala, TAH, El-Sinawi, AH, Gadalla, MA, Aidan, A. Performance analysis of a new designed PEM fuel cell. *International Journal of Energy Research* 2012; 36 (11): 1121-32.
- [34] Dufour, J, Serrano, DP, Galvez, JL, Moreno, J, Garcia, C. Life cycle assessment of processes for hydrogen production: environmental feasibility and reduction of greenhouse gases emissions. *International Journal of Hydrogen Energy* 2009; 34: 1370-76.
- [35] Burman, G. Hydrogen Isn't Yet the Miracle Fuel of the Future. *The Fresno Bee* 2003.
- [36] Turner, J, Sverdrup, G, Mann, MK, Maness, PC, Kroposki, B, Ghirardi, M, Evans, RJ, Blake, D. Renewable hydrogen production. *International Journal of Energy Research* 2008; 32: 379-407.
- [37] Dincer, I, Tolga, M. Potential thermochemical and hybrid cycles for nuclear-based hydrogen productions. *International Journal of Energy Research* 2011; 35: 123-37.
- [38] Giaconia, A, Sau, S, Felici, C, Tarquini, P, Karaginnakis, G, Pagkoura, C, Agrafiotis, C, Konstandopoulos, AG, Thomey, D, de Oliveria, L, Roeb, M, Sattler, C. Hydrogen production via sulfur-based thermochemical cycles: Part 2: Performance evaluation of Fe_2O_3 -based catalysts for the sulfuric acid decomposition step. *International Journal of Hydrogen Energy* 2011; 36: 6496-6509.
- [39] Abandes, S, Charvin, P, Lemont, F, Flamant, G. Novel two-step SnO_2/SnO water-splitting cycle for solar thermochemical production of hydrogen. *International Journal of Hydrogen Energy* 2008; 33: 6021-30.
- [40] Xiao, L, Wu, SY, Li, YR. Advances in solar hydrogen production via two-step water-splitting thermochemical cycles based on metal redox reactions. *Renewable Energy* 2012; 41: 1-12.
- [41] Gokon, N, Murayama, H, Nagasaki, A, Kodama, T. Thermochemical two-step water splitting cycles by monoclinic ZrO_2 -supported NiFe_2O_4 and Fe_3O_4 powders and ceramic foam devices. *Solar Energy* 2009; 83: 527-37.
- [42] Sadhankar, RR. Leveraging nuclear research to support hydrogen economy. *International Journal of Energy Research* 2007; 31: 1131-41.
- [43] Aghahosseini, S, Dincer, I, Naterer, G. Integrated gasification and Cu-Cl cycle for trigeneration of hydrogen, steam and electricity. *International Journal of Hydrogen Energy* 2011; 36: 2845-54.

- [44] Naterer, GF, Suppiah, S, Stolberg, L, Lewis, M, Ferrandon, M, Wang, Z, Dincer, I, Gabriel, K, Rosen, MA, Secnik, E, Easton, EB, Trevani, L, Pioro, I, Tremaine, P, Lvov, S, Jiang, J, Rizvi, G, Ikeda, BM, Lu, L, Kaye, M, Smith, WR, Mostaghimi, J, Spekkens, P, Fowler, M, Avsec, J. Clean hydrogen production with the Cu-Cl cycle - Progress of international consortium, II: Simulations, thermochemical data and materials. *International Journal of Hydrogen Energy* 2011; 36: 15486-501.
- [45] Naterer, GF, Suppiah, S, Stolberg, L, Lewis, M, Ferrandon, M, Wang, Z, Dincer, I, Gabriel, K, Rosen, MA, Secnik, E, Easton, EB, Trevani, L, Pioro, I, Tremaine, P, Lvov, S, Jiang, J, Rizvi, G, Ikeda, BM, Lu, L, Kaye, M, Smith, WR, Mostaghimi, J, Spekkens, P, Fowler, M, Avsec, J. Clean hydrogen production with the Cu-Cl cycle – Progress of international consortium, I: Experimental unit operations. *International Journal of Hydrogen Energy* 2011; 36: 15472-85.
- [46] Ratlamwala, TAH, Dincer, I. Energy and exergy analysis of a Cu-Cl cycle based integrated system for hydrogen production. *Chemical Engineering Science* 2012; 84: 564-73.
- [47] Ferrandon, MS, Lewis, MA, Tatterson, DF, Gross, A, Diozi, D, Croize, L, Dauvois, V, Roujou, JL, Zanella, Y, Carles, P. Hydrogen production by the Cu-Cl thermochemical cycle: Investigation of the key step of hydrolysing CuCl_2 to Cu_2OCl_2 and HCl using a spray reactor. *International Journal of Hydrogen Energy* 2010; 35: 992-1000.
- [48] Orhan, MF, Dincer, I, Rosen, MA. Design of systems for hydrogen production based on the Cu-Cl thermochemical water decomposition cycle: Configurations and performance. *International Journal of Hydrogen Energy* 2011; 36: 11309-20.
- [49] Zamfirescu, C, Dincer, I, Naterer, G. Thermophysical properties of copper compounds in copper-chlorine thermochemical water splitting cycles. *International Journal of Hydrogen Energy* 2010; 35: 4839-52.
- [50] Lewis, MA, Masin, JG, Vilim, RB. Development of the Low Temperature Cu-Cl Thermochemical Cycle. *International Congress on Advances in Nuclear Power Plants* 2010.
- [51] Soliman, MA, Conger, WL, Carty, RH, Funk, JE, Coss, KE. Hydrogen production via thermochemical cycles based on sulfur chemistry. *International Journal of Hydrogen Energy* 1976; 1; 265-70.
- [52] Brecher, LE, Spewock, S, Warde, CJ. The Westinghouse sulfur cycle for the thermochemical decomposition of water. *International Journal of Hydrogen Energy* 1977; 2: 7-15.
- [53] Jomard, F, Feraud, JP, Caire, JP. Numerical modeling for preliminary design of the hydrogen production electrolyzer in the Westinghouse hybrid cycle. *International Journal of Hydrogen Energy* 2008; 33: 1142-52.
- [54] Hinkley, JT, O'Brien, J, Fell, CJ, Lindquist, SE. Prospects of solar only operation of the hybrid sulfur cycle for hydrogen production. *International Journal of Hydrogen Energy* 2011; 36: 11596-603.

- [55] Corgnal, C, Summers, W. Solar hydrogen production by the Hybrid Sulfur process. *International Journal of Hydrogen Energy* 2011; 36: 11604-19.
- [56] Ratlamwala, TAH, Dincer, I, Naterer, GF. Energy and Exergy Analyses of Integrated Hybrid Sulfur Isobutane System for Hydrogen Production. *International Journal of Hydrogen Energy* 2012; 37 (23): 18050-60.
- [57] Charton, S, Rivalier, R, Ode, D, Morandini, J, Caira, JP. Hydrogen production by the Westinghouse cycle: modelling and optimization of the two-phase electrolysis cell. *WIT Transactions on Engineering Sciences* 2009; 65: 11-22.
- [58] Summers, WA (Savannah River National Laboratory). Hybrid Sulfur Thermochemical Cycle. Annual Merit Report. DOE Hydrogen Program; 2009 Report No.: SRNS-STI-2009-00223.
- [59] Jeong, YH, Kazimi, MS, Hohnholt, KJ, Yildiz, B. Optimization of the hybrid sulfur cycle for hydrogen production. *Nuclear Technology* 2007; 159: 147-57.
- [60] Uhrig, RE. Producing hydrogen using nuclear energy. *International Journal of Nuclear Hydrogen Production Application* 2008; 1: 179-93.
- [61] Forsberg, C, Bischoff, B, Mansur, LK, Trowbridge, L, Tortorelli, P. A lower temperature Iodine-Westinghouse-Ispra Sulfur process for thermochemical production of hydrogen. In Proc. American nuclear society 2003 winter meeting, New Orleans, 2003; November 16-20.
- [62] Brown, LC, Besenbruch, GE, Lentsch-Schultz, KR, Funk, JF, Pickark, PS, Marshall, AC, Showalter, SK. High efficiency generation of hydrogen fuels using nuclear power, Technical Report GA-A24285, 2002; General Atomics, San Diego, CA.
- [63] Orhan, FO. Energy, Exergy and Cost Analyses of Nuclear-Based Hydrogen Production via Thermochemical Water Decomposition Using a Copper-Chlorine (Cu-Cl) Cycle. MASC thesis, FEAS, UOIT, 2008.
- [64] Arachchige, SM, Brown, J, Brewer, KJ. Photochemical hydrogen production from water using the new photocatalyst $[(bpy)_2Ru(dpp)]_2RhBr_2(PF_6)_5$. *J Photochemistry and Photobiology A: Chemistry* 2008; 197: 13-7.
- [65] Baniasadi, E, Dincer, I, Naterer, GF. Performance analysis of a water splitting reactor with hybrid photochemical conversion of solar energy. *International Journal of Hydrogen Energy* 2012; 37: 7464-72.
- [66] Zamfirescu, C, Dincer, I, Naterer, GF. Molecular charge transfer and quantum efficiency analyses of a photochemical reactor for hydrogen production. *International Journal of Hydrogen Energy* 2012; 37: 9537-49.
- [67] Elvington, M, Brown, JR, Zigler, DF, Brewer, KJ. Supramolecular complexes as photo initiated electron collectors: applications in solar hydrogen production. *Solar Hydrogen and Nanotechnology* 2006; 6340: 1-13.
- [68] Schulz, M, Karnahl, M, Schwalbe, M, Vos, JG. The role of the bridging ligand in photocatalytic supramolecular assemblies for the reduction of protons and carbon dioxide. *Coordination Chemistry Reviews* 2012; 256: 1682-1705.

- [69] Prussin, AJ, Zigler, DF, Jain, A, Brown, JR, Winkel, BSJ, Brewer, KJ. Photochemical methods to assay DNA photocleavage using supercoiled pUC18 DNA and LED or xenon arc lamp excitation. *Journal of Inorganic Biochemistry* 2008; 102: 731-9
- [70] White, TA, Rangan, K, Brewer, KJ. Synthesis, characterization, and study of the photophysics and photocatalytic properties of the photoinitiated electron collector $[(\text{phen})_2\text{Ru}(\text{dpp})]_2\text{RhBr}_2(\text{PF}_6)_5$. *Journal of Photochemistry and Photobiology A: Chemistry* 2010; 209: 203-9.
- [71] Rangan, K, Arachchige, SM, Brown, JR, Brewer, KJ. Solar energy conversion using photochemical molecular devices: photocatalytic hydrogen production from water using mixed metal supramolecular complexes. *Energy Environment Science* 2009; 2: 410-9.
- [72] Arachchige, SM, Brown, JR, Chang, E, Jain, A, Zigler, DF, Rangan, K, Brewer, KJ. Design considerations for a system for photocatalytic hydrogen production from water employing mixed-metal photochemical molecular devices for photoinitiated electron collection. *Inorganic Chemistry* 2009; 48: 1989–2000.
- [73] Brewer, KJ, Elvington, M, Supramolecular complexes as photocatalysts for the production of hydrogen from water, Patent number: 7582584 2009.
- [74] Richter, MM, Brewer, KJ. Spectroscopic, electrochemical, and spectroelectrochemical investigations of mixed-metal osmium(II)/ruthenium(II) bimetallic complexes incorporating polypyridyl bridging ligands. *Inorganic Chemistry* 1992; 31:1594–98.
- [75] Rabbani, M. Design, analysis and optimization of hybrid photochemical hydrogen production systems. Ph.D. proposal, FEAS, UOIT, 2012.
- [76] Elvington, M, Brewer, KJ. Photoinitiated electron collection at a metal in a rhodium-centered mixed-metal supramolecular complex. *Inorganic Chemistry* 2006; 45: 5242–44.
- [77] Kamiya, M, Ohta, T. Solar-hydrogen energy systems. New York: Pergamon Press; 1979.
- [78] Buehler, N, Meier, K, Reber, JF. Photochemical hydrogen production with cadmium sulfide suspensions, *Journal of Physical Chemistry* 1984; 88: 3261- 8.
- [79] Reber, JF, Rusek, M. Photochemical hydrogen production with platinized suspensions of cadmium sulfide and cadmium zinc sulfide modified by silver sulfide. *Journal of Physical Chemistry* 1986; 90: 824-34.
- [80] Li, C, Wang, M, Pan, J, Zhang, P, Zhang, R, Sun, L. Photochemical hydrogen production catalyzed by polypyridyl ruthenium–cobaloxime heterobinuclear complexes with different bridges. *Journal of Organometallic Chemistry* 2009; 694: 2814-19.
- [81] Reber, JF, Meier, K. Photochemical Production of Hydrogen with Zinc Sulphide Suspensions. *Journal of Physical Chemistry* 1984; 88: 5903-13.
- [82] Xing, C, Zhang, Y, Yan, W, Guo, L. Band structure-controlled solid solution of Cd-ZnS photocatalyst for hydrogen production by water splitting. *International Journal of Hydrogen Energy* 2006; 31: 2018-24.

- [83] Amouyal, E. Photochemical production of hydrogen and oxygen from water: A review and state of the art. *Solar Energy Materials and Solar Cells* 1995; 38: 249–76.
- [84] Kang, HW, Lim, SN, Park, SB. Co-doping schemes to enhance H₂ evolution under visible light irradiation over SrTiO₃:Ni/M (M=La or Ta) prepared by spray pyrolysis. *International Journal of Hydrogen Energy* 2012; 37: 5540-49.
- [85] Yu, H, Yan, S, Li, Z, Yu, T, Zou, Z. Efficient visible-light-driven photocatalytic H₂ production over Cr/N-Codoped SrTiO₃. *International Journal of Hydrogen Energy* 2012; 37: 12120-27.
- [86] Kang, HW, Lim, SN, Song, D, Park, SB. Organic-inorganic composite of g-C₃N₄-SrTiO₃:Rh photocatalyst for improved H₂ evolution under visible light irradiation. *International Journal of Hydrogen Energy* 2012; 37: 11602-10.
- [87] Leilei, X, Lei, N, Weidong, S, Jianguo, G. Photocatalytic Activity for Hydrogen Evolution over Well-Dispersed Heterostructured In₂O₃/Ta₂O₅ Composites. *Chinese Journal of Catalysis* 2012; 33: 1101–08.
- [88] Xu, L, Shi, W, Guan, J. Preparation of crystallized mesoporous CdS/Ta₂O₅ composite assisted by silica reinforcement for visible light photocatalytic hydrogen evolution. *Catalysis Communications* 2012; 25: 54–58.
- [89] Khan, Z, Qureshi, M. Tantalum doped BaZrO₃ for efficient photocatalytic hydrogen generation by water Splitting. *Catalysis Communications* 2012; 28: 82–85.
- [90] Kanhere, P, Zheng, J, Chen, Z. Visible light driven photocatalytic hydrogen evolution and photophysical properties of Bi₃D doped NaTaO₃. *International Journal of Hydrogen Energy* 2012; 37: 4889-96.
- [91] Yang, J, Yan, H, Wang, X, Wen, F, Wang, Z, Fan, D, Shi, J, Li, C. Roles of cocatalysts in Pt–PdS/CdS with exceptionally high quantum efficiency for photocatalytic hydrogen production. *Journal of Catalysis* 2012; 290: 151–57.
- [92] Ikeue, K, Shinmura, Y, Machida, M. Ag-doped Mn–Cd sulfide as a visible-light-driven photocatalyst for H₂ evolution. *Applied Catalysis B: Environmental* 2012; 124: 84– 88.
- [93] Macias-Sanchez, SA, Nava, R, Hernandez-Morales, V, Acosta-Silva, YJ, Gomez-Herrera, L, Pawelec, B, Al-Zahrani, SM, Navarro, RM, Fierro, JLG. Cd_{1-x}Zn_xS solid solutions supported on ordered mesoporous silica (SBA-15): structural features and photocatalytic activity under visible light. *International Journal of Hydrogen Energy* 2012; 37: 9948-58.
- [94] Wang, J, Li, B, Chena, J, Li, N, Zhenga, J, Zhaoa, J, Zhu, Z. Enhanced photocatalytic H₂-production activity of Cd_xZn_{1-x}S nanocrystals by surface loading MS (M = Ni, Co, Cu) species. *Applied Surface Science* 2012; 259: 118– 23.
- [95] Yaoa, W, Songa, X, Huang, C, Xua, Q, Wua, Q. Enhancing solar hydrogen production via modified photochemical treatment of Pt/CdS photocatalyst. *Catalysis Today* 2013; 199: 42-47.

- [96] Wu, X, Song, Q, Jia, L, Li, Q, Yang, C, Lin, L. Pd-Gardenia-TiO₂ as a photocatalyst for H₂ evolution from pure water. *International Journal of Hydrogen Energy* 2012; 37: 109-14.
- [97] Onsuratoom, S, Puangpetch, T, Chavadej, S. Comparative investigation of hydrogen production over Ag-, Ni-, and Cu-loaded mesoporous-assembled TiO₂-ZrO₂ mixed oxide nanocrystal photocatalysts. *Chemical Engineering Journal* 2011; 173: 667– 75.
- [98] Parayil, SK, Kibombo, HS, Wua, CM, Peng, R, Baltrusaitis, J, Koodali, RT. Enhanced photocatalytic water splitting activity of carbon-modified TiO₂ composite materials synthesized by a green synthetic approach. *International Journal of Hydrogen Energy* 2012; 37: 8257-67.
- [99] Pérez-Larios, A, Lopez, R, Hernández-Gordillo, A, Tzompantzi, F, Gómez, R, Torres-Guerra, LM. Improved hydrogen production from water splitting using TiO₂-ZnO mixed oxides photocatalysts. *Fuel* 2012; 100: 139–43.
- [100] Matos, J, Marino, T, Molinari, R, García, H. Hydrogen photo production under visible irradiation of Au-TiO₂ activated carbon. *Applied Catalysis A: General* 2012; 418: 263– 72.
- [101] Design Expert V8, 2013 www.statease.com/dx8descr.html.
- [102] Gas pressure sensor, 2013 www.vernier.com/products/sensors/gps-bta.
- [103] pH sensor, 2013 www.vernier.com/products/sensors/ph-sensors/ph-bta.
- [104] Ion power inc., 2013 <http://www.ion-power.com/>.
- [105] TriSOL solar simulator, 2013 www.oainet.com/oai-solarsimulator-pp.html.
- [106] Digital linear power supplied, 2013 www.omega.com/pptst/PSU300.html.
- [107] Pyranometer, 2013 www.vernier.com/products/sensors/pyr-bta.
- [108] LabQuest mini, 2013 www.vernier.com/products/interfaces/lq-mini.
- [109] Logger Pro-lite, 2013 www.vernier.com/products/software/logger-lite.
- [110] Acula. Physics 1BB3. Laboratory Manual, Topic: "Modern physics for life sciences." Faculty of Science, McMaster University, Hamilton, McMaster, July 1,2013.
- [111] Bevington, PR, Robinson, DK. *Data Reduction and Error Analysis for the Physical Sciences*. 3rd ed. New York: McGraw Hill Education; 2003.
- [112] Fornasisni, P. *The Uncertainty in Physical Measurements*. New York: Springer; 2008.
- [113] Coleman, HW, Steele, WG. *Experimentation, Validation, and Uncertainty Analysis for Engineers*. New York: John Wiley & Sons; 2009.
- [114] Montgomery, DC. *Design and Analysis of Experiments*. 8th ed. John Wiley & Sons; 2012.
- [115] Montgomery, DC. *Introduction to Statistical Quality Control*. 6th ed. John Wiley & Sons; 2008.

- [116] Lind, I. Regressor and Structure Selection: Uses of ANOVA in System Identification. PhD Thesis, Linköpings Universitet, 2006.
- [117] Doncaster, CP, Davey, AJH. Analysis of Variance and Covariance. Cambridge University Press; 2007.
- [118] Quinn, GP, Keough, MJ. Experimental Design and Data Analysis for Biologists. Cambridge University Press; 2002.
- [119] Kalogirou, SA. Solar thermal collectors and applications. Progress in Energy and Combustion Science 2004; 30: 231-95.
- [120] Klein, SA. Engineering Equation Solver (EES): Academic Commercial. F-Chart Software, 2012 www.fChart.com.
- [121] Chandrand, RR, Chin, DT. Reactor analysis of chlor-alkali membrane cell. Electrochimica Acta 1986; 31: 39–50
- [122] Liu, RS. Electrochemical Technologies for Energy Storage and Conversion. Wiley-VCH; 2012.
- [123] Cengel, YA, Boles, MA. Thermodynamics: An Engineering Approach. 7th ed. New York: McGraw-Hill; 2011.
- [124] Sawyer, DT, Sobkowiak, A, Roberts, JL. Electrochemistry for Chemists. 2nd ed. New York: John Wiley; 1995.
- [125] Dincer, I, Rosen, MA, 2007. EXERGY-Energy, Environment and Sustainable Development, Elsevier: New York.
- [126] Xu, C, Wang, Z, Li, X, Sun, F. Energy and exergy analysis of solar power tower plants. Applied Thermal Engineering 2011; 31: 3904-13.
- [127] Secnik, E. Private Communication 2012.
- [128] Robertson, K, Athienitis, A. Solar energy for buildings. Canada Mortgage and Housing Corporation, 2012.
- [129] Aghahosseini, S, Rabbani, M, Shamim, R. Private Communication 2012.
- [130] Yu, PL. Multiple Criteria Decision Making: Concepts, Techniques, and Extensions. New York: Plenum Press; 1985.
- [131] Sayyaadi, H, Babaelahi, M. Multi-objective optimization of a joule cycle for re-liquefaction of the Liquefied Natural Gas. Applied Energy 2011; 88: 3012-21.
- [132] Bombarda, P, Invernizzi, CM, Pietra, C. Heat recovery from diesel engines: A thermodynamic comparison between Kalina and ORC cycles. Applied Thermal Engineering 2012; 30: 212-9.
- [133] Zamfirescu, C, Naterer, G, Dincer, I. Photo-electro-chemical chlorination of cuprous chloride with hydrochloric acid for hydrogen production. International Journal of Hydrogen Energy 2012; 37: 9529-36.

- [134] Naterer, GF, Fowler, M, Cotton, G, Gabriel, K. Synergistic roles of off-peak electrolysis and thermochemical production of hydrogen from nuclear energy in Canada. *International Journal of Hydrogen Energy* 2008; 33: 6849-57.
- [135] Lemus, RG, Duart, JMM. Updated hydrogen production costs and parities for conventional and renewable technologies. *International Journal of Hydrogen Energy* 2010; 35: 3929-3936.
- [136] Acar, C, Dincer, I. Comparative assessment of hydrogen production methods from renewable and non-renewable sources. *International Journal of Hydrogen Energy* 2013 (DOI:10.1016/j.ijhydene.2013.10.060).